

**PROCESSING OF NON-STATIONARY INTERFERENCE
PATTERNS: ADAPTED PHASE-SHIFTING ALGORITHMS
AND WAVELET ANALYSIS. APPLICATION TO DYNAMIC
DEFORMATION MEASUREMENTS BY HOLOGRAPHIC
AND SPECKLE INTERFEROMETRY**

THÈSE N° 1666 (1997)

PRÉSENTÉE AU DÉPARTEMENT DE GÉNIE CIVIL

ÉCOLE POLYTECHNIQUE FÉDÉRALE DE LAUSANNE

POUR L'OBTENTION DU GRADE DE DOCTEUR ÈS SCIENCES TECHNIQUES

PAR

Xavier COLONNA DE LEGA

Ingénieur diplômé de l'École Supérieure d'Optique, Orsay, France
de nationalité française

acceptée sur proposition du jury:

Prof. L. Pflug, directeur de thèse
Dr F. Ade, corapporteur
Dr A. Drygajlo, corapporteur
Prof. P. Jacquot, corapporteur
Dr J. Huntley, corapporteur
Prof. J. Taboury, corapporteur

Lausanne, EPFL
1997

Abstract

A new technique is presented, dynamic phase-shifting, which is based on a dedicated phase-shifting algorithm and a wavelet-transform analysis. This technique allows to perform measurements on non-static objects, using whole-field optical methods. These methods include classical, holographic and speckle interferometry as well as fringe projection and moiré. They cover a large domain of resolutions and dynamic ranges for the measurement of shape and deformation of rough and smooth objects. However, the lack of efficient solutions to process the fringe patterns obtained in dynamic conditions has hindered the development of high-potential methods such as speckle interferometry outside of the laboratory. The main goal of this thesis work is to find new answers to this problem.

The solutions we propose are based on the exploitation of the fringe movement produced by the deformation or displacement of the object. We observe that the corresponding phase variations of the interferogram can be used as a natural phase-shift to perform a quantitative phase evaluation. Moreover, it is shown that by adding a known phase step during image acquisition the sign of the displacement can be known without ambiguity. We demonstrate two particular techniques to process the image series recorded during dynamic phenomena. The first one is a 5-image phase-shifting algorithm, adapted to the problem of phase determination with unknown phase increments. The second solution is based on a wavelet-transform processing of the temporal signal recorded at each pixel of the camera. The goal is to estimate the phase of this sinusoidal signal as a function of time. We demonstrate that it can be obtained directly from the phase of the wavelet transform. The resulting method is highly immune to large signal noise. Moreover, we show that phase errors can be eliminated by combining the estimated phase evolution of neighboring pixels or by combining the corresponding real signals to create complex signals. This last approach is also used to extend the dynamic range of the technique.

Application examples in the case of holographic and speckle interferometry are presented and both processing methods compared. Their complementarity and robustness brings forth the possibility to apply optical interferometric techniques in situ, our goal being the development of such methods for civil engineering applications.

Keywords: dynamic measurement, interferometry, holography, speckle, phase-shifting, time-frequency analysis, wavelet transform.

Version abrégée

Nous présentons ici une technique originale, le décalage de phase dynamique, basée sur un algorithme du même nom et sur un traitement par transformée en ondelettes. Cette technique permet d'appliquer la plupart des méthodes optiques à champ complet aux objets non-stationnaires. Ces méthodes comprennent l'interférométrie classique, holographique et speckle ainsi que les moirés et la projection de franges. Dans le cadre de la mesure de forme ou de déformation d'objets polis ou rugueux, elles couvrent de larges domaines de sensibilité et de dynamique de mesure. Cependant, l'absence de méthodes d'analyse efficaces pour le traitement des figures de frange en mouvement a retardé l'application, hors du laboratoire, de méthodes à fort potentiel telles que l'interférométrie speckle. Le but principal de cette thèse est de répondre à ce besoin.

Notre travail s'articule autour de l'exploitation du mouvement des franges provoqué par la déformation ou le déplacement de l'objet. L'idée fondamentale consiste à observer que les variations de la phase de l'interférogramme fournissent un décalage de phase "naturel" permettant un dépouillement quantitatif. Nous montrons de plus que le signe du déplacement peut être déterminé de façon absolue lorsqu'un saut de phase connu est introduit pour chaque image enregistrée. Nous proposons deux techniques pour le traitement des séquences d'images enregistrées pendant un phénomène dynamique. La première est un algorithme à 5 images, adapté au problème de la détermination de la phase lorsque les incréments de phase sont inconnus. La deuxième solution est basée sur l'analyse par transformée en ondelettes du signal temporel enregistré par chaque pixel de la caméra. Le problème consiste alors à déterminer la phase de ce signal sinusoïdal au cours du temps. Nous montrons qu'elle peut être déduite directement de la phase de la transformée. Cette méthode présente d'excellentes caractéristiques de filtrage de bruit. Nous montrons également que certaines erreurs de phase peuvent être éliminées en combinant les lois d'évolution de phase de pixels voisins ou en créant des signaux complexes qui étendent par ailleurs la dynamique de mesure.

Des exemples d'application en interférométrie holographique et speckle permettent de comparer les deux approches. Leur complémentarité et leur robustesse rend possible l'application in situ des méthodes optiques interférométriques, notre but étant principalement le développement de tels outils pour la caractérisation d'éléments d'ouvrages d'art en génie civil.

Contents

Abstract.....	i
Version abrégée.....	ii
Contents.....	iii
Acknowledgments.....	viii
Conventions and notations.....	ix
1. Foreword.....	1
1.1 Background and technical goals.....	1
1.2 Original contribution of this dissertation work.....	3
1.3 Layout of the document; suggestions to the reader.....	3
1.4 Significance of this project.....	5
2. Shape and deformation measurement using whole-field optical techniques.....	7
2.1 Introduction, definitions.....	8
2.2 Classical interferometry.....	8
2.3 Holographic interferometry.....	11
2.4 Speckle interferometry.....	15
2.4.1 Fringe formation in speckle interferometry.....	16
2.4.2 Out-of-plane speckle interferometer.....	19
2.4.3 In-plane speckle interferometer.....	20
2.4.4 Speckle shearing interferometer.....	22
2.4.5 Contouring speckle interferometer.....	24
2.5 Fringe projection and moiré.....	25
2.6 Summary of the methods; Domain of application.....	27
2.6.1 Shape measurement.....	27
2.6.2 Deformation measurement.....	28

3. Fringe analysis techniques	31
3.1 Fringe enhancing techniques.....	32
3.2 Fringe skeletonization and fringe tracking	33
3.3 Phase-shifting	33
3.4 Single-image carrier-based methods	38
3.5 Wrapped phase enhancing	41
3.6 Phase unwrapping	42
3.7 Quantitative measurements in non-static conditions	45
4. Dynamic phase-shifting.....	49
4.1 Dynamic phase-shifting principle	49
4.1.1 Sampling rate considerations	50
4.1.2 Sign ambiguity in the phase estimation	55
4.1.3 Non-modulating pixels	56
4.1.4 Modulation loss	57
4.2 Phase extraction using phase-shifting algorithms.....	59
4.2.1 3+1 phase-shifting algorithm	61
4.2.2 Carré algorithm	62
4.2.3 5-image algorithm	63
4.2.4 Advanced phase-shifting algorithms	64
4.3 Phase extraction using time-frequency analysis.....	65
4.3.1 Fourier transform and windowed Fourier transform	67
4.3.2 Gabor transform	68
4.3.3 Wavelet analysis	69
4.4 Phase unwrapping in the case of DPS	72
5. Characterization of the 5-image algorithm	75
5.1 Overview of the 5-image algorithm	76
5.2 Phase increment estimation.....	77
5.3 Some properties of the arctangent function	81
5.4 Phase error distributions as a function of the phase.....	82

5.5	Phase error standard deviation as a function of the phase.....	84
5.6	Overall phase error standard deviation as a function of the phase increment	88
5.7	Influence of non-linear phase evolution	93
5.8	Implementation and examples	96
5.8.1	Application to holographic interferometry	97
5.8.2	Application in speckle interferometry	101
5.9	Conclusion	103
6.	Characterization of the wavelet-based phase extraction.....	105
6.1	The Morlet wavelet.....	106
6.2	Transform representation: spectrogram and scalogram	108
6.3	Examples of spectrograms	110
6.3.1	Transform of a sum of two signals	111
6.3.2	Transform of a signal with added Gaussian noise	112
6.3.3	Transform of a measured signal	114
6.3.4	Transform of a measured signal of varying frequency	114
6.4	Interference effects with the Morlet wavelet.....	116
6.4.1	Well-conditioned analysis	117
6.4.2	Low frequency interference effects	117
6.4.3	High frequency interference effects	119
6.5	Phase properties of the Morlet wavelet transform	120
6.5.1	Developed expression of the transform	121
6.5.2	Ridge extraction	123
6.5.3	Examples of ridge extraction	125
6.6	“Sensitivity” of the wavelet-based phase measurement	131
6.6.1	Impulse response of the wavelet phase analysis	132
6.6.2	Effect of large phase jumps	133
6.7	Phase errors due to non-linear phase evolution	134
6.7.1	Phase estimation error in the case of a sinusoidal frequency modulation	135
6.7.2	General effect of the second derivative of the phase	137
6.7.3	Harmonic generation due to incorrect phase-shifting device calibration	138

6.8	Phase errors in the presence of noise	140
6.9	Summary: wavelet-based phase analysis properties.....	142
7.	Phase-shifting algorithm and wavelet-processing software implementation.....	145
7.1	Adapted 5-image algorithm.....	145
7.1.1	Phase calculation	145
7.1.2	Spatial unwrapping of noisy wrapped phase maps	147
7.2	Wavelet-based phase analysis tools.....	149
7.2.1	DPSTools: wavelet-based processing of image series	150
7.2.2	Extension of the signal support	151
7.2.3	Mother wavelet sampling	154
7.2.4	Ridge extraction	155
7.2.5	Temporal unwrapping	157
7.2.6	Phase best-estimate	157
8.	DPS application examples	161
8.1	Acquisition set-up.....	161
8.1.1	Hisis 2001 digital camera	161
8.1.2	Production of a reference phase step	163
8.2	Thermal loading of a carbon-carbon composite.....	164
8.3	In-plane horizontal deformation of a rubber element	167
8.4	In-plane horizontal deformation of a concrete beam	171
8.5	Measurement in the case of total decorrelation	176
8.6	Cyclic loading measured with pulsed shearing speckle interferometry.....	181
8.7	Final observations.....	187
9.	Wavelet analysis extension	189
9.1	Chirped wavelets and combined phase-shifting/wavelet algorithm	189
9.1.1	Combination of the 5-image algorithm with wavelet analysis	190
9.1.2	Chirped wavelet analysis	191

9.1.3	Examples of correction of the phase systematic error	193
9.1.4	Improved robustness for rapid frequency transitions	194
9.2	Overcoming interference effects near the Nyquist limit	196
9.2.1	The need for a complex signal	196
9.2.2	Creation of a complex signal	199
9.2.3	Example of measurement in the Nyquist region	200
9.2.4	Benefit of the complex signal in the absence of interference effects	203
9.2.5	Beyond Nyquist?	205
10.	Conclusion and future prospects.....	207
10.1	Summary of completed work	207
10.2	Future prospects	209
Appendix A:	Speckle pattern properties	211
A.1	Properties of a single speckle pattern.....	211
A.1.1	Intensity and phase statistics	211
A.1.2	Average speckle dimensions	214
A.1.3	Speckle pattern evolution during object deformation	215
A.2	Speckle interferometry	216
A.2.1	Statistics of the modulation	216
A.2.2	Effect of speckle decorrelations	218
A.2.3	Optimum phase estimation	220
Appendix B:	Mathematical derivations	223
B.1	Morlet wavelet transform approximation	223
B.2	Morlet wavelet transform along the ridge.....	226

Acknowledgments

I first wish to thank Prof. Pflug for giving me the opportunity of making this thesis work in his laboratory. His constant efforts and faith in the interest of optical methods in the field of civil engineering provide a rich soil for the hatching of new ideas and techniques.

Many thanks to Prof. Jacquot who advised me and followed this work closely from the beginning. His scientific rigor and expertise in the field of optics have been a source of understanding and learning in our various metrological undertakings. I still remember our very first attempt at “dynamic phase-shifting” just after my arrival at IMAC, while studying the behavior of a composite structure. We did not know at the time that this would ultimately become the subject of a dissertation work...

Dr Drygajlo was a key player in the wavelet orientation that took this work. I owe him many thanks for his warm welcome and receptiveness, as well as for the time he spent to put me on the right track.

Thanks to Dr. F. Ade, Dr. A. Drygajlo, Dr. J. Huntley and Prof. J. Taboury for taking part in my dissertation jury.

Special thanks to Mathias Lehmann whose physicist insights led to many beneficial observations during this work. Equally important were his kindness and friendship.

I also wish to thank Alma di Tullio who developed the software part for the management of phase-shifting devices used in our applications. C. Gilliard built the corresponding hardware controller. May he be thanked for his rock-solid realizations as well as for their undocumented features.

Two Erasmus exchange students worked with me in these last 3 years. Alessandro Valdes took part to the early days of dynamic phase-shifting while David Venet solved quite elegantly the dreaded spatial-unwrapping problem in speckle interferometry. Many thanks and good luck to both of them.

We all come from different horizons at IMAC (civil engineering, physics, optics, electronics,...) and the resulting crossbreeding and exchange of ideas creates a rich research environment. Along the years I have learned to appreciate this prevailing and good-natured work atmosphere. I include everyone in my final thanks for the numerous professional and extra-professional relationships that developed in these few years.

Last but not least, I dearly thank Christine for her enduring patience, understanding and encouragements.

Conventions and notations

Throughout this document, equations and mathematical expressions are labeled in the form “(x-y)” where x is the chapter number and y the index of the equation in the chapter. Figures and tables are labeled similarly in the form “Figure x-y.” and “Table x-y.” respectively.

To prevent confusion with equations, which are referred to in the text without the keyword “Equation” or “Eq.”, references to figures, tables or paragraphs are made explicitly with the corresponding name.

Bibliographic references are grouped at the end of each chapter. There are no cross-references between chapters.

Since we are dealing with phase properties in several chapters, angular values will be repeatedly used. These angles are expressed in degrees or radians, depending on the context or on their magnitude. There are however many situations where the chosen unit is not actually specified. The symbol $^\circ$ will however be used for discriminating angles expressed in degrees instead of radians, the latter being usually written as a multiple or a fraction of π .

Symbols:

λ	wavelength of light (visible source)
φ	phase of a signal; phase of an interferogram
I_0	background intensity of an interferogram
I_M	modulation of an interferogram
$\Delta\varphi$	phase increment or phase variation that occurs between the acquisition of two successive samples of the interferogram
$\delta\varphi$	usually depicts a phase error or uncertainty
ω_s	instantaneous frequency (or pulsation) of a sinusoidal signal
ω_0	mother frequency of the Morlet wavelet
a	scale factor used in wavelet analysis; the actual central analysis frequency is given by ω_0/a
b	time at which the wavelet analysis is performed

1. Foreword

1.1 Background and technical goals

The work presented in this document took place in a very rich environment. The field of optical metrology is arguably more than one century old. However, major advances resulted from the invention of the laser about forty years ago. This new light source opened a realm of new techniques to both the physicist and the engineer. In particular, whole-field methods such as holography, speckle photography or speckle interferometry, coherent fringe projection,... cover an extended sensitivity domain and permit to measure shape, deformation, vibration modes,... or to detect defaults on almost every type of structure or material. Moreover, the capability to work with diffusing materials, that is, having a surface roughness larger than the wavelength of (visible) light, is a fundamental property of these recent tools.

The diffusion of such methods outside of the university laboratory into industry is a slow but accelerating process. As usual, high-technology domains such as space and aeronautics were the first to employ them, since there is a genuine need to understand the behavior of new materials and structures before sending them in the air or in outer space. Closer to us, the automotive industry has long used holography, for example to detect defects in tires or to study the vibration modes of car components, in order to detect potential failure points and reduce acoustic noise sources. Some manufacturers start using shape measurement methods to better control the complex shapes of car body parts that are assembled automatically by robots. This corresponds to a general need in the industry for better-characterized materials or parts. The development of the various ISO norms attests to it. Optical methods could and should play an important role in this context.

There still remains a good deal of research and development work to be done to augment the diffusion of whole-field optical techniques. We must remark that part of the technology is already mature; see for example the recent certification of shearography (or speckle shearing interferometry) by the Federal Aviation Administration. Industrial interest is also illustrated by the numerous European projects that deal currently with the development of new instruments or measurement systems based on speckle interferometry. The Stress Analysis Laboratory (IMAC) is involved in one of these projects, VISILAS, which aims at developing a high-acquisition-rate system for the characterization of large objects ($> 10 \text{ m}^2$), one of the goal being the application to civil engineering structures. These projects naturally ensure part of the necessary technology transfer from the research laboratories to the industry.

The remaining work for these same laboratories includes the improvement of the robustness of the existing techniques and the search for new approaches that extend their applicability. Robustness is essential when one consider using highly sensitive interferometric techniques outside of the controlled environment of the laboratory. Part of the solution resides in the “desensitization” of optical set-ups (readily possible for shearing and in-plane speckle interferometry), active stabilization of interferometers and the development of new processing methods to extract the useful information in adverse conditions. Furthermore, the lack of solutions to the problem of quantitative measurements in dynamic conditions has to be addressed. This dissertation proposes one such solution (see paragraph 1.2).

Among many possible application fields, IMAC is dedicated to the development of metrological tools adapted to civil engineering. This is quite challenging since usually large surfaces have to be considered. Moreover, large rigid-body displacements may often mask smaller displacement gradients related to stress concentrations in a loaded structure. Hence, both large dynamic-range and high-resolution systems are required. It seems that whole-field optical techniques are possible solutions that could usefully complement the mostly punctual measurement devices used in civil engineering. Possible applications include the study of new materials such as high-strength concretes or mixed wood-concrete or metal-concrete assemblies, the study of complex structures in order to refine finite-elements models and the study of the behavior of existing and aging structures. This last need is felt acutely in many industrialized countries such as Switzerland where recent studies indicate that more money is spent nowadays to maintain, retrofit or rebuild existing constructions than to construct new ones. In this context, it is important to provide the civil engineer

with additional evaluation tools. Eventually, this toolkit should enable a tighter control of the evolution of structures such as bridges, tunnels, dams,... along their life span. The outcome should be a more rational use of existing resources and an improvement of the effective security for the taxpayer-user.

1.2 Original contribution of this dissertation work

This work addresses the particular problem of measurements in dynamic conditions using whole-field optical techniques. Our original contribution is built on three main axes. The first one consists in recognizing the particular conditions that make possible the exploitation of the natural evolution of interferograms during dynamic events. This leads to the definition of the so-called dynamic phase-shifting technique, which permits to perform quantitative phase measurements with non-static interferograms. The second axis of development deals with the extension of existing fringe analysis algorithms to actually perform such phase extractions, which were until now impossible with the usual phase-shifting methods. The last and more important contribution is the development of a new processing approach based on time-frequency analysis and wavelet transforms. The outcome is a robust technique that permits to process interferogram movies and to reconstruct their temporal phase evolution. This makes possible absolute and continuous deformation measurements with a large number of whole-field optical methods, from holography and speckle interferometry to moirés.

1.3 Layout of the document; suggestions to the reader

We will briefly comment here on the organization of this document. The reader familiar with optical metrology can safely skip through Chapter 2 and the most part of Chapter 3 since the purpose of these chapters is to expose the rich background in which our developments take place. The central contributions of our work appear in Chapter 4, 5, 6 and 9, which deal with dynamic phase-shifting and wavelet-based processing. The main examples of application are grouped in Chapter 8.

A certain emphasis on speckle interferometry will appear throughout the text. This is a consequence of the current line of work of our laboratory. Indeed, the high potential of the method but also the corresponding difficulties offer an interesting research domain. This prompted us to group different topics related to speckle patterns in Appendix A.

Chapter 2 presents an overview of the whole-field optical techniques that can be used in the dynamic phase-shifting context. This includes classical, holographic and speckle interferometry, speckle photography, fringe projection and moiré. The examples of application show the types of interferograms that are usually obtained.

Chapter 3 describes the state-of-the-art in the field of fringe analysis. These image-processing tools are used to process the interferograms obtained with the methods presented in Chapter 2. We focus particularly on the techniques permitting a quantitative analysis of fringe patterns, by contrast with the methods used for defect detection and classification. The last paragraph in this chapter tries to identify the approaches that can be employed in the case of non-static interferograms.

Our original contribution begins in Chapter 4, which introduces the principles of dynamic phase-shifting. The requirements of the method are analyzed before discussing two possible approaches for the actual processing of the data recorded during dynamic phenomena. One solution, a 5-image algorithm, is derived from classical tools used in fringe analysis. The other one, based on a time-frequency analysis of the signals recorded along the time at each point of the interferogram, is completely new in the field of fringe analysis.

Chapter 5 is dedicated to the detailed characterization of the 5-image algorithm we adapted to the needs of dynamic phase-shifting. Most of this work is based on simulations. The last part of the chapter presents examples of phase measurement in holographic and speckle interferometry.

Chapter 6 is at the core of our more interesting results. Wavelet-based time-frequency analysis is first presented before detailing the particular phase properties of the Morlet wavelet. An algorithm used in the field of acoustic signal processing is then described. We show that it provides us with a very efficient means of estimating the phase of interferograms recorded temporally. Different properties of this new technique are characterized through simulations and actual examples.

Chapter 7 deals with practical details of software implementation of the two methods presented in Chapter 5 and 6. It includes a brief description of the spatial and temporal unwrapping algorithms we use. The last paragraph explains the process of maximum-likelihood phase estimation, which appears to be an essential tool for the processing of speckle interferograms.

Chapter 8 covers briefly the practical aspects of a measurement in dynamic phase-shifting conditions. In particular, we describe the digital CCD camera and

phase shifter used in our laboratory. Application examples follow including holographic and speckle interferometry experiments.

Chapter 9 presents recent results that extend the capabilities of the wavelet-based method, including a combination of wavelet processing with a 5-image algorithm, chirped wavelets and complex signals. This last possibility based on the particular phase properties of speckle patterns, leads to surprising results with respect to the Shannon's sampling theorem. This could actually permit to extend the measurement dynamic "beyond" the Nyquist cut-off frequency.

Chapter 10 summarizes the main points of our work and proposes a list of potential developments of the dynamic phase-shifting technique, in the field of deformation measurement as well as in other domains.

Appendix A presents speckle pattern properties useful to understand some of our developments, including maximum-likelihood arguments.

Appendix B is a short mathematical section that details the calculations used in Chapter 6 to obtain an approximated analytical expression for the wavelet transform.

1.4 Significance of this project

This thesis work brings forward new solutions to the problem of fringe analysis in the context of dynamic phenomena. As such, they provide new means to extend the domain of application of interferometric techniques outside of the laboratory. This important extension of their scope can particularly benefit the domain of civil engineering where the capability to operate in real and effective working conditions, added to high sensitivities and high measurement range can have an important impact on the understanding and assessment of the behavior of structures by the engineer.

2. Shape and deformation measurement using whole-field optical techniques

The field of optical metrology encompasses a large number of techniques allowing direct or indirect measurement of diverse physical quantities. The developments presented in this dissertation were conducted in the framework of “fringe-based” methods where the information ends-up coded as an intensity modulation of light. Such techniques can be punctual or spatial and usually rely on the use of an interference phenomenon or a specific structuring of light.

A particular focus is given here on so-called “whole-field” techniques, which provide direct measurement on a large number of points in a limited number of steps. Examples of application include measurement of shape, deformation, strain, refractive index, etc. Typically, one obtains an image of the object under study with superimposed alternately dark and bright fringes which are directly related to the measured quantity. When the image is formed on a 2-dimensional spatial detector such as an electronic camera, it becomes possible to sample the intensity distribution of light and code it in a digital form. A computer can then process this digital image to extract the useful information.

It is not our goal to present here a comprehensive, textbook-like study but rather to introduce the basic concepts related to this work. References to well-known optical textbooks will be proposed as a source of more detailed information. A particular emphasis will be placed on speckle interferometry techniques, which, by their ease of use, moderate cost and range of sensitivities, are good candidates for the development of integrated instruments usable outside of the controlled environment of the laboratory.

* The “dynamic phase-shifting” technique presented in the next chapters could as well be used in the case of punctual measurements.

2.1 Introduction, definitions

The optical techniques presented in the next sections are suitable tools for shape or deformation measurements on rough or smooth objects that can moreover be opaque or transparent. From the point of view of metrology they offer sensitivities ranging from the decimeter to the nanometer. Some of them are, by construction, more adapted to evaluate shape while others are better suited to evaluate displacement or deformation. In the domain of shape evaluation, classical interferometry is used for high precision measurements such as flatness testing while moiré and fringe projection techniques are less sensitive and thus adapted to 3-dimensional description of deep surfaces and their position in space. Large deformations can be evaluated by comparison of successive shapes while small deformations or displacements can be assessed with sensitive techniques such as holographic, speckle or grating interferometry. The latter are inherently differential methods but some particular set-ups have also been devised to perform “contouring”, i.e. shape measurement. For their part, shearing techniques used conjointly with speckle interferometry provide a means to evaluate directly out-of-plane displacement derivatives.

All techniques presented in the next paragraphs require at least a light source that illuminates the object under study and a detector capable of recording the light that is reflected, diffused or diffracted by the object. Methods such as classical, holographic, speckle and grating interferometry moreover demand that the source be sufficiently coherent. Lasers and occasionally filtered vapor lamps fulfill this requirement. The remaining methods, namely, moiré and fringe projection, do not need such source properties.

A typical image obtained with a whole-field technique consists of a fringe pattern overlaying an image of the object under study. The position and density of these fringes are governed by the measured physical quantity such that each fringe marks a region on the object where it has a constant value. We call “sensitivity” of a particular optical method the amount of this physical quantity that corresponds to a difference of one fringe.

2.2 Classical interferometry

The principles discussed here are common to all interferometric techniques¹. Interference patterns are created by the coherent interaction of two electromagnetic fields, usually described as complex quantities A of the form $a \cdot \exp(i\varphi)$ where a is the amplitude and φ is the phase. In optics, one usually speaks of optical wavefronts describing the propagation of such a field. The

working principle of any interferometer can be decomposed as follows. First, a wavefront produced by the light source is split in two. Next, the two new waves propagate along different “arms” of the interferometer. This propagation results in a change of the phase and amplitude of the two electromagnetic fields. The phase change $\Delta\varphi$ is actually proportional to the traveled optical path length:

$$\Delta\varphi = \frac{2\pi}{\lambda} \int_S n(s) ds \quad (2-1)$$

where λ is the wavelength of light and n is the refractive index profile of the medium along the trajectory S followed by the wavefront. At least one of the waves interacts with the object and this interaction is also reflected in its phase. Finally, the two components are brought together on the detector. At this point the fields add resulting in the complex amplitude A and the detector detects the corresponding intensity I :

$$I = A\bar{A} = (A_1 + A_2)(\bar{A}_1 + \bar{A}_2) \quad (2-2)$$

where the bar denotes complex conjugation. If we now develop this expression using the definitions of A_1 and A_2 , we obtain

$$A_1 = a_1 e^{i\varphi_1}, \quad A_2 = a_2 e^{i\varphi_2} \quad (2-3)$$

$$I = a_1^2 + a_2^2 + 2a_1 a_2 \cos(\varphi_1 - \varphi_2) \quad (2-4)$$

This equation can be written as

$$I = I_0 (1 + V \cos \varphi) \quad (2-5)$$

where I_0 is the background intensity, V is the contrast and φ is the phase of the resulting interferogram. An alternative expression that we will use at length is

$$I = I_0 + I_M \cos \varphi \quad (2-6)$$

where I_M is simply called the modulation.

The above equations are valid as long as the difference of optical path length traveled by the two waves is smaller than the coherence length of the source. The contrast of the interferogram is maximum when the two waves reach the detector at exactly the same instant. It decreases when one wave is delayed because it travels a longer optical path. The two waves are no longer present simultaneously on the detector when this additional path is larger than the coherence length of the source, hence the disappearance of the interference phenomenon (the contrast drops to zero). We can note that some commercial optical profilometers actually make use of the appearance and disappearance of

fringes when a source of limited coherence length is used to probe the measurement volume. To the temporal coherence property corresponds a spatial coherence property which is related to the spatial extent of the source. It actually limits the volume in which a fringe pattern can be observed, because of the superposition in space of the concurrent interferograms created by elementary regions of the source. This is usually not an issue when lasers are used. It remains however that care must be taken to balance the two arms of any interferometer to get the highest possible contrast or modulation. A detailed presentation of coherence properties can be found in Ref.2 and 3.

We define “classical interferometry” as the set of methods based on “smooth” wavefronts, as opposed to the “speckled” wavefronts found in holographic or speckle interferometry. Smooth wavefronts are produced when all the optical elements composing the interferometer, as well as the object under test, have a surface roughness negligibly small compared to the wavelength of light. The Michelson, Mach-Zehnder or Fizeau interferometers are typical set-ups¹. Most of them are based on the interferometric comparison of an object wave to a reference wave, usually produced by a flatness reference surface such as a highly polished mirror. These techniques are thus well suited for non-contact shape or deformation* measurement of reflective objects, as well as for optical testing where different refractive surfaces act onto the shape of the object wavefront.

We can also mention a particular method, grating interferometry, which provides a means to measure the components of displacement of a given object in its tangential plane. However, contrary to the other techniques presented in this chapter, it requires that gratings be deposited on the surface of the object, which excludes it from the group of non-contact optical methods. In-plane speckle interferometry is a non-contact alternative. Typically, the object is illuminated by two symmetrical beams A and B, which are diffracted by the grating. The +1 order of diffraction of beam A is combined with the -1 order of diffraction of beam B. The resulting fringe pattern is sensitive to the displacements of the object in the direction orthogonal to the grating's grooves.

More specific interferometric methods are not mentioned here since we limit the scope of this chapter to the main techniques used for shape and deformation measurement.

A classical 2-beam interference pattern is presented in Figure 2-1. The horizontal cut at the right shows the corresponding grey levels (coded from 0 to 255). We can observe that the profile is not exactly sinusoidal as expected. This

* These types of interferometers are sensitive to the deformation along the surface normal.

is due to different types of noise and to the non-linear response of the electronics of the camera. In this particular image, the main source of noise is spurious fringe patterns due to diffraction of the laser light on dust particles covering the various optical components.

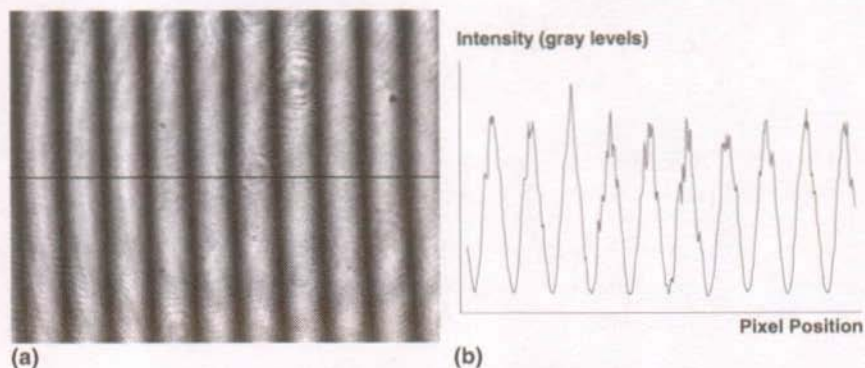


Figure 2-1. Michelson interferometer: (a) fringe pattern recorded by a CCD camera and digitized; (b) "Photometric" cut along the horizontal line drawn in (a).

2.3 Holographic interferometry

Holographic interferometry became a practical tool with the advent of lasers, thanks to their coherence properties. Applications cover shape and deformation measurement with the last topic being the domain of choice as holographic interferometry is inherently a differential method. It can be applied to both smooth and rough objects but we will focus on the last type.

Holography⁴ is based on the diffraction properties of light which provide a means to "record and replay" an optical wavefront. As a wavefront is characterized by a spatial distribution of amplitude and phase, both quantities need to be recorded. In photography, only the amplitude (or rather the corresponding intensity) is preserved and the "depth" information is lost. Unfortunately, physical detectors are only sensitive to intensity so this phase information needs to be converted into an intensity variation. This is achieved in holography by recording the interference pattern produced by the object wavefront and a reference wavefront, see Figure 2-2. Practical "detectors" in this case are holographic emulsions (in essence high-resolution photographic emulsions) or certain photothermoplastic materials. The interference pattern results in an absorption modulation (amplitude holograms) or a phase modulation (phase holograms).

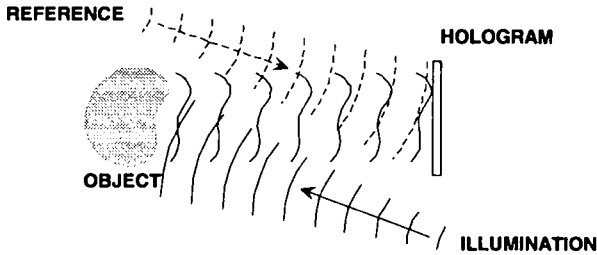


Figure 2-2. Recording of a hologram: The interference pattern of the object and reference waves is recorded in the holographic plate.

Diffraction now steps in with an interesting property: If a hologram is illuminated with one of the two waves that created the recorded pattern, part of the light is diffracted and recreates the second wavefront (Figure 2-3).

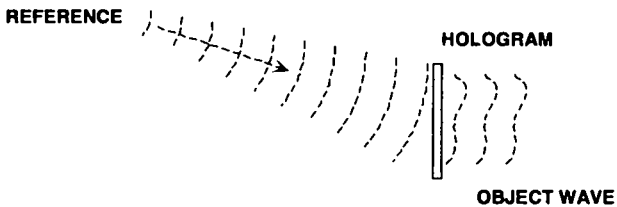


Figure 2-3. Restitution of the object wave by the illuminated hologram

A widespread application of these principles is the well known “display holography” but the engineer has found other uses for the technique: double-exposure and real-time holographic interferometry. The last technique consists of, first, recording a hologram of the object under study, second, developing and repositioning it with a high accuracy and third, reconstructing the object wave by illuminating the hologram with the reference beam while at the same time illuminating the object. If a detector (eye or camera) looks at the object through the hologram, it receives a wavefront produced by the illuminated object plus a similar wavefront diffracted by the hologram, see Figure 2-4. These two wavefronts interfere and their live interference pattern is a function of the displacement or deformation of the object with respect to its reference state recorded by the hologram.

With a similar principle, double-exposure holographic interferometry consists of recording two holograms at two different instants on the same plate.

Once reconstructed, the two object waves interfere and show the object deformation that occurred between the two exposures. This technique is well suited to the study of vibrating objects.

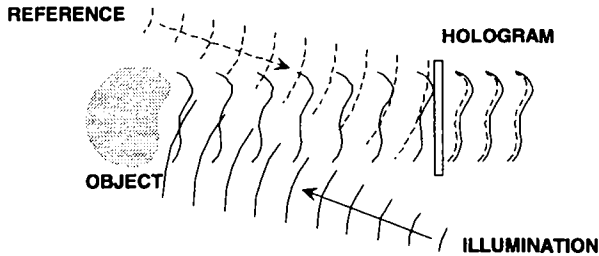


Figure 2-4. Superposition of the wavefront reconstructed from the hologram and the wavefront directly produced by the object.

When the surface of the object is rough compared to the wavelength of light, diffraction and diffusion of any impinging coherent beam produce a wavefront of granular nature called a speckle. This speckle is a fingerprint of the micro-roughness of the object. (The particular nature of speckle patterns and their statistical properties will be treated in the next paragraph and in Appendix A.) However, the interference pattern we described above is meaningful only when both waves (or speckles) are correlated. Here, correlation implies that the two speckles are identical and superposed in space. If this condition is not respected, no useful fringes will be obtained. This decorrelation can be produced by an inaccurate repositioning of the hologram after development, a large movement of the object with respect to its position at recording time or a change in its micro-roughness. One consequence is that one cannot compare directly two objects of the same shape with holography because of their different surfaces.

In the case of deformation measurements (which will be our major source of examples), one usually defines an observation direction as the line joining a current point M on the object to the center of the pupil of the observation objective (eye or camera). Similarly, an illumination direction is defined as the direction of the beam of light impinging the object at the current point. If we associate unit vectors to these directions, \mathbf{K}_o for observation and \mathbf{K}_e for illumination, a so-called "sensitivity vector" \mathbf{S} can be defined as $\mathbf{S} = \mathbf{K}_o - \mathbf{K}_e$.

This leads to a very general formula that can be used to understand most types of interferometric patterns. If we consider a particular point M on the

object that moves by an amount $d\mathbf{M}$, the corresponding phase change in the interferogram is given by

$$d\phi = \frac{2\pi}{\lambda} \mathbf{S} \cdot d\mathbf{M} \quad (2-7)$$

If a xyz coordinate system is defined on the object, with the x - and y -axis in the tangential plane to the object, the projection of \mathbf{S} along z defines the sensitivity to the "out-of-plane" displacement w of the point M . Similarly, the projection of \mathbf{S} on the plane xy defines two additional sensitivities corresponding to the quantities u and v , called horizontal and vertical "in-plane" displacements.

Depending on the shape of the object, a combination of out-of-plane and in-plane displacement components can be obtained in the interferogram. For example, in Figure 2-5, the fringes observed in the center of the image correspond to displacement of the cylinder along its local normal (pure radial deformation) whereas on the sides they correspond to a combination of radial and tangential deformation. Care must thus be taken when interpreting the fringes in term of object deformation.

Sensitivity variations are another source of concern. They result from variations of \mathbf{S} along the surface of the object. Typically, \mathbf{K}_o varies as the field of view of the observation objective while \mathbf{K}_e is constant for a plane wave illumination but changes in the case of spherical wave illumination. The consequence is a variable sensitivity across the field of view of the interferometer.



Figure 2-5. Holographic interferometry fringes showing out-of-plane deformation due to thermal loading of a cylinder made of Invar.

The simplest holographic interferometry set-ups are mostly sensitive to out-of-plane deformation. Multiple illumination beams are required if in-plane displacements need to be evaluated, increasing the arrangement complexity.

In-plane speckle interferometry must then be considered as a more practical solution. Shape measurement or contouring is achieved in holography by using two different wavelengths or by immersing the object in a liquid whose refractive index can be varied uniformly.

This introduction to holographic interferometry is again far from exhaustive and additional information can be found for example in books written by Vest⁵, Schumann⁶, Kreis⁷ or Jones and Wykes⁸.

2.4 Speckle interferometry

Speckle patterns are formed when a rough object is illuminated by any light source (see paragraph 2.3). We will restrict ourselves to the use of monochromatic light, usually produced by lasers. An introduction to the speckle phenomenon and its applications can be found in Ref.9. A summary of the properties related to speckle metrology is also presented in Appendix A.

Speckle techniques are usually separated in two large families, speckle interferometry and speckle photography^{10,11,9,8,7}. In both cases, a speckle pattern corresponding to a reference state of the object is recorded (on a photographic plate or by a camera). This reference is next compared to the current state of the object undergoing deformation. In the case of speckle photography the speckle grains actually act as markers whose movements are monitored and a single beam of light is needed to illuminate the object. Speckle photography is thus not by nature an interference method even though its post-processing usually imply the use of interference patterns⁸. The two speckle fields that are compared need to be identical but not necessarily superposed in space since speckle grains usually move by an amount larger than their own size with this technique. Speckle interferometry, on the other hand, requires a complete correlation between the two speckle patterns that are compared, as in holographic interferometry. Moreover, each set-up requires a 2-beam illumination of the detector, producing interference. Speckle interferometry is thus very close to its holographic counterpart. The main difference arises from the fact that in the case of holography the very fine fringe structure produced inside the speckle grains has to be recorded, hence the high resolution photographic plate. In the case of speckle interferometry only the intensity of the speckle grains usually needs to be recorded* (there are a few exceptions like the Duffy technique for in-plane measurements). The recorded speckle is produced by the interference of a

* As seen in Appendix A it is not even necessary to resolve the speckle grains themselves, especially when one uses a CCD camera as a detector.

speckle wave coming from the object and a smooth reference (out-of-plane set-up) or from two object speckle waves (in-plane or shearing set-ups).

As the method we wish to present is based on a “live” interference phenomenon, we will not consider speckle photography in the rest of this document. We note however that digital versions of the technique exist, based on numerical correlation of successive speckle images. The use of photographic plates in speckle interferometry is now obsolete with the availability of cheap CCD cameras and video acquisition boards for computers. The main advantage is the ease of use of these video set-ups where reference states can be obtained instantaneously, without any lengthy and messy chemical processing of photographic emulsions. This ease of use also permitted the conception of commercial instruments such as shearing speckle interferometers and integrated in-plane and out-of-plane instruments.

We will now briefly explain the principle of fringe visualization in speckle interferometry using electronic cameras and then describe the three basic configurations of speckle interferometers. The quantitative analysis of these fringe patterns will be treated in the next chapter.

2.4.1 Fringe formation in speckle interferometry

As mentioned above, the interferogram is either created by the interference of two speckle waves or one speckle wave plus a smooth reference. The result is another speckle pattern where no fringes appear directly, contrary to classical or holographic interferometry. One can simplify the approach to speckle interferometry by considering that each speckle grain in the image plane of the detector is itself a small interferogram that can be described as in (2-6) where the background intensity I_0 , the modulation I_M and the phase φ are constant quantities. This is a first-order approach as, first, it is difficult to define exactly the extent of a speckle grain, and second, these three quantities are susceptible to vary inside the grain itself. All the parameters characterizing this interferogram are random variables whose statistics are known (see Appendix A). In particular, the quantity of interest, i.e. the phase, is initially random and uniformly distributed over $[0, 2\pi]$. The statistics of the other two parameters depend among other things on the number of speckle grains that cover a single picture element, or pixel, of the detector. Until recently it was considered a good practice in speckle interferometry to actually resolve the speckle grains. This implied aperture numbers of the imaging lens on the order of F/40 (this depends of course on the actual size of one pixel). However, as mentioned in Chapter 4.3 of Ref.8, practical apertures on the order of F/8 still provide useful fringe patterns

with the added benefit of a better use of the available light, since a source 25 times less powerful gives the same illumination of the detector. These properties have been studied theoretically and experimentally^{12,13}, confirming the fact that speckles do not need to be resolved to obtain fringe patterns and showing that apertures as high as $F/2$ can actually be used. We will not distinguish between the resolved or unresolved case in the following paragraphs as the mathematical formalism is the same.

The detection stage of a typical speckle interferometer set-up nowadays consists of a camera and a frame grabber for numerical images acquisition. In most cases, the frame grabber digitizes the video signal produced by the camera. Non-standard "digital" cameras are also available that provide directly images in numerical format. In this case the individual electrical charges of each pixel are independently measured, contrary to the classical scheme where an analog video signal consists of continuous TV lines, thus losing the initial segmentation of the image plane.

In any case, one obtains numerical images that represent more or less accurately the intensity of the speckle pattern in the image plane. The computer can then perform any mathematical operation between these images. For visualization purposes, simple subtractions or additions are sufficient, leading to real-time* observation of interference fringes.

The first step of any experiment consists of recording the intensity of the speckle pattern. This is the reference state. The initial intensity recorded for each speckle grain is

$$I_i = I_0 + I_M \cos \varphi_i \quad (2-8)$$

After deformation of the object, a second image is recorded. The new intensity of a given speckle grain changes to

$$I_d = I_0 + I_M \cos(\varphi_i + \varphi_d) \quad (2-9)$$

where φ_d is the phase change produced by the deformation. It can be related to the actual displacement of the corresponding region on the object using (2-7). Because φ_i is a random variable, both images do not display any fringe pattern. However if we compute the square of the difference between the first and the second image we obtain

$$(I_d - I_i)^2 = 2I_M^2 \sin^2\left(\varphi_i + \frac{1}{2}\varphi_d\right)(1 - \cos \varphi_d) \quad (2-10)$$

* Real-time is of course a figure of speech. Standard cameras provide images at a rate of 25 or 30 Hertz, which is sufficient for the eye.

the envelope of which is a cosine function of φ_d . If the phase change is equal to an even number of π then the second parenthesis in (2-10) is null, creating a dark spot in the resulting image, independently of the values of I_M and φ_i . On the other hand, if the phase change is an odd number of π then the second parenthesis evaluates to 2. The result of the difference now depends on the respective values of I_M , φ_i and φ_d . The mathematical mean of the resulting random quantity is non-zero. This will appear as a "bright" fringe. However, there will always be dark points in these bright fringes. The corresponding interferograms appear as "grainy", which leads some authors to speak of "speckle noise" as in signal to noise ratio. We rather consider that the speckles actually are the signal, admittedly sometimes a poor one. Anyway, as in other interferometry techniques, one obtains fringe patterns, which are related to the actual displacements of the object under study. The main difference is that these fringes are "grainy" and no longer correspond to a 2-wave interference pattern of sinusoidal intensity profile. Consequently, the fringe analysis techniques used will be different.

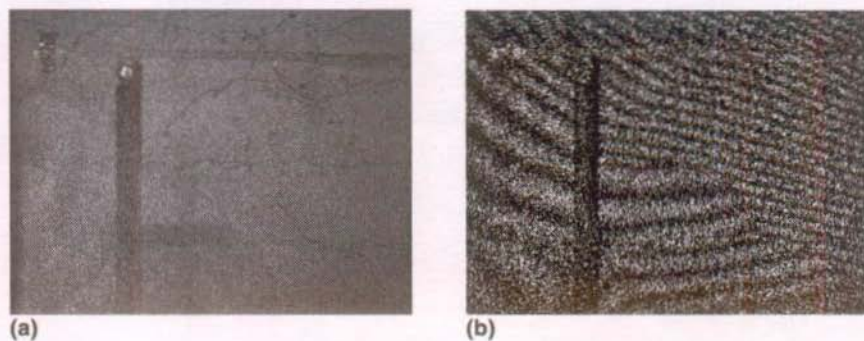


Figure 2-6. (a) Speckle image of a fractured concrete wall; (b) Subtraction of image (a) from a second image obtained after deformation. Equal out-of-plane displacement fringes are visible.

Figure 2-6 (a) shows a speckle pattern recorded in a set-up sensitive to out-of-plane displacement. The object is a concrete wall that was previously fractured. A second image was later recorded after a change of the load. The subtraction of the two images creates the fringe pattern seen in (b)*. The discontinuities of the fringes demonstrate the relative movements of the different regions of the wall separated by the cracks.

* The contrast of the fringes was enhanced using an histogram equalization of the image.

A second method consists of adding two intensity patterns such as (2-8) and (2-9). The problem is that the background intensity term no longer disappears:

$$I_d + I_i = 2I_0 + 2I_M \cos\left(\varphi_i + \frac{1}{2}\varphi_d\right)\cos\left(\frac{1}{2}\varphi_d\right) \quad (2-11)$$

This reduces the visual contrast of the fringes. However, it becomes possible to perform double-exposure experiments with very short delay between exposures¹⁴. Both exposures are added in the same camera frame. This allows one to perform deformation measurements on objects vibrating at high frequencies or submitted to transients, using a standard 25 Hz camera and a double-pulsed laser.

2.4.2 Out-of-plane speckle interferometer

Figure 2-6 above presents out-of-plane fringes obtained with a set-up similar to the one presented in Figure 2-7. A small portion of a laser beam is taken by a beamsplitter plate that directs the light through a high-aperture lens L. This produces a reference diverging beam on the CCD. The image of the focal point of L is ideally located at the center of the exit pupil EXP of the imaging lens IL. The main part of the initial laser beam goes through a microscope objective that illuminates the object, which is imaged by IL onto the CCD.

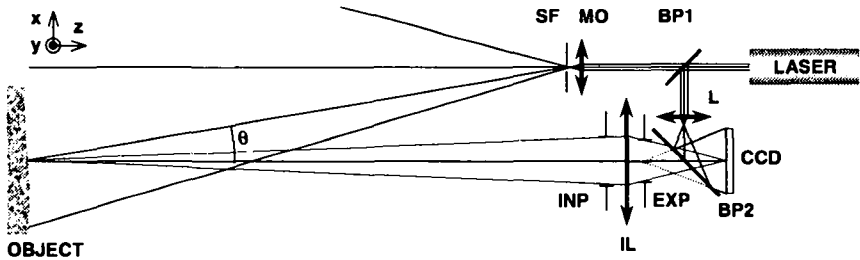


Figure 2-7. Example of out-of-plane speckle interferometer.

In the plane xz of the figure, the sensitivity or amount of deformation along the z -axis that produces one fringe is deduced from (2-7). This gives:

$$s = \frac{\lambda}{1 + \cos\theta} \quad (2-12)$$

where θ is the angle between the illuminating light beam and the observation direction from the entrance pupil of IL, at the point considered on the object.

In the same plane xz , the sensitivity to displacement along the x -axis is

$$s = \frac{\lambda}{\sin \theta} \quad (2-13)$$

As this in-plane component is usually not wanted for an out-of-plane set-up, θ should be kept as small as possible. By construction, the sensitivity along the y -axis is null in the plane xz . However, there will be a small sensitivity to this component above and below this plane.

To prevent sensitivity variations, θ should not vary much over the region of interest. A simple solution is to place the illuminating objective far from the object. The best solution would be to illuminate the object with a plane wave. To further limit unwanted sensitivities and their variations, the imaging lens should also be as far as possible from the object. It must be noted that the sensitivity to out-of-plane displacement is on the order of $\lambda/2$ and that there is no simple way to “lower” this sensitivity with the set-up as is. This high sensitivity means that most small perturbations in the experimental environment will translate in a *perturbation of the fringe pattern*.

In the case of large and distant objects, for example civil engineering structures, the set-up as depicted in Figure 2-7 can produce low-quality fringe patterns, as there is a large difference of optical path length between the two interfering beams. This is linked to the coherence length of the source. The problem can be overcome by first sending the reference beam on a mirror or corner-cube located near the object before imaging it on the CCD.

2.4.3 In-plane speckle interferometer

A typical in-plane speckle interferometer is presented in Figure 2-8. Two laser beams are focused using microscope objectives MO1 and MO2. The two diverging beams are then steered towards the object by mirrors M1 and M2. In a well-adjusted set-up, the beams should impinge on the object under symmetrical orientations with respect to the object normal \mathbf{N} , i.e. $\theta_1 = -\theta_2$.

This set-up can be understood as the superposition of two out-of-plane set-ups with opposite angles of illumination. The phase of the two speckle fields that interfere changes as in (2-7) when an object point \mathbf{M} moves by an amount $d\mathbf{M}$. As the phase of the interferogram is given by their difference, one obtains an overall phase change

$$\Delta\varphi = \frac{2\pi}{\lambda} (\mathbf{S}_2 - \mathbf{S}_1) \cdot d\mathbf{M} \quad (2-14)$$

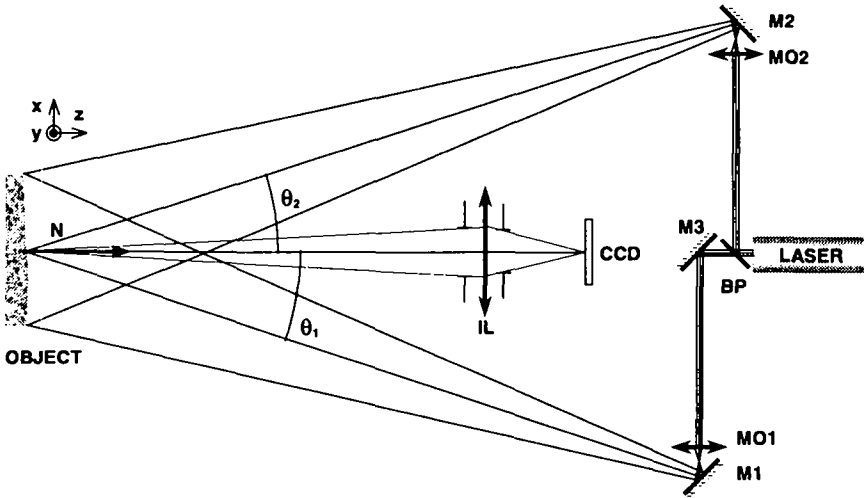


Figure 2-8. Example of in-plane speckle interferometer.

Consequently, the observation direction K_o disappears from the equation. In other words, the first-order sensitivity is not influenced by the position of the imaging camera. For each object point where the two illumination beams are symmetrical with respect to the local normal, $\theta_1 = -\theta_2 = \theta$, the in-plane sensitivity along the x -axis is

$$s_x = \frac{\lambda}{2 \sin \theta} \tag{2-15}$$

whereas the out-of-plane sensitivity s_z is null. For points where the two angles are no longer symmetrical, the x -axis in-plane sensitivity becomes

$$s_x = \frac{\lambda}{\sin \theta_1 - \sin \theta_2} \tag{2-16}$$

while the out-of-plane sensitivity along the z -axis becomes

$$s_z = \frac{\lambda}{\cos \theta_1 - \cos \theta_2} \tag{2-17}$$

As in the case of an out-of-plane set-up, there is a small sensitivity to y -axis in-plane displacement. Again, all unwanted sensitivities and their variations will be reduced when the source points are far from the object.

An interesting property of the in-plane set-up is the possibility to change its sensitivity by varying the illumination direction. Practical values range from a

few tens of λ down to $\lambda/1.8$. This provides a little immunity to external perturbations when a low sensitivity is used. It also makes possible measurements on large structures susceptible of large displacements.

Interpretation of in-plane fringes is not as easy as in the case of out-of-plane. For example, parallel horizontal fringes would indicate a rotation of the object in the plane xy . In Figure 2-9, the density of these fringes varies along the image. This denotes a combination of a rotation plus a bending of the object. Discontinuities in the fringe pattern indicate the presence of cracks. The sensitivity in this example was about $2 \mu\text{m}$ per fringe.

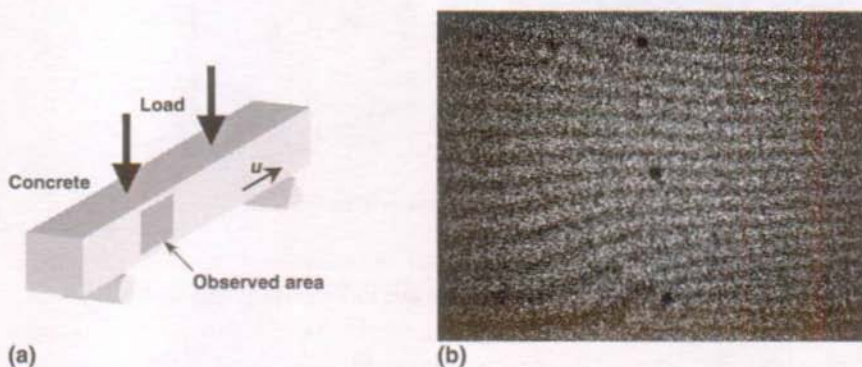


Figure 2-9. (a) 4-point bending experimental set-up. A 30 x 40-cm region of the concrete beam is observed with the camera. (b) In-plane displacement fringes obtained near one of the load insertion points.

2.4.4 Speckle shearing interferometer

The third essential set-up is the speckle shearing interferometer presented in Figure 2-10. A single beam of light illuminates the object, which is viewed by the camera through a Michelson interferometer. The purpose of this interferometer is to create two laterally shifted images on the detector. This is achieved by a tilt of one of the mirrors.

The two speckle fields that interfere at one given point of the detector correspond to two points on the object, say A and B, distant by an amount Δx . This lateral shift is adjustable through the rotation of the mirror M2. The sensitivity vector is the same as in out-of-plane speckle interferometry.

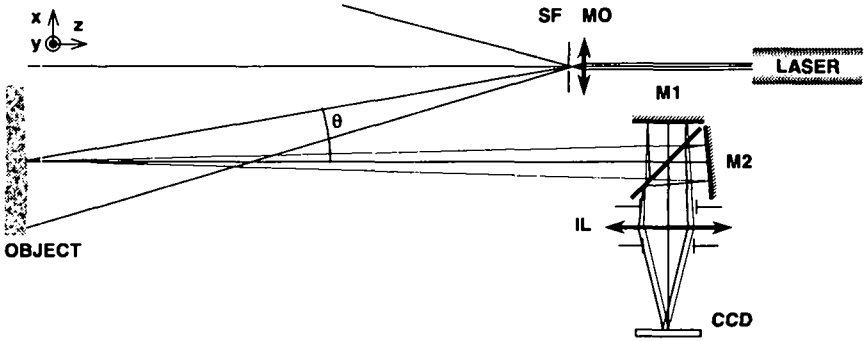


Figure 2-10. Example of speckle shearing interferometer.

The phase change of the interferogram is now proportional to the difference of displacement of the two points:

$$\Delta\varphi = \frac{2\pi}{\lambda} [(1 + \cos\theta)(w_B - w_A) - \sin\theta(u_B - u_A)] \tag{2-18}$$

where w_A and w_B are the displacements of the points along the z -axis and u_A and u_B are the displacements along the x -axis. Again, it is useful to have the angle θ as small as possible to limit the unwanted in-plane sensitivity. While neglecting this in-plane component, (2-18) is often rewritten with the lateral shift Δx to obtain a differential expression:

$$\Delta\varphi = \frac{2\pi\Delta x}{\lambda} (1 + \cos\theta) \frac{w_B - w_A}{\Delta x} \approx \frac{2\pi\Delta x}{\lambda} (1 + \cos\theta) \frac{\partial w}{\partial x} \tag{2-19}$$

Hence, speckle shearing interferometry is presented as a technique sensitive to the derivative of displacement in the direction of shear. A more rigorous interpretation based on (2-18) was recently proposed, along with a specific analysis method¹⁵. This technique permits to reconstruct the out-of-plane displacement map, transforming the speckle shearing interferometer in a variable-sensitivity out-of-plane interferometer.

An advantage of this technique is its relative simplicity and insensitivity to some perturbations as the two interfering waves are created very close to the detector. The set-up can be further simplified by replacing the Michelson interferometer by a bi-prism or, ideally, placing a bi-prism inside the objective, at the aperture stop position. Of course, the main advantage of the external interferometer is the possibility to change the shear angle and thus the sensitivity as well as the shear direction, making it a versatile instrument.

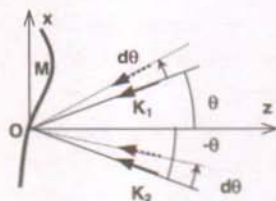
Similarly to in-plane speckle interferometry, fringe patterns obtained in shearing are not always easy to understand, as attests Figure 2-11. The object is the same as in Figure 2-6, but the field of view is smaller in this image. This region of the wall was covered by a network of parallel cracks oriented at plus and minus 30° with respect to the horizontal.



Figure 2-11. Fringes obtained for a vertical shear of the speckle pattern on the object of Figure 2-6.

2.4.5 Contouring speckle interferometer

The goal of this particular set-up is to perform shape measurements on rough objects. This is achieved with an interferometer similar to the one used for in-plane measurement. However, as there is no loading of the object, the fringes are produced by a rotation $d\theta$ of the two illumination beams in the same direction.



Let's call $\Delta\phi_0$ the total geometrical phase difference between the two symmetrical beams that illuminate the point O. The corresponding phase difference for a different point $M(x,z)$ is:

$$\Delta\phi_M = \Delta\phi_0 + \frac{2\pi}{\lambda} (\mathbf{K}_1 - \mathbf{K}_2) \cdot \mathbf{OM} \quad (2-20)$$

To simplify, we assume that the beams rotate by an angle $d\theta$ around the point O. If the rotation axis is somewhere else, which is usually the case in a real set-up, an additional phase constant is introduced at every point of the interferogram. With our hypothesis, $\Delta\phi_0$ does not change after rotation. For the point M, the new phase difference is given by (2-20) with the new vectors \mathbf{K}_1 and \mathbf{K}_2 . If $d\theta$ is

small, we obtain the total phase change between the two exposures for the point M as:

$$\Delta\phi = \frac{2\pi}{\lambda} 2z \sin\theta \sin d\theta \quad (2-21)$$

The sensitivity to the z coordinate (or surface height) is:

$$s = \frac{\lambda}{2d\theta \sin\theta} \quad (2-22)$$

The highest sensitivities are in the range of a few tens of λ . It is possible to obtain higher resolutions by cumulating successive $d\theta$ increments¹⁶, which also cancels decorrelation effects¹⁷. In Figure 2-12, the actual sensitivity is quite low, on the order of 1 mm. The object is a miniature propeller used for boat models.



Figure 2-12. Contouring fringes obtained on a miniature propeller.

The speckle contouring technique competes with fringe projection, as both methods provide the same kind of sensitivities. Its main advantage is that it can be easily integrated with an in-plane speckle interferometer.

2.5 Fringe projection and moiré

Although not interferometric techniques in essence, fringe projection and moiré provide fringe patterns very similar to 2-wave interferograms. Hence, the same fringe analysis methods can be used to obtain quantitative information. The main domain of application is shape measurement.

Fringe projection consists in creating a family of plane parallel "sheets" of light in the volume surrounding the object under investigation. Observation under an oblique angle gives an image where the fringe departure from straightness is related to the shape of the object. Figure 2-13 shows an

application to the measurement of the shape of the human face. The goal was to evaluate this technique as a tool for surgeons.

The "structuring" of light in sheets can be obtained with a simple slide projector using an incoherent source or, using a coherent source, a Michelson interferometer or a Wollaston cube used with a half-wave plate and a polarizer. Interferometric techniques have the double advantage of creating directly a sinusoidal fringe pattern with infinite depth of field. However, for a large and deep field of view, one can no longer consider the light sheets as being parallel and plane. Corrections and calibrations must be made to take into account their real nature, as they constitute a family of hyperboloids.

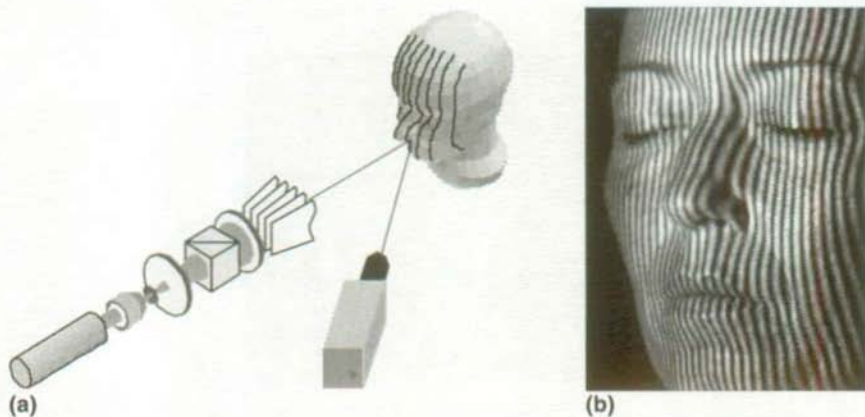


Figure 2-13. (a) Fringe projection using a Wollaston cube and polarized light; (b) Resulting image when applied to a human face.

The sensitivity of the technique is a function of the fringe spacing and the angle of observation. However, the main limitation is primarily the resolution of the imaging lens and camera used. Using state-of-the-art cameras and fringe analysis software, the depth resolution is on the order of one thousandth of the field of view.

Projection moiré is a way to increase the resolution of standard fringe projection. In particular, one can project on the object a very fine fringe pattern the image of which cannot be resolved directly by the detector*. However, if this fringe pattern is resolved by the imaging lens of the camera, one can place a reference grating at the image plane. This grating creates a moiré pattern with the fine line structure present on the object's image. The beat frequency is lower

* Commercial CCD cameras seldom resolve more than 50 lp/mm.

than the grating spatial frequency and can then be resolved by the detector. This is illustrated in Figure 2-14. The pattern at left is the reference pattern that would be placed in the image plane. The center pattern is the image of the deformed line structure created on the object. The right pattern shows the resulting moiré fringes. These fringes do not present a sinusoidal profile but the spatial frequency filtering performed by an actual lens would make them close substitutes. Consequently, the fringe processing techniques elaborated in the course of this dissertation work can also be applied.

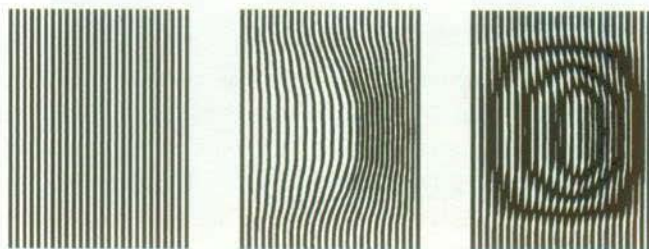


Figure 2-14. Reference grating (left), object grating (center) and resulting moiré fringe pattern (right).

Before the generalized availability of fringe analysis software, moiré techniques were very interesting for obtaining visually helpful fringe patterns. Nowadays, low sensitivity applications can be as easily performed using the much simpler fringe projection technique. However, moiré methods remain a way to “boost” the resolution of fringe projection when high resolution is required.

2.6 Summary of the methods; Domain of application

2.6.1 Shape measurement

Fringe projection and moiré are the “standard” whole-field methods for shape measurement of large and “deep” objects. Sensitivities can range from the decimeter to a fraction of millimeter. Such low sensitivities make these techniques insensitive to most environmental perturbations. Hence, their application is not limited to the laboratory. The Stress Analysis Laboratory used moiré in two civil engineering applications¹⁸. One was the measurement of the profile of road pavements with a moiré system mounted in a truck moving at 60 km/h. The other one was a large field-of-view moiré system (25 m²) used to

measure the shape of riverbed models. A current project deals with fringe projection on large (6 x 20 m) metallic box girders used in bridge construction.

Contouring with holography or speckle interferometry are used for smaller objects and higher resolutions. However, dual-wavelength or immersion holography is a complicated laboratory tool. Without the need for high-resolution media or vibration-isolated optical benches, speckle contouring could more easily gain some acceptance, for example in mechanical workshops where high-precision parts are manufactured.

2.6.2 Deformation measurement

Very low-sensitivity deformation measurements can be performed using fringe projection. One simply needs to compare shapes measured at different times. This tool has a large potential in the field of Civil Engineering where deformation amplitude of structures is usually large. However, it is limited to out-of-plane deformation measurements. There are many cases where a structure deforms in a predominant direction. It is sometimes interesting to study the resulting second-order deformations occurring in the other directions. One example is the study of stress distributions near joints of wood¹⁹. For this kind of displacements, holographic or speckle interferometry are ideal tools, thanks to their high-sensitivities to both in-plane and out-of-plane components. For example, the in-plane fringes of Figure 2-9 are sufficient to evaluate the variation of the local curvature of a concrete beam and detect invisible cracks by their disruption of both fringe pattern and curvature distribution. We recently used holography to study the behavior of a composite carbon-carbon structure of very-low thermal-expansion coefficient, under localized thermal loading. This structure is the body of a telescope developed by Aérospatiale for the European Space Agency.

The Laboratory of Stress Analysis has also been involved for the last couple of years in a Eureka program dedicated to the development of speckle interferometers for dynamic measurements on “large” surfaces, that is surfaces larger than 10 m². Part of the work covered in this dissertation was developed with this particular application in mind.

Besides structural testing, the fields of material testing and material science benefit also from these whole-field techniques. Poisson’s ratio, Young’s modulus, expansion coefficient, anisotropic properties of composite, concrete shrinkage²⁰ or concrete fracture mechanics^{21,22} are all examples of physical parameters that can be precisely measured or studied.

Whole-field techniques can also play a role in defect detection where defects appear as features of displacement fields. Shearing speckle interferometry is often used to detect delamination in composite panels. Another application is for example the study of concrete damage caused by frost²³. A lot of work has also been done to combine these optical techniques with knowledge based software systems to automatically detect and classify defects in various types of materials²⁴.

If fringe projection can provide a resolution on the order of the millimeter or sometimes better, holographic and speckle interferometry provide resolutions down to tens of nanometer for out-of-plane displacement. In-plane deformations can be measured with resolutions ranging from hundreds of nanometers to tens of microns, depending on the sensitivity chosen. A rule of thumb for all these methods is to consider that the fringe analysis techniques used for processing the interferograms can bring a resolution that ranges from a tenth to a hundredth of the sensitivity. These analysis techniques are presented in the next chapter.

Bibliography

- 1 W. H. Steel, "Interferometry", 1967, Cambridge University Press, .
- 2 M. Born, E. Wolf, "Principles of Optics", Pergamon Press, 1970.
- 3 L. Mandel, E. Wolf, "Optical coherence and quantum optics", Cambridge University Press, 1995, ISBN 0-521-41711-2.
- 4 R.J. Collier, C.B. Burckhardt, L.H. Lin, "Optical holography", Academic Press, 1971.
- 5 C. M. Vest, "Holographic Interferometry", 1979, John Wiley & Sons Ed, ISBN 0-471-90683-2.
- 6 W. Schumann, M. Dubas, "Holographic interferometry", Springer Verlag, 1979.
- 7 T. Kreis, "Holographic Interferometry: Principles and Methods", 1996, Akademie Verlag, ISBN 3-05-501644-0.
- 8 R. Jones and C. Wykes, "Holographic and Speckle Interferometry", 1983, Cambridge University Press, ISBN 0-521-23268-6.
- 9 "Laser Speckle and Related Phenomena", Ed. J.C. Dainty, 1975, Springer Verlag, ISBN 3-540-07498-8.
- 10 "Speckle metrology", Ed. R.K. Erf, Academic Press, 1978.
- 11 M. Françon, "Granularité laser. Speckle. Applications en optique", Masson, 1978.

- 12 M. Lehmann, "Phase-shifting speckle interferometry with unresolved speckles: A theoretical investigation", *Optics Com.* 128 (1996), pp. 325-340.
- 13 M. Lehmann, "Measurement optimization in speckle interferometry: The influence of the imaging lens aperture", *Optical Engineering*, scheduled for publication in April 1997.
- 14 A.J. Moore, C. Pérez-López, "Double-pulsed addition ESPI for harmonic vibration and transient deformation measurements", *Proceedings of the Appl. Opt. Div. Conf. of the IOP*, Reading 1996, pp. 228-238.
- 15 S. Waldner, "Removing the image-doubling in shearography by reconstruction of the displacement field", *Optics Com.* 127 (1996), pp. 117-126
- 16 M. Hertwig, "Application of improved speckle contouring technique to surface roughness measurements", *Optics and Lasers in Engineering* 26 (1997), pp. 115-130.
- 17 P. Jacquot, X. Colonna de Lega, "Mesure de forme par interférométrie speckle digitale", *Compte-rendu du congrès: "Mesure optique des formes 3D et des grandes déformations"*, 1994, Holo3 ed., Saint-louis, pp. 51-58.
- 18 S. Oesch, L. Pflug, "Relevé en continu de la topographie fine des chaussées et des médèles hydrauliques par moiré de projection", *Revue Française de Mécanique* 1988-2, pp. 61-67.
- 19 J. Sandoz, P.K. Rastogi, M. Walgenwitz, "Grading and reliability of glued laminated timber", *Proc. Pacific Timber Engineering Conference, Australia* (1994), pp. 663-670.
- 20 P. Jung, "Contribution of holographic interferometry to the numerical simulation of concrete shrinkage", *SPIE Vol. 599, Optics in Engineering Measurement* (1985), pp. 32-39.
- 21 P. Regnault, E. Brühwiler, "Holographic interferometry for the determination of fracture process zone in concrete", *Engineering Fracture Mechanics* Vol. 35 (1990), No. 1/2/3, pp. 29-38.
- 22 P. Jacquot, P.K. Rastogi, "Speckle metrology and holographic interferometry applied to the study of cracks in concrete", chapter 3.4 in "Fracture Mechanics of Concrete", edited by F.H. Wittmann, 1983, Elsevier Science Publishers.
- 23 P.K. Rastogi, P. Jacquot, L. Pflug, "Holographic interferometry applied at subfreezing temperatures: study of damage in concrete exposed to frost action", *Optical Engineering* 27(2) 1988, pp. 172-178.
- 24 W. Jüptner, T. Kreis, U. Mieth, W. Osten, "Application of neural networks and knowledge based systems for automatic identification of fault indicating fringe patterns", *Proc. SPIE "Interferometry 94"*, Vol. 2342 (1994), pp. 16-26.

3. Fringe analysis techniques

We presented in Chapter 2 a set of whole-field optical techniques, which are used as metrological tools. They share the property of providing images where the information is coded as a sinusoidal modulation of intensity. Different types of qualitative diagnostics are possible with a visual analysis of these fringe patterns. However, more and more applications require that a complete quantitative analysis be performed. Phase measurements can be performed in many ways but we will restrict ourselves to methods based on digitized images of the interferograms. The corresponding fringe processing techniques largely benefited from the computational power of affordable computers, creating an expanding research field for the last fifteen years or so. The potential gain is important as these techniques can bring precisions on the order of one hundredth of the sensitivity of a given interferometer. Two main families of methods can be considered according to the number of images they require. Single image techniques are historically the oldest but new refinements still appear every year. Multiple-image approaches, dating back to the first phase-shifting algorithm proposed by Carré in 1966, offer additional possibilities that have not yet been fully exploited.

In this chapter, we briefly present fringe enhancing techniques that are of interest mainly for single-image based analysis such as skeletonization and fringe tracking. Next, the multiple-image phase-shifting algorithms are described before considering carrier-based single-image methods using Fourier transformation or “spatial phase-shifting”. As most of these methods provide a modulo 2π phase map of the interferogram, the difficult task of phase unwrapping (or demodulation) is next presented, along with pre-processing algorithms. Finally the problem of phase measurements in non-static conditions is considered. The fringe processing methods described before are discussed in

this context, possible solutions are identified and the so-called “dynamic phase-shifting” is introduced.

Numerous books have been written on these subjects in the past years. We will however propose two recent works, one edited by Robinson and Reid¹, the other written by Osten and Jüptner², as the main sources of information for additional references and discussion of these topics.

3.1 Fringe enhancing techniques

We assume in the following paragraphs that the fringe pattern of interest has a sinusoidal profile of the form:

$$I(x, y) = I_0(x, y) + I_M(x, y) \cos \varphi(x, y) \quad (3-1)$$

where (x, y) are the spatial coordinates in a reference frame of the image.

From Chapter 2, we know that in the case of speckle correlation fringes the background intensity I_0 and equivalent modulation I_M are random variables. For all other types of interferometers, I_0 and I_M are usually smooth functions of x and y over the image. However, their variations can be large, owing to variations of reflectivity of the object and non-uniformity of the illumination. This last point is frequent with the Gaussian beams produced by lasers. Hence, once an image has been digitized, different techniques, known as shading corrections, can be used to correct for these variations. Advanced methods perform a least-square fit of the functions I_0 and I_M over the image, with the help of the fringe skeletons³.

The second family of enhancement techniques addresses the problem of noise suppression. Electronic noise sources are present in the acquisition chain. “Optical” noise can result from unwanted diffusion of light. Finally, speckle is present in the image as soon as rough objects are illuminated with coherent light. In the case of holography this results in a small additive noise. In the case of speckle interferometry, it is closer to a multiplicative noise term. Numerous filters have been elaborated to eliminate these various levels of “degradation” of the fringes. Most perform under the assumption of a high spatial frequency noise content versus low frequency fringes. Examples include non-specific filters⁴ such as the median or Wiener filters while some, such as the Crimmins filter⁵ (which is similar to a convex-hull morphological filter⁶) are specifically designed for noisy fringe patterns. An interesting approach is the use of directional filters, which perform a low-pass filtering along the local fringe direction, thus reducing fringe blurring. Recently, another successful adaptive filter has been proposed for speckle correlation images⁷. It is based on a local analysis of the intensity variance.

All these pre-processing tools are important for the quantitative analysis of single fringe patterns, particularly in view of the application of methods such as fringe skeletonization or fringe tracking. However, obtaining a visually “pleasant” image should not be a goal in itself since it becomes difficult to estimate the precision of a measurement based on a heavily filtered image, particularly when non-linear filters are used.

3.2 Fringe skeletonization and fringe tracking

Advanced fringe skeletonization techniques use morphological operators⁶ that find the center of mass of pixel clusters obtained by thresholding the gray level fringe image. Skeletons represent the set of points where the phase is an odd or even multiple of π , assuming that I_0 and I_M are locally constant. Once these skeletons have been obtained, a phase map can be reconstructed by interpolation. However, there is not enough information in a single fringe pattern to determine the sign of the phase change between successive fringes. “Automatic” or semi-automatic fringe numbering algorithms help reconstruct the actual shape of this phase map but a complete analysis usually requires an a priori knowledge².

Fringe tracking is another way of obtaining skeletons. Special algorithms are constructed to “follow” paths along maximum and minimum intensity regions defining bright and dark fringes. They perform poorly in images where these extremes are loosely defined, as in speckle correlation fringes.

One could characterize these methods as “last-chance” resources that must be used when none of the methods presented below can be used with a particular experiment. Particularly, their precision is seldom better than a tenth of the sensitivity, as strong hypotheses are made regarding I_0 and I_M in order to extract the phase from a single intensity measurement.

3.3 Phase-shifting

Phase-shifting techniques constitute one of the two main families of fringe analysis tools⁸. They are based on the possibility of obtaining multiple versions of a given interferogram. These images are acquired after modification of the phase of one of the two interfering waves. The result is a movement of the fringes in the image, without however changing the shape of the phase map. A simple analogy can be made with topographic maps. If fringes represent height contour plots, changing the phase difference of the waves by a constant quantity is equivalent to changing the origin of the contour lines. The contour lines are

located differently but they still accurately describe the surface. These different versions of the interferogram lead to a mathematically correct extraction of the phase φ and permit the determination of its sign.

An ubiquitous device is the piezoelectric transducer (PZT), which can move optical components, typically mirrors, by very small amounts with a resolution close to a few tens of nanometers. This element has proven to be essential for the practical realization of phase-shifting. Some early experiments were based on a constant speed translation of such a PZT while images were grabbed at equal time intervals. In this case, the fringes are moving during the exposure time of the camera, hence the names *phase-shifting* or “integrating-buckets” methods. A practical consequence is a lowering of the actual modulation of the fringes in the resulting image (see Chapter 4). The *phase-stepping* method, on the other hand, consists in moving the PZT step-wise. There is no corresponding fringe movement during the acquisition of one image. Both methods are nowadays designed under the name “phase-shifting” and we will use this term indiscriminately throughout the text.

With the capability to introduce controlled phase changes $\Delta\varphi$ in an interferogram, (3-1) becomes:

$$I(x, y) = I_0(x, y) + I_M(x, y) \cos(\varphi(x, y) + \Delta\varphi(x, y)) \quad (3-2)$$

The phase change or phase increment $\Delta\varphi$ can vary across the interferogram, hence the possible dependence in (x, y) . We will however drop the (x, y) term in most formulas, for clarity's sake.

If $\Delta\varphi$ is known, at least three equations are required to solve (3-2) for the value of φ . A simple 3-image solution consists in recording images as follows:

$$\begin{cases} I_1 = I_0 + I_M \cos(\varphi - \Delta\varphi) \\ I_2 = I_0 + I_M \cos(\varphi) \\ I_3 = I_0 + I_M \cos(\varphi + \Delta\varphi) \end{cases} \quad (3-3)$$

$$\Rightarrow \begin{cases} \varphi = \text{Arc tan} \left(\frac{1 - \cos \Delta\varphi}{\sin \Delta\varphi} \frac{I_1 - I_3}{2I_2 - I_1 - I_3} \right) \\ I_M = \frac{\sqrt{(1 - \cos \Delta\varphi)^2 (I_1 - I_3)^2 + (\sin \Delta\varphi)^2 (2I_2 - I_1 - I_3)^2}}{2 \sin \Delta\varphi (1 - \cos \Delta\varphi)} \\ I_0 = \frac{I_1 + I_3 - 2 \cos \Delta\varphi I_2}{2(1 - \cos \Delta\varphi)} \end{cases} \quad (3-4)$$

When $\Delta\phi$ is equal to $2\pi/3$, (3-4) is simplified as in (3-5):

$$\begin{cases} \varphi = \text{Arc tan} \left(\sqrt{3} \frac{I_1 - I_3}{2I_2 - I_1 - I_3} \right) \\ I_M = \frac{1}{3} \sqrt{3(I_1 - I_3)^2 + (2I_2 - I_1 - I_3)^2} \\ I_0 = \frac{1}{3} (I_1 + I_2 + I_3) \end{cases} \quad (3-5)$$

The phase is numerically obtained as an arctangent function. Taking into account the sign of both numerator and denominator, this yields a value in the $[0, 2\pi]$ range. The resulting modulo- 2π image is often called a "wrapped phase map". The removal of this modulation is discussed in paragraph 3.6.

If we apply the simple algorithm (3-5) to the three images shown at left in Figure 3-1 we obtain the wrapped phase map shown at right. The cut underneath this image illustrates the modulo- 2π effect, which creates a "saw-tooth" graph.

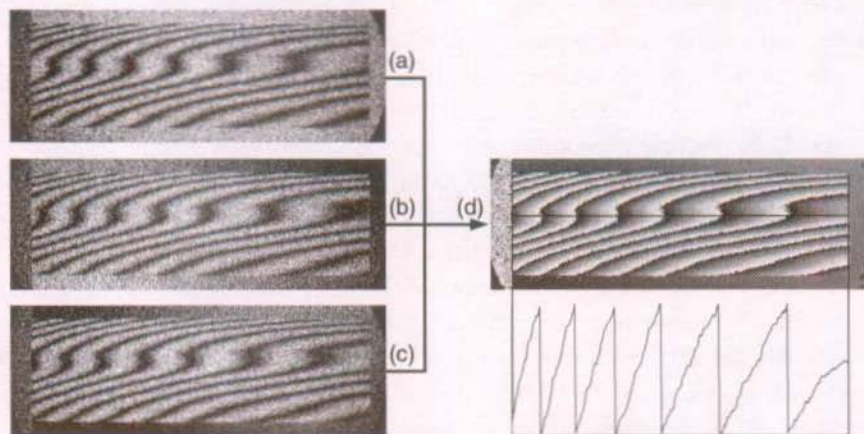


Figure 3-1. (a), (b) and (c): phase shifted fringe patterns obtained for a transparent object observed with holographic interferometry; (d) wrapped phase map of image (b), calculated with equation (3-5).

The simple 3-image algorithm presented above can be generalized to N images. The chapter by Creath in Ref.1 reviews the different types of available tools. The possibilities are endless. In particular, an extended work has been performed to characterize the behavior of these algorithms when phase-shifting errors and detector non-linearities are present. For example, a sound analysis of

the properties of the arctangent function leads to a family of “N+1” algorithms⁹ that are very tolerant to these types of error.

If we restrict ourselves to the set of methods where the phase increment $\Delta\phi$ is unknown, we still find several solutions, sometimes called “self-calibrating” algorithms. The phase increment is a function of both space (the coordinate of the point in the interferogram) and time (the position of the image in the sequence of phase-shifted images). We can distinguish the case where $\Delta\phi$ is the same for each point of the interferogram, for a given image, but is not constant between images ($\Delta\phi(x,y,t_1) = \Delta\phi_0(t_1)$, $\Delta\phi_0(t_1) \neq \Delta\phi_0(t_2)$), from the case where $\Delta\phi$ is not constant across the interferogram but is constant between images ($\Delta\phi(x_1,y_1,t_1) \neq \Delta\phi(x_2,y_2,t_1)$, $\Delta\phi(x_1,y_1,t_1) = \Delta\phi(x_1,y_1,t_2)$).

As the first case corresponds to the practical situation of a phase measurement with imperfect phase-shifting, several solutions have been developed, some based for example on iterative least-square fitting¹⁰. A particular approach was also proposed where a large number of images with random phase increments¹¹ are accumulated. It can actually work with $\Delta\phi$ values varying both spatially and temporally. The object must however be static.

The second case of variation of $\Delta\phi$ is of more interest to us. A “classical” solution is the Carré¹² method, based on four images. It is however a mathematically complex procedure, requiring the computation of a few square roots additionally to the usual arctangent, for each image point. Moreover, the computed phase does not correspond to any of the four initial images. In our applications, we rather use an extended version of a 5-image algorithm first presented in Ref.13 and later characterized in Ref.14. In these papers, it is assumed that the phase increment is $\pi/2$ while the “N+1” nature of the algorithm corrects for the different types of errors that can occur during the actual phase-shifting. We use a modified version where $\Delta\phi$ is actually computed at each pixel before the evaluation of the phase itself. The resulting method can accommodate $\Delta\phi$ ranging from $\pi/4$ to $3\pi/4$.

The phase-shifting algorithms presented above can be applied directly to fringe images obtained with 2-waves interferometers. The case of speckle interferometry is slightly different. As seen in Chapter 2, the correlation fringes obtained by subtraction of a reference image from an image recorded after deformation, do not present a truly sinusoidal profile:

$$(I_d - I_{ref})^2 = 2I_M^2 \sin^2\left(\phi_i + \frac{1}{2}\phi_d + \frac{1}{2}\Delta\phi\right)(1 - \cos(\phi_d + \Delta\phi)) \quad (3-6)$$

If the phase-shift $\Delta\phi$ is changed, both sine and cosine expressions in (3-6) change, which does not correspond to the phase-shifting formulas presented

before. It is however tempting for some authors, because of the envelope term " $1 - \cos\phi_d$ " and the visual aspect of the fringes, to try to apply directly phase-shifting algorithms to correlation fringes. Figure 3-2 presents in (a) a fringe pattern obtained by speckle contouring of a quail's egg. The image in Figure 3-2(b) is the corresponding wrapped phase map calculated with a 3-image algorithm without any filtering of the correlation fringes. The result is very noisy and confirms the fact that a very strong filtering of the initial images is first required to approach more closely a sinusoidal profile. The filter presented in Ref.7 seems to be a promising solution.

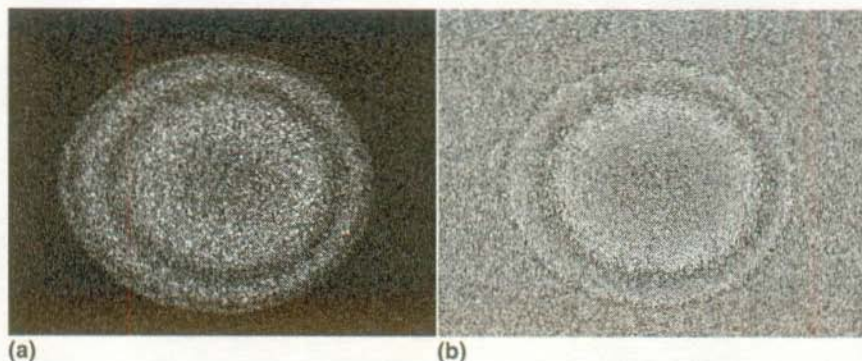


Figure 3-2. (a) Contour fringes of a quail's egg produced by a speckle contouring interferometer; (b) Wrapped phase map computed from 3 correlation images obtained in the same manner as (a).

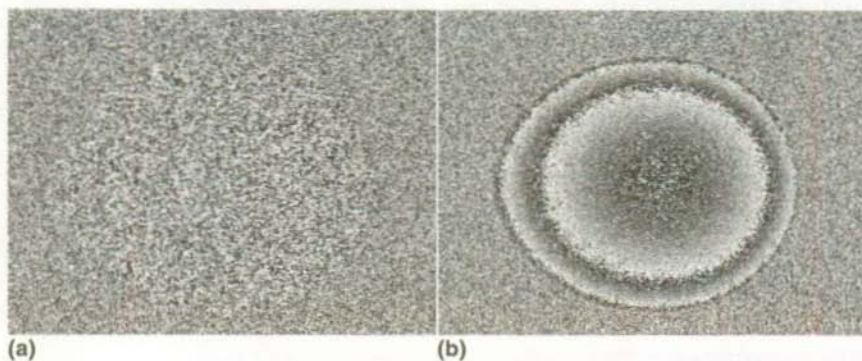


Figure 3-3. (a) Random phase map of a reference interferogram; (b) Difference between a second random phase map (obtained after rotation of the illumination beams) and the reference map (a).

We prefer the rigorous solution based on the observation that the recorded speckle field is indeed a 2-wave interferogram where the phase $\varphi_r(x,y)$, background intensity I_0 and modulation I_M are random variables different for each pixel. Phase-shifting algorithms can thus be applied directly and a first random phase map is computed as in Figure 3-3(a) while the object is in its reference state. The object cannot be distinguished from its surroundings in this image since phase values are random everywhere.

Once the object has undergone its deformation or the illumination beams have been displaced (the particular case of contouring), a second random phase map is computed. As long as there is no decorrelation during the experiment (see Appendix A), the random initial phase $\varphi_r(x,y)$ of a given pixel does not change. Hence, the total phase of a pixel becomes $\varphi_r(x,y) + \varphi_d(x,y)$ where φ_d is the quantity we wish to compute. A modulo- 2π subtraction of the first phase map from the second then yields this phase, shown in Figure 3-3(b). The result is much better than in Figure 3-2(b). It is however not as smooth as what would be obtained in classical or holographic interferometry. This is due to the speckle statistics that give a good probability of having a very low modulation I_M at any point of the interferogram. Considering that the dynamic range of the digitized images is usually limited to 256 gray levels, small values of I_M will produce intensity variations during phase-shifting that are too small to be accurately detected over the acquisition system noise. In this case, the measured phase is truly random from one measurement to the other. The filtering of these noisy data points will be presented in paragraph 3.5.

3.4 Single-image carrier-based methods

The second large family of quantitative analysis techniques is based on the use of “carrier fringes”, which consist basically in a set of parallel fringes of constant spacing. These initially straight fringes are deformed by the phase change induced by a deformation, or by the shape of the object in the case of fringe projection. The production of these fringes depends on the type of interferometer. In effect, a phase wedge must be introduced in the interferogram. This can become quite complicated in some cases, for example with shearing speckle interferometry. However, the main advantage is the use of a single image to perform the phase evaluation. The knowledge of the phase slope corresponding to the carrier fringes solves the problem of the absolute sign of the phase.

Let us assume that the carrier fringes are vertical in the image and that their spatial frequency is f_0 . The intensity profile is then given by:

$$I(x, y) = I_0(x, y) + I_M(x, y) \cos(2\pi f_0 x + \varphi(x, y)) \quad (3-7)$$

Two methods are available to process the digitized version of this interferogram. One, known as “spatial phase-shifting”¹⁵, consists in considering that the phase $\varphi(x, y)$ is constant over sets of adjacent pixels, in the horizontal direction (constant y value). One is then brought back to a set of equations similar to (3-3) where I_1 , I_2 and I_3 are the intensity values $I(x, y)$, $I(x+1, y)$ and $I(x+2, y)$ of the adjacent pixels and where the phase-shift $\Delta\varphi$ is introduced by the carrier term $2\pi f_0 x$. The frequency f_0 does not need to be precisely known when one uses self-calibrating algorithms that evaluate the average $\Delta\varphi$ at each set of pixels. However, this technique supposes that I_0 and I_M are locally constant, which is never the case with speckle interferometry. The field of application is thus limited to classical interferometry, fringe projection and good-quality holographic interferometry.

The second method, the Fourier technique, was proposed in Ref.16 and has been widely used, particularly in the field of optical components testing where no abrupt fringe discontinuities exist. It can be understood if we write equation (3-7) in a complex form as:

$$I(x, y) = a(x, y) + b(x, y) \exp(2i\pi f_0 x) + \bar{b}(x, y) \exp(-2i\pi f_0 x) \quad (3-8)$$

with:

$$a(x, y) = I_0(x, y) \quad \text{and} \quad b(x, y) = \frac{1}{2} I_M(x, y) \exp i\varphi(x, y) \quad (3-9)$$

If we compute the 2-dimensional Fourier transform of this image we obtain:

$$\tilde{I}(u, v) = A(u, v) + B(u - f_0, v) + \bar{B}(u + f_0, v) \quad (3-10)$$

where u and v are the horizontal and vertical spatial frequencies and $B(u, v)$ is the 2-D Fourier transform of the quantity $b(x, y)$. In essence, one obtains three peaks located at the spatial frequencies $u = -f_0$, 0 and $+f_0$. The processing then consists in deleting all the data points except in a window isolating the peak located at $+f_0$ (Hamming, Kaiser, \cos^4 , ... filters can be used for this purpose) and shifting it to the 0 frequency. The result is a complex-valued image containing $B(u, v)$. The inverse Fourier transform then yields the complex function $b(x, y)$, the phase of which is $\varphi(x, y)$. The technique can also be applied without carrier fringes¹⁷ but additional processing is required to compose the final wrapped phase image and eliminate the sign ambiguity.

As an illustration, Figure 3-4(a) shows a fringe pattern obtained while measuring the out-of-plane deformation of a vibrating plate. A pulsed laser is used to "freeze" the speckle field during each camera exposure. The reference wave is tilted between the two exposures; this produces the carrier fringes. The filter used to isolate one of the peaks in the Fourier domain is a box filter of elliptical shape convolved with a 7×7 Gaussian filter. Its surface covers only 0.5% of the total spectral domain! The resulting wrapped phase is shown in Figure 3-4(b).

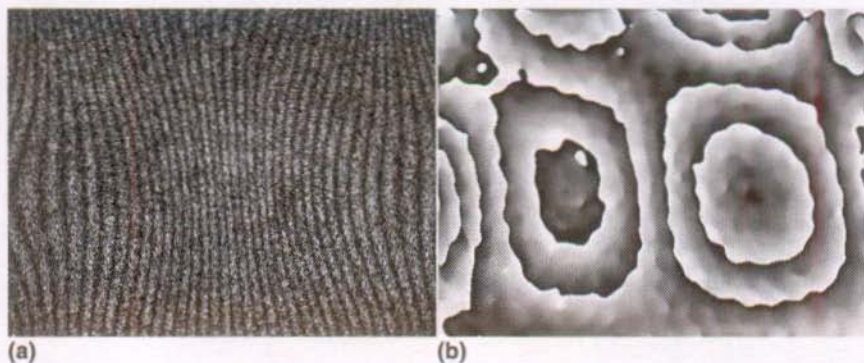


Figure 3-4. (a) Deformed carrier fringes obtained in out-of-plane speckle interferometry applied to a vibrating plate; (b) Wrapped phase map computed with the Fourier transform method.

From a practical point of view, the number of fringes created by the deformation should not be larger than the number of carrier fringes. The width of the peaks in the Fourier domain is a function of the pitch variations in the initial image. If the gradient of the fringes due to the deformation becomes too high, the peaks spread out and overlap, making the selection of a single peak impossible.

The formulas presented above are valid for carrier fringes of infinite support. This is obviously not the case with an image of limited dimensions. Consequently, the computed phase near the edge of the image is distorted¹⁷. The same problem arises when the fringe pattern does not fill completely the image¹⁵. Moreover, the choice of a filter to isolate the peaks is guided by a compromise between the amount of details that can be lost and the efficiency of speckle "noise" suppression. Consequently, fine features of the fringe pattern

* Fringe image courtesy of Holo3.

can be lost⁷. This is a problem, for example in the domain of material testing where discontinuities in the fringe patterns mark cracks in the specimen.

3.5 Wrapped phase enhancing

In the same manner that fringe-enhancing techniques were developed for intensity images, tools have been developed to enhance wrapped phase maps¹⁸. There are two benefits. One is "cosmetic", that is, fringes usually appear more clearly in phase images than in intensity images. The second is the actual preprocessing of the wrapped phase map with respect to the phase unwrapping procedure, presented in paragraph 3.6.

The major difficulty with these images is that they present sharp discontinuities caused by their modulo- 2π nature, which must be preserved at all cost for their successful unwrapping. Hence, no simple low-pass filter can be directly used. One of the most efficient solutions consists in computing two additional images that represent the sine and cosine of the original wrapped phase map. Thanks to their 2π -periodicity, these functions provide images where the only discontinuities left correspond to physical ones, for example caused by cracks. It is then possible to filter them with classical low-pass filters before computing a new wrapped phase map as the arctangent of the sine and cosine filtered images.

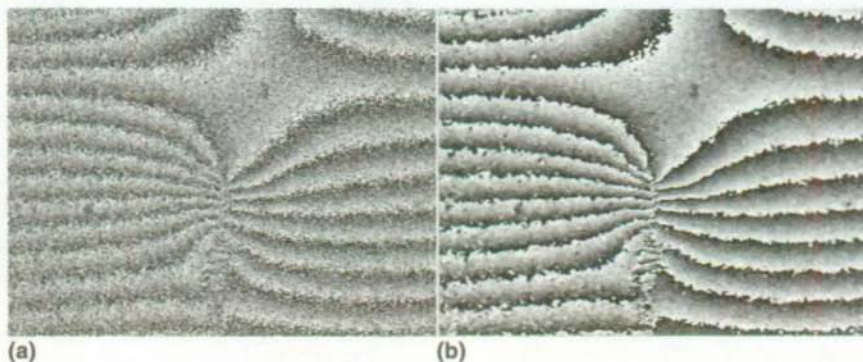


Figure 3-5. (a) Wrapped phase map; (b) Phase map reconstructed from low-pass filtered sine and cosine images made from (a).

Figure 3-5 illustrates this procedure with a phase map obtained in a in-plane speckle interferometer used to measure crack propagation in concrete samples. The image (a) is the initial phase map. The image (b) was obtained

after filtering three times the sine and cosine of this phase map with 3×3 box filters. The use of linear filters such as box or Gaussian filters is an obvious approach. A median filter can also be used with slightly finer results as large phase errors in some pixels have a smaller influence on the resulting value of their neighbors.

We can go one step further if we consider that more information is usually available. In effect, as discussed in paragraph 3.3, we know that the phase estimation becomes imprecise or even provides random results for low-modulation pixels. This is particularly important with speckle interferometry where very low modulations can be obtained. Hence, one idea is to eliminate the pixels whose modulation is lower than a given threshold. These pixels are then simply ignored when the sine and cosine images are low-pass filtered. From a statistical point of view, this amounts however to discarding the little information that is still present in these low-modulation pixels. A weighted average would be more efficient. Huntley shows in Ref.19 that the two main error sources on the estimation of the intensity of a given pixel, electronic noise and speckle decorrelation, produce phase errors of similar distributions. Since these distributions are, to a good approximation, Gaussian, a maximum-likelihood argument leads to compute weighted average phase values of group of pixels. The weight assigned to each pixel is the product of its modulations $I_M(t_1)$ and $I_M(t_2)$ corresponding to the reference and deformed states of the object. By considering the statistical effect of decorrelations in speckle interferometry, Lehmann comes to the same conclusion²⁰. Hence, the optimum phase enhancement filter consists in first computing the modulation and the phase at each point of the interferogram. These values are then used to calculate a weighted average of the phase or, equivalently, of its sine and cosine. This point is developed in Appendix A as we will use this argument in our developments.

3.6 Phase unwrapping

The process of phase unwrapping is the last difficult step of the quantitative measurement. It is a field of research in itself and a recent review is given in Ref.18. The goal of this procedure is to remove the 2π -phase discontinuities produced by the arctangent function. This process seems fairly obvious in the case of Figure 3-1(d) where the phase jumps are clearly defined. However, apart from the field of optical testing, this idyllic situation is seldom encountered.

The unwrapping process consists, in one way or another, in comparing pixels or groups of pixels to detect and remove the 2π phase jumps. Numerous solutions exist to process single wrapped phase images, based on path dependent or path independent algorithms, branch cut methods, tile processing using a minimum spanning tree, discrete cosine transform, simulated annealing, cellular automata, neural networks and so on (the useful references are found in Ref.18). They all present advantages and disadvantages, emphasizing the fact that no single tool can solve all problems in this field.

There are basically three difficulties in performing a correct phase unwrapping. The first one is related to the extent of the fringes in the image. As seen in Figure 3-3(b), meaningful fringes do not necessarily cover the image. Unwrapping errors can easily propagate from the random phase region to the actual fringes. One common solution is to create a mask of the region of interest and restrict the unwrapping to the masked area. An image of the object under white-light illumination over a dark background can be a starting point for this mask. The modulation image can also be used. This masking process is however time consuming for complex shapes of varying modulation. Ideally, the unwrapping algorithm should not require a mask...

The second difficulty simply comes from erroneous phase values, frequent in the case of speckle interferometry. The correct filtering of the wrapped phase map can greatly improve the image, as long as the proportion of bad phase values within the image stays reasonable, say less than 30%. Above this ratio, the effectiveness of the filtering process is limited. Unwrapping algorithms based on the processing of groups instead of individual pixels usually perform better in the presence of noise.

The third difficulty arises from physical discontinuities in the wrapped phase map. They correspond to brutal steps on the object in the case of shape measurement, or discontinuities of the surface of the object in the case of deformation measurement, cracks for example. Figure 3-5 illustrates this problem. In particular, the phase change between the two sides of a physical discontinuity is not necessarily high, which makes its detection even more difficult. Sometimes, a phase "valley" or saddle point (most tempting for path following algorithms) joins these two sides. Branch cuts methods try to prevent this "trespassing" by detecting specific "non self-consistent" points marking the extremities of the pass.

We can also mention the problem that appears when the fringes are located in unconnected zones in the image. The different zones can be unwrapped but

they do not share a common phase origin. It is left to the user to link them in a consistent manner.

The example presented in Figure 3-6(a) is the unwrapped version of Figure 3-5(b). Figure 3-6(b) shows a different representation. It must be kept in mind that the measured value is an in-plane displacement. A homemade unwrapping algorithm was used in this particular case. It will be presented in Chapter 7.

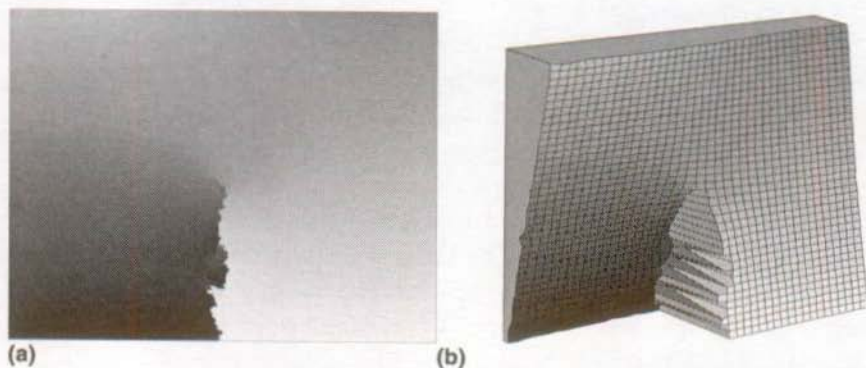


Figure 3-6. (a) Unwrapped version of the phase map of Figure 3-5(b); (b) Same image presented as a wireframe.

The algorithms briefly discussed above are "spatial" algorithms in the sense that the phase map is unwrapped by comparing adjacent pixels or pixel regions within a single image. A completely different approach was proposed in Ref.21 where several wrapped phase images are used. Each corresponds to a step in the deformation process of an object and the unwrapping is conducted along the time axis for each pixel taken individually. No spatial relationship is used. The advantages are manifold. First, erroneous phase values do not propagate in the image. Second, physical discontinuities are automatically respected. Third, isolated regions in the interferogram are correctly unwrapped, without any uncertainty concerning their relative phase order. The limitation is that the experiment must be conducted step by step, which can be a problem when a load has to be controlled precisely or if relaxation of the object is possible during a load plateau. Thermal loading is also a particular case where constant steps can be difficult to obtain. The phase should not change by more than π for each load increment. Hence, large number of steps can be necessary. We will discuss this method in more details in the next chapters as it is very well adapted to the continuous measurements we propose to perform with dynamic phase-shifting.

Once the unwrapping process is completed, the phase map has to be transformed into the corresponding physical quantity, for example displacement or shape. This is done using the sensitivity vector. The process is not always easy or accurate as unwanted sensitivities as well as sensitivity variations need to be taken into account. Sometimes, the user has to make hypotheses on the actual behavior of the object, for example if a set-up is sensitive to both in-plane and out-of-plane displacements. Ref.22 presents an example where the shape of a complex object is measured, which later allows one to reconstruct its 3-dimensional deformation field.

3.7 Quantitative measurements in non-static conditions

All the fringe analysis techniques described up to now perform well in the case of static or quasi-static experiments, that is, when phase variations in the interferograms are negligible during the acquisition of one or more images. Some of them can also be used when vibrating objects are studied²³. In this case, time-averaged images are used as well as pulsed lasers. Synchronized stroboscopic systems even permit the application of phase-shifting in the case of stationary vibrations. One goal of this dissertation work was to propose a method that can be used between these two extreme types of applications, when the observed phenomenon is time-dependent but of temporal characteristics comparable to the acquisition rate of our cameras. Applications include the study of creep, shrinkage and crack propagation, material testing with mechanical or thermal loading and stress-strain experiments.

We will now briefly identify possible fringe analysis solutions that can be used in this context. Carrier-fringes based methods such as the Fourier transform or the so-called "spatial phase-shifting" require only one image for each measurement point. However, the production of the necessary carrier fringes is sometimes difficult (for example in a shearing speckle interferometer) and limits the observable deformation dynamic as well as introduces unwanted decorrelations. Moreover, "spatial phase-shifting" is of limited use with speckle interferometry while the Fourier transform does not preserve well the image details.

For their part, phase-shifting techniques usually require that the phase of the observed interferogram be static during the acquisition. A number of multiple-image interferometers have been proposed where three or four phase-shifted images are produced and recorded simultaneously¹⁵. They can be obtained thanks to polarization splitting and phase-shifting with quarterwave

plates²⁴ or with moving interference gratings. The images are either recorded side by side with one camera or separately with several cameras. These set-ups are complicated, hence difficult to adjust and calibrate. In particular, the three or four intensity values required to compute the phase of one point of the interferogram are measured by different pixels of one detector, or worse, by different pixels of different cameras. Apart from synchronization problems, the response curves of these pixels must be calibrated to obtain intensity values consistent with the requirement of the phase-shifting algorithms, that is, equal background intensity and modulation values.

Another approach²⁵, very similar to the “scanning phase-shift technique” presented in Ref.11, consists in first measuring the background intensity I_0 and modulation I_M by changing continuously the phase of the interferometer. It is then possible to record successive images while the object undergoes its deformation. The phase of each image is estimated by interpolation of the cosine function (3-1). The accuracy of the phase estimation is however limited and a phase-shift is required one image every two to determine the phase sign. The principle of the technique holds only for temporally constant I_0 and I_M values. Hence, another limitation arises from the large modulation variations produced by decorrelations in the case of speckle interferometry.

We tried to present in the preceding paragraphs the possible solutions to the problem of measurement with time-dependent phenomena. We admittedly emphasized their limitations to show that some room is left for improvement or the introduction of new techniques; they must not however be deemed useless! We will propose such a new technique in the following chapters. It is based on the utilization of the deformation-induced phase change of the interferogram. By analogy with other methods, we call it “dynamic phase-shifting”.

Bibliography

- 1 "Interferogram Analysis", Ed. D.W. Robinson and G.T. Reid, 1993, IOP Publishing, ISBN 0-7503-0197-X.
- 2 W. Osten, W. Jüptner, Chapter 3 in "Handbook of Methods in Optical Metrology", Ed. P.K. Rastogi, Artech House Books, London, June 1997, ISBN 0-89006-516-0.
- 3 Q. Yu, K. Andresen, W. Osten, W. Jüptner, "Noise free normalized fringe patterns and local pixel transforms for strain extraction", *Appl. Opt.* 35 (1996) 20, pp. 3783-3790.
- 4 "Picture processing and digital filtering", Ed. T.S. Huang, 1979, Springer-Verlag, ISBN 0-387-09339-7.
- 5 T.R. Crimmins, "Geometric filter for speckle reduction", *Appl. Opt.* 24 (1985) 10, pp. 1434-1443.
- 6 J. Serra, "Image analysis and mathematical morphology", Academic Press, 1982, ISBN 0-12-637240-3.
- 7 A. Dávila, G.H. Kaufmann, D. Kerr, "Scale-space filter for smoothing electronic speckle pattern interferometry fringes", *Optical Engineering* 35 (1996), No. 12, pp. 3549-3554
- 8 K. Creath, "Temporal phase measurement methods", Chapter 4 in Ref.1.
- 9 K.G. Larkin, B.F. Oreb, "Design and assessment of symmetrical phase-shifting algorithms", *J. Opt. Soc. Am. A*, Vol. 9, No. 10 (1992), pp. 1740-1748.
- 10 I.-B. Kong, S.-W. Kim, "General algorithm of phase-shifting interferometry by iterative least-squares fitting", *Optical Engineering* 34 (1995), pp. 183-187.
- 11 E. Vikhagen, "Nondestructive testing by use of TV holography and deformation phase gradient calculation", *Appl. Opt.* 29 (1990) 1, pp. 137-144.
- 12 P. Carré, "Installation et utilisation du comparateur photoélectrique et interférentiel du Bureau International des Poids et Mesures", *Metrologia* 2 (1966), pp. 13-23.
- 13 J. Schwider, R. Burow, K. E. Elssner, J. Grzanna, R. Spolaszyk, K. Merkel, "Digital wave-front measuring interferometry: some systematic error sources", *Appl. Opt.* 22 (1983), pp. 3421-32.
- 14 P. Hariharan, B. F. Oreb, T. Eiju, "Digital phase-shifting interferometry: a simple error-compensating phase calculation algorithm", *Appl. Opt.* 26 (1987), pp. 2504-2505.
- 15 M. Kujawinska, "Spatial phase measurement methods", Chapter 5 in Ref.1.
- 16 M. Takeda, H. Ina, S. Kobayashi, "Fourier-transform method of fringe-pattern analysis for computer-based topography and interferometry", *J. Opt. Soc. Am.* Vol. 72 (1982), pp. 156-160.
- 17 T. Kreis, Chapter 4.6 in "Holographic Interferometry: Principles and Methods", 1996, Akademie Verlag, ISBN 3-05-501644-0.
- 18 D.W. Robinson, "Phase unwrapping methods", Chapter 6 in Ref.1.

- 19 J.M. Huntley, "Random phase measurement errors in digital speckle pattern interferometry", Proc. SPIE 2544 (1995), pp. 246-257.
- 20 M. Lehmann, "Decorrelation-induced phase errors in phase-shifting speckle interferometry", Appl. Opt., scheduled for publication April 1997.
- 21 J. M. Huntley, H. Saldner, "Temporal phase-unwrapping algorithm for automated interferogram analysis", Appl. Opt. 32 (1993), pp. 3047-3052.
- 22 W. Jüptner, W. Osten, P. Andrä, W. Nadeborn, "Nondestructive quantitative 3D characterization of a car brake", Proc. SPIE Vol. 2861 (1996), pp. 170-179.
- 23 P.H. Hariharan, "Applications of interferogram analysis", Chapter 8 in Ref.1.
- 24 A. J. P. van Haasteren and H. J. Frankena, "Real-time displacement measurement using a multicamera phase-stepping speckle interferometer", Appl. Opt. 33 (1994), pp. 4137-4142.
- 25 J. Wang and I. Grant, "Electronic speckle interferometry, phase-mapping, and nondestructive testing techniques applied to real-time, thermal loading", Appl. Opt. 34 (1995), pp. 3620-3627.

4. Dynamic phase-shifting

Chapters 2 and 3 give an introduction to whole-field optical methods and the associated fringe analysis techniques. The problems encountered in the case of dynamic phenomena, as well as possible solutions, are described at the end of Chapter 3. In the current chapter, we present our original contribution to this topic, which makes the bulk of this dissertation work. Starting from an initial observation, we present the framework in which phase measurements become possible thanks to the so-called “dynamic phase-shifting” approach¹. We then propose two different processing methods. The first one² is based on analytic solutions as in “classical” phase-shifting and is adapted to temporally localized phase evaluations or experiments limited in time. The second one³, based on a time-frequency analysis, is particularly adapted to continuous deformation measurements. These techniques are fully characterized in Chapters 5 and 6.

4.1 Dynamic phase-shifting principle

The main principle of this new technique can be easily understood when one looks at a sequence of images such as those presented in Figure 4-1. They show the out-of-plane deformation of a metallic membrane that acts as one of the walls of a depression chamber. These successive images were obtained using holographic interferometry during a pressure variation inside the chamber. If we compare the first five images we can observe that one fringe appears in the center of the circular pattern (there are five fringes in the first image and six in the last). To the observed intensity variations corresponds a phase variation of the interferogram. The speed of this phase variation varies in the image. For example, the intensity of the point located at the center of the circular pattern is roughly the same in the first and fifth images. Hence, its overall phase variation

is close to 2π , which corresponds to a $\pi/2$ phase change per acquisition interval. Our idea consists of observing that this "natural" phase variation is equivalent to the phase-shifting that we would otherwise introduce "artificially" to perform a phase evaluation, in the case of a static interferogram. Finding means to take advantage of this naturally occurring phase-shift is our goal. The immediate benefit is the ability to perform phase measurements in non-static conditions. The second benefit is the possibility to extend the method to continuous deformation measurements. Both points are developed in the next paragraphs. However, we must first clarify the conditions that are required in practice to reach this goal, as it is clear that not just *any* fringe movement will permit a phase measurement.

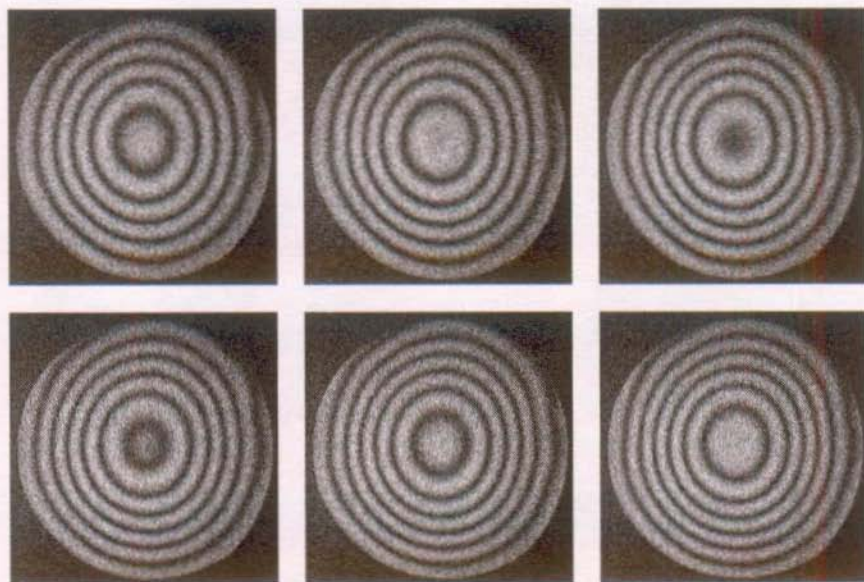


Figure 4-1. Six successive images obtained at 25 Hz while observing a metallic membrane in holographic interferometry.

4.1.1 Sampling rate considerations

The sampling rate requirements can be first intuitively presented with the help of Figure 4-2 where concentric circles represent five fringes of interference order one to five. From (a) to (b) and from (b) to (c) the phase of the whole interferogram increases by $\pi/2$. The overall visual impression is that of an expansion of the fringes. In the second case, from (d) to (e) and (e) to (f) the

phase increment is $3\pi/2$. In this case the visual impression is that of a contraction of the fringes. Hence, one could interpret these sketches as showing two fringe patterns evolving at the same “speed”, one expanding and the other one contracting, while in reality they both expand, the second one three times faster. This ambiguity results from the fact that the second phenomenon is not sampled rapidly enough.

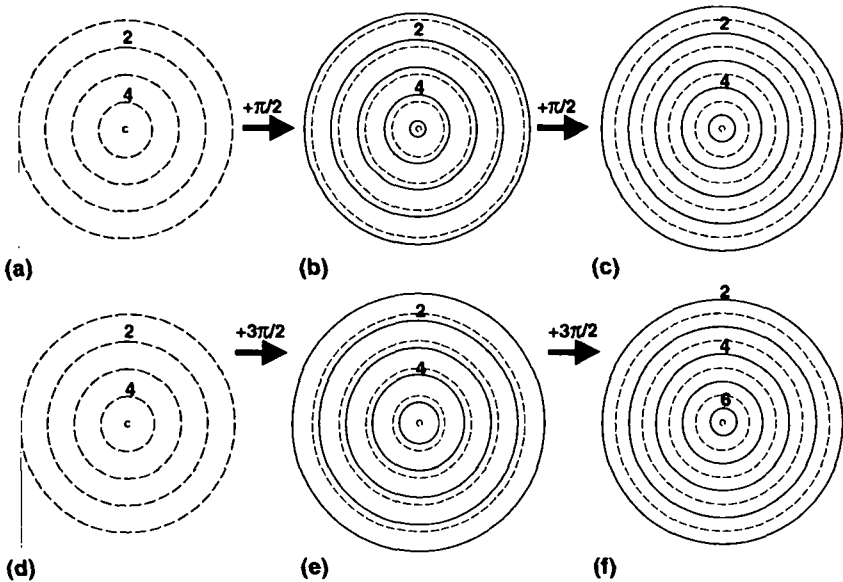


Figure 4-2. (a), (b), (c) Fringe pattern where the phase increases uniformly by $\pi/2$; (d), (e), (f) Same with uniform increment of $3\pi/2$.

The same reasoning holds for the temporal signal observed at a given pixel, as illustrated in Figure 4-3.

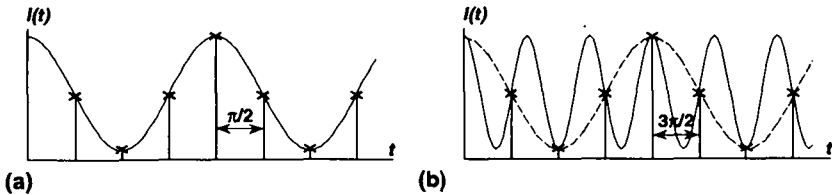


Figure 4-3. (a) Intensity measured at one pixel for a phase change of $\pi/2$ between samples; (b) Same for a phase change of $3\pi/2$.

In Figure 4-3(a) the phase increment between the acquisition of two successive samples is $\pi/2$. The crosses represent the resulting intensity samples that would permit to reconstruct the signal accurately. In Figure 4-3(b), the phase increment is again $3\pi/2$. In this case the signal is undersampled, that is, the samples would lead to the reconstruction of the cosine function plotted in the dashed line.

The two observations made above can be rigorously explained by Shannon's theorem. It states that in order to obtain a correct sampling of an unknown signal, the sample acquisition frequency should be at least twice the highest frequency present in the spectrum of the signal. Hence, to a fixed sampling rate f_s corresponds a cut-off frequency $f_c = f_s/2$, sometimes called the Nyquist limit, that defines the maximum tolerable extent of the signal spectrum, see Figure 4-4(a). If this condition is verified, the signal can be exactly reconstructed from its samples. If not, one obtains the aliasing phenomenon illustrated in Figure 4-4(b). Part of the spectrum is "folded back" on itself, which results in a modification of its amplitude. One recalls that the signal's spectrum gives the "list" and relative weights of all the frequencies that must be used in a sum of cosine functions to reconstruct this signal. The spectrum contains both an amplitude and a phase part; only the amplitude is shown here.

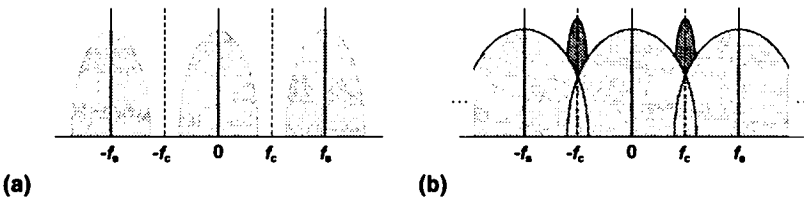


Figure 4-4. (a) Amplitude spectrum of a correctly sampled signal; (b) Spectrum aliasing in the case of an undersampled signal.

The demonstration of Shannon's theorem is quite interesting. In particular, it shows that the n -th derivatives of a normalized signal s are bounded by constants given by its spectral width Ω (all frequency component of s fall within $[-\Omega, \Omega]$):

$$|s'(t)| \leq 2\pi\Omega \quad \text{and more generally} \quad |s^{(n)}(t)| \leq (2\pi\Omega)^n \quad (4-1)$$

As stated in Chapter 5 of Ref.4, this bounding of the signal derivatives actually guarantees that no "surprises" can occur between the samples, as long as Ω is smaller than f_c . As a consequence, the signal can be reconstructed from its samples.

The temporal signal produced in a 2-waves interferogram is of the form:

$$I(t) = I_0(t) + I_M(t) \cos \varphi(t) \quad (4-2)$$

Frequently, $I_0(t)$ and $I_M(t)$ present “slow” variations in the time dimension, compared with the phase evolution. In the case of holographic or classical interferometry, these quantities indeed vary very slowly, if at all. However, decorrelations in speckle interferometry can introduce faster variations. The ideal case for us happens when the phase evolution can be locally (in the time dimension) approximated by a linear function of time:

$$\varphi(t) = \varphi_0 + \omega t \quad (4-3)$$

The signal is then locally monochromatic, that is, there are two symmetrical narrow peaks in its spectrum, corresponding to the positive and negative frequencies obtained by decomposition of the cosine function in its complex form:

$$\cos \omega t = \frac{1}{2} \exp(i\omega t) + \frac{1}{2} \exp(-i\omega t) \quad (4-4)$$

When the phase evolution is that simple it is clear that we can tolerate that ω become close to $\omega_c = 2\pi f_c$. However, accepting higher frequencies, that is, spectrum aliasing, would require additional information that is not present in the sampled signal. This could result from an a priori knowledge on the behavior of the deforming object. As soon as the phase evolution can no longer be approximated by a linear function of time, the signal’s spectrum starts to spread out in larger peaks and the peak central frequency can no longer come close to ω_c . We must note that the limitation to half the sampling frequency is a limitation concerning real signals. We will see in Chapter 9 that we can create a complex signal of the form $A \exp(i\omega t) + B \exp(-i\omega t)$ with $B \ll A$, from several real signals of the form $\cos(\omega t)$. In well-conditioned cases, the disappearance of the negative frequency component when $B \rightarrow 0$ allows to identify and follow the positive frequency component beyond the Nyquist limit.

If we come back to the situation of Figure 4-3 and suppose that we acquire signal samples at a frequency of 1 Hz, the corresponding cut-off frequency is 0.5 Hz or π rad/s. Hence, a $\pi/2$ phase change per sample is lower than the Nyquist limit and the signal is correctly sampled. In the second case, the phase change is $3\pi/2$, which is higher than the admissible limit. The aliasing effect folds back the two peaks $+3\pi/2$ and $-3\pi/2$ rad/s to the $-\pi/2$ and $+\pi/2$ frequencies. This explains why the apparent signal of Figure 4-3(b) has a frequency of $\pi/2$. The phase spectrum is folded in a similar fashion, which results in the opposite sign for the phase of the two peaks. Hence, if one were to use these samples to

compute the phase value of the signal at a given instant, the opposite of the actual value would be obtained.

We will adopt the following conventions in the rest of this document. First, we will use the name frequency when talking about a frequency f measured in Hz or about the corresponding pulsation $\omega = 2\pi f$ measured in rad/s. Second, in all the developments dealing with frequencies and phase-changes per sample we will consider that the image acquisition rate is 1 Hz. Hence, a phase change of $\pi/2$ between two successive images will correspond to a frequency (or pulsation) of $\pi/2$ rad/s.

To conclude this paragraph, we observe that obtaining a correct phase measurement is possible only if the acquisition rate is sufficiently high that the absolute phase variation of each point of the interferogram stays lower than π . This is a necessary but not sufficient condition. Depending on the method we intend to use to calculate the phase, other conditions will be required. In particular, if we wish to apply a "classical" phase-shifting algorithm, the hypothesis of a locally linear time evolution of the phase will have to be made. Moreover, a practical measurement can be ruined if external perturbations such as vibrations provoke phase variations that exceed the sampling requirements. A small high-frequency phase "noise" due to such perturbations is not too much of a problem as long as it does not create important intensity variations. As soon as this noise becomes important, the phase change induced by the object motion is "drowned" in apparently random phase variations. High-frequency phase perturbations amount to the creation of a larger signal spectrum, which becomes undersampled. This is a major problem in the case of in situ applications, such as those envisaged in the field of civil engineering. Particularly, desensitized interferometric set-ups have to be used.

For practical measurements, the tolerable speed of deformation of an object will depend mainly on the speed of the camera. Standard CCD cameras offer rates of 25 or 30 Hz in the "full-frame" mode of operation. Fast hard drives and state-of-the-art image acquisition boards make possible the acquisition of sequences thousands of images long. Other non-standard cameras offer higher rates. In our laboratory we use a digital camera operating at 160 Hz in the 512 x 512 pixels resolution. Newer, faster cameras start reaching the market nowadays. Some offer rates as high as 1 kHz.

4.1.2 Sign ambiguity in the phase estimation

When one applies the “classical” phase-shifting technique to static interferograms, the necessary phase increments are introduced with a controlled device, for example with a PZT. In this case, the direction or sign of these increments is known or can be calibrated once and for all.

Let us assume now that we dispose of an algorithm capable of computing a phase map from the images shown in Figure 4-1, where the unknown phase increments are provided by the deformation. This algorithm is necessarily built with the assumption that the phase shifts between images are all positive or negative. However, the images themselves do not provide a means to determine the sign of the actual phase shifts that occurred during acquisition. This is illustrated in Figure 4-5 where the simulated temporal signal of a pixel is drawn along with the two possible phase evolutions that could cause it.

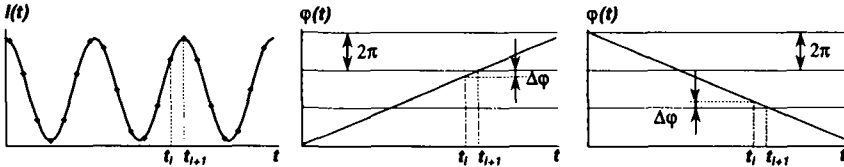


Figure 4-5. Simulated intensity signal of a pixel and corresponding possible graphs of the phase as a function of time.

This sign ambiguity problem is due to the parity of the cosine function. Indeed, the same successive intensity values are measured when the phase φ changes by an amount $\Delta\varphi$ between images or when the opposite phase $-\varphi$ changes by an amount $-\Delta\varphi$, regardless of the actual sign of φ and $\Delta\varphi$:

$$\begin{aligned}
 I(t - n\Delta t) &= I_0 + I_M \cos(\varphi - n\Delta\varphi) = I_0 + I_M \cos(-\varphi + n\Delta\varphi) \\
 &\vdots \\
 I(t) &= I_0 + I_M \cos(\varphi) = I_0 + I_M \cos(-\varphi) \quad (4-5) \\
 &\vdots \\
 I(t + n\Delta t) &= I_0 + I_M \cos(\varphi + n\Delta\varphi) = I_0 + I_M \cos(-\varphi - n\Delta\varphi)
 \end{aligned}$$

Hence, a standard phase-shifting algorithm applied to these intensity measurements can not determine the correct sign of the phase.

In the example of Figure 4-1, the fringes represent contour lines of the shape of a metallic membrane. The fact that one fringe appears in the center of a radially expanding circular fringe pattern can result from the membrane becoming more convex or more concave. Hence, we do not know the sign of the

deformation if we do not have additional information, such as the sign of the pressure variation in this particular case.

There are admittedly some experiments where a sufficient knowledge of the actual behavior of the object permits to determine the sign of the deformation and correct the calculated phase values if necessary. However, many interesting experiments deal with unknown behaviors and/or very complex fringe patterns where the phase variation can be positive in some regions of the interferogram and negative in others.

The solution we propose consists in introducing an additional phase-step α during acquisition. The idea is to offset the total phase increment at each pixel so that its sign is always positive (or always negative). The resulting method is a combination of a classical phase-stepping technique (addition of a constant phase α at each point of the interferogram) and of an integrating bucket method (continuous phase-shift caused by the object motion).

The choice of α is guided by theoretical as well as practical reasons. From a practical point of view it is better to choose α as an integer fraction of 2π , say $2\pi/n$. In this case the phase shifter can be used in a cyclic fashion. Instead of adding $2\pi/n$ steps continuously, which would require a very large range for the phase modulator in the case of long experiments, the use of the n -periodicity ensures that it always works within the same limited range, which can be accurately calibrated. Moreover, a precise calibration is required only for the $n - 1$ phase increments that will be used.

From a theoretical point of view we need to consider the acceptable range for the total phase shift. As seen in paragraph 4.1.1, its value should not become higher than π . Moreover, it should not become lower than zero (this is the goal of the introduction of a controlled step). If there is no a priori reason for the deformation-induced phase change to be predominantly positive or negative, the logical choice for α is $\pi/2$. The tolerable phase change produced by the deformation is thus within $[-\pi/2, \pi/2]$ in this case. The device used to introduce the additional phase steps only needs to be calibrated to realize $\{0, \pi/2, \pi, 3\pi/2\}$ cycles. Practical phase modulation schemes are presented in the chapter dedicated to dynamic phase-shifting applications.

4.1.3 Non-modulating pixels

Another limitation inherent to dynamic phase-shifting is that the phase-shift produced at a given point is proportional to the product of the corresponding deformation by the sensitivity of the interferometer. Hence, there are usually regions of an interferogram where no significant phase variations can be

observed. For example, these points can be located near the regions of contact between the object and its holder or, simply, far away from the region where loading is applied. In any case, a phase evaluation with quasi-null phase increments is usually impossible as it amounts to trying to reconstruct a cosine function with a few ill-distributed samples. Even if this is mathematically feasible in an ideal case, the inherent noise of any acquisition set-up makes this calculation highly imprecise. This is illustrated in Figure 4-6(a) where the phase of the third image of the sequence presented in Figure 4-1 is computed from the first five frames with the 5-image algorithm presented in paragraph 4.2. The wrapped phase map was low-pass filtered once in the sine and cosine domain. A profile along a diameter is shown in Figure 4-6(b). One can observe that the phase estimation becomes meaningless in the outer region of the circular pattern.

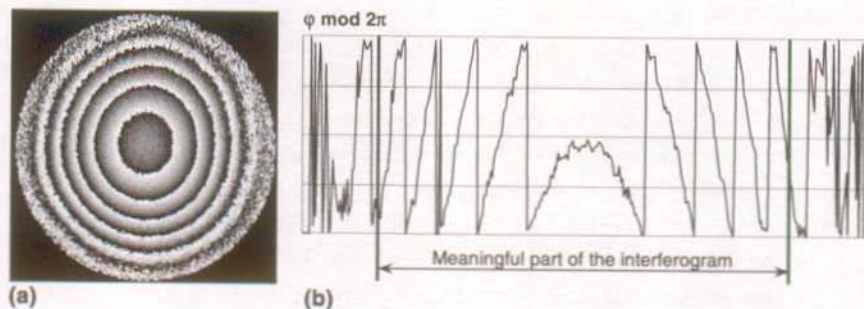


Figure 4-6. (a) Wrapped phase map of the third image of the sequence shown in Figure 4-1, after filtering; (b) Cut along a diameter

Again, the introduction of an additional phase-step during acquisition solves this problem. It simply amounts to a classical phase-shifting measurement for the static regions of the interferogram. Besides, it permits to distinguish between pixels where there are no temporal intensity variations because there is no significant deformation, and the pixels where the interferogram modulation is simply too low to produce a useful signal.

4.1.4 Modulation loss

It is worth mentioning that there is a fringe modulation loss during the acquisition of interferograms in the dynamic phase-shifting regime. It depends on the exposure time T_e of the camera. If this interval is very short, for example if a pulsed laser is used, one measures an intensity given by equation (4-2). If this interval is no longer small compared to the phase variation, the

corresponding intensity variations are integrated, which amounts to a blurring of the fringes. This can be written as:

$$I(t_i) = \frac{1}{2\delta\varphi} \int_{-\delta\varphi}^{\delta\varphi} I_0 + I_M \cos(\varphi(t) + \alpha) d\alpha \quad (4-6)$$

where $2\delta\varphi$ is the total phase change during T_e and φ is the corresponding average phase value. Assuming that I_0 and I_M do not change during that small interval and that φ can be approximated by a linear function of time, this expression leads to:

$$I(t_i) = I_0 + I_M \operatorname{sinc} \delta\varphi \cos \varphi(t_i) \quad (4-7)$$

where $\operatorname{sinc}(x)$ is equal to $\sin(x)/x$. Incidentally, this demonstrates that the integrating-bucket and corresponding phase-shifting methods rely on the same analytic solutions for φ . The consequence of the sinc function is a loss of modulation by a factor function of $\delta\varphi$, the half phase variation during T_e at this point of the interferogram. In a worst-case scenario, the exposure time is equal to the acquisition period. In the case of a sufficient sampling rate, the maximum useful phase change is π . The resulting measured modulation is then 64% of the modulation obtained for a similar static interferogram. If T_e is now half of the sampling period, the maximum modulation loss is limited to 10%. If there are points of the interferogram where the phase change is larger than the Nyquist limit, their modulation will drop more sharply. This is a natural way to filter out these ill-conditioned regions, if the phase-extracting algorithms use the modulation of a pixel as a measure of the confidence that can be accorded to its calculated phase.

One needs to find a compromise that gives the highest amount of modulation for a given illumination of the object. This problem is of no concern if a pulsed laser is used. However, it must be taken into account when the object is illuminated with a continuous laser. Very short exposure times are not the solution when the laser power is limited, as only a small fraction of the light is collected by the detector. In the case of a static interferogram observed with a linear-response detector, the potential modulation at each pixel is directly proportional to the exposure time. In the case of phase variations during T_e , this linear increase is counterbalanced by the sinc function described above, with the argument $\delta\varphi = \alpha T_e$. Actually, as long as saturation is of no concern, the exposure time should be as long as possible since:

$$I_M \propto T_e \operatorname{sinc} \delta\varphi = \frac{1}{\alpha} \sin(\alpha T_e) \quad (4-8)$$

Hence, for a given phase increment rate α such that $2\delta\phi < \pi$, the optimum modulation is obtained with large T_e .

The other parameter that can play a positive role is the lens aperture. The higher it is, the lower is the exposure time that gives the maximum achievable modulation (short of saturation). Moreover, large apertures are always beneficial in the case of speckle interferometry (see Appendix A).

4.2 Phase extraction using phase-shifting algorithms

Our first idea when we decided to look for solutions to the problem of phase measurements in the case of object motion, was to try using phase-shifting algorithms adapted to this natural phase shift. This requires a strong hypothesis to be made on the phase temporal variation, namely, that it behaves locally as a linear function of time. Here “locally” means the time interval covered by the acquisition of the n images used by the algorithm. This is sketched in Figure 4-7 where two simulated phase evolutions are plotted along with the corresponding intensity fluctuations measured at the detector. The five dashed lines indicate the instant of acquisition of five successive samples.

Our hypothesis on the object behavior is indeed very strong but it does correspond to many physical phenomena where a deformation is more or less proportional to the applied load. Hence, smooth, sometimes even monotonic evolutions can be observed, simply due to the mechanical properties of most materials. The question remains whether the phase behaves approximately linearly at the required time scale. In the case of material or structural testing, elastic and inelastic deformations are well suited to fulfil the above requirements as the applied loads usually have a simple and more or less adjustable time evolution. There is no particular problem if cracks appear and propagate slowly (like well-monitored Compact-Tension experiments) as this is equivalent to a physical discontinuity of the object. The information will be lost in pixels directly covering the cracks without however affecting their neighbors. On the other hand, if cracks appear rapidly like in a brittle rupture, the phase of many pixels increases much faster than what is tolerable between two successive images. In this case there is a large undersampling of the signal and the continuity of the measurement is lost.

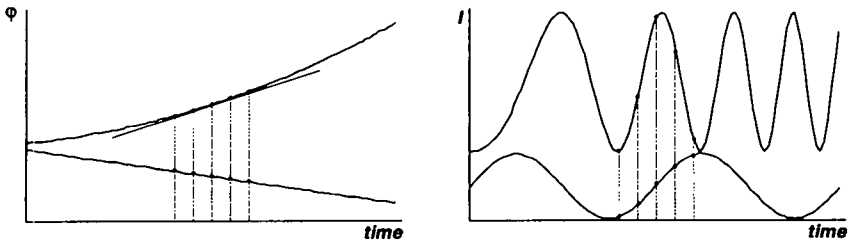


Figure 4-7. (a) Simulated temporal phase evolution of two pixels; (b) Corresponding detected intensity modulation.

Let us assume that the phase follows the hypothesis stated earlier. We call $\Delta\varphi$ the average phase increment between two successive images and φ the phase value we wish to calculate from n images. There are two other unknowns, the background intensity I_0 and the modulation I_M . Hence, a minimum of four equations is required. We present different solutions in the following paragraphs.

Two types of application can be envisioned for these methods. In one case, the goal is to perform a single phase measurement, in non-static conditions. The dynamic phase-shifting phenomenon is then used conjointly with a controlled phase-step to compute the phase, but the phase variations are rather seen as a nuisance the effect of which is taken into account by the algorithm. An example could be the measurement of the shape or deformation of a large object in presence of air turbulence. The main requirement in this case is simply that one can find time intervals where the temporal phase evolution is approximately linear. There is however no long-term requirement on the behavior of the perturbations. Algorithms requiring only a few images are particularly interesting for this application.

The other class of applications concerns continuous deformation measurements and some specific shape measurement techniques where for example the pitch of the fringes is continuously changed. In this case, the stability requirements are more stringent since the phase evolution is actually the quantity of interest. Sometimes, a controlled phase-step is not even needed to obtain images suitable to phase extraction. Images have to be recorded continuously during the experiment and their processing, if successful, yields a "movie" of the phenomenon, bringing insight into the object's temporal behavior.

4.2.1 3+1 phase-shifting algorithm

The simplest possible algorithm is based on three successive images acquired at a sampling frequency of $1/\Delta t$:

$$\begin{aligned} I(t - \Delta t) &= I_1 = I_0 + I_M \cos(\varphi - \Delta\varphi) \\ I(t) &= I_2 = I_0 + I_M \cos\varphi \\ I(t + \Delta t) &= I_3 = I_0 + I_M \cos(\varphi + \Delta\varphi) \end{aligned} \quad (4-9)$$

This algorithm is a sibling of a “2 + 1” algorithm proposed in the domain of optical shop testing of large telescope elements where one usually obtains high-modulation interferograms with no significant variations of background intensity or modulation. As the interferogram is static in that particular case, only two phase-shifted images are required. For our application we need three. One unknown, I_0 , has to be first evaluated before the beginning of the experiment. This can be done by averaging a large number of frames while the phase of the interferogram is perturbed, or by averaging two images obtained with and without a π phase shift. The phase increment and the phase are then calculated with:

$$\begin{aligned} \cos \Delta\varphi &= \frac{I_1 + I_3 - 2I_0}{2(I_2 - I_0)} = \frac{I_M \cos \varphi \cos \Delta\varphi}{I_M \cos \varphi} \\ \tan \varphi &= \frac{I_1 - I_3}{2(I_2 - I_0)} \frac{1}{\sin \Delta\varphi} = \frac{I_M \sin \varphi \sin \Delta\varphi}{I_M \cos \varphi} \frac{1}{\sin \Delta\varphi} \end{aligned} \quad (4-10)$$

The first equation gives an estimation of $\Delta\varphi$ as a function of I_0 , I_1 , I_2 and I_3 . The numerator and denominator are developed on the right hand side, before simplification of their common factors. This helps to understand the influence of intensity measurement errors on the calculated $\Delta\varphi$ value. In this case, we see that whenever φ is close to an odd multiple of $\pi/2$, both numerator and denominator tend to zero. As a consequence, the estimation of $\Delta\varphi$ becomes highly imprecise. The $\sin\Delta\varphi$ term in the numerator of the tangent expression is also a source of imprecision. The direct dependence on I_M emphasizes the observations made in Appendix A, that is, the higher the modulation, the higher the precision. Actually, all phase-shifting algorithms share this obvious property...

In our case, we used the above equations to first estimate φ and $\Delta\varphi$ before recalculating I_0 . Hence, an iterative algorithm is obtained that supposedly should adjust itself in the case of variations of I_0 and I_M . A visiting student implemented this technique, only to find out its catastrophic behavior in the presence of noise or low-modulation interferograms. Part of the problem is due to the iterative

algorithm that has a certain tendency to diverge. Moreover, as explained earlier, all phase-shifting algorithms fail when the phase increment $\Delta\varphi$ becomes close to zero. This particular algorithm was shown to fail earlier, that is, for higher $\Delta\varphi$ values than other more sophisticated methods. Hence, this algorithm was not retained for our developments.

4.2.2 Carré algorithm⁵

This technique is often presented as the first phase-shifting algorithm, dating back to 1966. It is based on the acquisition of four samples, phase-shifted by equal but unknown amounts $\Delta\varphi$:

$$\begin{aligned} I(t - 2\Delta t) &= I_1 = I_0 + I_M \cos\left(\varphi - \frac{3}{2}\Delta\varphi\right) \\ I(t - \Delta t) &= I_2 = I_0 + I_M \cos\left(\varphi - \frac{1}{2}\Delta\varphi\right) \\ I(t) &= I_3 = I_0 + I_M \cos\left(\varphi + \frac{1}{2}\Delta\varphi\right) \\ I(t + \Delta t) &= I_4 = I_0 + I_M \cos\left(\varphi + \frac{3}{2}\Delta\varphi\right) \end{aligned} \quad (4-11)$$

The phase φ and phase increment $\Delta\varphi$ are obtained with:

$$\begin{aligned} \tan \frac{\Delta\varphi}{2} &= \sqrt{\frac{3(I_2 - I_3) - (I_1 - I_4)}{I_2 - I_3 + I_1 - I_4}} \\ \tan \varphi &= \frac{\sqrt{(3(I_2 - I_3) - (I_1 - I_4))((I_2 - I_3) + (I_1 - I_4))}}{(I_2 + I_3) - (I_1 + I_4)} \end{aligned} \quad (4-12)$$

Because of the square root in the expression of $\tan\varphi$, one can not use directly the numerator and denominator to determine the actual sign of φ . Instead, one can observe that the quantity $I_2 - I_3$ is proportional to $\sin\varphi$, while $I_2 + I_3$ is proportional to $\cos\varphi$. This actually works only if the sign of $\Delta\varphi$ is known, which is the case if we add a phase step during acquisition. One small drawback of the technique is that the computed phase does not relate to any of the recorded images, but rather corresponds to the average of the phase in the four images. Another limitation appears if we develop both numerator and denominator:

$$\tan \varphi = \frac{\sqrt{I_M^2 \sin^2 \varphi \sin^2 \Delta\varphi \sin^2 \frac{1}{2}\Delta\varphi}}{I_M \cos \varphi \sin \Delta\varphi \sin \frac{1}{2}\Delta\varphi} \quad (4-13)$$

We observe that the combination of measured intensity values in the numerator is proportional to the square of $\sin\varphi$. Hence, for a given level of intensity perturbations, the phase determination is more imprecise when φ is close to an integer multiple of π , compared to other phase-shifting algorithms where the intensity combination is directly proportional to $\sin\varphi$. Besides, the product of the

two other squared sine functions of argument $\Delta\varphi$ and $\Delta\varphi/2$ yields very imprecise estimations of φ for small values of $\Delta\varphi$. This confirms the observations made in Ref.6, where this algorithm is found to perform well for phase increments ranging from 60° to 160° , the optimum value being 110° .

We will use this technique for comparison purposes with the 5-image method described next, in the case of continuous phase measurements.

4.2.3 5-image algorithm

We now briefly introduce a well-known algorithm based on five intensity measurements. It was the starting point of our investigations and remains our principal solution to the problem of phase measurements with small sequence of images. As such it is more fully studied in Chapter 5.

From five successive intensity samples:

$$\begin{aligned}
 I(t - 2\Delta t) &= I_1 = I_0 + I_M \cos(\varphi - 2\Delta\varphi) \\
 I(t - \Delta t) &= I_2 = I_0 + I_M \cos(\varphi - \Delta\varphi) \\
 I(t) &= I_3 = I_0 + I_M \cos\varphi \\
 I(t + \Delta t) &= I_4 = I_0 + I_M \cos(\varphi + \Delta\varphi) \\
 I(t + 2\Delta t) &= I_5 = I_0 + I_M \cos(\varphi + 2\Delta\varphi)
 \end{aligned} \tag{4-14}$$

one can calculate the phase at each point with:

$$\tan \varphi = \frac{2(I_2 - I_4)}{2I_3 - I_1 - I_5} \sin \Delta\varphi = \frac{I_M \sin \varphi \sin \Delta\varphi}{I_M \cos \varphi \sin^2 \Delta\varphi} \sin \Delta\varphi \tag{4-15}$$

This algorithm is frequently used in classical phase-shifting experiments with a phase increment close to $\pi/2$. It has been largely characterized in this situation, where $\Delta\varphi$ is not calculated but assumed to be $\pi/2$. For example, Creath⁷ shows that it is quite tolerant to non-linearities of the phase-shift as well as to detector non-linear response. This is explained by Oreb⁸ who investigated the interesting properties of so-called “N+1” algorithms. The “+1” actually represents the last image of the acquisition, which is supposed to be identical to the first one. This principle helps detect and correct phase-shifting errors. One can intuitively explain the “good-natured” behavior of this algorithm near $\pi/2$ by observing that the numerator and denominator in (4-15) are function of the sinc and squared sine of $\Delta\varphi$. First, these quantities are close to one for the chosen phase increment and second, their variations are with the square, respectively fourth power of the difference between the actual phase increment and $\pi/2$. This is actually equivalent to observing that both functions have a horizontal tangent

near $\pi/2$. Hence, quite large variations of $\Delta\varphi$ with respect to its target value do not cause large errors in the determination of the phase φ .

The above mentioned properties are interesting in our case, particularly for slowly deforming regions of the object, when a $\pi/2$ phase step is added during acquisition. However, the perfect algorithm for dynamic phase-shifting should perform well in the largest possible domain of phase increments within $[0, \pi]$. It can be assumed that for $\Delta\varphi$ values no longer close to $\pi/2$, the ideal properties described above might be lost. Robust means of determining $\Delta\varphi$ are required. Several solutions exist and we characterize some of them in Chapter 5 where the behavior of the full algorithm is studied in more details, particularly with respect to noise influence.

4.2.4 Advanced phase-shifting algorithms

The “classical” algorithms presented in the preceding paragraphs have more or less well-known properties and they can be adapted to the particular problem of dynamic phase-shifting. It is clear however, that dedicated algorithms could be constructed to provide better noise immunity and most importantly, permit to relax the hypothesis of a linear temporal phase evolution at each point of the interferogram. However, robustness will usually imply the use of more intensity samples to lower the influence of individual elements. Such is the case with iterative least-square fitting of a sine function to the measured signal of each pixel. This, in turn, makes the hypothesis of a linear phase evolution more difficult to obtain practically. One can then think of approximating this phase evolution by a second-degree function, but this introduces a new unknown. Moreover, it might become necessary to take into account the possible variations of I_0 and I_M . Hence, more samples are required to get a better fit. The conclusion is that there is a trade-off between obtaining robust algorithms that perform better in the presence of noise, the required number of samples and the accuracy of the estimation. The problem remains to find mathematical arguments that help design efficient N -image algorithms without exploring randomly the endless possibilities.

Another point can also be raised with respect to phase-shifting algorithms based on a fixed number of images. Let us imagine that in a sequence of images we find two pixels where the temporal phase evolution is linear. One has a phase increment of say, $\pi/6$, while the other one has an increment of $5\pi/6$. Both are then correctly sampled as the corresponding $\Delta\varphi$ are within $[0, \pi]$. However, during the time it takes for the slower one to see a phase change of 2π , the faster one accumulates five complete 2π periods. It is quite clear that these two

situations are not similar from the point of view of signal processing. A 4- or 5-image algorithm might be well suited to process the faster signal, but it would perform poorly for the slower one where less than a fourth of a period is sampled over this interval. The reverse would be true for a 10-image algorithm. Indeed it seems there is a heuristic rule that suggests that a well-designed phase-shifting algorithm should work with samples distributed over one period of the signal. It might then be tempting to try using different algorithms at the same time, the optimum one being chosen according to the signal apparent frequency. The difficult problem of actually estimating this frequency nonetheless remains.

In regard of these considerations, we decided not to limit our search to the field of phase-shifting algorithms but also to look in the larger domain of digital signal processing. The promising features of time-frequency analysis prompted us to forego the “quest” of the ideal phase-shifting algorithm and to explore less orthodox techniques (at least for someone used to fringe analysis methods), based in part on wavelet transforms.

4.3 Phase extraction using time-frequency analysis

Let us first observe the signal of a single pixel, Figure 4-8, obtained during an in-plane measurement using a speckle interferometer. Here, 512 samples were recorded during a rigid body translation of the object. They are plotted on a scale ranging from 0 to 255.

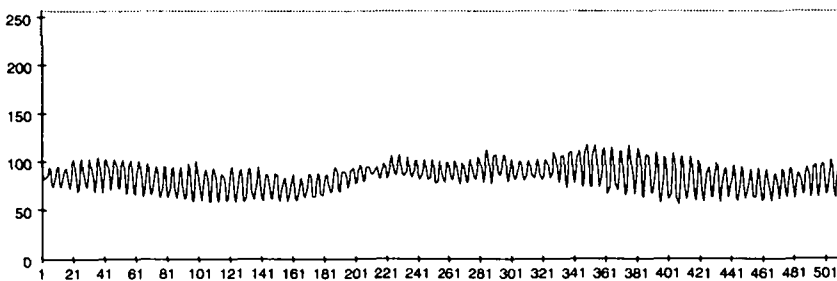


Figure 4-8. 512 samples of a pixel signal obtained in in-plane speckle interferometry for an object moving at a constant speed.

This example shows what could be qualified as a “good” signal, at least in the case of speckle interferometry. Indeed, the observed modulation $2I_M$ varies between 50 and 15 gray levels. This second value is obtained for a short period of time. The variations of I_M and I_0 are due to speckle decorrelations, as the

speckle field on the detector undergoes a translation of four pixel-widths during the experiment. These decorrelations certainly introduce phase perturbations as well. It is worth noting here that the signal depicted in Figure 4-8 is very similar to the signals obtained in speckle interferometry velocimetry.

If we look at this signal as a whole, the analogy with a modulated “single” frequency sinusoidal signal is evident. It would actually correspond to the case of an amplitude modulation (AM) and frequency modulation (FM) of the apparent carrier frequency (if we neglect the slow variations of I_0). In this example, the constant speed displacement creates a more or less constant frequency signal, the carrier. In more complicated deformation situations, the introduction of a $\pi/2$ phase-step between images, as described in paragraph 4.1.2, creates this essential carrier frequency. The amplitude modulation can result from variations of the illumination of the object or decorrelations in the case of speckle-based methods. In the example of Figure 4-8, the laser power was stabilized by a feedback loop. The frequency modulation results from the deformation itself. If we consider a pixel where the instantaneous phase change is $-\pi/4$ rad/s (assuming a 1 Hz sampling rate), the measured signal in the case of a $\pi/2$ rad/s carrier has a frequency of $+\pi/4$ rad/s. Similarly, a pixel where the phase increases by $+\pi/4$ rad/s produces a $3\pi/4$ rad/s signal. The major interest of the carrier frequency is to allow the determination of the sign of the displacement by looking at the positive or negative frequency shift. And, as mentioned earlier, it permits to measure a phase for pixels where no significant phase change occurs. Without the carrier frequency, they would produce a DC signal, difficult to interpret. Of course, as observed at the beginning of this chapter, the shifted frequency should remain within the band $[0, \pi]$ rad/s in order to have a correctly sampled signal.

The observation that the instantaneous phase increment translates in a frequency shift of the signal makes us wonder if this shift can be measured accurately. Indeed, if we can calculate the instantaneous frequency, or phase increment per sample $\Delta\phi$, we can solve some of the problems mentioned at the end of paragraph 4.2.4. Particularly, the knowledge of $\Delta\phi$ allows to choose a well-adapted phase-shifting algorithm. Another possibility, assuming we can obtain a graph of the frequency as a function of time, could be to “integrate” this frequency signal, yielding the phase we are actually interested in. In other words, we would simply sum the $\Delta\phi$ measured as a function of time. The question remains whether it is possible to measure this frequency with a sufficient accuracy and time resolution. This leads to the particular field of time-frequency analysis methods.

In the course of our search for the necessary tools and thanks to the help of Dr Drygajlo, we happened upon methods used in the field of acoustic signal processing. People working in this field are usually not interested in the phase content of their complicated signals but they observed interesting phase properties of the Gabor transform and of a particular wavelet transform. These properties provide a very efficient means to extract the different harmonics of their signals. It was thus very interesting for us to study these processing tools and determine if they could give us *directly* the phase information we are looking for, with the required precision and resolution.

In the next paragraphs we introduce the framework of time-frequency analysis, starting with windowed-Fourier transform. The Gabor transform is then briefly described to prepare the introduction of wavelet analysis.

4.3.1 Fourier transform and windowed Fourier transform

The Fourier transform (FT) is the standard tool for obtaining the frequency spectrum of a given signal $s(t)$ over its total duration. We use the following definition of this transformation:

$$\hat{s}(\omega) = \int_{-\infty}^{+\infty} s(t) e^{-i\omega t} dt \quad (4-16)$$

The spectrum $\hat{s}(\omega)$ is usually complex. Its amplitude represents the weight of the different frequencies that constitute the signal. The inverse Fourier transform permits to reconstruct s from \hat{s} :

$$s(t) = \frac{1}{2\pi} \int_{-\infty}^{+\infty} \hat{s}(\omega) e^{i\omega t} d\omega \quad (4-17)$$

The properties of Fourier transformation are well known. We will only recall here the Parseval-Plancherel theorem that will help us move back and forth between the time and frequency domains. It establishes the following relation for two functions $f(t)$ and $g(t)$:

$$\int_{-\infty}^{+\infty} f(t) \bar{g}(t) dt = \frac{1}{2\pi} \int_{-\infty}^{+\infty} \hat{f}(\omega) \bar{\hat{g}}(\omega) d\omega \quad (4-18)$$

where \bar{g} is the complex conjugate of g .

Obtaining the complete spectrum of a whole signal is fine for some applications but in our case we are rather interested by its “instantaneous” spectrum. In the case of a locally monochromatic signal with long-term frequency variations this instantaneous spectrum reduces to a narrow peak while the complete spectrum is large, all frequencies being represented regardless of

their time localization. Hence, we want to analyze the signal as locally in time as possible. This is achieved by using a windowed-Fourier transform (WFT). In this case, a sliding window $W(t-\tau)$, localized at time τ , is used to isolate a small portion of the signal $s(t)$. The product $\overline{W}(t-\tau)s(t)$ is then Fourier transformed to yield an estimation of the instantaneous spectrum $S(\omega, \tau)$:

$$S(\omega, \tau) = \int_{-\infty}^{+\infty} s(t)\overline{W}(t-\tau) e^{-i\omega t} dt = \frac{1}{2\pi} \int_{-\infty}^{+\infty} \hat{s}(\alpha)\overline{\hat{W}}(\alpha-\omega) e^{i\alpha\tau} d\alpha \quad (4-19)$$

The second expression is a consequence of (4-18). It shows that to the time localization corresponds a frequency localization. In particular, a spectrum component $S(\omega, \tau)$ is “influenced” by the weighted value of $s(t)$ in a region surrounding τ and, conversely, is influenced by the set of frequencies α such that $\hat{W}(\alpha-\omega) \neq 0$. There is thus a trade-off between time and frequency localization as the narrower $W(t)$ is, the larger is $\hat{W}(\omega)$ and vice versa. For example, in the case of a FT applied to the complete signal, $W(t)$ is as large as the signal support. Hence, the corresponding frequency band can be very narrow. In other words, the frequency resolution is high. If, on the other hand, a very narrow time window is used, a high time resolution is obtained conjointly with a very low spectral resolution. This trade-off is the consequence of the uncertainty principle that states that the product of the temporal width Δt of a window function by its spectral width $\Delta\omega$ is necessarily larger than a constant factor. Depending on the definition of these widths⁹, one obtains the simple relation: $\Delta t\Delta\omega \geq 1/2$. Equality is obtained if and only if the function is Gaussian. Hence, no function can be better localized in the temporal and spectral domains than a Gaussian window. The use of this window in WFT is called the Gabor transform, after Denis Gabor who proposed the use of such functions as “information grains” in the context of communication theory¹⁰.

4.3.2 Gabor transform

The Gabor transform $G(\omega, \tau)$, is one way to obtain an instantaneous spectrum of the signal. Actually, it permits to “explore” the 2-dimensional time-frequency domain. In other words, it is possible to know, in a signal s , the importance of a band of frequencies centered at ω in a time region centered at τ .

$$G(\omega, \tau) = \int_{-\infty}^{+\infty} s(t) \exp\left(-\frac{(t-\tau)^2}{2\sigma^2}\right) e^{-i\omega(t-\tau)} dt \quad (4-20)$$

The only parameter is the variance σ^2 of the gaussian window, which permits to reach the best time-frequency localization compromise for a given situation. We

can observe that the real window function is also multiplied by a phase term $\exp(i\omega\tau)$, which guarantees that the oscillating term $\exp(-i\omega\tau)$ is always “in phase” with the center of the window.

Similarly to the problem identified in 4.2.4 for n -image phase-shifting algorithms, the number of time samples for the analysis is fixed once σ has been chosen. This can be troublesome when the actual frequency of a signal can range from very low frequencies up to the Nyquist frequency, which is the case with dynamic phase-shifting. Similar observations led Morlet, working in the field of seismic signals¹¹, to devise a different type of analysis where the width of the analyzing window is automatically adapted to the particular frequency band of interest. Intuitively, it makes sense to use a large window when exploring the low-frequency components of a signal, and a narrow one when looking for high-frequency components or transients. His work was one of the main roots of what is loosely known today as “wavelet” analysis.

4.3.3 Wavelet analysis

Wavelet analysis has been a rapidly expanding field in the last decade as mathematicians started to establish the wide-ranging and non-trivial mathematical properties of what were at first convenient engineer tools^{9,4,12}. An interesting historical account by Daubechies¹³ shows that different domains of physics and engineering have for years developed methods that can all be brought in a larger perspective based on wavelets. For example, the “quadrature mirror filters” used in electrical engineering are actually a sibling of the “multi resolution analysis” (MRA), which is a subband analysis based on orthogonal wavelets. Applications are numerous. The most evident include time-frequency analysis where one is interested in the features of the spectrum of a signal and “signal representation” where the goal is to decompose a continuous signal in a limited series of components. This leads in this case to signal compression (huge compression rates of video signals have been obtained using wavelets¹⁴), or signal filtering by selecting and modifying the frequency subbands used to later reconstruct the signal.

A wavelet decomposition of a given signal $s(t)$ is performed through the use of a dilated and translated basic window function $g(t)$, sometimes called the “mother wavelet”. The wavelet transform is calculated for different values of the scale or dilation parameter a , and the time translation b :

$$S(a, b) = \frac{1}{a} \int_{-\infty}^{+\infty} s(t) \bar{g}\left(\frac{t-b}{a}\right) dt \quad (4-21)$$

The transform can also be written as:

$$S(a,b) = \frac{1}{2\pi} \int_{-\infty}^{+\infty} \hat{s}(\omega) \bar{\hat{g}}(a\omega) e^{i\omega b} d\omega \quad (4-22)$$

as a consequence of (4-18). This expression will be useful to understand the phase properties of the Morlet wavelet and the influence of the FT of the time window. As in the case of FT or WFT, a reconstruction formula can be used to rebuild the signal from its wavelet coefficients $S(a,b)$:

$$s(t) = \frac{2}{C} \iint_{-\infty}^{+\infty} \sqrt{a} S(a,b) g\left(\frac{t-b}{a}\right) \frac{dadb}{a^2} \quad (4-23)$$

Where C is given by:

$$C = 2\pi \int_{-\infty}^{+\infty} \frac{|\hat{g}(\omega)|^2}{\omega} d\omega < \infty \quad (4-24)$$

In practice, this reconstruction is not very useful for the particular application we have in mind, but the fact that C must exist leads to some admissibility conditions on the function g . We do not wish to review them in details, a rigorous discussion being made in Ref.9. However, we mention here the conditions that have practical consequences. First, g must be a square-integrable complex-valued function (noted $g \in L^2(\mathbf{R})$), that is:

$$\int_{-\infty}^{+\infty} |g(t)|^2 dt < \infty \quad (4-25)$$

As g is supposed to be a window function, it should also verify:

$$\int_{-\infty}^{+\infty} |g(t)| dt < \infty \quad (4-26)$$

Consequently, \hat{g} is a continuous function. It follows from (4-24) that $\hat{g}(0)$ must be 0. We will see in the next chapter the problems that arise when this condition is not respected. We must emphasize here that *any* function g of $L^2(\mathbf{R})$ satisfying the above-mentioned requirements is susceptible of being used as a mother wavelet.

As explained earlier, the wavelet analysis is performed differently for high and low frequencies. This is sketched in Figure 4-9 where the elementary analysis "cells" in the time-frequency domain are compared for wavelet and fixed-width windowed FT.

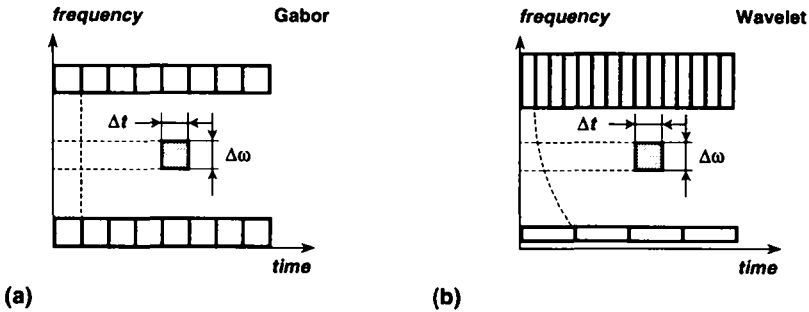


Figure 4-9. Time-frequency analysis cell in the case of: (a) a WFT such as the Gabor transform, (b) a wavelet transform.

Accordingly, wavelet transforms present a better frequency resolution in the low frequencies domain, at the expense of time localization, and a higher temporal resolution at high frequencies, at the expense of spectral resolution. In both cases however, the “surface” of an individual cell remains constant, only its aspect-ratio changes.

The wavelet decomposition as presented with the integral wavelet transform can be continuous but a standard approach is to “explore” a signal at a specific number of locations obtained by “binary dilation” and “dyadic translation”⁹. In other words, wavelet coefficients are calculated for the set of points $a = 2^j$, where j is integer¹¹. In the case of orthogonal wavelets this yields an efficient and non-redundant decomposition of the signal. Many algorithms¹⁵ have been developed in this context, leading among other tools to MRA. However, our goal is not to filter or compress our signal but rather to extract its instantaneous frequency and possibly its phase as accurately as possible. Hence, redundant information is not an issue in itself. We will see in the next chapter that a simple approach gives us this phase information with a limited number of estimations of $S(a,b)$ for a given time b .

Because of the particular phase properties of the Morlet wavelet described by researchers working in the field of acoustic signals¹⁶, we decided to investigate the possibility of applying it to our temporal signals. This investigation is still running but the results so far show that a wavelet analysis of our interferometric signals is indeed a powerful method. Hence, this solution to the problem of continuous deformation measurement will be characterized in detail in the next chapters, along with the 5-image algorithm presented earlier, both tools addressing overlapping domains of application of the dynamic phase-shifting principle.

4.4 Phase unwrapping in the case of DPS

The preceding paragraphs emphasized the difficulty of performing a phase measurement in dynamic conditions. Whichever particular solution is adopted, the computed phase ends up as a modulo- 2π value. Hence, phase unwrapping is required. As described in Chapter 3, this unwrapping can be conducted spatially or temporally.

Two possible applications of dynamic phase-shifting were described in the introduction of paragraph 4.2. In one case, small sequences of images are recorded from time to time during a dynamic event. Each sequence yields one wrapped phase map, using for example an n -image phase-shifting algorithm. In this case, the only possibility consists in performing a spatial unwrapping of this image (in the particular situation of speckle interferometry, it would be the difference modulo- 2π between this image and a reference that would need to be unwrapped). Spatial unwrapping can be difficult because of noise, phase jumps caused by physical discontinuities and disconnected fringe regions in the image. We do not go in more details here since a description of these problems and a review of possible solutions is given in Chapter 3. The particular spatial unwrapping algorithm we use in practice is described in Chapter 7.

The other application of dynamic phase-shifting consists of recording a continuous sequence of images during, for example, object deformation. In this case, the phase can be obtained by use of a phase-shifting algorithm or a time-frequency based analysis. In any case, we obtain a *3-dimensional* phase “map”. One could again use spatial unwrapping algorithms. However, it is much more interesting to perform the work along the time dimension. The phase of each pixel is then unwrapped independently of its neighbors. The consequence is that there can no longer be spatial error propagation in the image. Besides, physical discontinuities or separated regions are not a problem any more, since no spatial relationship has to be assumed in the image. Most importantly, the resulting “movie” of unwrapped images gives a *continuous* and *absolute* measure of the deformation of the object, contrary to the other acquisition scheme where small sequences of images are recorded separately.

One-dimensional unwrapping is much simpler than 2-dimensional as we know that the discontinuities of the phase result only from the modulo- 2π jumps produced by the arctangent function. The continuity of the phase and of its derivatives are properties that can be used to perform a fit of its general evolution and thus correct erroneous values. Moreover, in the case of dynamic phase-shifting, the instantaneous phase increment $\Delta\varphi(t)$ (smaller than π) has to be determined. Hence, if the phase $\varphi(t)$ at time t is unwrapped we can estimate

the probable phase $\varphi(t+1)$ by calculating $\varphi(t)+\Delta\varphi(t)$. This estimation helps to choose the number of 2π -multiples that need to be added to the wrapped value at $t+1$. Furthermore, if a known phase step is introduced during acquisition (see paragraph 4.1.2), and this will usually be the case for our applications, we have the additional knowledge that the phase variation is monotonic. All these arguments make the temporal unwrapping a very straightforward process. Its implementation, combined with optimum phase filtering is presented in Chapter 6.

One last property of continuous deformation measurements using dynamic phase-shifting must be emphasized here. Two-dimensional phase unwrapping is possible only if the fringes are sufficiently well sampled by the pixels of the camera. This is actually another application of Shannon's theorem, this time in the spatial domain. The practical consequence is that there must be at least two pixels per fringe in the image. In the case of dynamic phase-shifting this requirement disappears completely since what is required is a modulation of the pixel signal in the time dimension only. One can easily imagine an experiment where two adjacent pixels look at parts of an object that move at different speeds, for example an object tilting at a constant speed, observed in out-of-plane speckle interferometry. The phase increment difference between these two points can be quite small. However, after the accumulation of hundreds of images the difference of their unwrapped phase can be very large, which would be equivalent to a very high fringe gradient in an interferometric image. The corresponding interferogram would actually be completely undersampled. This does not however prevent us from obtaining the unwrapped phase images, thanks to temporal unwrapping.

Bibliography

- 1 X. Colonna de Lega, P. Jacquot, "Deformation measurement with object-induced dynamic phase-shifting", *Appl. Opt.* 35 (1996), No. 25, pp. 5115-5121.
- 2 X. Colonna de Lega, P. Jacquot, "Interferometric deformation measurement using object induced dynamic phase-shifting", *Proceedings SPIE, Europto Series*, Vol. 2782 (1996), pp. 169-179.
- 3 X. Colonna de Lega, "Continuous deformation measurement using dynamic phase-shifting and wavelet transforms", *Proc. Appl. Opt. Div. Conf.*, Reading 1996, Institute of Physics Publishing, pp. 261-267.
- 4 G. Kaiser, "A friendly guide to wavelets", Birkhäuser, 1994, ISBN 0-8176-3711-7.
- 5 P. Carré, "Installation et utilisation du comparateur photoélectrique et interférentiel du Bureau International des Poids et Mesures", *Metrologia* 2 (1966), pp. 13-23.
- 6 Y.-Y. Cheng, J. C. Wyant, "Phase shifter calibration in phase-shifting interferometry", *Applied Optics* 24 (1985), pp. 3049-3052.
- 7 K. Creath, "Phase-measurement interferometry techniques", in "Progress in optics XXVI", ed. E. Wolf, Elsevier Science Publishers, 1988.
- 8 K.G. Larkin, B.F. Oreb, "Design and assessment of symmetrical phase-shifting algorithms", *J. Opt. Soc. Am. A*, Vol. 9, No. 10 (1992), pp. 1740-1748.
- 9 C.K. Chui, "An introduction to wavelets", Academic Press, 1992.
- 10 D. Gabor, "Theory of communication", *Journal of Inst. Electr. Eng. (London)*, Vol. 93 (1946), pp. 429-457.
- 11 P. Goupillaud, A. Grossmann, J. Morlet, "Cycle-octave and related transforms in seismic signal analysis", *Geoexploration*, Vol. 23 (1984), pp. 85-102.
- 12 I. Daubechies, "Ten lectures on wavelets", SIAM, Philadelphia 1992.
- 13 I. Daubechies, "Where do wavelets come from?-A personal point of view", *Proc. of the IEEE*, Vol. 84 (1996), No. 4, pp. 510-513.
- 14 M. Vetterli, J. Kovacevic, "Wavelets and subband coding", Prentice Hall PTR, 1995, ISBN 0-13-097080-8.
- 15 M.V. Wickerhauser, "Adapted wavelet analysis from theory to software", Wellesley Massachusetts, ISBN 1-56881-041-5.
- 16 N. Delprat, B. Escudié, P. Guillemain, R. Kroland-Martinet, P. Tchamitchian, B. Torrésani, "Asymptotic wavelet and Gabor analysis: extraction of instantaneous frequencies", *IEEE Transactions on Information Theory*, Vol. 38 (1992), No. 2, pp. 644-664.

5. Characterization of the 5-image algorithm

In Chapter 4, we presented the general principles of dynamic phase-shifting and its fundamental limitations due to finite sampling rate. Two different solutions to the problem of phase measurement in non-static conditions were then proposed. One is based on modified phase-shifting algorithms used habitually in static conditions^{1,2}. It was seen that they suffer from their very nature, namely, the need for a fixed number of images, which prevents somehow their application to very fast and very slow phase variations. On the other hand, since they require a limited number of images, they can be used as a tool for single phase measurements in difficult conditions. For example, short packets of images can be acquired from time to time in a perturbed environment. Their processing with, for example, the 5-image algorithm we chose, yields phase maps that relate to the instantaneous deformation state of the object under investigation. Because of the perturbations, some of these phase maps might be simply meaningless. We will refer to this method as the “spatial solution” since no long-term temporal information is required nor expected.

The goal of this chapter is to characterize the robustness of the 5-image algorithm as well as its useful domain of application (with respect to the rate of phase variation in the interferogram). This study is mainly based on simulations. The Carré algorithm³ is also used for comparison purposes, since it appears to be well suited to our particular problem.

5.1 Overview of the 5-image algorithm

The main advantage of this algorithm is the relatively limited number of images it requires, which makes more probable the hypothesis of a linear temporal phase variation. We will use the following notation for the five temporal samples recorded for each pixel:

$$\begin{aligned}
 I(t - 2\Delta t) &= I_1 = I_0 + I_M \cos(\varphi - 2\Delta\varphi) \\
 I(t - \Delta t) &= I_2 = I_0 + I_M \cos(\varphi - \Delta\varphi) \\
 I(t) &= I_3 = I_0 + I_M \cos\varphi \\
 I(t + \Delta t) &= I_4 = I_0 + I_M \cos(\varphi + \Delta\varphi) \\
 I(t + 2\Delta t) &= I_5 = I_0 + I_M \cos(\varphi + 2\Delta\varphi)
 \end{aligned} \tag{5-1}$$

where Δt is the sampling period. The phase corresponding to the central sample is computed with:

$$\tan \varphi = \frac{2(I_2 - I_4)}{2I_3 - I_1 - I_5} \sin \Delta\varphi = \frac{I_M \sin \varphi \sin \Delta\varphi}{I_M \cos \varphi \sin^2 \Delta\varphi} \sin \Delta\varphi \tag{5-2}$$

A first observation of (5-2) indicates that the phase estimation should become imprecise when $\Delta\varphi$ tends towards 0 or π , since the ratio becomes very “sensitive” to noise when both numerator and denominator tend towards 0. This will limit in practice the maximum and minimum acceptable rates of phase variation in the interferogram. We will come back to this point later.

Many solutions exist to first evaluate $\Delta\varphi$ from the five intensity measurements. We will restrict ourselves to four simple possibilities of calculating $\cos\Delta\varphi$. We label them A, B, C and D. In the following equations we give also the development of the numerator and denominator, before simplification of the common factors. This helps to understand when a particular method is going to become unreliable.

$$\begin{aligned}
 \text{(A)} \quad 2\cos\Delta\varphi &= \frac{I_5 - I_1}{I_4 - I_2} = \frac{\sin \varphi \sin 2\Delta\varphi}{\sin \varphi \sin \Delta\varphi} \\
 \text{(B)} \quad 2\cos\Delta\varphi &= \frac{I_5 - I_2}{I_4 - I_3} - 1 = \frac{\sin(\varphi + \Delta\varphi/2)\sin(3\Delta\varphi/2)}{\sin(\varphi + \Delta\varphi/2)\sin(\Delta\varphi/2)} - 1 \\
 \text{(C)} \quad 2\cos\Delta\varphi &= \frac{I_4 - I_1}{I_3 - I_2} - 1 = \frac{\sin(\varphi - \Delta\varphi/2)\sin(3\Delta\varphi/2)}{\sin(\varphi - \Delta\varphi/2)\sin(\Delta\varphi/2)} - 1 \\
 \text{(D)} \quad 2\cos\Delta\varphi &= \frac{2I_3 - I_5 - I_1}{2I_3 - I_4 - I_2} - 2 = \frac{\cos \varphi \sin^2 \Delta\varphi}{\cos \varphi \sin^2(\Delta\varphi/2)} - 2
 \end{aligned} \tag{5-3}$$

For example, we observe that the methods A and D will become unreliable when the phase φ is close to 0 or π for A and $\pm\pi/2$ for D, which makes them complementary with respect to φ . B and C are not as simple as the dependence on φ can not be isolated from $\Delta\varphi$.

If we look only at the factors depending on $\Delta\varphi$, we see that the four solutions will behave differently. Experience shows that in the presence of noise the above formulas perform better when the numerator tends towards 0 while the denominator is maximized. For A, this corresponds to the situation where $\Delta\varphi$ is close to $\pi/2$, for B and C $\Delta\varphi$ should be close to $2\pi/3$ and for D the optimum is $\Delta\varphi$ close to π . As the ideal algorithm should work as well for $\Delta\varphi$ ranging from 0 to π we need to find out which of these methods provides us with the largest acceptable range. If none is sufficiently robust, we can try to build a combination of these solutions. Hence, in the following paragraphs, we first look at the accuracy of the $\Delta\varphi$ estimation in presence of noise. Next, we look at the resulting error on the phase estimation. An additional method, "Known", will be added to most graphs. It represents the particular case where $\Delta\varphi$ is supposed to be known. This corresponds to the preliminary determination of the phase increment, for example with the help of a wavelet analysis.

5.2 Phase increment estimation

In the following simulations, the accuracy of the methods A, B and D are compared for five values of $\Delta\varphi$ (30° , 60° , 90° , 120° and 150°) and three noise situations (no noise, Gaussian noise with standard deviation σ of two and five grey levels respectively). Method C is not included since it corresponds to the same equation as B, using samples I_1 to I_4 instead of I_2 to I_5 . The shape of graphs plotted as a function of the phase φ are identical for B and C, one being shifted by an amount $\Delta\varphi$ with respect to the other.

The model we use is that of an interferogram where the background intensity I_0 is equal to 128 grey levels and the modulation I_M is equal to 32 grey levels. The resulting intensity values are coded as 8 bits integers. For each possible combination {method, $\Delta\varphi$, σ }, we estimate $\Delta\varphi$ from five simulated intensity values I_1 to I_5 , the phase ranging from 0° to 360° with a step of 1° . The computation is actually repeated one hundred times for each phase value (except when $\sigma = 0$), using 100 noisy samples $\{I_1, I_2, I_3, I_4, I_5\}$. The corresponding distributions are presented in the next figures.

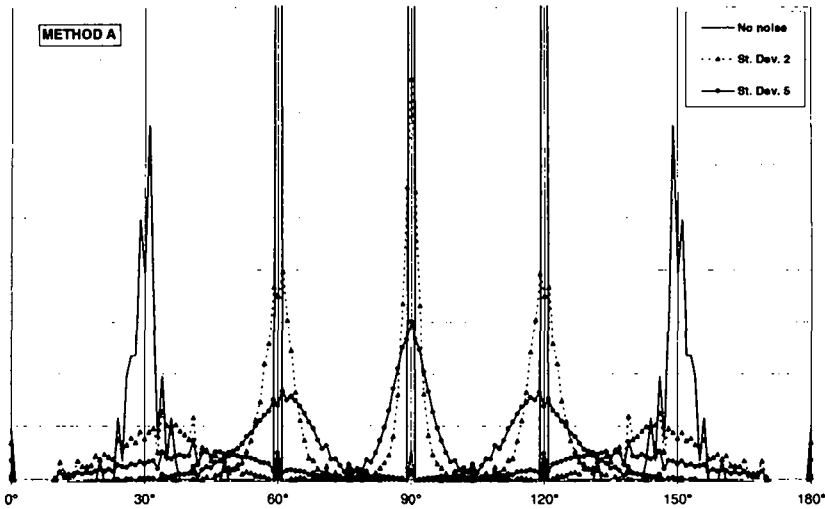


Figure 5-1. Computed $\Delta\phi$ distribution using method A for five nominal values (30° , 60° , 90° , 120° and 150°) and three noise levels.

Figure 5-1 illustrates the results obtained for method A. The vertical scale is cropped in order to display the shape of the distributions when noise is present. Without noise, the highest distribution corresponding to $\Delta\phi = 90^\circ$ is four times as high as the maximum height in this graph. The non-zero width of the distributions in the “no noise” situation result from the 8 bits digitization, which is equivalent to introducing a noise of standard deviation $1/(2\sqrt{3})$ grey levels. We observe that, as supposed earlier, method A gives a good estimation of $\Delta\phi$ around 90° , even for a high noise level. The distributions tend to spread out for 60° and 120° and become very wide for 30° and 150° . By construction, the accuracy of this method is “symmetrical” with respect to 90° . This is interesting in our case since we usually introduce a known phase step of $\pi/2$ during acquisition.

Another parameter of interest is the “success rate” of the method. Quite simply, it corresponds to the number of times where the $\cos\Delta\phi$ value estimated from the ratio presented in (5-3) is within $[-1, 1]$. When this is not the case, because of noise or grey level quantization of intensity, $\Delta\phi$ can not be calculated. The percentages corresponding to Figure 5-1 are presented in Table 5-1. Again, we find a symmetrical behavior relative to 90° . We note that there is a sharp decrease in the transition from 60° to 30° and from 120° to 150° . 35% of

the samples $\{I_1, I_2, I_3, I_4, I_5\}$ do not permit an actual estimation of $\Delta\phi$ for both these extreme values with the higher noise level.

$\Delta\phi$	30°	60°	90°	120°	150°
No noise	97	100	100	100	97
$\sigma = 2$	79	98	99	96	79
$\sigma = 5$	65	94	97	94	65

Table 5-1. Percentage of possible $\Delta\phi$ estimations for method A.

We repeat the same simulations for method B. The corresponding distributions and success rates are presented in Figure 5-2 and Table 5-2.

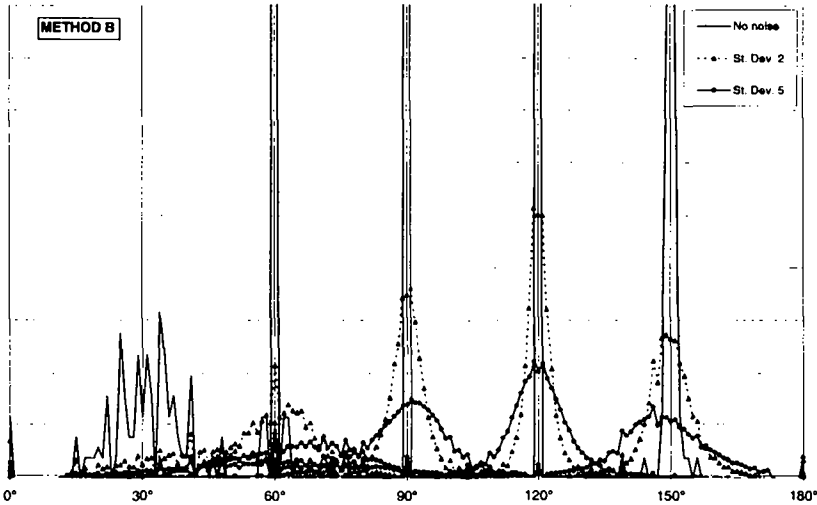


Figure 5-2. Computed $\Delta\phi$ distribution using method B for five nominal values (30°, 60°, 90°, 120° and 150°) and three noise levels.

$\Delta\phi$	30°	60°	90°	120°	150°
No noise	93	100	100	100	99
$\sigma = 2$	63	93	98	98	94
$\sigma = 5$	57	81	94	96	83

Table 5-2. Percentage of possible $\Delta\phi$ estimations for method B.

We observe in this case that there is a shift of the $\Delta\phi$ domain where method B performs better. It corresponds to the $2\pi/3$ (120°) value that we hinted at by looking at the corresponding ratio in (5-3). We note also that the behavior near 30° is catastrophic, even when the only limiting factor is the grey level quantization.

The results for method D are shown in Figure 5-3 and Table 5-3.

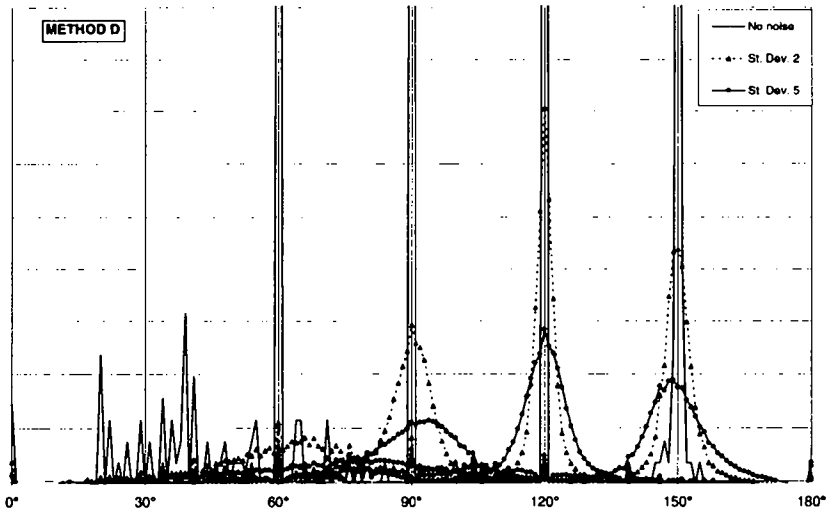


Figure 5-3. Computed $\Delta\phi$ distribution using method D for five nominal values (30° , 60° , 90° , 120° and 150°) and three noise levels.

$\Delta\phi$	30°	60°	90°	120°	150°
No noise	71	99	100	100	100
$\sigma = 2$	56	86	97	98	97
$\sigma = 5$	57	70	92	97	91

Table 5-3. Percentage of possible $\Delta\phi$ estimations for method D.

Not surprisingly, method D performs better than A and B for high $\Delta\phi$ values but seems very unreliable at 60° and below.

These simulations confirm the observations that could be made from the formula presented in (5-3). Method A appears as the most “balanced” because of its symmetrical behavior with respect to 90° . It is moreover the most reliable for $\Delta\phi$ values below 90° . However, none of these approaches seems to perform

correctly for small phase increments near and below 30° . This is understandable as the samples $\{I_1, I_2, I_3, I_4, I_5\}$ cover only one third of the period of the cosine function, which is thus poorly sampled. We must not forget however that the estimation of $\Delta\varphi$ is one step of the calculation. It is more important to evaluate the behavior of the whole algorithm in terms of error distributions on the calculated phase φ .

5.3 Some properties of the arctangent function

Before looking at the phase error distributions we need to look at one important property of the arctangent function. The question is: what kind of errors do we introduce on the calculation of φ when $\Delta\varphi$ is not correctly estimated? As we ultimately use the value $\sin\Delta\varphi$ in (5-2), we can see the influence of this term in the computation. Let us suppose that the correct phase increment at two pixels is $\pi/2$ and $\pi/6$. Let us moreover assume that the estimation of $\Delta\varphi$ is grossly wrong, that is, (5-3) yields a $\Delta\varphi$ value equal to $\pi/6$ in the first case and $\pi/2$ in the second. We chose this example since it corresponds to a $\sin\Delta\varphi$ that is half of the correct value in one case and twice the correct value in the other. We can now plot the phase error obtained for a phase ranging from 0° to 90° , when these erroneous $\sin\Delta\varphi$ values are used in (5-2). The results are presented in Figure 5-4 where we see that the maximum error is close to $+20^\circ$ in one case and -20° in the other. The even worse situation where $\Delta\varphi$ is estimated as $\pi/2$ when its true value is $\pi/9$ is also plotted. In this case the error amounts to $\pm 30^\circ$.

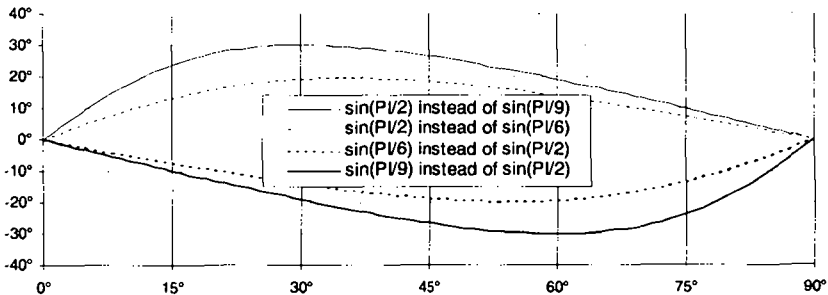


Figure 5-4. Error on the calculated phase φ when $\Delta\varphi$ equals $\pi/2$ (resp. $\pi/6$) but is incorrectly evaluated as $\pi/6$ (resp. $\pi/2$).

This behavior of the arctangent function is good news in the sense that it attenuates largely the effect of a wrong $\Delta\varphi$ estimation. However, this does not

exempt us from trying to estimate $\Delta\phi$ as precisely as possible, as this systematic error source will add in practice to other errors.

5.4 Phase error distributions as a function of the phase

As observed from the equations presented in (5-2) and (5-3) there is an influence of the actual ϕ value on the magnitude of the different terms used to estimate $\Delta\phi$ and ϕ itself. Hence, we want to know the distribution of the error $\delta\phi$ as a function of the phase, the noise level and the method used to estimate $\Delta\phi$. One solution consists in drawing systematically images of these $\delta\phi$ distributions as in Figure 5-5 where the probability density of the calculated phase is plotted as a function of the nominal phase ϕ . In this figure, the results obtained with the method A and D as well as with the Carré algorithm (described in Chapter 4) are presented for a phase increment value of 30° , a noise standard deviation of 5 grey levels and a modulation I_M of 32 grey levels. 50000 phase estimations are made for each nominal phase value ranging from 0 to 360° with a step of 5° . The estimations are accumulated in steps of 5° (for example, 183° and 187° are counted in the same "bucket" as 185°). Successive contour lines correspond to a change of probability density of 500. A diagonal line is superimposed to help evaluate the deviation from the exact phase value.

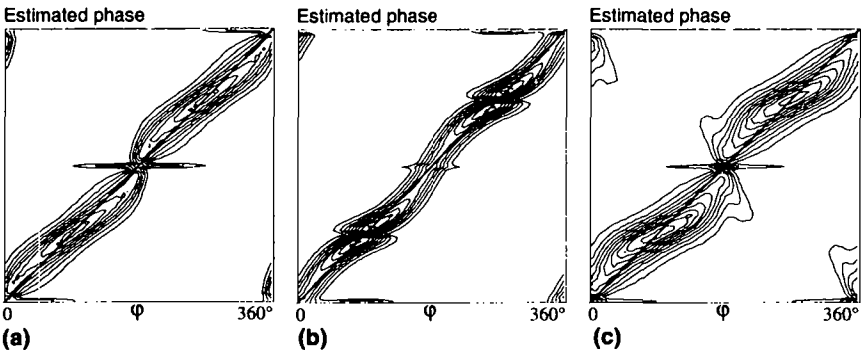


Figure 5-5. (a) Probability density of the calculated phase using equations (5-3)A and the 5-image algorithm (5-2) for a noise standard deviation of 5 grey levels and a phase increment $\Delta\phi$ of 30° ; (b) Same using (5-3)D and (5-2); (c) Same using the Carré algorithm.

This figure shows that the error is somehow reasonable using the 5-image algorithm with method A or, surprisingly, D for the computation of $\Delta\phi$. The two complementary phase domains of these algorithms appear in the image. We see

that phase estimations based on A are quite good near $\pi/2$ and $3\pi/2$ which are troublesome for method D, while D provides good results near 0 and π where A is imprecise. However, as seen in Table 5-1 and Table 5-3, only 65% (A) and 57% (D) of the estimations actually lead to a phase value that can be taken into account in these graphs. In particular, holes are created in the distributions near the problematic phase values. The “weakness” of the Carré algorithm also appears for such a small phase increment value. It is interesting to note that all these algorithms produce systematic phase errors that do not disappear in the averaging process. They are shown to be symmetrical in the four phase quadrants.

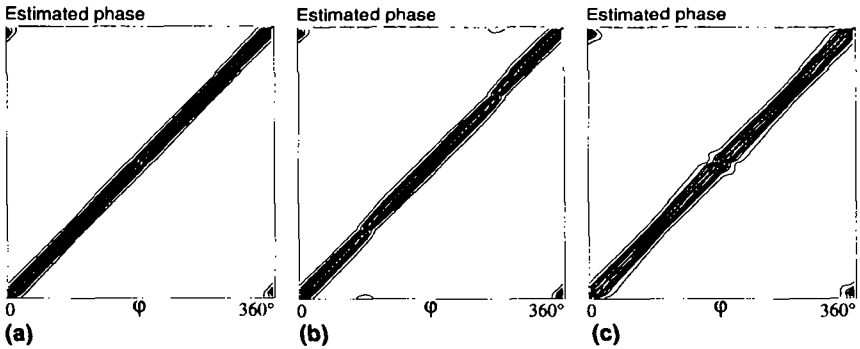


Figure 5-6. (a) Probability density of the calculated phase using equations (5-3)A and the 5-image algorithm (5-2) for a noise standard deviation of 5 grey levels and a phase increment $\Delta\phi$ of 90° ; (b) Same using (5-3)D and (5-2); (c) Same using the Carré algorithm.

The second example presented in Figure 5-6 is obtained for $\Delta\phi$ equal to 90° where a minimum of errors should be committed. Successive contour lines correspond in these images to a change of probability density of 2000. As this is the ideal $\Delta\phi$ value, it is not surprising to obtain an excellent behavior of the 5-image algorithm based on method A and D. The Carré algorithm performs well also.

The situation where $\Delta\phi$ is equal to 150° is presented in Figure 5-7. In this situation, we expect the 5-image algorithm based on method D and the Carré algorithm to provide interesting results. Successive contour lines correspond in these images to a change of density of 1000.

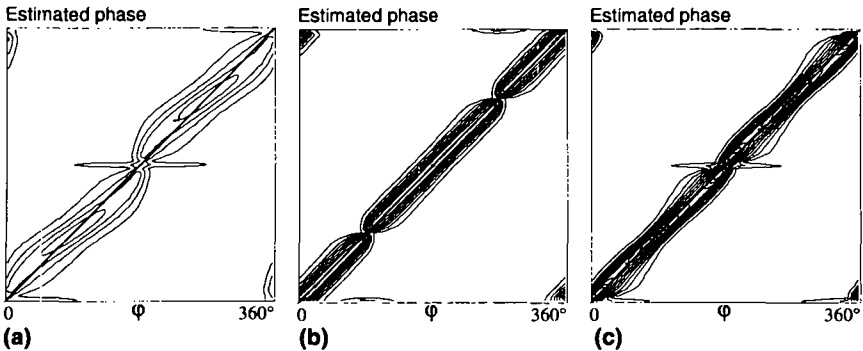


Figure 5-7. (a) Probability density of the calculated phase using equations (5-3)A and the 5-image algorithm (5-2) for a noise standard deviation of 5 grey levels and a phase increment $\Delta\phi$ of 150° ; (b) Same using (5-3)D and (5-2); (c) Same using the Carré algorithm.

Method A gives the same results that were obtained in Figure 5-5 for $\Delta\phi = 30^\circ$ while method D and the Carré algorithm give “acceptable” errors. We note however that the method D is always unreliable when ϕ is close to $\pi/2$ or $3\pi/2$. Consequently, a lot of samples can not be calculated in these regions, which explains the corresponding “holes” in the distribution.

In order to compare more easily methods A, B and D, the case where $\Delta\phi$ is already known, and the Carré algorithm, we will now work with graphs of the standard deviation of the error $\delta\phi$.

5.5 Phase error standard deviation as a function of the phase

In the next six figures we show the standard deviation of the error $\delta\phi$ for five different $\Delta\phi$ values, in the situation of a noise standard distribution of five grey levels and a modulation I_M of 32 grey levels. In each graph, the deviation is computed from 50000 samples for each phase value ranging from 0° to 360° with a step of 1° . The error standard deviation is given in degree on a scale ranging from 0° to 30° in the last five graphs while the scale goes up to 50° in the first one to accommodate the large errors encountered with the Carré algorithm (the first and second graph are thus identical). Again, situations where $|\cos\Delta\phi| > 1$ are not included in the calculation of the standard deviation.

For the 5-image algorithm, $\Delta\phi$ is estimated with methods A, B and D, or is supposed “known”, for example as the result of a wavelet analysis.

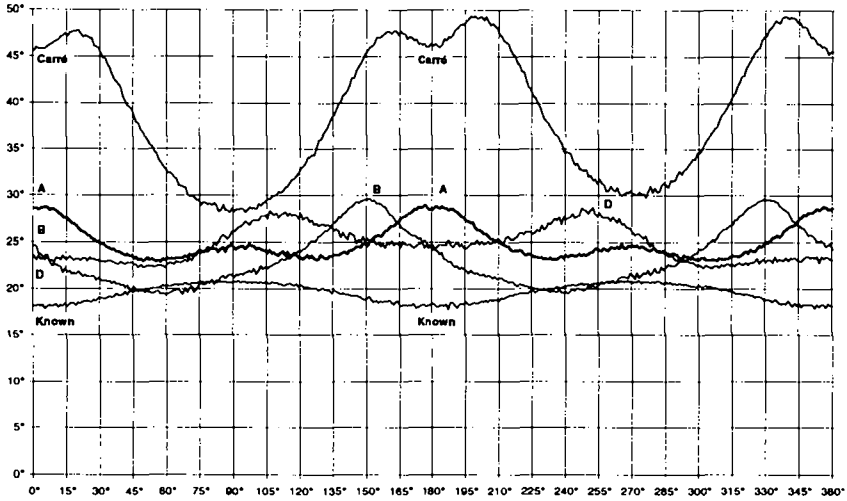


Figure 5-8. Standard deviation (expressed in degrees) of the phase error committed with the 5-image and Carré algorithms for $\Delta\phi = 30^\circ$.

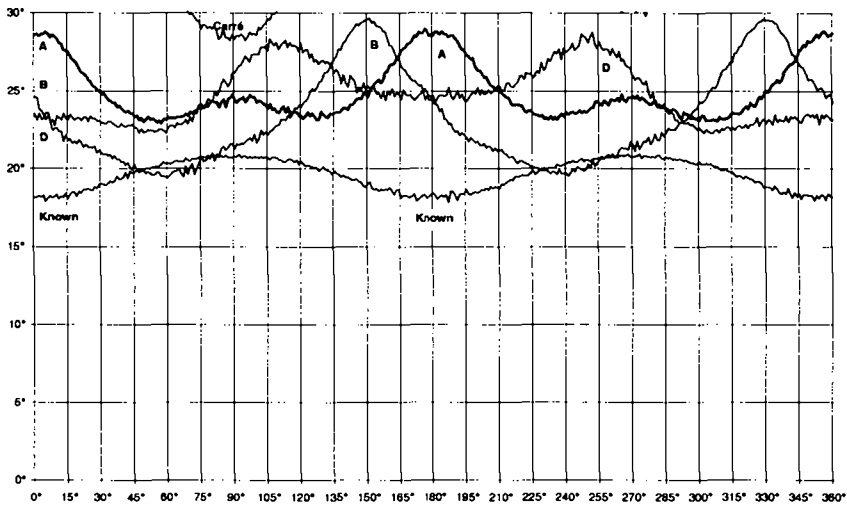


Figure 5-9. Standard deviation (expressed in degrees) of the phase error committed with the 5-image and Carré algorithms for $\Delta\phi = 30^\circ$.

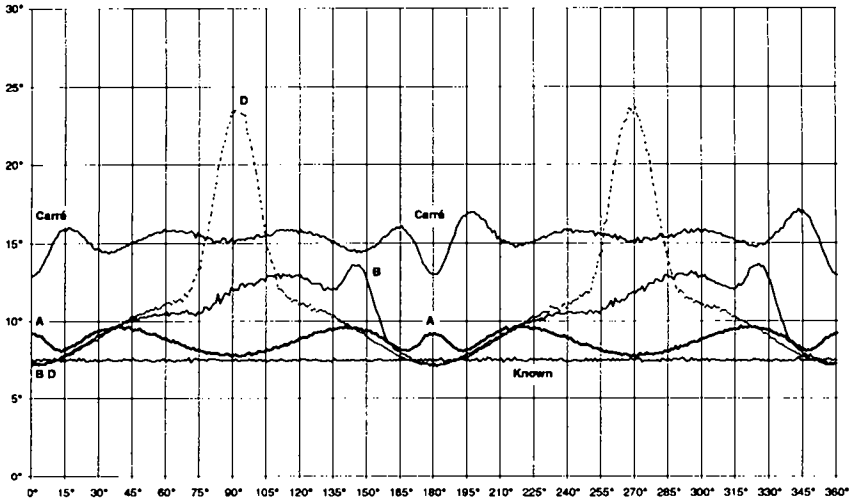


Figure 5-10. Standard deviation (expressed in degrees) of the phase error committed with the 5-image and Carré algorithms for $\Delta\varphi = 60^\circ$.

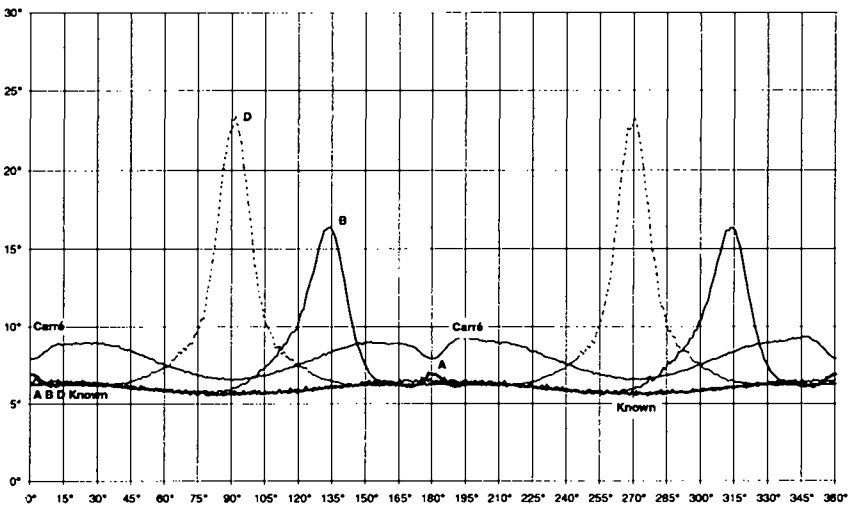


Figure 5-11. Standard deviation (expressed in degrees) of the phase error committed with the 5-image and Carré algorithms for $\Delta\varphi = 90^\circ$.

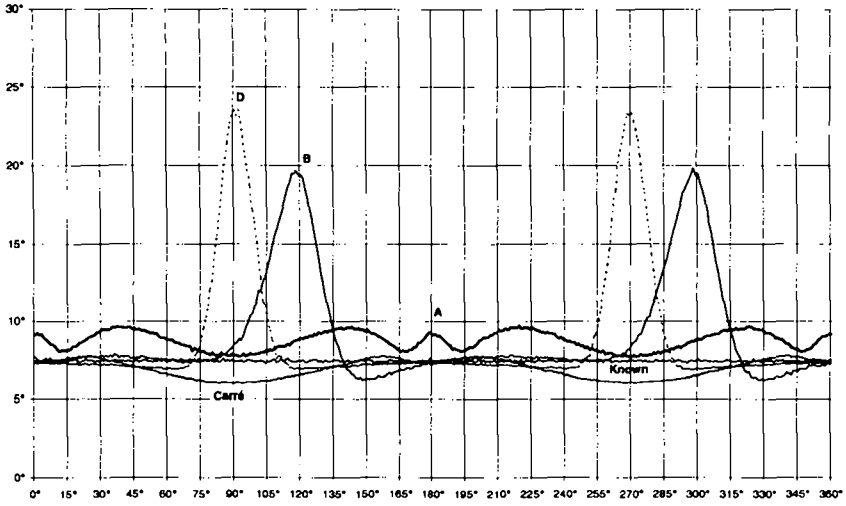


Figure 5-12. Standard deviation (expressed in degrees) of the phase error committed with the 5-image and Carré algorithms for $\Delta\varphi = 120^\circ$.

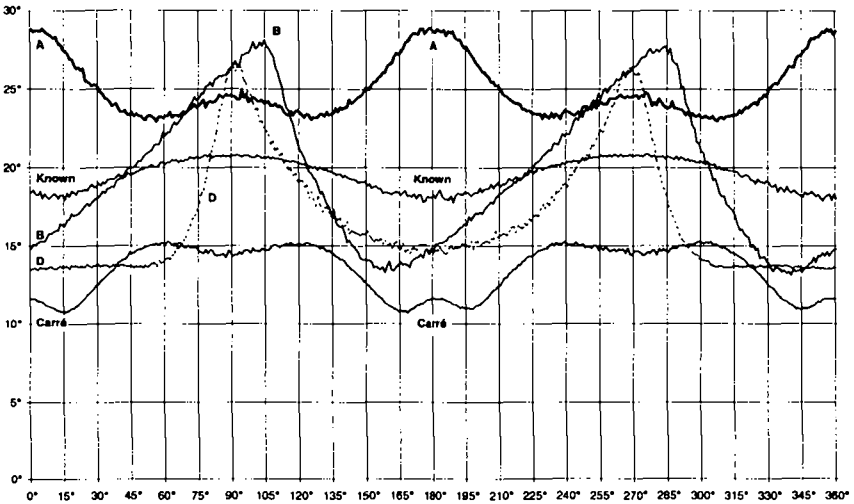


Figure 5-13. Standard deviation (expressed in degrees) of the phase error committed with the 5-image and Carré algorithms for $\Delta\varphi = 150^\circ$.

We can use different criteria to compare these graphs. One could be the “fairness” of the error distribution, that is, the way one algorithm behaves for different phase values. Apart from the case where $\Delta\varphi$ is known, which gives very smooth and constant results, it appears that when method A is used to determine this phase increment, the error standard deviation does not oscillate much as a function of the phase itself. This oscillation is smaller than 2° for $\Delta\varphi$ ranging from 60° to 120° and on the order of 5° for 30° and 150° . Hence, method A does not put much “discrimination” on the phase values. This is certainly not the case for methods B and D. Indeed, D performs very poorly when φ is close to $\pi/2$ and $3\pi/2$, with error standard deviations close to 25° when $\Delta\varphi$ goes from 60° to 120° . Its best result is actually obtained for $\Delta\varphi = 120^\circ$ in which case the phase domain where large errors are produced is limited to about 30° . Method B is slightly better but far from the result obtained with A. We can verify that the “peaks” where method B yields its less precise results are shifted according to the value of $\Delta\varphi$ (see (5-3)).

A second way to characterize these different methods is to simply look at the overall amount of error committed. The situation where $\Delta\varphi$ is supposed known is usually the less error prone even though, for $\Delta\varphi$ larger than 150° , some other methods perform better. This implies that the actual determination of the phase increment helps correct the noisy phase estimation for B and D. Method A is clearly the best for $\Delta\varphi$ ranging from 60° to 120° . For small phase increments (30°) it becomes as unreliable as B and D while these last two perform better for large ($>150^\circ$) phase increments.

The Carré algorithm shows a quite definite preference for large phase increments. It is clearly useless when $\Delta\varphi$ is on the order of 30° and it still performs poorly near 60° . However, it gets better above 90° and is the most precise algorithm for $\Delta\varphi$ larger than 120° .

5.6 Overall phase error standard deviation as a function of the phase increment

Bearing in mind that the error standard deviation is not uniform as a function of φ for some of the methods studied here, we now “integrate” this error standard deviation over the complete phase range, in order to plot graphs as a function of the phase increment. This should help to understand the limits of the different algorithms, regarding the acceptable speeds of deformation.

The standard deviation is calculated for a given $\Delta\varphi$ by estimating 100 times each phase value from 0° to 360° . Five different situations are presented. The

first three correspond to a modulation I_M equal to 32 grey levels with no noise, a Gaussian noise of standard deviation equal to 2 grey levels and a noise of 5 grey levels. The two remaining situations are obtained for a noise level of 5 and lower modulations of 16 and 8 grey levels. These last cases are relevant to speckle interferometry where low modulation values are common.

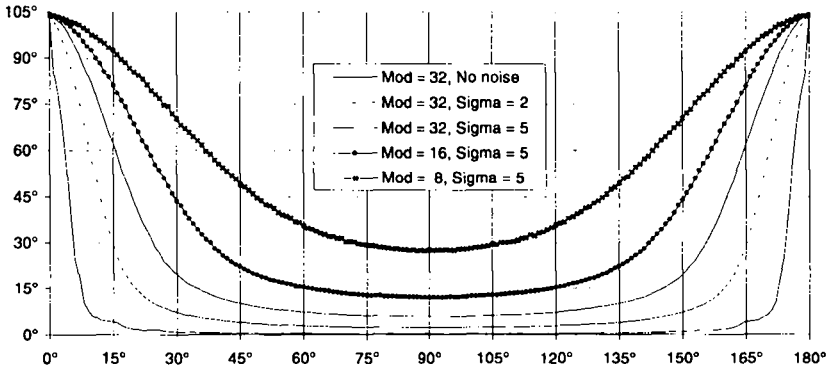


Figure 5-14. Phase error standard deviation as a function of the phase increment $\Delta\phi$ for different modulations and noise levels. The phase is computed with the 5-image algorithm, $\Delta\phi$ is supposed known.

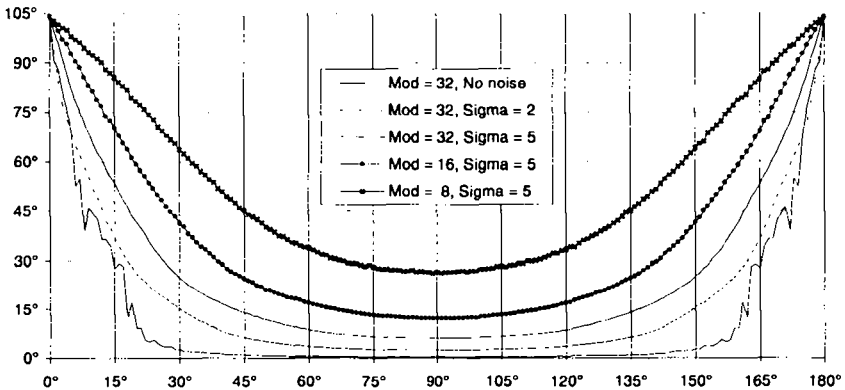


Figure 5-15. Phase error standard deviation as a function of the phase increment $\Delta\phi$ for different modulations and noise levels. The phase is computed with the 5-image algorithm based on method A.

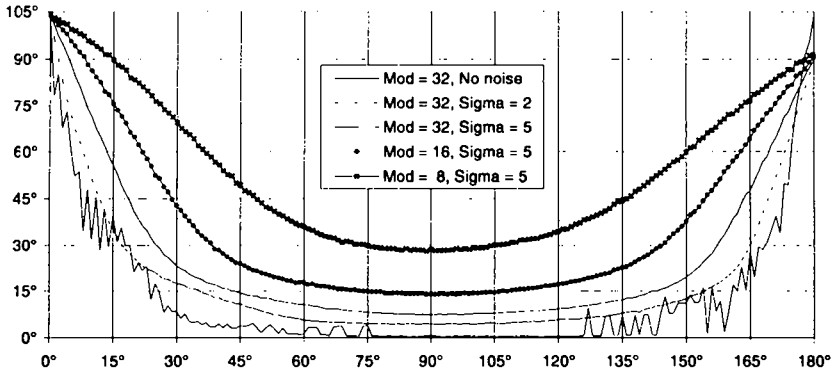


Figure 5-16. Phase error standard deviation as a function of the phase increment $\Delta\phi$ for different modulations and noise levels. The phase is computed with the 5-image algorithm based on method B.

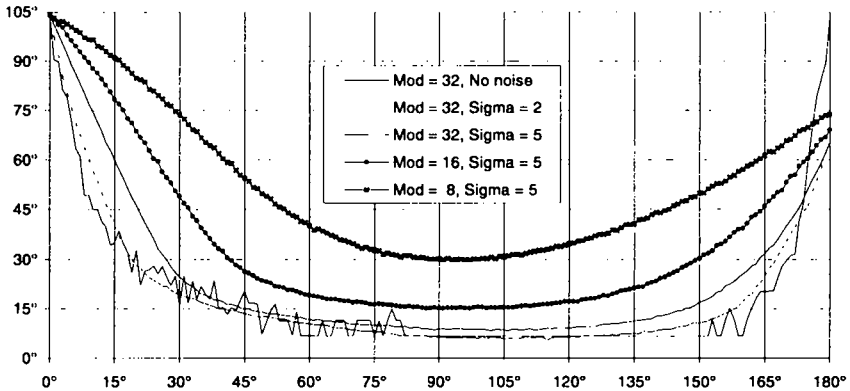


Figure 5-17. Phase error standard deviation as a function of the phase increment $\Delta\phi$ for different modulations and noise levels. The phase is computed with the 5-image algorithm based on method D.

For all the algorithms tested, the phase computation becomes totally random when $\Delta\phi$ is close to 0° . This means that the estimated phase is uniformly distributed over $[0, 2\pi]$. The resulting standard deviation is then $\pi/\sqrt{3}$ radians $\approx 104^\circ$, which corresponds well to the limit found in these simulations.

The last figure is obtained using the Carré algorithm:

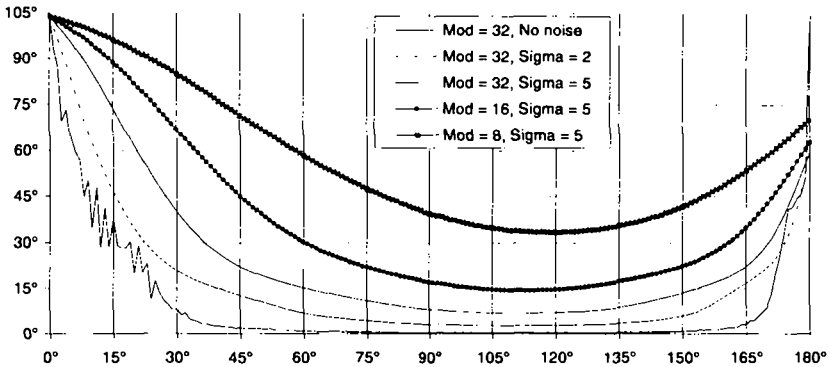


Figure 5-18. Phase error standard deviation as a function of the phase increment $\Delta\phi$ for different modulations and noise levels. The phase is computed with the Carré algorithm.

The interpretation of these figures is difficult as they do not reflect the actual number of phase values that can be computed for a given $\Delta\phi$ (see paragraph 5.2). This does actually lower the overall error standard deviation, particularly for method D.

We can first observe that the “no noise” situation shows how sensitive the different algorithms are to the quantization errors. In particular, this adds an important offset in the case of method D. The case where $\Delta\phi$ is supposed to be exactly known gives the smallest phase errors for high signal-to-noise ratios ($I_M = 32$, $\sigma \approx 2$). However, for lower ratios, it appears that the actual estimation of $\Delta\phi$ (with B or D) allows to correct part of the phase error and provides slightly better results for large $\Delta\phi$ values. Method A has a very similar behavior, symmetrical on both sides of $\Delta\phi = \pi/2$ while methods B and D exhibit a better accuracy towards higher $\Delta\phi$ values. The Carré algorithm appears to be the best contender for $\Delta\phi > 120^\circ$, a fact that was already observed in paragraph 5.5, and which confirms the observations made in Ref.4.

If we look at the situation ($I_M = 32$, $\sigma = 5$) and decide that a tolerable phase error standard deviation should not be above 15° , we find that all the algorithms present a domain of application that covers from 95° to 100° of the total possible 180° . This is illustrated in Figure 5-19 where the vertical scale has been magnified. Apart from the case where $\Delta\phi$ is known, method A gives the best results from 45° to 125° (not taking into account the Carré algorithm).

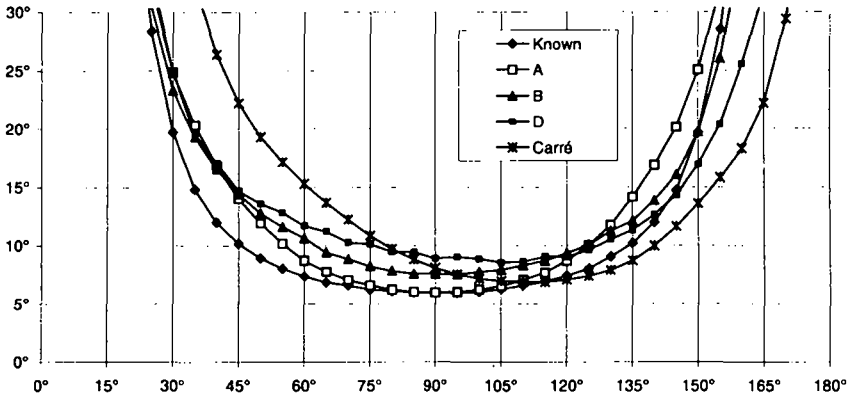


Figure 5-19. Phase error standard deviation as a function of the phase increment $\Delta\phi$ for $M = 32$ and $\sigma = 5$ grey levels.

As a conclusion to the graphs shown in paragraphs 5.2 to 5.6, the 5-image algorithm based on the estimation of $\Delta\phi$ with method A seems to offer a good compromise. First, it is symmetrical relatively to $\pi/2$ which corresponds to the phase step that we will introduce during acquisition. Hence, $\pi/2$ acts as the origin of the domain of the phase increments we wish to measure. This symmetry allows to use the algorithm with the same accuracy for pixels where the phase increment is $+\Delta\phi$ or $-\Delta\phi$. Overall, this solution generates smaller errors on the domain $[45^\circ, 135^\circ]$, even though the difference with the other methods is small. Some marginal gain could be obtained by trying to combine method A with, for example, D for $\Delta\phi$ values above 120° . However, all these methods start to diverge fast above 135° and a standard deviation of 25° rather than 30° still basically results in *large* errors on the phase estimations. It is clear anyway that high accuracy will not be obtained with this algorithm when $\Delta\phi$ is outside of the domain $[60^\circ, 120^\circ]$. Another point in favor of method A is its relative error uniformity as a function of the phase, as shown in 5.5, contrary to method D and to a lesser extent B.

The noise levels we used in these simulations can seem to be high, particularly if we consider that state-of-the-art CCD cameras and frame grabbers can deliver intensity noise levels on the order of one grey level. However, as soon as we intend to work in non-static conditions, environmental perturbations such as turbulence and mechanical vibrations can create a phase noise that sometimes results in large intensity variations. Admittedly, the independent Gaussian noise model we used is not exactly adapted to describe such noise

sources but we guess that we obtain a rough estimate of the actual behavior of this quite simple phase-shifting algorithm.

5.7 Influence of non-linear phase evolution

As mentioned earlier, the hypothesis of a linear phase evolution during acquisition of five images might not be always verified. It is thus interesting to try to evaluate the systematic errors that can be produced, in a first approach, by a second-degree phase evolution (we can imagine that third-degree variations will tend to cancel in this symmetrical algorithm). Creath⁵ made similar simulations but always in the case where $\Delta\phi$ is fixed equal to $\pi/2$.

We simulate the response of the 5-image algorithm based on method A using two different amount of non-linearity, (1) and (2), as shown in Figure 5-20. No noise is added in these simulations. However, grey level quantification of intensity remains (the modulation is again $I_M = 32$). The second non-linear situation is already quite demanding as the phase of the first intensity sample is $\phi - \Delta\phi$ instead of $\phi - 2\Delta\phi$ and the phase of the last intensity sample is $\phi + 3\Delta\phi$ instead of $\phi + 2\Delta\phi$.

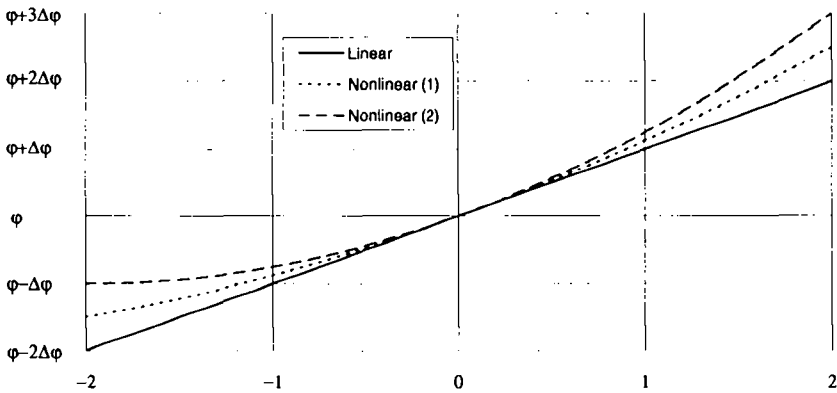


Figure 5-20. Non-linear phase evolution as a function of time.

The figures below show the phase error in degree as a function of the initial phase, for seven different $\Delta\phi$ values. Whenever the estimated $\cos\Delta\phi$ is outside of the domain $[-1, 1]$ the phase is not estimated and the corresponding symbol is removed from the scatter plot.

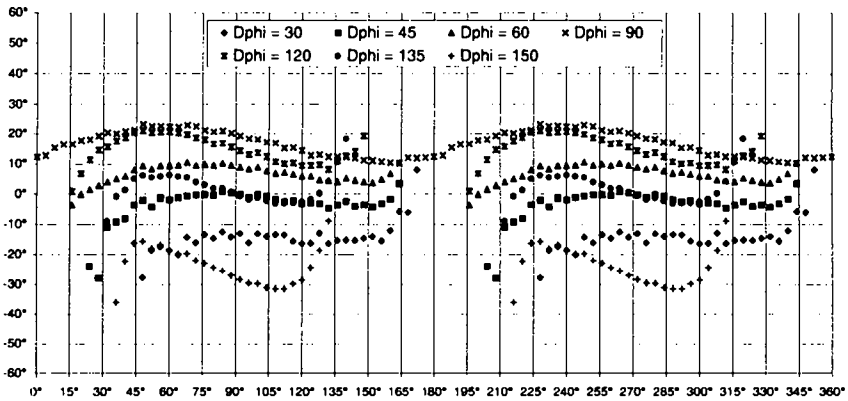


Figure 5-21. Phase error in the case of the non-linear phase evolution (1) using method A with the 5-image algorithm.

We observe that the phase error is quite important, ranging from $+20^\circ$ to -30° for $\Delta\phi$ in the domain $[30^\circ, 150^\circ]$. The variation of the error as a function of ϕ gets bigger with higher $\Delta\phi$ values. We observe also that method A which is used to determine $\Delta\phi$ fails in the regions where ϕ is close to 0 or π , except when $\Delta\phi = 90^\circ$. Hence, a non-linearity in the phase evolution will further lower the “success rate” described in paragraph 5.2. Figure 5-23 below shows that the Carré algorithm does not fare any better for the same non-linear phase evolution.

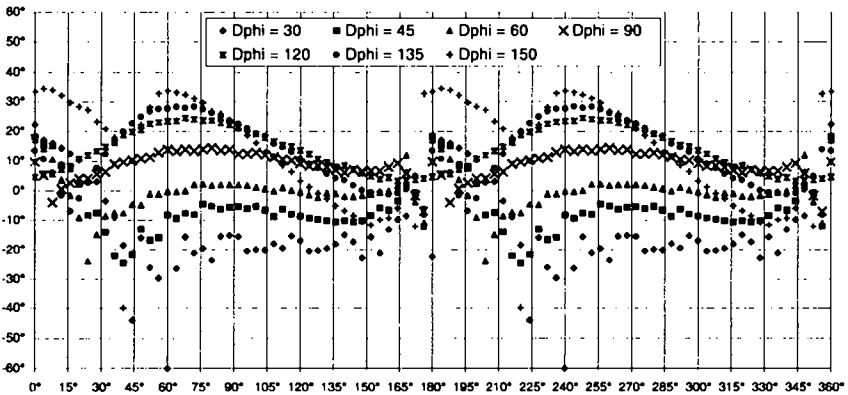


Figure 5-22. Phase error in the case of phase evolution (1) using the Carré algorithm.

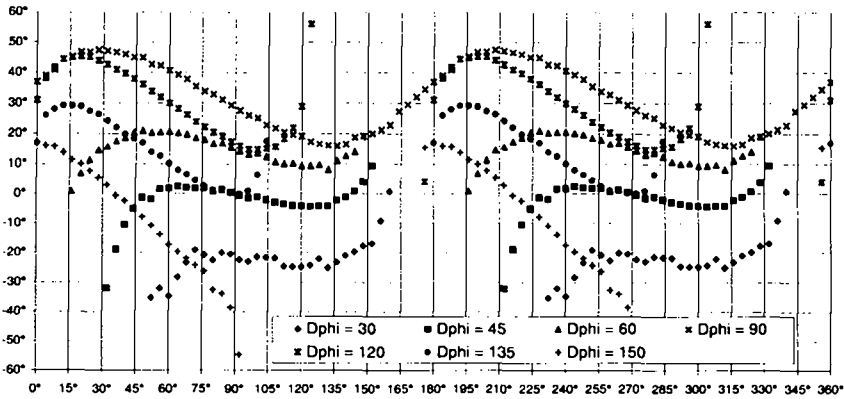


Figure 5-23. Phase error in the case of the non-linear phase evolution (2) using method A with the 5-image algorithm.

Figure 5-23 obtained for the non-linear phase evolution (2) shows a quite similar behavior to what is obtained with the non-linear phase evolution (1). The errors are amplified and it becomes visible that the average systematic error produced for one given $\Delta\phi$ value goes from negative values (about -30° for $\Delta\phi = 30^\circ$) up to a maximum (about $+30^\circ$ for $\Delta\phi = 90^\circ$) and back to negative values (about -10° for $\Delta\phi = 150^\circ$). The shape of the error distributions changes at the same time. It is quite flat for a small $\Delta\phi$ and gets steeper and steeper when it increases. This is quite understandable as in the case of small $\Delta\phi$ the absolute phase error for the different intensity samples is minimized. However, the systematic variation of the average error with $\Delta\phi$ appears more difficult to explain intuitively. Figure 5-24 shows that the result is similar when $\Delta\phi$ is not computed with method A but assumed known. Hence, this behavior is essentially a result of (5-2).

The conclusion is that non-linearities will introduce systematic errors that will be higher for pixels where the total phase change is large. The second example of large non-linear phase evolution shows that errors as large as $\pm\pi/4$ can be obtained. This is certainly troublesome in the case of experiments where a small number of fringes are present in the image, since the relative error is then more important. However, if there are indeed few fringes in the interferogram, chances are that the phase variation rate $\Delta\phi$ must not vary much in the image. Hence, similar errors should be produced and the end result is a smaller relative error plus an unknown phase offset. It is nonetheless clear that accuracy on the order of hundredth of a fringe will not be obtained in the context of dynamic phase-shifting, a tenth of a fringe is more realistic.

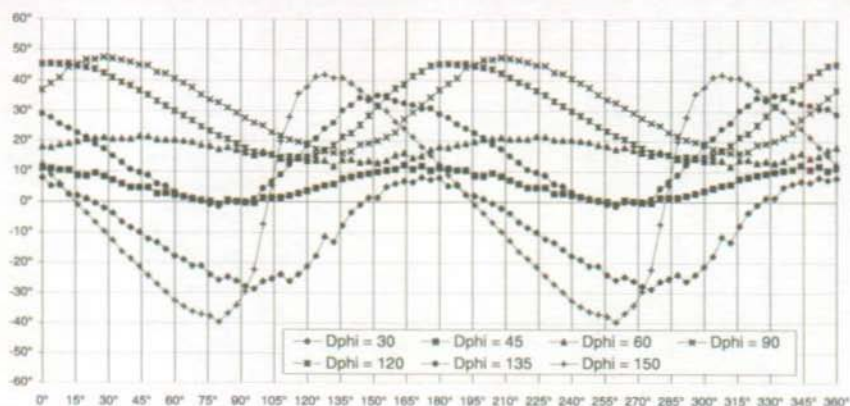


Figure 5-24. Phase error in the case of phase evolution (2) when $\Delta\phi$ is supposed known.

5.8 Implementation and examples

The implementation of the 5-image algorithm is straightforward. We developed different specific versions that were added to the commercial image processing programs Optocat 5 and Visilog 4.

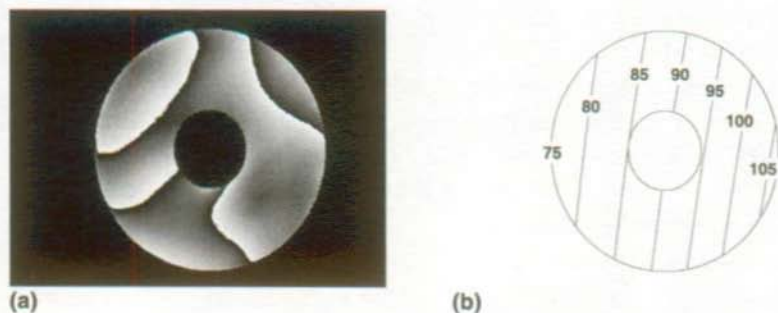


Figure 5-25. (a) Wrapped phase map showing the flatness of an aluminum disc. The average sensitivity is 12 micron per fringe. (b) Contour lines of the computed phase increment (in degree).

One particular version is adapted to process interferograms produced by a desensitized flatness-measurement instrument⁶ where large sensitivity variations make impossible the creation of uniform phase shifts. Figure 5-25(a) shows the wrapped phase map obtained while measuring a rough aluminum disc used as a substrate for the manufacture of computer hard disk. The sensitivity in this

image ranges from 14 to 10 micron/fringe from left to right. The contour lines of Figure 5-25(b) show that when a phase-step of 90° is introduced in the center of the field of view, phase-steps of respectively 75° and 105° are introduced at the left and right edges of the object. These lines are obtained from a best-fit estimation of the $\Delta\phi$ map with a polynomial surface of degree 2. This is possible because the sensitivity variation in the interferometer is smooth and monotonous in the field of view.

However, in the case of dynamic phase-shifting we can not assume any continuity of the phase increment distribution in the image. For example, two points on opposite lips of a crack might have very different $\Delta\phi$. Hence, we need to compute the phase increment on a pixel by pixel basis. It is true that for most pixels the local $\Delta\phi$ value should be pretty close to that of its immediate neighbors. This is a way to improve the robustness of the algorithm. We have seen that method A becomes unreliable when the phase of the interferogram is close to 0 or π , which usually leads to $|\cos\Delta\phi| > 1$. It is then interesting to look in the surrounding pixels to find one that has a different phase and thus permits a more reasonable evaluation of the local $\Delta\phi$. This solution is not yet implemented but we can guess that it would work quite well in the case of speckle interferograms where the phase is random from one pixel to the other. Classical or holographic interferograms would benefit from this improvement in the regions where the fringes are not too widely spaced, since the phase does not change much at the scale of 3×3 pixels windows in large fringes. In the meantime, our current implementation simply assigns a phase value of 0 or π to pixels where $|\cos\Delta\phi| > 1$. The choice between these two values is governed by the fact that both I_2 and I_4 are larger or smaller than I_3 .

We can mention here that we tried at the beginning of this dissertation work to combine methods A, B and C to calculate $\Delta\phi$ more robustly. The idea was to change by ± 1 grey level the five measured intensities and look at the resulting variance of the calculated $\Delta\phi$ value. We hoped that this would help to choose the more adapted method, i.e. the one less sensitive to noise for these particular intensity samples. However, the gain was only marginal and not worth the much increased computation time.

5.8.1 Application to holographic interferometry

Let us now look at a first example of application of the 5-image algorithm, based on method A, in the case of images recorded in non-static conditions. Other examples will be proposed in Chapter 8 where the 5-image algorithm is also compared to phase extraction using the wavelet analysis.

The example presented in Figure 5-26 was obtained with holographic interferometry applied to a small object that consists of a 2 mm thick rectangle of sand-blasted aluminum. Two cuts were made on each small side. They extend inward to about a third of the length of the rectangle, creating 6 strips merging near the middle of the object. The top center, bottom left and bottom right strips were clamped with screws on a base plate. A large range PZT (45 microns) was fitted through a hole in this plate to load the object in its center. A voltage ramp was applied to this PZT during acquisition of a 128 frames sequence at 40 Hz while a PZT-mounted mirror was producing $\pi/2$ reference phase steps between images. The cycle was actually reversed ($0, 3\pi/2, \pi, \pi/2, 0$ instead of $0, \pi/2, \pi, 3\pi/2, 0$) to have the phase-shift induced by the deformation and the reference phase step with opposite signs. This will ultimately produce a negative of the actual deformed shape of the object. The non-standard CCD camera used for this experiment is described in more details in Chapter 7.

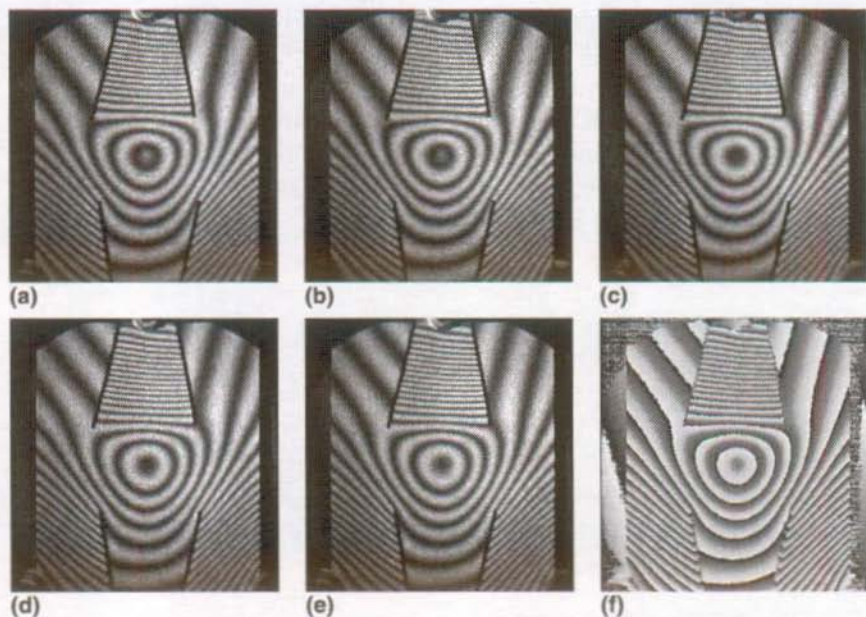


Figure 5-26. (a) to (e): 5 successive images obtained with holographic interferometry during deformation of a metal plate loaded in its center; (f) wrapped phase map corresponding to image (c).

Figure 5-26(a) to (e) show the interferograms obtained near the end of the recording for images #122 to #126. It is clear that the deformation is minimal at

the fixation points, for example at the top of the upper center strip where part of a screw can be seen. If we look at the region directly underneath this screw we see a dark fringe in (a) that changes to a bright fringe in (c) and back to dark in (e). This confirms that the introduced phase step is $\pi/2$. Meanwhile, there is a bright fringe in the center of the object in (a) and a dark one in (e). The total phase change is on the order of π at that point, which indicates that the actual phase shift between images is on the order of $\pi/4$. We can then conclude that the deformation introduces a $-\pi/4$ shift while the mirror produces a $+\pi/2$ step. The calculated wrapped phase map is shown without any filtering in (f). If we look closely at the wrapped fringes it appears that we indeed obtained the reverse of the deformation. This illustrates the fact that the sign of the deformation is known without ambiguity when the reference phase step is known.

It appears to the trained eye that the wrapped phase map suffers from the effect of a non-linear phase shift. This can be seen in the vertical cut presented in Figure 5-27. This cut corresponds to the center of the object, from top to bottom. As the phase is coded on 8 bits in this image, the value 127 corresponds to π radians.

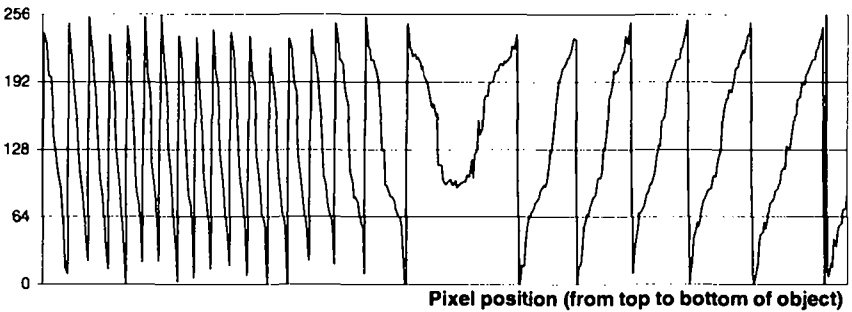


Figure 5-27. Vertical cut of Figure 5-26(f) showing the non-linear fringes caused by a miscalibration of the reference phase step.

The particular departure from straightness of the fringes is the signature of either a miscalibration of the PZT that introduces the reference steps or of a sudden change of the force applied by the loading device. Moreover, as seen in paragraph 5.4, the phase calculated for small $\Delta\phi$ values suffers from a non-linear response of the algorithm, even for linear phase shifts. This could also contribute to the distorted profile of the fringes in the central region of the object. However, the same defect is present near the top of the object (left part of the graph) where $\Delta\phi$ is close to 90° and where the response of the algorithm is

supposed to be very linear. Hence, there must be another cause of error. Tests performed later on the same reference PZT showed that it started to vibrate when it was driven near 40 Hz. Hence, the actual phase step introduced between images was not always the supposed $\pi/2$ value, particularly for the large transition from $3\pi/2$ back to 0. This is in fact a situation where the phase increment is relatively constant for three acquisition intervals and very different for the fourth. In this case, we are far from a smooth second-degree phase evolution, as presented in paragraph 5.7. It could be possible to apply a correction to the wrapped phase map using a look-up-table to correct to a certain extent the defaults resulting from the inaccurate phase shift.

It is also interesting to have a look at the phase increment map computed with method A. A smoothed version is presented as a pseudo-3D surface in Figure 5-28(a). A cut of the unfiltered image is presented in Figure 5-28(b). It shows the evolution of this phase increment along a vertical line passing in the center of the object. The noisy curve shows the raw $\Delta\phi$ value computed by the algorithm. The high peaks correspond to points where the cosine is larger than one. In this case they get the value 255, to mark the corresponding pixel as bad. The raw $\Delta\phi$ curve was low-pass filtered with a median filter of width 5. The smooth curve is the result of a polynomial fit of this filtered cut, showing the evolution of the phase increment on the object. Not surprisingly, $\Delta\phi$ is close to 90° near the top screw (left part of graph) and goes down to a little less than 45° in the central region.

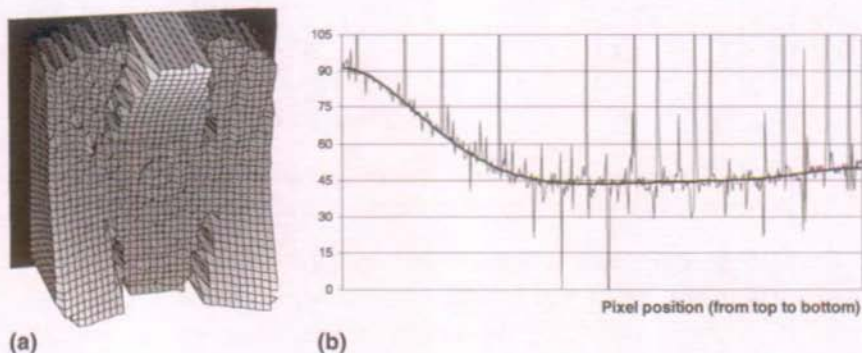


Figure 5-28. (a) Surface plot of the filtered phase increment computed with method A (scale goes from 0° to 90°); (b) Vertical cut showing the raw $\Delta\phi$ value measured in degree, and a polynomial fit.

To estimate the influence of the term $\sin\Delta\phi$ in formula (5-2) and thus the importance of a correct estimation of $\Delta\phi$, we compute two new phase maps where $\Delta\phi$ is imposed to be equal to 90° and 45° . The phase map of Figure 5-26(f) is then subtracted modulo- 2π from these images. We actually draw the absolute value of these differences in Figure 5-29. In these images, "black" represents an exact match with Figure 5-26(f) while "white" represents a difference of $\pm 15^\circ$.

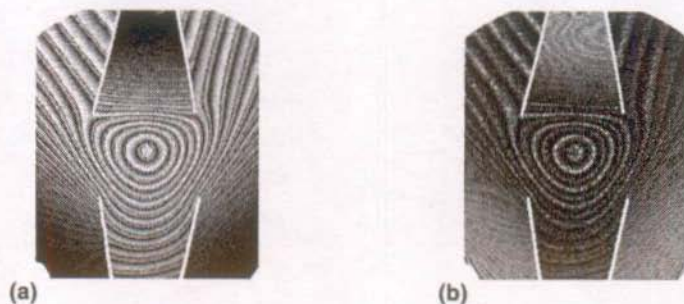
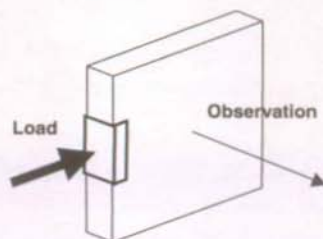


Figure 5-29. (a) Absolute phase difference between Figure 5-26(f) and a phase map computed with an imposed $\Delta\phi$ of 90° ; (b) Same with $\Delta\phi = 45^\circ$. Maximum scale (white) represents a difference of $\pm 15^\circ$.

These two images show the interest of a correct evaluation of $\Delta\phi$. The maximum systematic error is on the order of $\pm 15^\circ$ in (a) and $\pm 12^\circ$ in (b). A calculation similar to what was done in paragraph 5.3 shows that the error due to the exchange of $\pi/2$ with $\pi/4$ should be on the order of $\pm 10^\circ$. We find larger errors in this example because of the imperfect phase-stepping.

5.8.2 Application in speckle interferometry

This second example was obtained using speckle interferometry on a square piece of rubber of dimension 60×60 mm and 8 mm thick. For this experiment the interferometer is sensitive to horizontal in-plane displacement.



The object is loaded on its left hand side by a PZT that pushes a U-shaped metallic clamp. Again, 128 images are recorded while a linear tension ramp is applied to the loading PZT, while a PZT-mounted mirror on one arm of the interferometer introduces the $\pi/2$ reference phase steps. The acquisition rate is 20 Hz in this case.

Figure 5-30 shows the histograms of the phase increment maps calculated for images #1 to #5 just before the beginning of loading and for images #123 to #127 at the end of the experiment. The $\Delta\phi$ images (not shown here) show more or less constant plateaus of phase increment over the object. Only the average value is shifted from 90° at the beginning of the experiment to about 130° at the end.

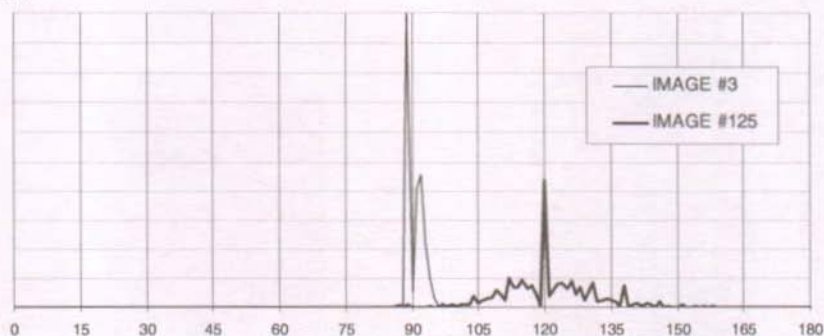


Figure 5-30. Histogram of $\Delta\phi$ at for image #3 and image #125.

The difference modulo- 2π of the two wrapped phase maps corresponding to images #3 and #125 is shown in Figure 5-31. Each fringe is a contour line of equal horizontal in-plane displacement. A difference of one fringe corresponds to a displacement of 1 micron.

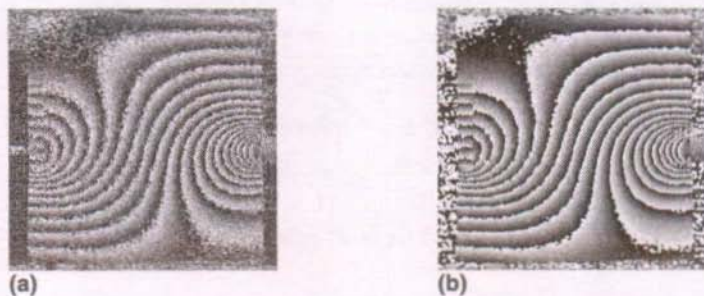


Figure 5-31. (a) Difference modulo- 2π of the random wrapped phase map of image #3 and image #125, showing horizontal in-plane displacement contours; (b) Same after filtering.

The algorithm performs quite successfully in this example. We can even note a set of small parallel fringes on the left of the object. They correspond to the in-plane rotation of the metallic plate that transmits the load to the rubber piece.

A horizontal cut in the filtered image Figure 5-31(b) shows that the fringes do not exhibit a perfectly straight profile, see Figure 5-32. However, we cannot identify the typical shape observed in Figure 5-27. Again, if $\Delta\phi$ is incorrectly estimated during the calculation of the phase images #3 and #125, the systematic, phase-dependent error depicted in paragraph 5.3 is obtained. However, and contrary to Figure 5-27, the phase of adjacent pixels is randomly different, so that the error due to $\Delta\phi$ is randomly distributed in the image. Hence the subtraction creates the macroscopic fringes seen in Figure 5-31, where the systematic errors result now in a noise of average value equal to zero.

There is actually an underestimation of $\Delta\phi$ in image #125. We will come back to this experiment in Chapter 8 where the 5-image algorithm is compared to the wavelet processing. In particular, the wavelet analysis indicates that phase increments approach 150° to the left of the object, at the end of the sequence. This explains why the phase map in Figure 5-31(a) appears noisier in the left region.

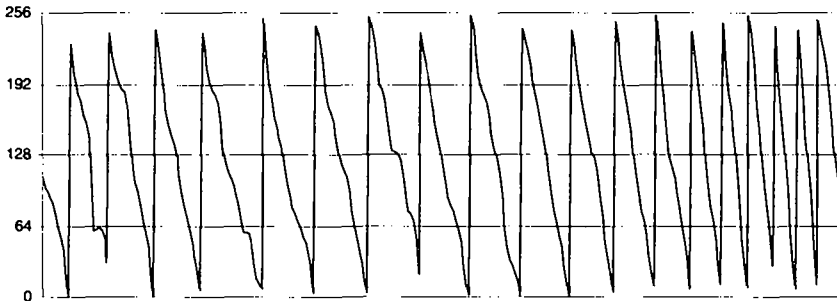


Figure 5-32. Horizontal cut of the phase map shown in Figure 5-31(b).

5.9 Conclusion

We showed in this chapter that we can use a simple phase-shifting algorithm, based on a limited number of images, to process interferograms obtained during object deformation. The principle of dynamic phase-shifting has thus been demonstrated. Simulations and two examples show that the useful domain of application has to be realistically limited to deformation speeds on the order of $\pm\pi/4$ radian per acquisition period, when an additional $+\pi/2$ reference phase step is introduced. Systematic errors are obtained when the actual temporal phase evolution is no longer linear. An estimation of the phase error standard deviation

as a function of the interferogram modulation and acquisition noise gives also an idea of this algorithm's limitations. We see for example that for a modulation equal to 32 grey levels, which is common in holographic interferometry, and a Gaussian intensity noise of standard deviation 5 grey levels, a phase error with a standard deviation of 15° is obtained. This corresponds to a standard error on the order of $\pm 1/24^{\text{th}}$ of a fringe. The precision will be lower when lower modulation interferograms are used, as in speckle interferometry, and when external perturbations introduce additional random phase variations. PZT miscalibrations enter this last type of perturbations. Also, erroneous determination of $\Delta\varphi$ introduces other phase error contributions. Hence, taking into account possible non-linear phase evolutions, phase noise and low modulations, it is difficult to give a general estimation of the actual precision of the method. As a rule of thumb, a reasonable estimation of the overall precision can be on the order of a tenth of a fringe for "well-behaved" experiments.

Bibliography

- 1 J. Schwider, R. Burow, K. E. Elssner, J. Grzanna, R. Spolaszyk, K. Merkel, "Digital wave-front measuring interferometry: some systematic error sources", *Appl. Opt.* 22 (1983), pp. 3421-32.
- 2 P. Hariharan, B. F. Oreb, T. Eiju, "Digital phase-shifting interferometry: a simple error-compensating phase calculation algorithm", *Appl. Opt.* 26 (1987), pp. 2504-2505.
- 3 P. Carré, "Installation et utilisation du comparateur photoélectrique et interférentiel du Bureau International des Poids et Mesures", *Metrologia* 2 (1966), pp. 13-23.
- 4 Y.-Y. Cheng, J. C. Wyant, "Phase shifter calibration in phase-shifting interferometry", *Applied Optics* 24 (1985), pp. 3049-3052.
- 5 C. Creath, "Phase measurement interferometry techniques", in *Progress In Optics XXVI*, Elsevier Science Publishers, 1988, pp. 350-393.
- 6 P. Jacquot, X. Colonna de Lega, P. M. Boone, "Common-path holographic interferometer for flatness testing", *SPIE Vol. 2248* (1994), pp. 125-135.

6. Characterization of the wavelet-based phase extraction

Wavelet analysis, the second solution to the problem of phase measurements in non-static conditions, was presented briefly in Chapter 4. It requires a continuous acquisition of images and is more demanding on the environmental stability than the 5-image phase-shifting algorithm presented in Chapter 5. However, this technique opens a new field of applications since a complete sequence of images can be processed to yield a “movie” of the absolute deformation of an object.

It is the achievements of people working in the field of acoustic signal processing^{1,2} that gave us a lead in the use of wavelet analysis to get the phase information we are looking for. Their field of application is quite different from ours since they deal with usually complicated signals where many components and their harmonics are mixed. Our signals are much closer to simple sinusoidal signals with some added noise. Their signals are usually sufficiently oversampled that they do not suffer from any aliasing problem. In our case, we intend to use as much as possible of the acceptable frequency domain. Hence we sometimes have to work with signals of frequency close to the Nyquist frequency. We are thus easily confronted with aliasing problems. Last, they are not interested in the phase of the different frequencies present in their signals while this is the quantity of prime importance for us. However, they take advantage of some phase properties of the Gabor or Morlet wavelet transform to extract these frequencies. This point proves to be crucial for our developments.

Consequently, the properties of wavelet analysis using the Morlet wavelet are detailed in this chapter. The possibility to extract directly the phase of the interferogram is presented as well as a study of some limitations of this technique.

6.1 The Morlet wavelet

Quite similarly to the window function used in the Gabor transform (defined in Chapter 4), the Morlet wavelet $M(t)$ is the product of a real Gaussian window by a complex oscillating exponential function³:

$$M(t) = \exp\left(-\frac{t^2}{2}\right) \exp(-i\omega_0 t) \quad (6-1)$$

where ω_0 is the “mother” frequency, the only parameter that has to be chosen. We also note that there is no parameter acting as a standard deviation in the Gaussian term. The different wavelets used during time-frequency analysis are derived from the mother wavelet by a time dilation a and time translation b . a is often called the “scale” of the transform. Hence, a wavelet derived from the mother wavelet takes the form:

$$M_{a,b}(t) = M\left(\frac{t-b}{a}\right) = \exp\left(-\frac{(t-b)^2}{2a^2}\right) \exp\left(i\frac{\omega_0}{a}(t-b)\right) \quad (6-2)$$

We see that in fact the scale parameter determines the width of the analysis window. At the same time, it defines the analysis frequency $\omega = \omega_0/a$. Hence, and contrary to the Gabor transform, the functions used at different frequencies have the same “shape” and a varying width. This is illustrated in Figure 6-1 below where the real part of Morlet wavelets and Gabor windows are plotted for three frequencies, along with their Gaussian envelopes.

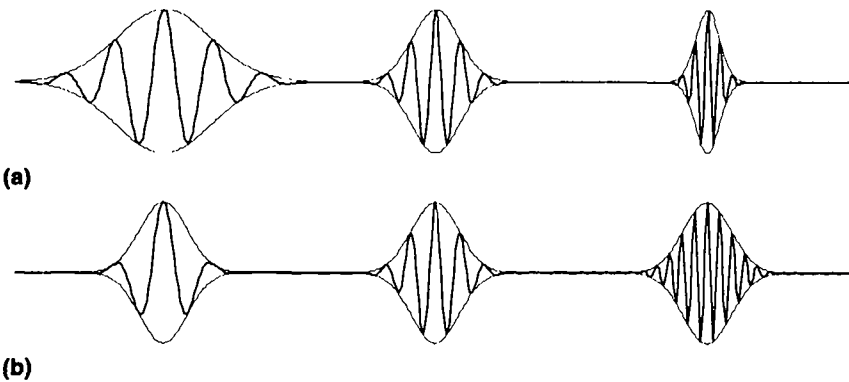


Figure 6-1. (a) Real part of the Morlet wavelet plotted for three frequencies $\omega_0/2$ ($a=2$), ω_0 ($a=1$) and $2\omega_0$ ($a=1/2$). (b) Real part of the Gabor window for the same frequencies.

It appears clearly in this figure that the extent of the analysis window depends on the analysis frequency of the Morlet wavelet. Hence, whether we are searching for high or low frequency components of a given signal, the window support isolates a time interval containing a fixed number of periods of a high or low frequency sinusoidal function. The analysis support is thus automatically adapted to the region of interest. Wavelets are “constant shape” windows in the sense that there is always the same number of oscillations in the window, whatever the scaling factor. This is obviously not the case for the Gabor window.

From Chapter 4, a wavelet coefficient is calculated as:

$$S(a,b) = \frac{1}{a} \int_{-\infty}^{+\infty} s(t) \exp\left(-\frac{(t-b)^2}{2a^2}\right) \exp\left(-i\frac{\omega_0}{a}(t-b)\right) dt \quad (6-3)$$

Most authors actually use a normalization factor $1/|a|^{1/2}$, which ensures that all dilated wavelets have the same energy. We rather use a factor $1/a$, which amounts to dividing the integral by the area under the Gaussian envelope (its actual area is $a\sqrt{2\pi}$). In this way, the modulus of the transform has the same magnitude for signals of different frequency but equal amplitude. This is useful in our case as we will estimate the amplitude directly from the transform. This results however in time and frequency windows of varying energy.

We can remark that a could be negative as well as positive. We restrict ourselves to the positive frequency domain, since the spectral information of a *real* signal is completely and equivalently represented in both the positive and negative frequency domains. Hence, a will be strictly positive in the following.

Using the Parseval-Plancherel theorem, (6-3) can also be written as:

$$S(a,b) = \frac{1}{\sqrt{2\pi}} \int_{-\infty}^{+\infty} \hat{s}(\omega) \exp\left(-\frac{a^2}{2}\left(\omega - \frac{\omega_0}{a}\right)^2\right) \exp(i\omega b) d\omega \quad (6-4)$$

This last expression shows that the wavelet coefficient is obtained by an integral on the product of the Fourier transform of the signal by a frequency window of the form:

$$W(\omega) = \exp\left(-\frac{a^2}{2}\left(\omega - \frac{\omega_0}{a}\right)^2\right) \exp(i\omega b) \quad (6-5)$$

which is a Gaussian window of variance $1/a^2$, centered at $\omega = \omega_0/a$, multiplied by a phase term. This illustrates the fact that the frequency band used to calculate a particular wavelet coefficient varies according to the central analysis frequency. Actually, if we define $\Delta\omega$ as the width of the frequency window, we

find that the wavelet analysis is performed at constant $\Delta\omega/\omega$ whereas the Gabor transform performs an analysis at constant $\Delta\omega$. This appears readily in Figure 6-2 where we show the real part of these windows for three different analysis frequencies, along with their Gabor equivalent.

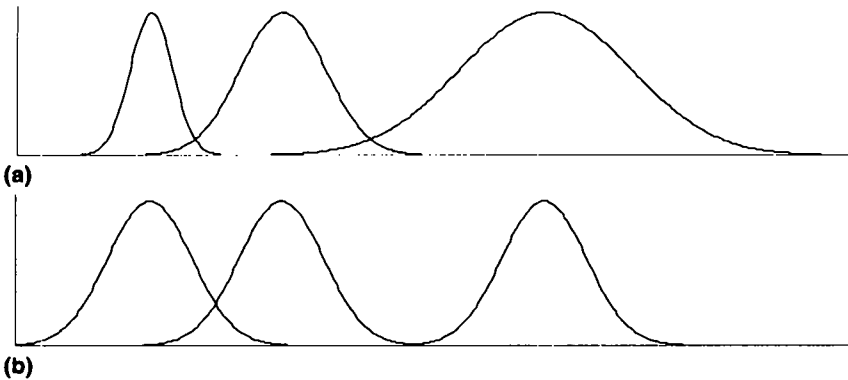


Figure 6-2. (a) Frequency windows obtained with the Morlet wavelet for three central analysis frequencies $\omega_0/2$ ($a = 2$), ω_0 ($a = 1$) and $2\omega_0$ ($a = 1/2$); (b) Same windows obtained in the Gabor case.

In the wavelet case, Figure 6-1 and Figure 6-2 illustrate the fact that a high frequency resolution is obtained for low frequency signals, while the corresponding time localization is poor. The reverse is true for high frequency signals. The behavior of the Gabor transform is simpler as the same frequency resolution and time localization are obtained for all frequency components of a signal. In the wavelet case, the choice of the mother frequency ω_0 determines the overall “balance” between time and frequency resolution. For example, high ω_0 values imply the use of large temporal windows (since a is larger for a given analysis frequency $\omega = \omega_0/a$) but provide a finer analysis of the frequency content of a signal.

6.2 Transform representation: spectrogram and scalogram

As the wavelet or Gabor transforms are functions of two variables, frequency and time in one case, scale and time in the other, they are usually presented in the form of “spectrograms” or “scalograms”⁴. We wrote a small program to visualize such graphs. The example shown in Figure 6-3 is the spectrogram of a linear chirp (the signal frequency increases linearly with time). The signal is plotted in the first part of the image. It is sampled and coded as 8 bits values, hence its scale ranges from 0 to 255 grey levels. Next, the modulus of its

wavelet transform is shown. The vertical scale indicates the frequency which increases linearly from $\pi/10$ rad/s (bottom) to π rad/s (top). We recall that we suppose to have a sampling rate of 1 Hz which corresponds to a cut-off frequency of π rad/s. The last part of the image shows the phase modulo- 2π of the transform, with the same frequency scale.

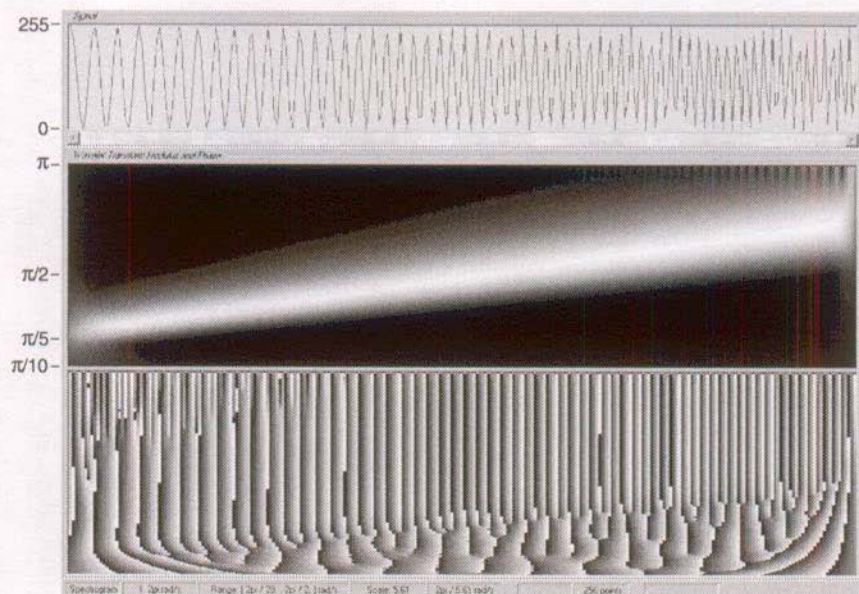


Figure 6-3. Morlet wavelet transform of a linear chirp, presented as a spectrogram. The vertical scale goes from $\pi/10$ to π rad/s.

We note that the maximum of the modulus is the same at all frequencies, as is the case for the signal amplitude. This results from our choice of a $1/a$ normalization factor. The consequence is that the energy spectrum of the signal appears to increase towards higher frequencies.

The second type of representation is the scalogram, Figure 6-4, where the linear frequency scale is replaced by a linear representation of the “scaling factor” a . The top of the image corresponds to the lowest dilation ($a = 2$ for $\omega_0 = 2\pi$ in this graph, which corresponds to $\omega = \omega_0/a = \pi$ rad/s), while the bottom of the image corresponds to the largest dilation ($a = 20$). Thus the frequency domain is identical in Figure 6-3 and Figure 6-4. Scalograms are interesting as they show the frequency content of a signal in a way very similar to a musical score. Indeed, each octave occupies the same height in a scalogram. This is actually a quite “natural” representation of acoustic signals. In our case

however, the frequency content does not have the same physical meaning since couples of frequencies located symmetrically with respect to $\pi/2$ rad/s, for example $\pi/6$ and $5\pi/6$ rad/s, simply represent deformations of same magnitude but opposite signs. We will thus use spectrograms rather than scalograms, because of their linear representation of frequency.



Figure 6-4. Morlet wavelet transform of a linear chirp, presented as a scalogram. The vertical scale goes from $\pi/10$ to π rad/s.

The representations shown above correspond to a “continuous” wavelet analysis. By contrast, wavelet decompositions are often performed in discrete frequency bands, for example octaves. Again, the continuous analysis and its representation are more adapted for our practical goal, which is not to identify the principal spectral components of a complicated signal but rather to follow precisely the frequency evolution of a quasi-sinusoidal signal.

6.3 Examples of spectrograms

The chirp example presented in Figure 6-3 illustrates the fact that the modulus of the wavelet transform can provide graphically the “trajectory” of the frequency of a signal in the time-frequency domain. We will come later to the properties of the phase of the transform but we can already note that the rate of

change of the phase seems to be proportional to the actual frequency of the signal in this figure.

The following examples illustrate the effect of the choice of the mother frequency, as well as noise filtering properties of the wavelet transform.

6.3.1 Transform of a sum of two signals

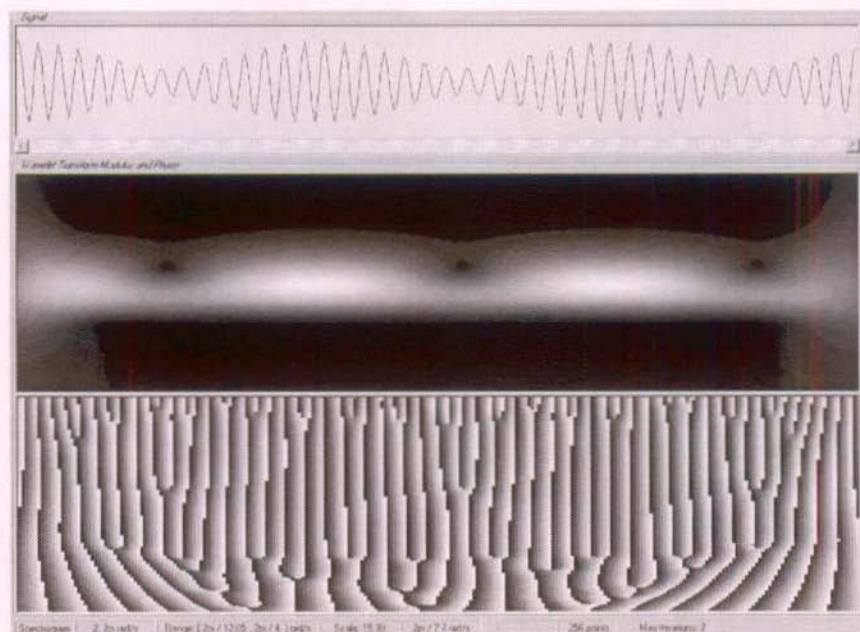


Figure 6-5. Wavelet transform of a sum of two signals with $\omega_0 = 4\pi$. The vertical scale ranges from $\pi/6$ (bottom) to $\pi/2$ (top).

Figure 6-5 shows an example of spectrogram obtained for the sum of two “monochromatic” sinusoidal signals of frequencies $\omega_1 = \pi/2.9$, $\omega_2 = \pi/3.1$ and respective amplitudes 32 and 64 grey levels. The transform is computed with $\omega_0 = 4\pi$. In this case, the two components are too close to each other to be correctly resolved in the spectrogram. This appears also in the phase graph where only one type of phase evolution is present in the part of the frequency domain where the modulus of the transform is non zero.

If we change ω_0 to 24π we get the spectrogram shown in Figure 6-6 where the two frequencies now distinctly appear in the modulus image. The two different frequencies also appear as two bands of slightly different phase in the

phase image. Of course this amelioration of the frequency resolution is obtained at the expense of the temporal localization since the scale used to calculate the transform at $\omega = \omega_0$ is now 72 instead of 12. The Gaussian window is thus 6 times larger.

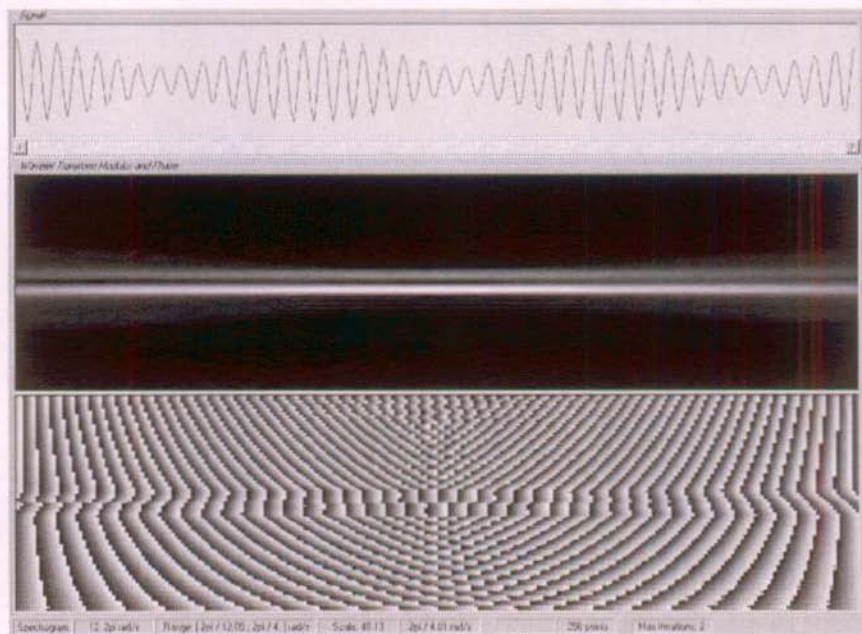


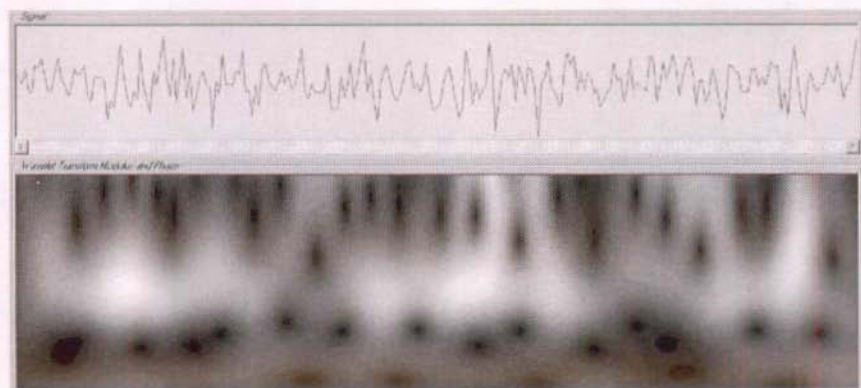
Figure 6-6. Wavelet transform of a sum of two signals with $\omega_0 = 24\pi$. The vertical scale ranges from $\pi/6$ (bottom) to $\pi/2$ (top).

6.3.2 Transform of a signal with added Gaussian noise

Figure 6-7 shows the modulus of the spectrograms obtained for a simulated sinusoidal signal of frequency $\pi/3.1$ and modulation $I_M = 32$, to which is added a Gaussian noise of standard deviation 32. This can be envisioned as a case where the signal-to-noise ratio (SNR) is equal to 1. The frequency scale ranges from $\pi/6$ to $\pi/2$ rad/s. The three spectrograms are obtained for $\omega_0 = 2\pi, 4\pi$ and 8π .

It is clear that not much of the sinusoidal signal is visible in the signal plot of Figure 6-7(a). Accordingly, the analysis with a very well temporally localized wavelet, $\omega_0 = 2\pi$, does not give us much information about the signal's actual frequency evolution. However, doubling the mother wavelet frequency, Figure 6-7(b), provides a better frequency resolution and the peak we are looking for becomes visible. When the wavelet coefficients are calculated near the signal's

frequency, only a small frequency band is used, which limits the amount of noise that contributes to the transform. In other words, the SNR increases. If ω_0 is doubled once more, Figure 6-7(c), most of the noise is filtered out, showing more clearly the frequency evolution of the signal.



(a)



(b)



(c)

Figure 6-7. Modulus of the wavelet transform of a sinusoidal signal of frequency $\pi/3.1$ and amplitude 32 grey levels, to which is added a Gaussian intensity noise of standard deviation equal to 32. (a) Analysis with $\omega_0 = 2\pi$; (b) $\omega_0 = 4\pi$; (c) $\omega_0 = 8\pi$.

6.3.3 Transform of a measured signal

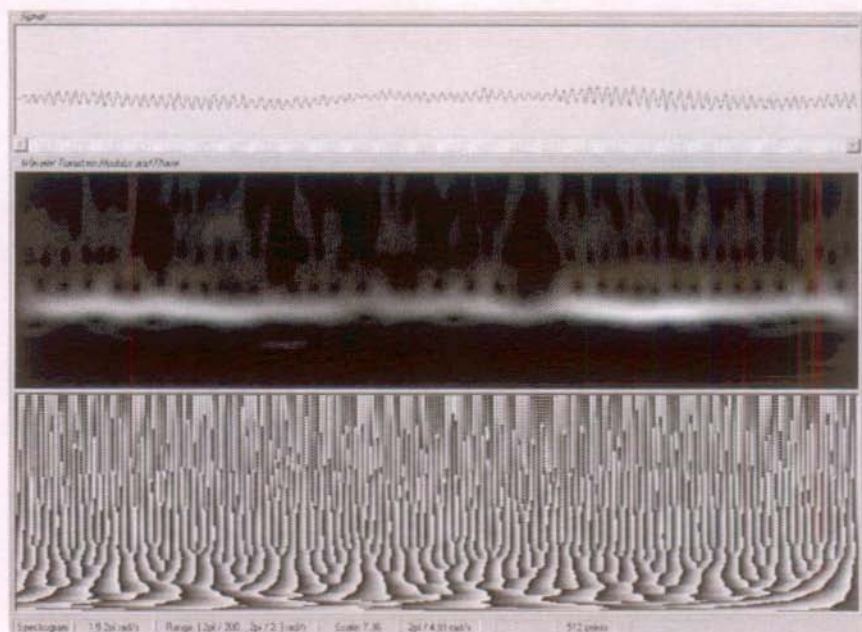


Figure 6-8. Transform of a measured signal (speckle interferometry).

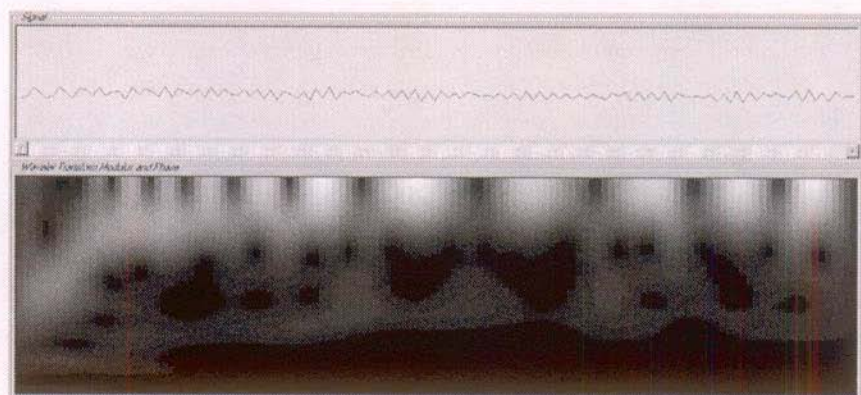
Figure 6-8 shows the transform of the measured signal presented at the beginning of Chapter 4. The mother frequency ω_0 is equal to 3π in this case. The frequency scale ranges from $\pi/500$ to π rad/s.

This signal was obtained during the translation of a metallic plate in its plane, observed with an in-plane speckle interferometer. The acquisition rate is 160 images per second. One fringe corresponds to a displacement of about 0.6 microns. No reference phase step is added for this experiment. A small electric motor is used to produce the constant speed translation. Since there is no feedback on the actual speed of rotation of the motor, small speed variations occur, causing the frequency fluctuations observed in the modulus of the transform. The same fluctuations can be observed for other pixels taken randomly in the image sequence.

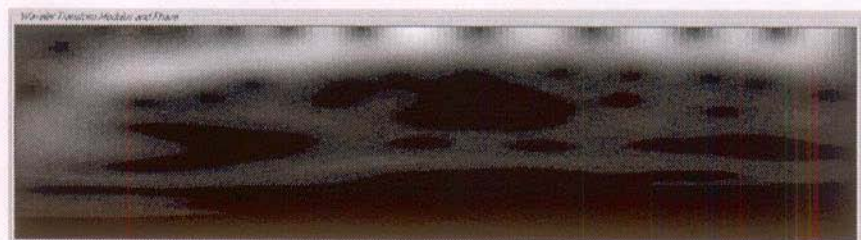
6.3.4 Transform of a measured signal of varying frequency

The previous examples might lead the reader to conclude that large ω_0 values are always beneficial. This is true only when the signal frequency does not

change significantly. The following example shows that time localization should be preserved in order to keep the analysis tool flexible.



(a)



(b)



(c)

Figure 6-9. Sudden change of frequency at the beginning of a signal obtained in speckle interferometry. Analysis for (a) $\omega_0 = 2\pi$; (b) $\omega_0 = 4\pi$; (c) $\omega_0 = 6\pi$.

This example was obtained with an in-plane speckle interferometer. The object is a piece of rubber loaded by a PZT pusher (see the corresponding example in Chapter 5). The frequency scale ranges from $\pi/10$ to π rad/s in Figure 6-9.

Since a $\pi/2$ reference phase step is introduced during this experiment, a $\pi/2$ frequency “peak” is observed in the transform near the signal’s beginning. As the load is applied there is a sudden frequency increase towards $3\pi/4$. This transition is visible in Figure 6-9(a) where the analysis is performed for $\omega_0 = 2\pi$. Next, as the loading progresses, the frequency continues to increase and the modulus of the transform starts to oscillate (this effect is explained in paragraph 6.4). To get rid of these oscillations that mask the actual frequency evolution, one is tempted to increase ω_0 . This is done in (b) where $\omega_0 = 4\pi$ and in (c) where $\omega_0 = 6\pi$. The modulus of the transform is indeed improved but the rapid frequency variation at the beginning of the experiment gradually disappears. This is a good illustration of the problems encountered with certain real signals. Striking a good time/frequency resolution balance is difficult in this case, particularly if the analysis is supposed to be automatic.

6.4 Interference effects with the Morlet wavelet

In order to understand the behavior of the transform near the limits of the frequency domain $[0, \pi]$, as shown for example in Figure 6-9, we suppose here that we dispose of a real signal $s(t)$ of constant frequency and amplitude over the analysis window:

$$s(t) = A + 2B \cos \varphi_s(t) = A + 2B \cos(\omega_s t) = A + B e^{i\omega_s t} + B e^{-i\omega_s t} \quad (6-6)$$

Actually, the hypothesis made on $s(t)$ corresponds to the linear-phase-evolution hypothesis used in the case of phase-shifting algorithms. We also assume that the frequency ω_s is within $[0, \pi]$ which means that the signal is correctly sampled. The Fourier transform of this signal is simply:

$$\hat{s}(\omega) = A\delta(0) + 2\pi B\delta(\omega_s) + 2\pi B\delta(-\omega_s) \quad (6-7)$$

where δ is the Dirac distribution. The 2π factor that gives a weight to the δ function results from our definition of the Fourier transform⁵. Calculating the wavelet coefficients $S(a,b)$ for this ideal signal yields:

$$S(a,b) = \frac{1}{\sqrt{2\pi}} A \exp\left(-\frac{\omega_0^2}{2}\right) + \sqrt{2\pi} B \exp(i\omega_s b) \exp\left(-\frac{a^2}{2}\left(\omega_s - \frac{\omega_0}{a}\right)^2\right) + \sqrt{2\pi} B \exp(-i\omega_s b) \exp\left(-\frac{a^2}{2}\left(\omega_s + \frac{\omega_0}{a}\right)^2\right) \quad (6-8)$$

Let us now observe what happens when we calculate these coefficients for different analysis and signal frequencies.

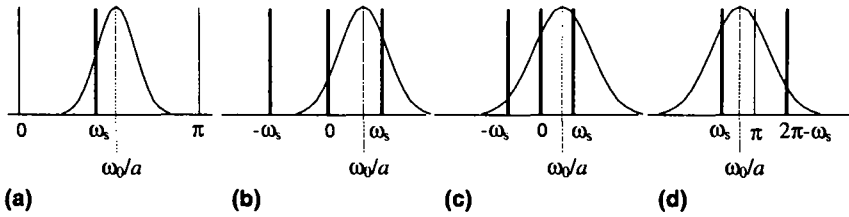


Figure 6-10. Signal spectrum and analysis window.

6.4.1 Well-conditioned analysis

In this case, the Gaussian frequency window of the transform is sufficiently narrow and the frequency ω_s is neither too high nor too low, see Figure 6-10(a). When the analysis frequency is close to ω_s ($a \approx \omega_0/\omega_s$), the frequency component $+\omega_s$ is the only contributing term to the transform. Consequently:

$$S(a, b) = \sqrt{2\pi} \exp\left(-\frac{a^2}{2} \left(\omega_s - \frac{\omega_0}{a}\right)^2\right) B \exp(i\omega_s b) \quad (6-9)$$

The transform modulus is constant as a function of time b and maximum when the analysis frequency ω_0/a is equal to ω_s . Moreover, in a frequency band around ω_s , the phase of the transform is equal to the signal's phase $\omega_s b$. We will come back to this crucial point in paragraph 6.5.

6.4.2 Low frequency interference effects

In a second case, ω_s is too low or the Gaussian window is too large, see Figure 6-10(b). Consequently, the component of the signal located at $\omega = 0$ (sometimes called the DC component), is included in the window when the analysis frequency is close to ω_s . In this situation we can write (6-8) as:

$$S(a, b) = C + D \exp(i\omega_s b) \quad (6-10)$$

where C and D are constant functions of time b . The modulus and phase of the transform are then given by:

$$|S(a, b)| = \sqrt{C^2 + D^2 + 2CD \cos \omega_s b} \quad \tan \varphi_{S(a, b)} = \frac{D \sin \omega_s b}{C + D \cos \omega_s b} \quad (6-11)$$

The modulus is no longer constant as a function of time b and the phase is no longer equal to the signal's phase. We remark however that it could be possible to estimate ω_s from the "oscillations" of the modulus of the transform. A

preliminary high-pass filtering of the signal to remove its DC component could reduce this perturbation.

The third case is similar to the second when ω_s is still closer to frequency 0, Figure 6-10(c). In this situation, the negative frequency component of the signal is also included in the frequency window when the analysis frequency ω_s/a is close to ω_s . The result is an “interference” effect between the two components. The wavelet transform coefficients become:

$$S(a, b) = C + D \exp(i\omega_s b) + E \exp(-i\omega_s b) \quad (6-12)$$

where C , D and E are constant functions of time b . The modulus and phase of the transform are then given by:

$$\begin{aligned} |S(a, b)| &= \sqrt{C^2 + D^2 + E^2 + 2DE \cos 2\omega_s b + 2C(D + E) \cos \omega_s b} \\ \tan \varphi_{S(a, b)} &= \frac{(D - E) \sin \omega_s b}{C + (D + E) \cos \omega_s b} \end{aligned} \quad (6-13)$$

The more complex behavior of the modulus makes it difficult to estimate ω_s from its oscillations. The phase is again hard to relate to the signal's phase.

These problems are always present in the case of the Gabor transform, which uses a fixed-width frequency window. Increasing the temporal size of the window is the only way to limit the interference effect between the different signal components. The situation is quite different in the wavelet case since the width of the frequency window is proportional to the center frequency in that window ($\Delta\omega/\omega$ is constant). In particular, the weight associated to the DC component of the signal is independent of the actual analysis frequency ω_s/a . More precisely, the DC component adds a factor proportional to $\exp(-\omega_0^2/2)$ in $S(a, b)$, for all possible values of a . This brings us back to the admissibility conditions required for a function to qualify as a mother wavelet (see Chapter 4). One of them asked that the Fourier transform of the analyzing window at the frequency 0 be null, or even better, that the Fourier transform be null for all frequencies $\omega \leq 0$. Strictly speaking, this cannot be achieved with Gaussian windows, since these functions have an infinite support. However, from a practical and “computational” point of view, the Morlet wavelet becomes admissible if we chose ω_0 sufficiently high. Indeed, Morlet³, and later Daubechies⁶, showed that the required correcting factor is no longer necessary for $\omega_0 > 1.7 \pi$. In our applications, the mother frequency is always at least equal to 2π . In this case, the DC term has a weight lower than $3 \cdot 10^{-9}$ times the weight obtained for the central analysis frequency. Consequently, the wavelet analysis

is not affected by interference effects in the low frequency domain, contrary to the Gabor transform.

6.4.3 High frequency interference effects

Figure 6-10(d) depicts the situation where the signal's frequency ω_s becomes too close to the Nyquist frequency. In this case, the periodicity of the spectrum caused by the discrete sampling creates a peak of frequency $2\pi - \omega_s$ in a position symmetrical to that of the peak at $+\omega_s$. This peak corresponds to the negative frequency component of the signal. When the analysis frequency is close to ω_s , this second component appears in the wavelet coefficients. (6-8) can then be written as:

$$S(a,b) = D \exp(i\omega_s b) + E \exp(-i\omega_s b) \quad (6-14)$$

where D and E are constant functions of time b . The modulus and phase of the transform are then given by:

$$|S(a,b)| = \sqrt{D^2 + E^2 + 2DE \cos 2\omega_s b} \quad \tan \varphi_{S(a,b)} = \frac{D - E}{D + E} \tan \varphi_s(b) \quad (6-15)$$

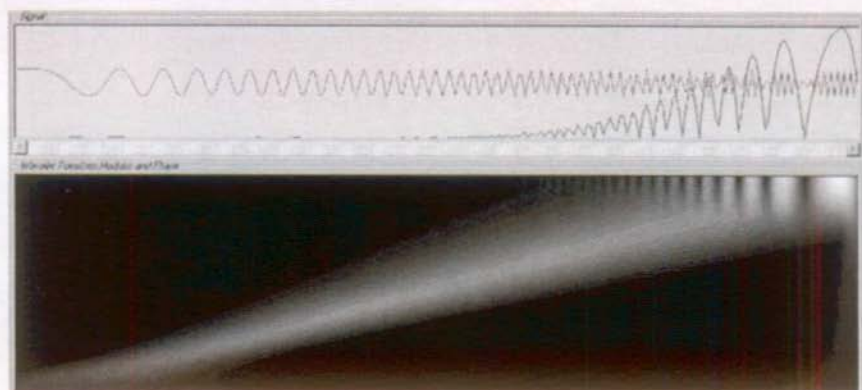
Again, a modulation of the modulus appears while the phase is a distorted version of the signal's phase. In particular, oscillations with "contrast" unity are produced when the analysis frequency is equal to the cut-off frequency, since $D = E$ in this case:

$$|S(a,b)| = \sqrt{2D} \sqrt{1 + \cos 2\omega_s b} = 2D |\cos \omega_s b| \quad (6-16)$$

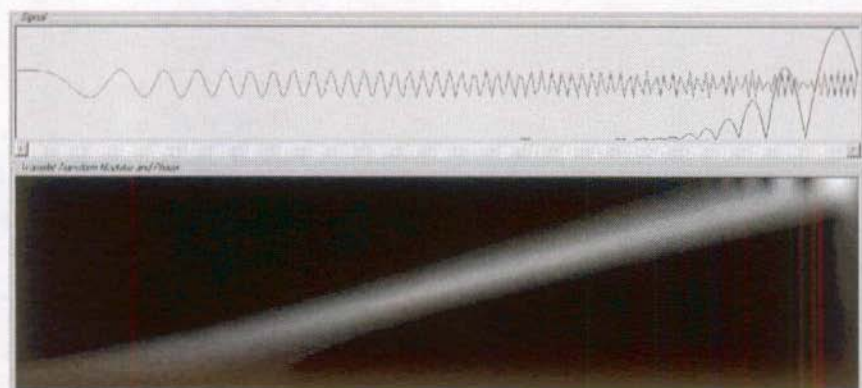
However, $2\omega_s$ is above the cut-off frequency and we observe in practice an undersampled version of (6-16), at an apparent low frequency $2\pi - 2\omega_s$. This is illustrated in Figure 6-11 where a chirp signal is analyzed with a mother wavelet of frequency 2π and 4π . The signal is plotted along with the modulus of the transform obtained for the cut-off frequency π . The frequency scale goes from $\pi/25$ to π rad/s. Again, in cases where the noise level is low, it could be possible to estimate ω_s from the observed oscillations calculated at $\omega = \pi$.

These perturbations are inherent to the nature of wavelet analysis, since the frequency window becomes larger for higher frequencies. Their effects can be attenuated, but not eliminated, by increasing ω_0 as illustrated in Figure 6-11(b). These troubles are of course caused by the negative frequency component of the signal. We will see in Chapter 9 that under some circumstances it is possible to attenuate it sufficiently for the oscillations to become negligible.

Before closing this paragraph we can also remark that no perturbations exist in the low frequency part of the transform, as concluded in paragraph 6.4.2.



(a)



(b)

Figure 6-11. (a) Analysis of a chirp with a mother wavelet frequency $\omega_0 = 2\pi$; (b) Same for $\omega_0 = 4\pi$. A profile of the transform modulus calculated at $\omega = \pi$ is plotted in both cases next to the graph of the signal.

6.5 Phase properties of the Morlet wavelet transform

The examples seen so far show that the instantaneous frequency information appears in the spectrograms in the form of a “peak” in the modulus. Its vertical displacement reflects the signal frequency variations. The width of this peak for a given time b is given by the width $\Delta\omega$ of the Gaussian frequency window. This is why the peak appears larger at higher frequencies since $\Delta\omega/\omega$ is constant (see for example Figure 6-11). In the same fashion the signal influences the phase of the transform in a domain proportional to $\Delta\omega$. This is clear when we compare the phase in Figure 6-5 and Figure 6-6 where the width of the window decreases

by a factor 6. We can see in the second figure that the two signal components create adjacent “bands” in the phase of the transform. These effects can be readily understood for monochromatic signals of constant amplitude with the help of (6-9). In particular, we observe that, in the support of the Gaussian frequency window, the phase of the transform is exactly equal to the phase of the signal. However, the signals encountered in practice seldom exhibit such ideal characteristics. It is thus necessary to obtain a more realistic estimation of the transform’s behavior.

6.5.1 Developed expression of the transform

The expression of $s(t)$ in (6-6) is oversimplified as there are usually frequency and amplitude variations during an experiment (*no* variations would account for a very boring experiment). In the following, we will consider that the phase φ_s , of the signal can be approximated by its second-order Taylor expansion, over the temporal width of the analysis window centered at time b . In fact, we could wish to use higher orders in the development of φ_s but, to the best of our knowledge, an analytic expression of $S(a,b)$ could no longer be obtained. The signal amplitude (or modulation I_M in the case of interferometry) is represented by its complete Taylor expansion, since this does not complicate the calculations. However, to be meaningful, the development of the wavelet coefficients will have to be limited to the second order with respect to time. Hence, $s(t)$ becomes:

$$s(t) = A(t) + B(t) \exp(i\varphi_s(t)) + B(t) \exp(-i\varphi_s(t)) \quad (6-17)$$

with:

$$\begin{aligned} \varphi_s(t) &= \varphi_s(b) + \varphi'_s(b)(t-b) + \frac{1}{2} \varphi''_s(b)(t-b)^2 \\ B(t) &= \sum_{k=0}^{\infty} \frac{1}{k!} B^{(k)}(b)(t-b)^k \end{aligned} \quad (6-18)$$

The instantaneous frequency of the signal at time b is defined as:

$$\omega_s = \frac{\partial \varphi_s}{\partial t}(b) = \varphi'_s(b) \quad (6-19)$$

We will now develop the expression of $S(a,b)$ in the case where only the positive frequency component of the signal is present in the analysis window. In this case the signal is simply the complex term $B(t)\exp(i\varphi_s(t))$. These particular mathematical derivations are inspired by similar calculations made in Ref.2 for the Gabor transform. The main difference arises from the fact that the width of

the analyzing window is a function of the analysis frequency in the wavelet case, whereas it is fixed in the Gabor case. The complete developments are presented in Appendix B. The end result is:

$$S(a,b) = \sqrt{2\pi} \left(1 + a^4 \varphi_s^{\prime 2}(b)\right)^{\frac{1}{4}} \exp\left(i\varphi_s(b) + \frac{i}{2} \arctan(a^2 \varphi_s^{\prime\prime}(b))\right) \times \sum_{k=0}^{\infty} (-i)^k \frac{B^{(k)}(b)}{k!} \frac{\partial}{\partial x^k} \exp\left(-\frac{1}{2} \frac{(\omega_0 - ax)^2}{1 - ia^2 \varphi_s^{\prime\prime}(b)}\right) \Big|_{x=\varphi_s'(b)} \quad (6-20)$$

We observe first that in the case of a constant-amplitude monochromatic signal ($B(t) = B$, $\varphi_s'(b) = \omega_s$ and $\varphi_s^{(k)} = 0$ for $k > 1$) (6-20) reduces to (6-9). In this situation, the transform $S(a,b)$ is exactly proportional to the signal contribution $B \exp(i\omega_s t)$, with a maximum modulus when $\omega_0/a = \omega_s$.

If the modulation variations are negligible over the analysis window, as is the case with many interferometric applications, (6-20) becomes:

$$S(a,b) = \sqrt{2\pi} \left(1 + a^4 \varphi_s^{\prime 2}(b)\right)^{\frac{1}{4}} \exp\left(\frac{i}{2} \arctan(a^2 \varphi_s^{\prime\prime}(b))\right) \times \exp\left(-\frac{a^2}{2} \left(\varphi_s'(b) - \frac{\omega_0}{a}\right)^2 \frac{1}{1 - ia^2 \varphi_s^{\prime\prime}(b)}\right) B(b) \exp(i\varphi_s(b)) \quad (6-21)$$

Again we find that $S(a,b)$ is proportional to the signal $B(b) \exp(i\varphi_s(b))$ but with many correcting factors. We also recognize the term representing the Gaussian frequency window corrected by a complex factor. This contributes to the phase errors due to the second derivative of the phase. We observe that its influence is magnified by the scaling factor. Hence, a larger sensitivity to this error is obtained for low frequency signals or when ω_0 is increased.

To reduce somehow the complexity of (6-20) we look at its behavior along the so-called ridge of the transform. The ridge is defined as the set of couples $(a(b), b)$ in the time-frequency domain for which the analysis frequency is equal to the instantaneous frequency of the signal:

$$\omega = \frac{\omega_0}{a(b)} = \varphi_s'(b) \quad (6-22)$$

We will discuss possible solutions to find this ridge in the next paragraph. The restriction of the transform to the ridge is called the skeleton of the transform. As seen in Appendix B, the odd derivatives of $B(b)$ disappear in this case. Hence, we can now obtain a reduced form of $S(a(b), b)$ when the temporal evolution of B is a *linear* function of time over the analysis window:

$$S(a(b), b) = \sqrt{2\pi} \left(1 + a^4(b) \varphi_s^{\prime\prime 2}(b)\right)^{\frac{1}{4}} \exp\left(i \frac{1}{2} \arctan a^2(b) \varphi_s^{\prime\prime}(b)\right) \times B(b) \exp(i\varphi_s(b)) \quad (6-23)$$

Both modulus and phase of the transform are distorted versions of the signal. However, the modulus is not a quantity of prime interest for us. Hence, the only truly detrimental error is a phase error term, depending on the second derivative of the signal's phase. Note that the absolute value of this error is always smaller than $\pi/4$. We can then conclude that the restriction of the Morlet wavelet transform to its ridge provides us with a good representation of signals that have a locally linear amplitude evolution plus a weakly parabolic phase evolution. We must emphasize that this property is at the core of our developments since it leads us towards a new tool, the ridge extraction algorithm, used to evaluate the phase of the signals obtained with the dynamic phase-shifting method.

We note that the linear-phase-evolution hypothesis made in the context of phase-shifting algorithms is somehow relaxed in the wavelet case. However, we must remember that the phase-shifting algorithm we selected works over a smaller temporal support. A stronger hypothesis in this case is then reasonable.

One might wonder about the interest of obtaining a copy of the original signal through the wavelet transformation. First, we recall that the signal is now bandpass filtered by a filter automatically centered over the instantaneous frequency ω_s , which results in an improvement of the SNR. Second, the above property is true only along the ridge of the transform. Finding the ridge is equivalent to finding $\omega_s(b)$. At this point, one could imagine integrating $\omega_s(b)$ to go back to $\varphi_s(b)$. However, this is not even necessary since the transform implicitly yields $\varphi_s(b)$, that is, the phase of the interferometric signal. The question remains to efficiently determine the ridge.

6.5.2 Ridge extraction

We could attempt the extraction of the ridge of the transform by looking for the maximum of $|S(a, b)|$ at each time point b . However, this would be quite time consuming as the whole time-frequency domain would have to be explored. Moreover, as in all extrema search problems, the presence of noise can create situations where a spurious peak is mistakenly identified in place of the actual one. In particular, we will see in the case of speckle interferometry that the amplitude of the signal can become very low over large time intervals before rising again. It is then important to be able to follow such low energy peaks.

A more elegant solution, based on the aforementioned phase properties of the transform is presented in Ref.1 and Ref.2. The idea is based on the fact that,

for constant frequency signals, there is a band of analyzing frequencies centered on ω_s for which the phase of the transform $\varphi_{S(a,b)}$ is equal to the phase φ_s of the signal. In other words, the transform's phase is equal to $\omega_s b$. The width of this band is simply given by the width of the Gaussian analyzing window in the frequency domain. A similar property is obtained for signal of slowly varying instantaneous frequency (6.5.1). Hence, when the analysis frequency $\omega = \omega_s/a$ is close or equal to ω_s , the rate of variation of the phase of the transform, $d\varphi_{S(a,b)}/db$, is actually equal to ω . Finding this frequency implicitly yields ω_s . A fixed point algorithm is used to this end.

The algorithm starts with a rough estimation of ω_s , which gives a first value a_0 for the scaling factor. A new frequency ω_1 is then calculated as $d\varphi_{S(a_0,b)}/db$. The corresponding scale factor $a_1 = \omega_s/\omega_1$ is then used to estimate $\omega_2 = d\varphi_{S(a_1,b)}/db$. The algorithm stops when $(a_{i+1} - a_i)/a_i$ gets lower than a given precision. In practice, two or three iterations are usually sufficient. Once $\omega_s(b)$ has been found, the algorithm continues at time $b+1$ with $a_0 = \omega_s/\omega_s(b)$. The convergence of the algorithm is proven in Ref.1. Intuitively, we can understand it from the fact that the phase of the transform is equal to the phase of the signal in a frequency band that frames the ridge. Hence, the derivative of $\varphi_{S(a,b)}$ is close to ω_s , even at the first iteration.

The same algorithm can be used for more realistic signals. We recall from (6-21) that $\varphi_{S(a,b)}$ is equal to φ_s plus a phase shift depending on $\varphi_s^*(b)$. Since this phase shift is quasi-constant for two successive time samples b , the derivative of $\varphi_{S(a,b)}$ is again close to the signal instantaneous frequency, hence the convergence of the algorithm. Of course, the subsequent estimation of φ_s from the transform computed at $a = \omega_s/\omega_s$ still includes the phase error term dependent on $\varphi_s^*(b)$.

The process of extracting the ridge of the transform is very similar to the function of a phase-lock-loop in electronics. These circuits simply try to stay in phase with an input signal. In our case the ridge extraction amounts to "tune" the analysis frequency into the signal's instantaneous frequency.

Again, we must emphasize the importance of the method described here since the ridge extraction algorithm is the fundamental tool that permits to process the temporal signals recorded in the dynamic phase-shifting context. It solves completely the problem of measuring the phase of a sinusoidal signal. It must also be noted that the whole process takes uniquely advantage of the phase properties of the transform. Indeed, the transform modulus is not considered at all in the algorithm. However, we will see that the ridge usually follows a trajectory very close to that of the maximum of the modulus of the transform.

6.5.3 Examples of ridge extraction

Ridge extraction does not present any particular problem for noiseless, simulated signals with smooth frequency evolution. Hence, we rather present here the results obtained for a simulated signal with added noise, some of the measured signals presented earlier as well as new ones.

The spectrogram displayed in Figure 6-12 corresponds to a constant frequency signal to which a large intensity Gaussian noise is added (see also paragraph 6.3.2). The resulting signal-to-noise ratio is 1. The analysis is performed for $\omega_0 = 2\pi$.

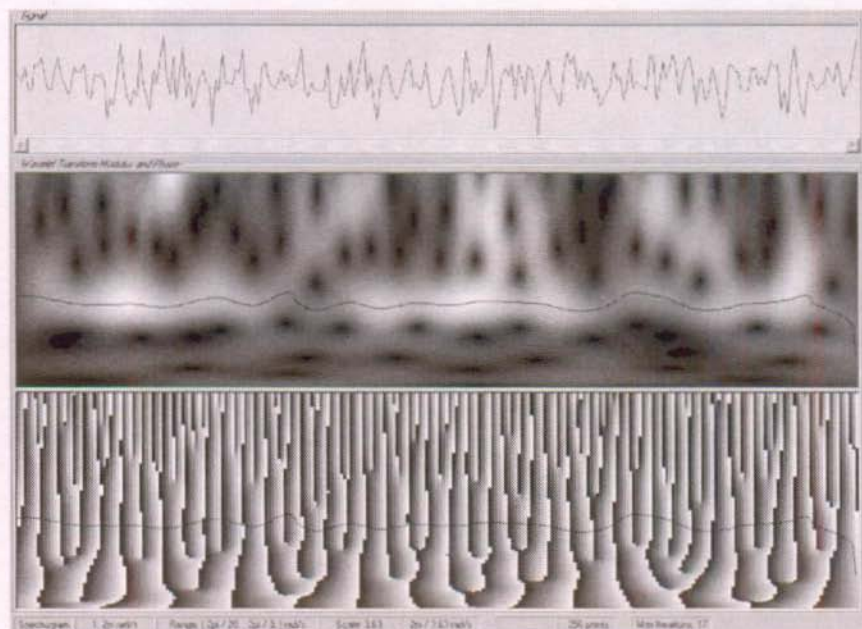


Figure 6-12. Ridge extraction on the signal of Figure 6-7. The vertical scale ranges from $\pi/10$ to $2\pi/3$. Analysis performed for $\omega_0 = 2\pi$.

The modulus of the transform is quite “bumpy” and we can imagine the difficulty of identifying the ridge from the maximum of $|S(a,b)|$ in this intensity image. However, a quite correct ridge is obtained here (black line in the figure) by application of the simple ridge extraction algorithm based on the phase. We can note that the ridge drops down suddenly for the last samples of the signal. This is a boundary effect due to the artificial extension of the signal’s support. This point is explained in more detail in the next chapter.

The second example shown in Figure 6-13 corresponds to a signal obtained during the same experiment as the signal of Figure 6-8. This time, large fluctuations of the modulation and background intensity are clearly visible. They result from the large image-plane decorrelation produced during this experiment.

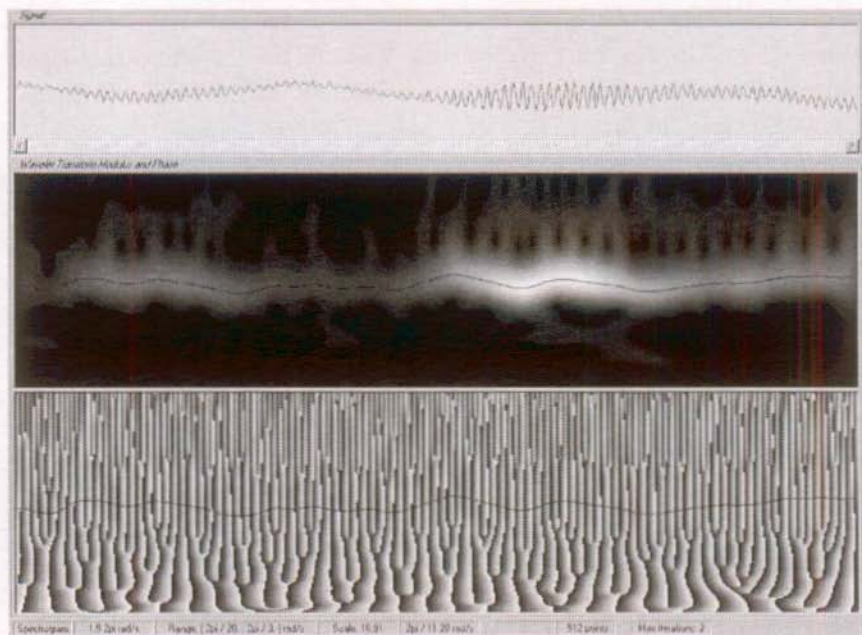


Figure 6-13. Ridge extraction for a signal measured with speckle interferometry. Analysis is performed at $\omega_0 = 2\pi$. The vertical scale ranges from $\pi/10$ to $2\pi/3$.

The large variations noted above or the weak signal modulation in some regions clearly do not cause any problem regarding the ridge extraction as very little noise is present in the measured signal.

We now present a measurement obtained in shearing speckle interferometry. The object is a metal plate that is cyclically loaded in its center at a frequency of 0.5 Hz by a large-range PZT. The maximum displacement is on the order of 70 microns. The acquisition itself is performed using a pulsed laser at 25 Hz and a reference phase step of $\pi/2$ is introduced between successive images with a PZT-mounted mirror. The amount of shear in the interferometer is quite small since we obtain at most one fringe in the classical butterfly fringe pattern corresponding to the bump on the surface. The signal

shown in Figure 6-14 corresponds to a pixel located in the region where maximum phase variations are obtained.

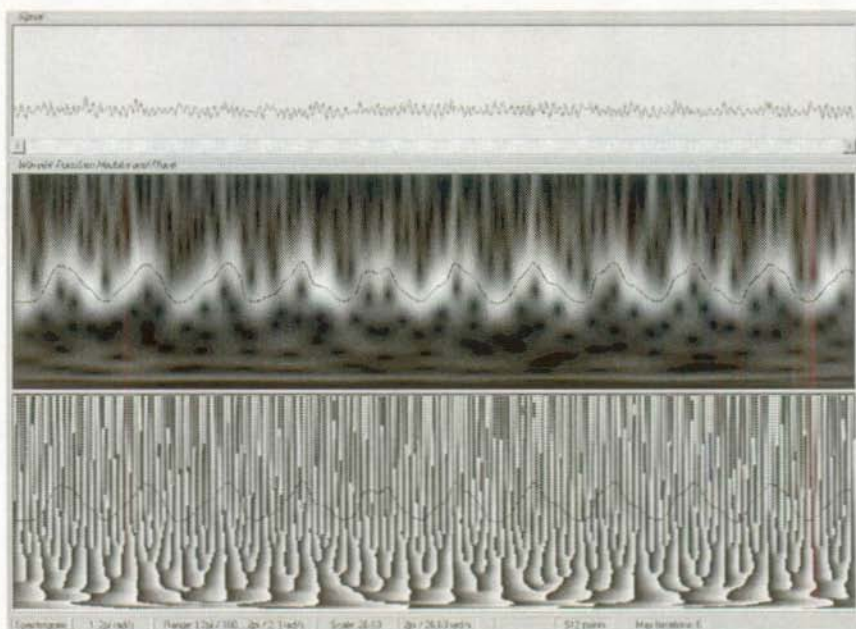


Figure 6-14. Ridge extraction for a signal measured with a shearing speckle interferometer during the cyclic loading of a metallic plate. Analysis is performed at $\omega_0 = 2\pi$. The scale ranges from $\pi/50$ to π .

We observe about ten periods of oscillation over the 512 recorded samples. The frequency of the signal oscillates between $2\pi/3$ and $2\pi/5$. These frequency variations are sufficiently slow that the algorithm can follow the instantaneous frequency trajectory. However, if the analysis is performed with a higher mother wavelet frequency the ridge extraction becomes impossible as illustrated in Figure 6-15 where ω_0 is equal to 4π . The width of the temporal window is on the order of the period of the frequency oscillations in this case and the accordingly poor time localization no longer permits to resolve sharp frequency variations.

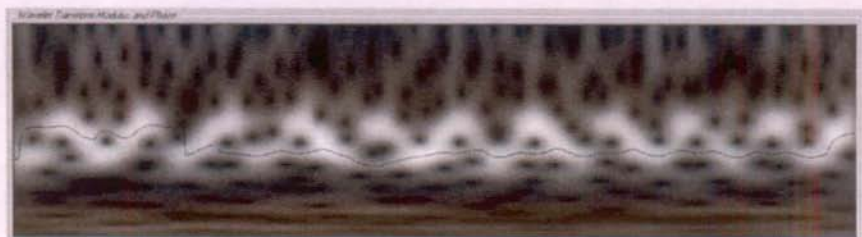


Figure 6-15. Same as Figure 6-14 with $\omega_0 = 4\pi$. The ridge extraction fails because frequency details are blurred.

The phase of the transform calculated along the ridge of Figure 6-14 is presented in Figure 6-16. The plot actually shows the phase (in degree) obtained after subtraction of the 90° reference phase steps introduced between images during the acquisition. The phase is arbitrarily chosen to be equal to 0° for the first sample of the signal in this image since the initial phase of the speckle interferogram is random. The curve is quite smooth, because of the low-pass filtering performed by the wavelet transformation. The dashed curve in this graph is the phase measured along the ridge obtained for a similar simulated signal. The sinusoidal frequency modulation of this signal is chosen to approach as much as possible the phase evolution of the original signal. It will be used later to characterize the systematic phase error due to the second derivative of the phase.

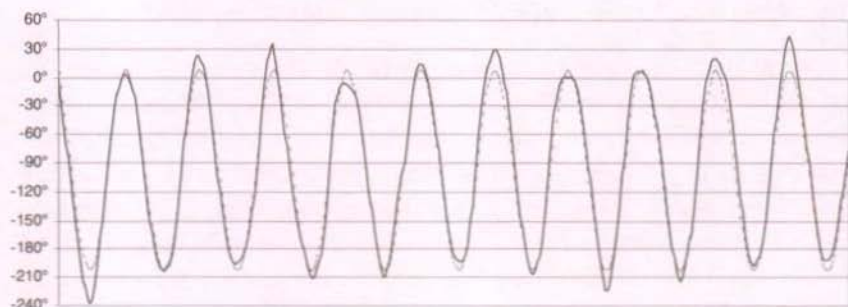


Figure 6-16. Solid line: phase (in degree) measured along the ridge in Figure 6-14. Dashed line: phase measured along the ridge obtained for a simulated signal with similar sinusoidal frequency modulation.

We will come back to this experiment in Chapter 8, where different application examples of dynamic phase-shifting are presented.

Next we show the example of a signal measured in holographic interferometry. This case is interesting as it illustrates a problem in the ridge extraction when the instantaneous frequency of the signal changes very rapidly. This is caused here by the abrupt beginning of the loading of the object under study. A $\pi/2$ reference phase step is also introduced during this experiment.

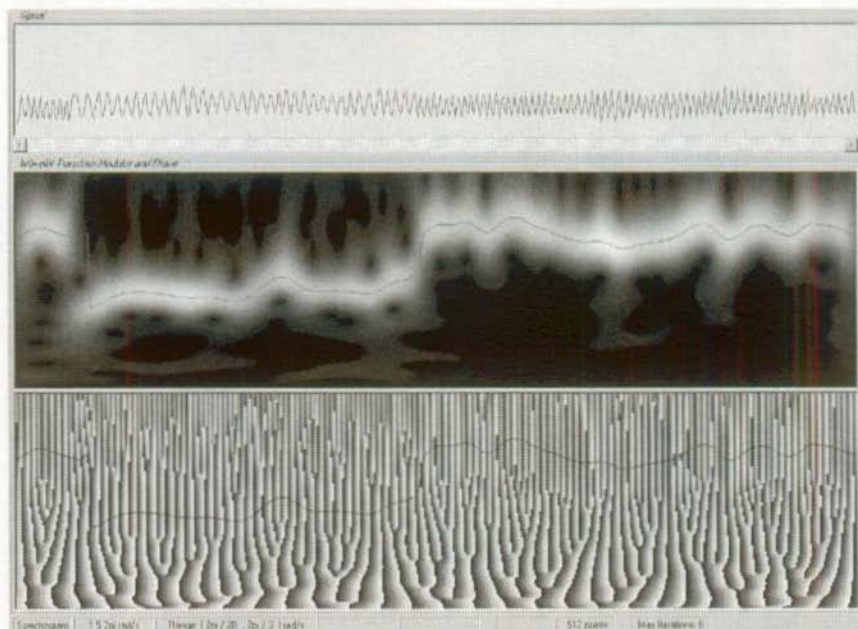


Figure 6-17. Thermal loading of an object observed with holographic interferometry. Analysis performed for $\omega_0 = 3\pi$. The vertical scale ranges from $\pi/10$ to $2\pi/3$ in this image.

The instants where the loading starts and ends are clearly visible in Figure 6-17. We observe that the algorithm finds correctly the ridge except for the first transition where it hesitates before jumping from $\pi/2$ to less than $\pi/3$. A zoom on this transition can show that a phase error of one fringe is introduced at this point, see Figure 6-18. In this figure, the phase of the skeleton is plotted in the form of a saw-tooth graph along the signal. We observe that the analysis created two “high-frequency” fringes in the first low-frequency period of the signal. Hence a 2π error is introduced in this measurement. This example actually illustrates the limit of the technique with respect to transients. The sudden frequency jump is too rapid to be correctly sampled in this case.

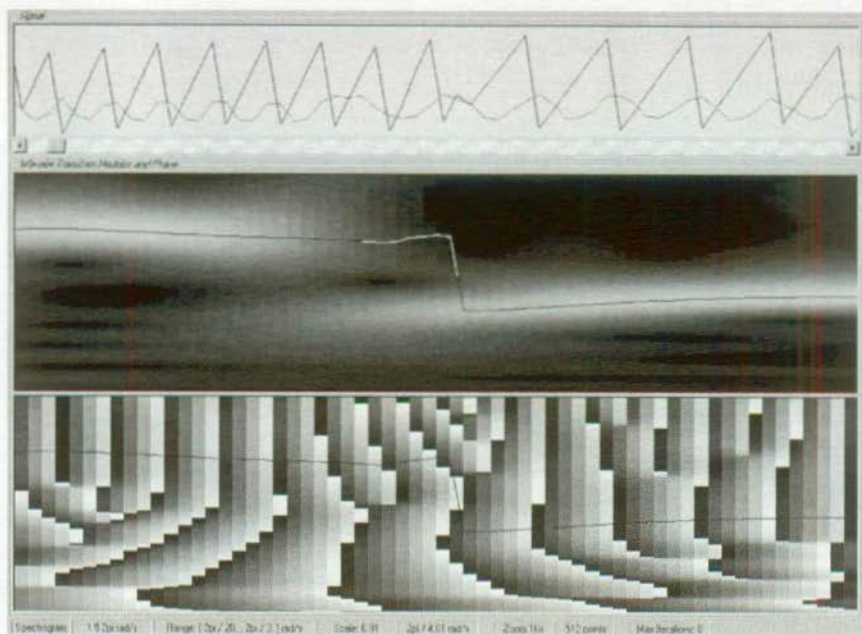
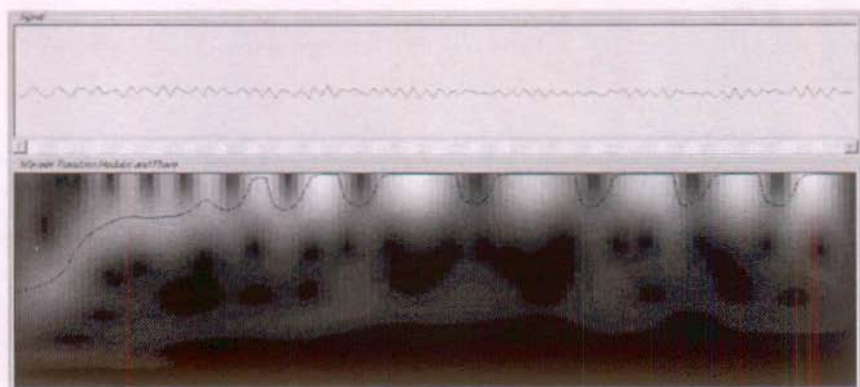


Figure 6-18. 16x zoom of Figure 6-17 near the first frequency jump.

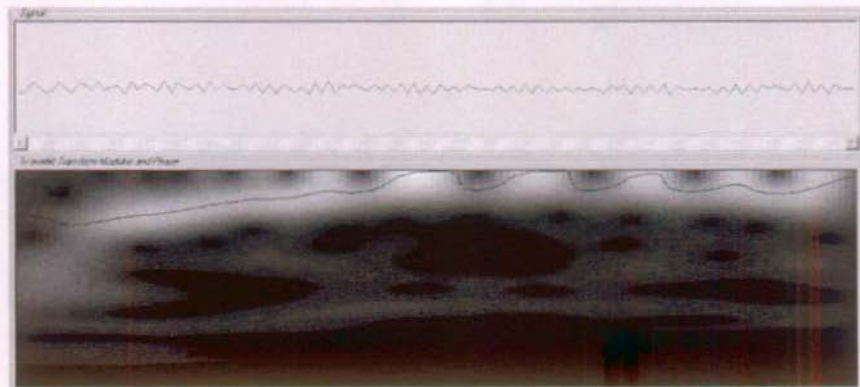
The last example presented here illustrates the problems encountered when the instantaneous frequency of the signal gets too close to the Nyquist limit. It corresponds to the experiment described in paragraph 6.3.4. In Figure 6-19(a), the analysis frequency ω_0 is equal to 2π . In this case, the frequency transition at the beginning of the experiment is preserved, thanks to the sufficient time localization of the analysis window. However, since the analysis window in the frequency domain is large, an interference effect is obtained with the negative frequency component of the signal when its frequency increases (see paragraph 6.4.3). The modulus starts to oscillate and the phase is distorted. The ridge extraction algorithm fails in this case. The image presented in (b) corresponds to ω_0 equal to 4π . The interference effects are now reduced but the algorithm still creates an oscillating ridge that does not correspond to the physical behavior of the object. Moreover, the larger analyzing window does not preserve as well the initial frequency transition. As a consequence, the algorithm fails to identify it properly.

It seems that the phase of this particular signal cannot be processed with the wavelet analysis described up to now. We will see in Chapter 9 that a solution actually exists to dampen or even remove completely interference effects near

the cut-off frequency, in which case the ridge extraction performs very well while preserving at the same time the initial frequency transition.



(a)



(b)

Figure 6-19. Ridge extraction problems in the case of frequencies close to the Nyquist limit. (a) Analysis for $\omega_0 = 2\pi$. The initial frequency transition is correctly identified but the ridge extraction fails at higher frequencies. (b) Analysis for $\omega_0 = 4\pi$. The frequency transition is lost but the ridge is slightly better.

6.6 “Sensitivity” of the wavelet-based phase measurement

Contrary to the phase-shifting algorithm presented in Chapter 5, the wavelet analysis implies the use of a large number of time samples for each phase evaluation. It has been seen earlier that this results in a low-pass filtering of the signal and its phase. It is thus interesting to know the behavior of the method

with respect to phase “details”. This is briefly characterized in one of the following paragraphs. A particular phase detail might result from the fine behavior of the object under study or, more frequently, from a phase fluctuation due to the environmental perturbations of the experimental setup. The effect of large and sudden phase jumps is studied in 6.6.2.

6.6.1 Impulse response of the wavelet phase analysis

In a simplified manner, we look here at the response of the method to a single phase step of amplitude 5° . For this purpose we generate three signals of frequency $\pi/4.1$, $\pi/2.1$ and $3\pi/4.1$, with the added phase step at the center of the signal support, and analyze them in the case of a mother frequency ω_0 equal to 2π and 4π . The results are presented in Figure 6-20.

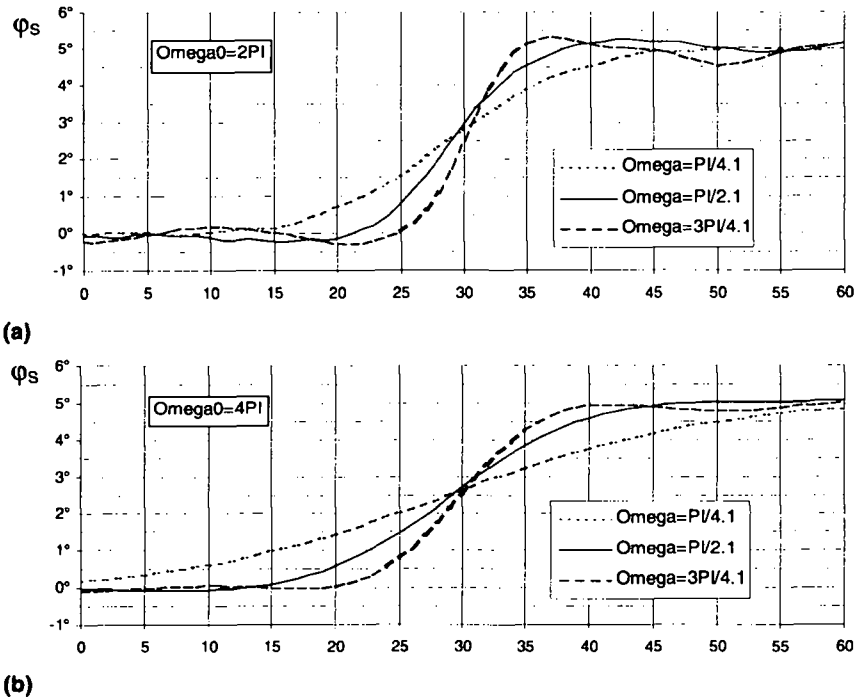


Figure 6-20. Effect of a 5° phase step on the phase φ_s calculated along the ridge. (a) Analysis for $\omega_0 = 2\pi$; (b) Analysis for $\omega_0 = 4\pi$.

The graphs show the impulse response of the wavelet transform. Not surprisingly, slower responses are obtained for the large temporal windows that

are used for low-frequency signals ($\pi/4$) compared to high-frequency signals ($3\pi/4$). Similarly, increasing the mother wavelet frequency amounts to increase the response time at all frequencies. If we use the rise-time τ defined in electronics as the time interval necessary to go from 10% to 90% of the transition, we find τ equal to 2.6 periods of the signal for $\omega_0 = 2\pi$ and $\omega_s = \pi/2.1$. τ equals 2.4 periods for $\omega_s = 3\pi/4.1$ and 2.7 periods for $\omega_s = \pi/4.1$. In the case $\omega_0 = 4\pi$ we find τ equal to 4.4, 4.8 and 5.1 periods for ω_s equal to $3\pi/4.1$, $\pi/2.1$ and $\pi/4.1$. The conclusion is that small transient phase details that occur at time scales smaller than two signal periods are not detected for mother wavelet frequencies larger than 2π . Only larger scale events, such as the permanent phase step depicted above, do register in the phase of the transform.

We note that larger jumps produce equivalent graphs, showing that the rise-time is actually independent of the height of the jump itself.

6.6.2 Effect of large phase jumps

In paragraph 6.6.1 we looked at the “sensitivity” of the method to small phase variations. In this paragraph we look briefly at the effect of larger phase steps that can be induced by a sudden variation of the measured physical quantity or simply by an external perturbation.

Figure 6-21 shows the transform of a signal of constant frequency $\pi/2.1$ to which three permanent phase jumps of $\pi/2$, π and $3\pi/2$ are added. Adding suddenly a phase offset amounts to increase locally the instantaneous frequency of the signal, as long as there is no aliasing effect. This is readily apparent for the first phase jump of height $+\pi/2$. Since the maximum instantaneous frequency (slightly less than π at the instant of the jump) is still within the Nyquist domain $[-\pi, \pi]$, no ambiguity exists in the signal. A much smaller frequency change actually appears in the transform because of the time localization uncertainty.

In the case of the second jump of height π two different possible paths appear in the transform modulus. To these paths corresponds a dislocation of the transform’s phase. In effect, changing the phase by $+\pi$ or $-\pi$ produces the same real signal. However, the instantaneous frequency increases in one case and decreases in the other. This explains the appearance of the two possible paths. Taking the upper path instead of the lower path corresponds to adding one fringe to the phase of the signal. In effect, both phase evolutions are equally probable. Therefore, the particular choice of the ridge in this case is arbitrary.

In the third case, a jump of $+3\pi/2$ is equivalent to a jump of $-\pi/2$, once brought back in the interval $[-\pi, \pi]$. This results in a decrease of the instantaneous frequency.

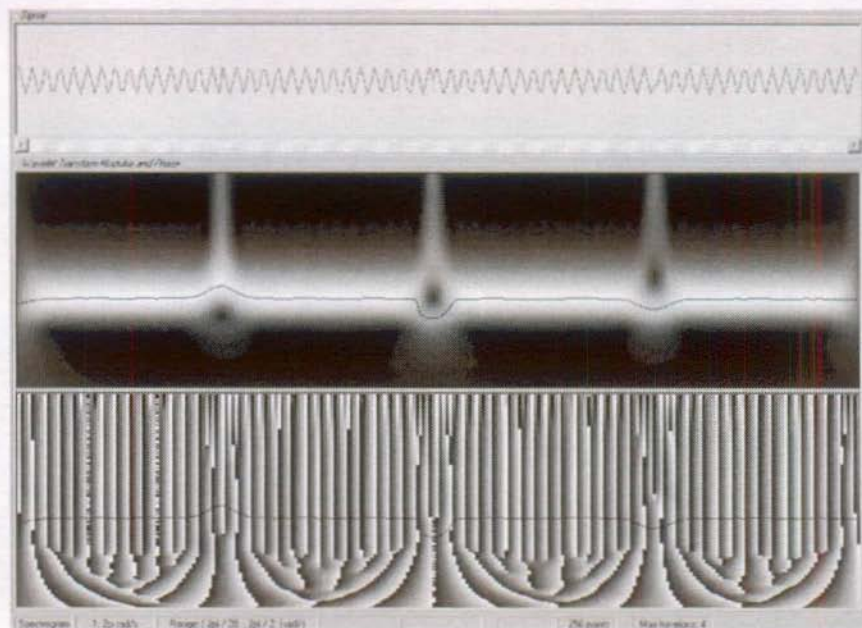


Figure 6-21. Effect of three phase jumps on the phase of the transform of a constant frequency signal.

The holes in the modulus and the dislocations in the phase of the transform are the signature of sudden phase changes that are commonly obtained in real experimental conditions. One can observe this kind of features in Figure 6-14. More precisely, a phase dislocation can appear if and only if the modulus drops to zero locally, which results in the phase being undetermined at that point. A loop around such a point yields a phase change of 2π . (This is actually very similar to what is obtained in a fully developed speckle pattern.) Thus, choosing one path instead of the other around a dislocation amounts to a phase difference of exactly one fringe. Therefore, important phase errors can be accumulated when vibrations introduce a large phase noise in the interferogram.

6.7 Phase errors due to non-linear phase evolution

We are interested here in the phase errors that are obtained when the phase evolution law of the signal can no longer be considered linear in the temporal analysis window. The example described in paragraph 6.7.1 shows the error produced by the derivatives of order higher than two, in the case of a sinusoidal frequency modulation. Next, in 6.7.2, we characterize the error induced by the

second derivative of the phase, assuming that the higher derivatives are negligible. In the last paragraph, we study another type of non-linearity of the phase evolution, which is obtained when the phase-shifting device that produces reference phase steps during an experiment is incorrectly calibrated. The resulting cyclic phase jumps ultimately create troublesome signal harmonics.

6.7.1 Phase estimation error in the case of a sinusoidal frequency modulation

Sinusoidal frequency modulation is an interesting case where the derivatives never totally disappear. We try to estimate here the amount of error made when estimating the phase of the signal shown in Figure 6-14. To simplify the problem, we first create a signal of characteristics as close as possible to what is actually measured. Hence, we build a signal using a sinusoidal frequency modulation to which is added a carrier frequency of $\pi/2$ rad/s. We adjust the initial phase and frequency modulation law until the phase measured along the ridge of the transform of the simulated signal matches with the experimentally measured phase. The result is shown in Figure 6-22.

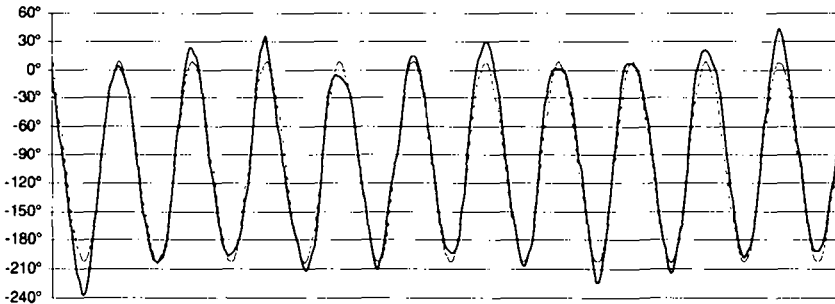


Figure 6-22. Phase measured along the ridge in Figure 6-14 (continuous line) and approximation (dashed line) obtained along the ridge of a simulated signal.

Working with the simulated phase evolution $\varphi_{\text{sim}}(t)$, we can now estimate analytically the different derivatives of the phase.

We first plot the phase measured along the ridge for the simulated signal (labeled “skeleton phase”) and compare it to the actual simulated phase $\varphi_{\text{sim}}(t)$ (see Figure 6-23). The difference, plotted as a thick line, oscillates between plus or minus 15° , which represents a relative error of $\pm 13\%$ for the phase extrema.

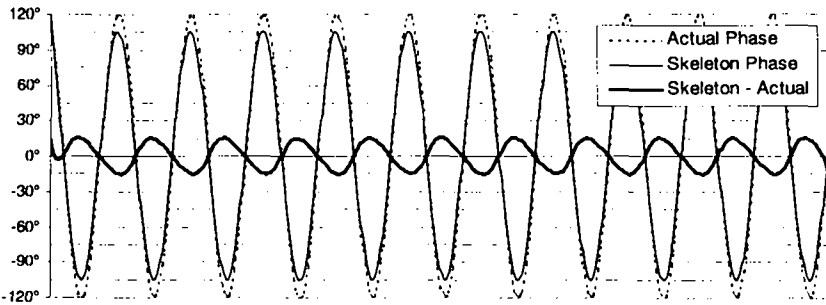


Figure 6-23. Comparison of the phase of the simulated signal, measured along the ridge, with its actual value. Units are in degrees.

The next step is to evaluate the theoretical error contribution of the second derivative of the phase and compare it to the error shown in Figure 6-23. This is done in Figure 6-24 where the term

$$\frac{1}{2} \arctan a^2 \varphi_{sim}''(b) \quad (6-24)$$

is estimated and plotted with the label “Second derivative error”. This time, the difference with the error obtained in Figure 6-23 oscillates between plus and minus 2°. The remaining error is a function of the higher derivatives of the phase.

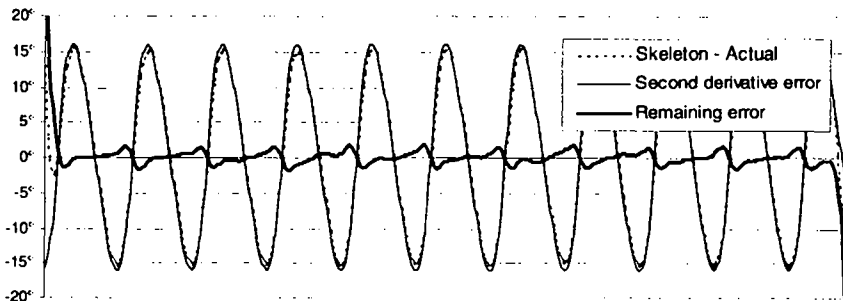


Figure 6-24. Comparison of the measured phase error with the theoretical error due to the second derivative of the phase. Units are in degrees.

This same example is again treated in Chapter 9 where different solutions are proposed in order to eliminate directly the predominant second derivative error.

6.7.2 General effect of the second derivative of the phase

We will assume here that derivatives of order higher than two are negligible over the temporal analysis window and that the signal modulation changes linearly in this same window. In order to get an idea of the behavior of the factor shown in (6-24) we write the second derivative φ_s'' as being proportional to the instantaneous signal frequency φ_s' by a factor $1/\alpha$:

$$\varphi_s'' = \frac{\varphi_s'}{\alpha} \Leftrightarrow \alpha = \frac{\omega_s}{\omega_s'} \tag{6-25}$$

Note that α has the dimension of time. We can now write the phase error $\delta\varphi$ as:

$$\delta\varphi = \frac{1}{2} \arctan \frac{\omega_0^2}{\alpha\omega_s} \tag{6-26}$$

In the next figure we plot the contour lines of $\delta\varphi$ when ω_0 equals 2π . The vertical scale represents the signal instantaneous frequency ω_s , covering the range $[0, 180]$ °/s, and the horizontal scale gives the value of the coefficient α , ranging from 0 to 100 s. The contour lines correspond to 5° steps of the error $\delta\varphi$.

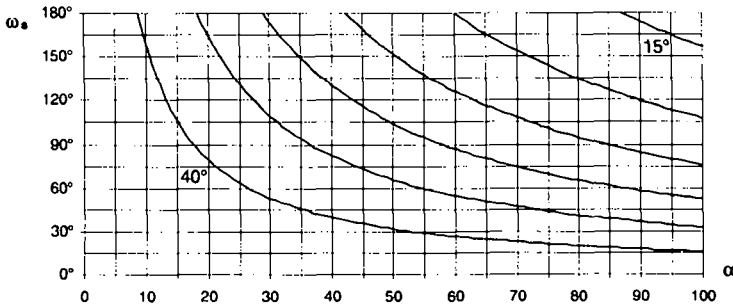


Figure 6-25. Contour plot of the phase error as a function of the signal frequency ω_s and the ratio $\alpha = \omega_s/\omega_s'$, when $\omega_0 = 2\pi$.

We observe that the phase error grows very fast with the second derivative of the phase. The effect is amplified for low-frequency signals because of the larger temporal window used to process them (α is larger). Fortunately, the error cannot become larger than 45° (as far as our model of phase and modulation evolution of the signal holds). Still, a systematic error of at least 15° is obtained for any ω_s value, when ω_s' is larger than $\omega_s/20$. Hence, most frequency transitions of the measured signal result in an error oscillating between plus and minus 45° . However, it is important to note that as soon as the frequency

stabilizes, the error disappears altogether. As mentioned earlier, we can make an analogy between the process of wavelet-based phase measurements with an electronic phase-lock-loop that tries to lock with the phase of a signal. We can imagine that the PLL has a certain inertia that prevents it from following frequency variations without an additional phase delay. Fortunately, this delay disappears when the frequency becomes stationary, which permits to the PLL to lock back. The practical consequence is that there is *no* accumulation of the error due to the second derivative of the phase. Whenever it is negligible, the phase of the transform is really equivalent to the signal's phase.

Equation (6-26) shows that the situation becomes worse when higher mother wavelet frequencies are used. Hence, correcting the second derivative error is an important topic in the development of the wavelet based phase measurement. Solutions to this problem, in particular the use of chirped wavelets, are presented in Chapter 9.

6.7.3 Harmonic generation due to incorrect phase-shifting device calibration

This point deals with a very practical aspect of the measurement in dynamic phase-shifting conditions. We show in Chapter 4 that the introduction of a known phase step in the interferogram, between each image acquisition, is essential to determine the absolute sign of the phase change induced, for example, by the object deformation. To create such reference steps we usually drive PZT-mounted mirrors in a cyclic fashion. The idea is to have phase steps that are integer fractions of 2π , say $2\pi/n$, so that the mirror comes back to its initial position after n such $2\pi/n$ steps. Typically, we use cycles of $\{0, \pi/2, \pi, 3\pi/2, 0\}$ which correspond to $n = 4$.

Let us now look at what happens when the PZT element is not calibrated correctly. In this case, phase increments ϕ are introduced instead of $2\pi/n$ and the actual cycle is $\{0, \phi, 2\phi, 3\phi, \dots, (n-1)\phi, 0\}$. All steps are then equal except the last one, equal to $2\pi - (n-1)\phi$. In the absence of a deformation-induced phase change, the measured signal $s(t)$ is periodic of period n , as required, but is no longer a sinusoidal function of time. $s(t)$ can now be written as:

$$s(t) = \sum_{k=-\infty}^{\infty} a_k \cos\left(k \frac{2\pi}{n} t\right) = \text{Re}\left(\sum_{k=-\infty}^{\infty} a_k \exp\left(ik \frac{2\pi}{n} t\right)\right) \quad (6-27)$$

A perfect calibration implies that $a_k = 0$ for $k \neq \pm 1$. A consequence of (6-27) is that there are now harmonics of the fundamental frequency in the signal. This creates new peaks in its wavelet transform.

Let us now consider a point of the interferogram where the deformation produces a phase change $\omega_0 t$. The measured signal becomes:

$$s(t) = \sum_{k=-\infty}^{\infty} a_k \cos\left(\left(\omega_0 + k \frac{2\pi}{n}\right)t\right) = \operatorname{Re}\left(\exp(i\omega_0 t) \sum_{k=-\infty}^{\infty} a_k \exp\left(ik \frac{2\pi}{n} t\right)\right) \quad (6-28)$$

The signal spectrum now contains harmonics at the frequencies $\omega_0 + k2\pi/n$, which could interfere with the harmonic of interest at $k = 1$.

To illustrate these effects we simulate the case where $n = 4$ and $\phi = \pi/3$ instead of $\pi/2$. Hence, cycles $\{0, \pi/3, 2\pi/3, \pi, 0\}$ are obtained. (Fortunately, PZT calibrations are usually much more precise). In the first half of the simulation, the deformation-induced phase change is constant, its frequency being $-\pi/10$. In the second part, its frequency increases from $-\pi/10$ up to $+\pi/6$. The resulting transform is shown in Figure 6-26, where $\omega_0 = 6\pi$.

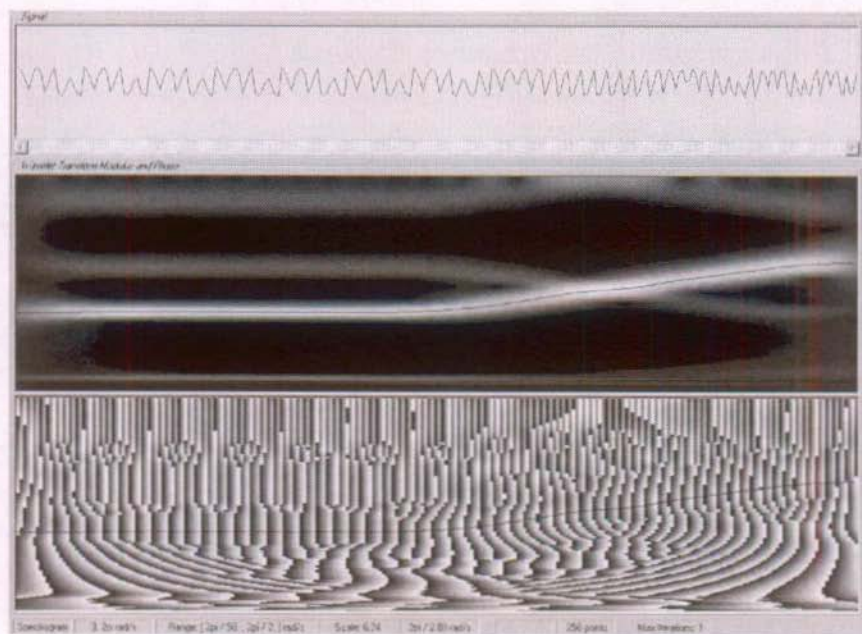


Figure 6-26. Harmonic generation in the form of additional frequency components, caused by a miscalibration of the element producing the reference phase steps.

The four different peaks present in this image correspond to the first five positive and negative harmonics of the signal. There is, from bottom to top, the

frequency $2\pi/20$ ($k=0$ and $k=-2$), the frequency of interest $2\pi/5$ ($k=1$), correctly identified by the ridge extraction algorithm, the frequency $2\pi/(10/3)$ ($k=-1$) and the frequency $2\pi/(20/9)$ ($k=2$).

The second part of the figure shows that the different components move according to ω_s . In particular, the harmonics -1 and $+1$ interfere when they cross one another, which results in a distortion of the ridge and of the skeleton's phase.

The conclusion is that attention should be paid to the phase shifter calibration, since the task of extracting the ridge is usually sufficiently difficult without the added inconvenience of signal harmonics. However, the ridge extraction remains possible since the amplitude of the useful harmonic stays much higher than that of the others, even when the calibration error is large, as seen in this example.

6.8 Phase errors in the presence of noise

As illustrated in Figure 6-7, the bandpass filtering inherent to wavelet processing usually eliminates a large part of the noise present in a signal. In order to estimate the influence of intensity noises of varying standard deviations we create a simulated sequence of 512 256 x 256-pixels images. Each pixel "records" an interferometric signal of amplitude I_M equal to 32 grey levels. The initial phase of these pixels varies from 0 to π along horizontal lines of the first image. The first line corresponds to a noise standard deviation σ_N of 0 grey levels while the last corresponds to $\sigma_N = 64$ grey levels. The frequency of the signal varies in the same manner for all pixels: it is $\pi/6$ in the first image and $5\pi/6$ in the last. In this way, we can process the signal of different pixels along the time axis and obtain an idea of the phase error produced for different noise levels and different signal instantaneous frequencies ω_s .

This image sequence is processed with a program presented in Chapter 7. We actually look at the phase evolution of the five pixel lines where $\sigma_N = 0, 2, 4, 8$ and 16 grey levels. We can then compare the calculated phase of the 256 pixels to the theoretical phase value and compute the standard deviation of the difference $\delta\phi$ as a function of time or, equivalently, as a function of the frequency ω_s . The results are presented in Figure 6-27.

We choose to make the simulation this way because the chirp permits to explore rapidly the frequency domain. The alternative would be to create a bunch of constant frequency signals and analyze them. Since the filtering effect of the transform is stronger at low frequencies, we can imagine that the error is

larger at higher frequencies. However, a potential problem with our simulation is that the success of the analysis at high frequencies depends on the result of the analysis at low frequency, since the ridge extraction propagates along the time. Hence, we can fear that errors accumulate and give an artificially higher noise level towards the end of the sequence. The consequence is that we can imagine two different processes that contribute to make the phase standard deviation larger for larger values of ω_s . To make sure that the second possibility, error accumulation, is actually negligible, we process a second simulated sequence of images where the frequency varies from $5\pi/6$ down to $\pi/6$ and we plot the result obtained for the same noise levels. We remark that in this second case the second derivative of the phase has the same absolute value but an opposite sign.

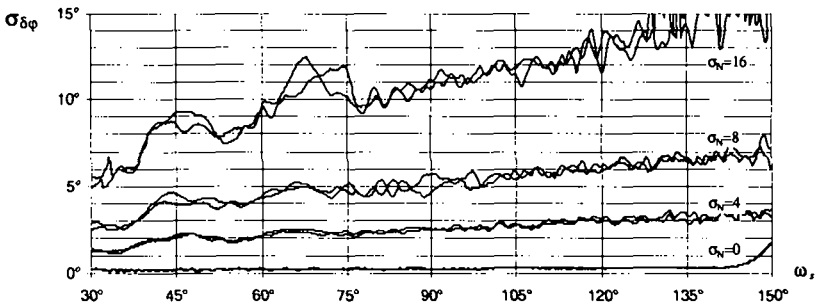


Figure 6-27. Standard deviation of the phase error obtained for signal frequencies ranging from $30^\circ/s$ to $150^\circ/s$ and for 4 different noise levels.

We indeed observe an increase of the error standard deviation towards high ω_s values. However, the two curves obtained for the transition $\pi/6 \rightarrow 5\pi/6$ and $5\pi/6 \rightarrow \pi/6$ are very similar. This confirms that there is no significant error accumulation effect in these estimations. In other words, the estimations can be considered to be fairly independent of the ridge propagation direction. The hypothesis of a higher accuracy due to better noise rejection for low values of ω_s is also confirmed. The maximum standard deviation is on the order of 15° for a signal-to-noise ratio of 2, over the whole domain $[30^\circ, 150^\circ]$. This compares very favorably to the results obtained with the 5-image algorithm depicted in Chapter 5, where this error level is only obtained for a SNR larger than 3, on the reduced domain $[60^\circ, 120^\circ]$. The curves are quite noisy since we use only 256 samples per ω_s value to make these estimations whereas we use about 36000 samples for each equivalent ω_s value in the case of the 5-image algorithm.

Each standard deviation value is calculated from 256 phase estimations. However, similarly to what we did for the 5-image algorithm, we first remove the points for which the ridge is grossly wrong. No points have to be removed for the noise standard distributions of 0, 4 and 8 grey levels. 10 points are removed for $\sigma_N = 16$. This means that more than 95% of the points are correctly processed at these noise levels.

After studying the phase error standard deviation, we can look at the average error value. As seen earlier, we expect a systematic error due to the second derivative of the phase, which is constant for a linear chirp. Using equation (6-26) we can estimate the systematic error to be 15° for $\omega_s = 30^\circ$, 7.3° for $\omega_s = 45^\circ$ and 1.9° for $\omega_s = 90^\circ$. These values match very closely with what we find in Figure 6-28 where we plot the average phase error corresponding to the four noise situations of Figure 6-27. Note that we plot in this figure the opposite value of the error obtained for the transition $5\pi/6 \rightarrow \pi/6$. We also note a sharp drop for frequencies smaller than 35° . This is actually a boundary effect caused by the prolongation of the signal by a constant frequency signal, for negative time values.

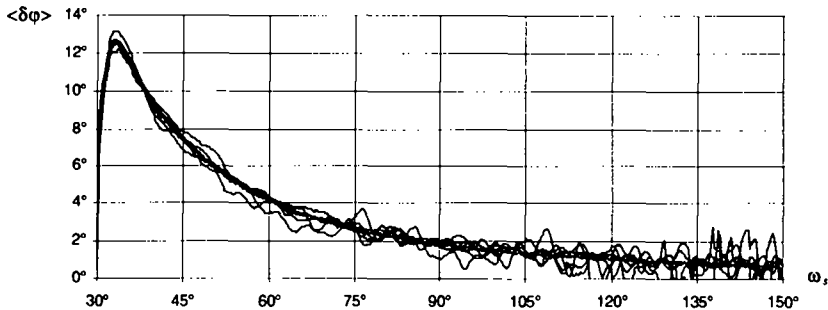


Figure 6-28. Average phase error as a function of the instantaneous signal frequency.

6.9 Summary: wavelet-based phase analysis properties

This chapter gives us some insight into the behavior of the wavelet transform and its phase properties. We observe that it is a well-adapted tool for the processing of the temporal signals that are obtained when performing continuous measurements based on the dynamic phase-shifting principles. In particular, the inherent noise filtering brings robustness to the method. Moreover, the ridge extraction algorithm proves to be an efficient way to extract directly the phase

evolution of interest to us. Also, the analysis can be performed almost up to the limits of the available frequency domain, $[0, \pi]$, which is impossible with the 5-image algorithm studied in Chapter 5.

Three limitations of the technique can be noted. There is first a difficulty to follow very sudden frequency variations. Second, systematic phase errors appear when the phase evolution is not a linear function of time over the support of the temporal analysis window. Third, the ridge extraction becomes difficult when the signal frequency gets too close to the Nyquist limit, because of an interference effect in the transform.

We present in the next two chapters the details of the practical software implementation of the method as described up to now and a series of application examples. Chapter 9 then introduces two fundamental improvements of the technique that address the limitations mentioned earlier. One is the creation of complex signals, the other is the use of chirped wavelets.

Bibliography

- 1 N. Delprat, B. Escudié, P. Guillemain, R. Kronland-Martinet, P. Tchamitchian, B. Torrèsani, "Asymptotic wavelet and Gabor analysis: extraction of instantaneous frequencies", *IEEE Transactions on Information Theory*, Vol. 38 (1992), No. 2, pp. 644-664.
- 2 P. Guillemain, R. Kronland-Martinet, "Characterization of acoustic signals through continuous linear time-frequency representations", *Proceedings of the IEEE*, Vol. 84 (1996), No. 4., pp. 561-585.
- 3 P. Goupillaud, A. Grossmann, J. Morlet, "Cycle-octave and related transforms in seismic signal analysis", *Geoplot*, Vol. 23 (1984), pp. 85-102.
- 4 A. Grossmann, R. Kronland-Martinet, J. Morlet, "Reading and understanding continuous wavelet transforms", in "Wavelets, Proceedings of the first conference", J.M. Combes, A. Grossmann, P. Tchamitchian, Eds, Marseille, Springer 1987.
- 5 A. Papoulis, "The Fourier integral and its applications", McGraw-Hill Book Company Inc., 1962.
- 6 I. Daubechies, "The wavelet transform, time-frequency localization and signal analysis", *IEEE Transactions on Information Theory*, Vol. 36 (1990), No. 5, pp. 961-1005.

7. Phase-shifting algorithm and wavelet-processing software implementation

The two solutions we propose in this dissertation, an adapted phase-shifting algorithm and a wavelet-based analysis solve the problem of the phase extraction from a sequence of images recorded in dynamic phase-shifting conditions. The behavior of these approaches has been characterized in the two preceding chapters. In this chapter we briefly present the solutions we chose for the practical software implementation of the corresponding algorithms.

In particular, the maximum-likelihood phase estimation presented in paragraph 7.2.6 is shown to be an essential tool for robust processing of images obtained in the context of speckle interferometry.

7.1 Adapted 5-image algorithm

The phase calculation is a very straightforward process. Hence, we take advantage of this paragraph to rapidly describe the spatial unwrapping algorithm that we use in this case.

7.1.1 Phase calculation

The algorithm itself is described in Chapter 5. Five intensity samples I_1 to I_5 are used to determine the phase of the interferogram at each pixel in the image. We choose one particular solution for the estimation of the average phase increment $\Delta\phi$, called method A in Chapter 5. This preliminary calculation actually yields $\cos\Delta\phi$. In some cases, because of noise or when the phase of the interferogram is close to an integer multiple of π , the absolute value of the estimated cosine is sometimes larger than one. In this case, our algorithm assigns to this particular pixel a phase value that depends on the relative magnitude of the intensity

samples: if I_3 is larger, respectively smaller, than both I_2 and I_4 , the phase is 0, respectively π .

The estimation of the phase ϕ and phase increment $\Delta\phi$ require the computation of different ratios where both numerator and denominator are linear combinations of the five intensity samples. Since these samples are integer values, it is possible that some denominators are equal to 0. Rather than test systematically for this condition in our programs, we add a small constant, such as 10^{-30} , to each calculated denominator.

Once the phase increment is estimated, the phase itself is obtained as the arctangent of a second ratio multiplied by $\sin\Delta\phi$. The usual arctangent function yields a value within the domain $[-\pi/2, \pi/2]$. Since $\Delta\phi$ is supposed to be within $[0, \pi]$, $\sin\Delta\phi$ is a positive value. Hence, the numerator and denominator are proportional to the sine and cosine of the phase. From the sign of these quantities it is possible to obtain a phase value within $[0, 2\pi]$. This is necessary for our programs written in Visual Basic. Fortunately, the two other compilers we use, a Pascal compiler and a recent C compiler (Visual C++), provide the so-called `atan2()` function, which takes two arguments, the numerator multiplied by $\sin\Delta\phi$ and the denominator, and yields directly a value within $[-\pi, \pi]$.

We mention in Chapter 5 that in our current implementation of this algorithm we have the possibility to perform a least-square fit of the $\Delta\phi$ map before calculating the phase itself. However, this cannot be used in a systematic manner in the case of dynamic phase-shifting since the $\Delta\phi$ map might be of a discontinuous and complex shape, whereas the fit is a third-degree polynomial surface.

The algorithm was first implemented in Pascal and added to the commercial package `Optocat` that runs on PC computers. This program provides many useful functions to perform phase measurements based on the phase-stepping method. However, because of the difficulty to develop and add new functions to this package (limited DOS memory) we decided to base our image processing developments on the `Visilog` package that runs under Windows on PC as well as under various Unix flavors. This is a complete general-purpose image-processing environment, including many high-level morphological processing tools. However, it does not propose the dedicated tools used for phase measurement. Hence, we modified the user interface and added different compiled C functions to be able to compute phase values with 3- or 5-image algorithms as well as with the Fourier method, import or export such phase values, low-pass filter them in the sine and cosine domain and unwrap them in a convenient manner.

To process the long sequence of images that we obtain with dynamic phase-shifting, we made a few “scripts”, which are written in C code and interpreted directly by Visilog, based on the available phase- and image-processing functions. The computation of the wrapped phase maps corresponding to a 512-image sequence takes about one hour and a half on a 120 MHz Pentium PC.

The problem of phase unwrapping in the context of speckle interferometry was actually proposed as a subject to an exchange student who created a very powerful unwrapping tool, which is described in the next paragraph.

7.1.2 Spatial unwrapping of noisy wrapped phase maps

The problem of the spatial unwrapping of noisy phase maps obtained particularly with speckle interferometry was proposed to an Erasmus exchange student, David Venet¹. The subject was far reaching since its goal was to unwrap noisy phase images possibly presenting physical discontinuities, without preliminary masking. The resulting algorithm actually went beyond our expectations and is described below.

The unwrapping of an image is performed in the following manner:

1) Calculation of a merit function for all the pixels in the image. This consists in selecting a 3x3- or 5x5-pixel window around each pixel. Next, this miniature image is unwrapped with respect to the central pixel. The unwrapping is performed on a pixel by pixel basis. The variance of the resulting image is then computed and acts as the merit function for 3x3-pixels windows. In the 5x5 case, a best-fit plane is first subtracted from the unwrapped region, before calculating the variance. This helps process regions in the interferogram where the fringes are closely spaced.

2) Based on the maximum, minimum and distribution of the merit function, 20 “quality” classes are defined in the image.

3) The algorithm looks for a pixel belonging to the first class. The fringe order of this point is arbitrarily chosen as zero. This search is performed on a grid and starts from one corner of the image. Once this pixel is found (it is defined as the first “current pixel”), the coordinates of its 8 neighbors are sorted in different buffers, according to their class. There are actually as many buffers as classes. These pixels are also flagged as “in use” in a bookkeeping image B while the current pixel is flagged as “processed”.

4) The algorithm now looks in the buffers, starting from the one corresponding to the highest quality. As soon as it finds one that is non-empty it unwraps the phase φ_i of the corresponding pixel with respect to the phase φ_c of

the current pixel. This consists in adding or subtracting an integer number of 2π to φ_i so that the difference $|\varphi_i - \varphi_c| < \pi$. The newly unwrapped pixel is now flagged as "processed" in B, and its neighbors that are not yet flagged as "processed" or "in use" are placed in the buffers.

5) The process continues to 4) until all pixels in the image have been unwrapped or until the remaining pixels belong to classes lower than a given threshold. In this last case, the algorithm goes back to 3) to look for a new starting point. This permits to unwrap correctly images where unconnected regions exist, while providing at the same time a mask of these regions.

The resulting method is fast since a 512x512 image is unwrapped in about 10 seconds on a 150 MHz Pentium PC. One of its main advantages is that it usually does not require a mask of the regions of interest, but, on the contrary, creates such a mask as a byproduct. A mask can still be provided, if the algorithm fails, in the form of cuts forbidding some unwrapping paths in the image. We remark that preliminary filtering is seldom necessary with speckle images. Moreover, physical discontinuities are usually correctly preserved. It must be emphasized here that the success of this approach is mostly due to the intelligent definition of the initial merit function. Many possibilities were indeed studied before selecting a final set of functions, which are adapted to different unwrapping situations.

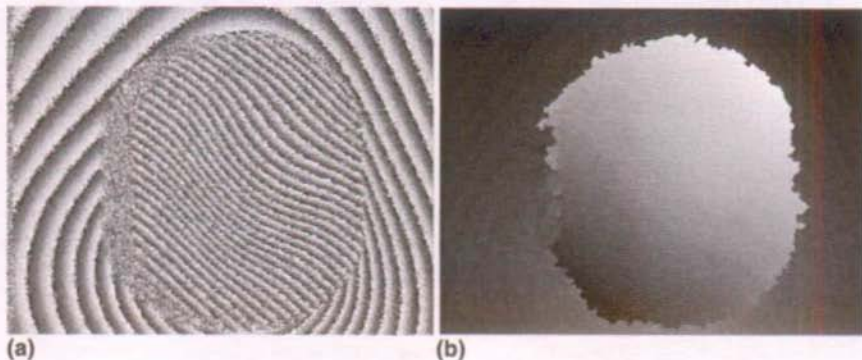


Figure 7-1. (a) Wrapped phase map showing the deformation of a bolt head and underlying metal plate when the nut is tightened (holographic interferometry); (b) Directly unwrapped phase map.

Figure 7-1 shows a wrapped phase map obtained with holographic interferometry applied to the study of the failure of a nut and bolt assembly. There are many fringe discontinuities in this image, as well as a random phase

region caused by the bolt head shadow. The image in (b) is the result of the direct unwrapping of (a), without any filtering or masking. The two adjacent fringe regions have been correctly separated. The remaining unknown is their relative positions (fringe order). This would actually be known without ambiguity if dynamic phase-shifting had been used during this experiment.

The example of Figure 7-2 shows an image obtained with contouring speckle interferometry used to measure the shape of a cavity milled in a metal plate with a high-precision milling machine. One fringe represents a height difference of $22\ \mu\text{m}$. Figure 7-2(a) shows the wrapped phase map. Figure 7-2(b) shows the unwrapped phase map, obtained again without masking or filtering. One can actually observe in this image 10 successive milling steps.

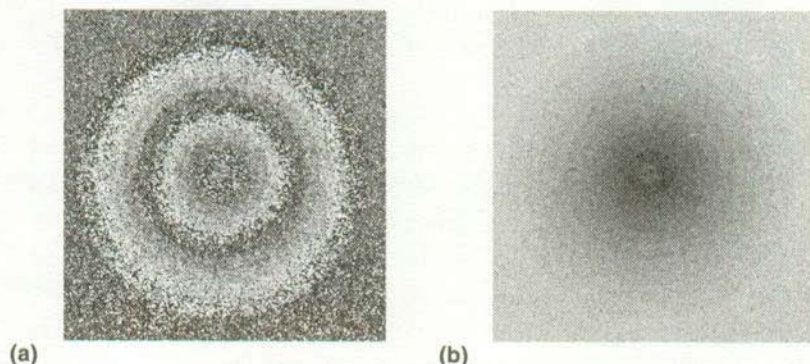


Figure 7-2. (a) Wrapped phase map showing contour fringes obtained in speckle interferometry; (b) Directly unwrapped phase map.

7.2 Wavelet-based phase analysis tools

We wrote a first program, simply called “Wavelet”, to understand the principles of wavelet analysis, study the influence of various parameters and develop the ridge extraction algorithm. In particular, it creates images of a signal’s wavelet transform. The examples of Chapter 7 were obtained this way. Once we got a better understanding of the process of phase extraction with the Morlet wavelet we decided to write a second program, called DPSTools, dedicated to the complete processing of image sequences. Instead of processing one signal at a time, it permits to process automatically the more than 260000 signals obtained with our digital camera (see Chapter 8). This program is described in paragraph 7.2.1. The following paragraphs detail different steps of the wavelet processing that are common to both programs.

7.2.1 DPSTools: wavelet-based processing of image series

This program is made of two distinct parts. It runs under Windows95 or Windows NT on compatible PC. The interface, built in Visual Basic 4, provides a graphical interface to the user. Since Visual Basic 4 creates partially interpreted applications, it lacks the raw processing speed that can be obtained with compiled code. Hence, the processing core is made of multithreaded Dynamic Link Libraries (DLL) called by the interface. These DLL are developed in C, using Visual C++ 4.2. A great deal of time was actually lost because of bugs in the optimizing compiler of this development environment.

The program provides the following possibilities to the user:

1) *Visualization of images belonging to a particular sequence.* The user can zoom in on specific regions, and interactively demand a plot of a selected pixel's signal. The plot can also include the signal of the 8 surrounding pixels.

2) *Selection of the region to be processed.* One can select a single pixel, a line of pixels (not limited to rows or columns) or a rectangular array of pixels (for example the whole image). The selection can be performed graphically with the mouse or using a parameter input window that moreover allows to choose the number of pixels included in the selection by specifying sampling steps. Additionally, the user can specify the time interval of interest within the temporal sequence.

3) *Selection of one or three reference pixels in the image.* This selection is also performed with the mouse or with a parameter-input window. If only one point is selected, its phase evolution is used as a reference that is subtracted from the phase of all other processed pixels (piston correction). The goal here is to correct for a temporally varying phase offset perturbing the whole interferogram. Hence, the chosen point must belong to a static region of the interferogram. If three points are chosen, their phase evolution defines a phase plane that is used as a reference for the other pixels of the selection. The effect is to correct for tilts and piston movements.

4) *Determination of the wavelet analysis parameters.* One window is used to choose the mother wavelet frequency, the threshold that defines the extent of the wavelet support, the maximum and minimum analysis frequencies, the carrier frequency that must be subtracted from the unwrapped phase of each processed signal and the modulation threshold used to eliminate bad pixels from the maximum-likelihood phase estimate (see paragraph 7.2.6).

5) *Choice of the type of output.* There are many possible formats for the result of the analysis. One can obtain simple text files, Excel files (created through an OLE process), binary files with 1 byte per pixel (unsigned byte) or

binary files using 4 bytes per pixel (IEEE floating point format). If, for example, the user selects a rectangular group of pixels, the output can consist of as many files as there are points in the selection, as many files as there are columns or rows, or of as many files as there are selected time samples. Hence, the output can be a sequence of images depicting the state of deformation of the object at different instants (one image per time sample) or a series of images showing the evolution of a profile of the object as a function of time (one image per row or column in the selection).

6) *Process checklist*. This step occurs just before the actual processing starts. The user is presented with a list of the current selection and processing parameters, including the size of the files to be produced (the availability of the necessary disk space is checked), the generic name of the output files (default or chosen by the user) and the type of processing. This can be the simple extraction of the intensity signal of pixels and/or their complete wavelet analysis that provides phase and modulation evolution.

In the current version of this program, the processing of a sequence of 512 512x512-pixels 8 bits images takes about ten hours on a 150 MHz Pentium PC (see paragraph 7.2.4). This corresponds to the processing of 128 MByte of data and can result in up to five times this quantity in output files if we code the phase as a 4-byte floating point number and the modulation as a single byte. In our case, we use recordable CDROMs to store the input and output data.

This brief presentation of the program DPSTools is complemented in the next paragraphs by a description of the main computation steps and by application examples in Chapter 8.

7.2.2 Extension of the signal support

Practically, the computation of the wavelet coefficients consists in calculating the real and imaginary parts of the wavelet for the time samples where the Gaussian envelope is higher than a given threshold ϵ (typically 10^{-3} in our case). Since the variance of the Gaussian function is simply the square of the scaling factor a , the half-support *sup* of the temporal window is equal to:

$$sup = a\sqrt{-2 \ln \epsilon} \quad (7-1)$$

We actually take the integer part of this quantity and we calculate $2sup + 1$ samples of the wavelet function. We can now multiply these samples by the corresponding signal samples centered at a time b . The sum of these products yields an estimation of the wavelet coefficient $S(a,b)$. We have not yet looked for optimized implementation solutions, maybe similar to what is done with the Fast Fourier Transform algorithm, which could lower the processing time.

There is however a problem near the beginning and the end of the signal support. For example, when the analysis is performed for the first time sample, there are only $sup + 1$ available signal samples while $2sup + 1$ are required. One solution could be to begin the wavelet analysis for a sample located at a time larger than sup . However, we do not know in advance the instantaneous frequency of the signal in that region. Hence, it would be necessary to use the value of sup that corresponds to the lowest analysis frequency that we allowed. This would finally amount to discarding a lot of samples.

We rather perform a prolongation of the signal support, by adding as many new data points as necessary for the largest possible value of sup . These new points have all the same value, equal to the first signal sample. In practice, we do not create a new signal, we simply sum the wavelet coefficients corresponding to the missing data points and multiply the resulting real and imaginary sums by the value of the first signal point. The same artifice is used near the signal's end.

However, the instantaneous frequency becomes brutally discontinuous with this simple prolongation scheme, from the signal's frequency at the extremities of its support down to zero. This usually creates a "bending" of the transform towards lower frequencies and the phase of the transform no longer represents the phase of the signal near the discontinuity point. The extent of the perturbation is of the order of the half-width of the analysis window. For $\omega_0 = 2\pi$ and a signal frequency of $\pi/2$, there are about 10 perturbed points. In experiments where the loading process can be controlled, we usually record ten or twenty images before actually starting loading. These images act as a buffer. Moreover, since they correspond to the reference phase step $\pi/2$, it is easy to find a starting point for the ridge near the signal's beginning.

A different solution can be obtained using an iterative algorithm. The signal is first extended as just described. Next, a sinusoidal signal prolongation is created based on the frequency, modulation and phase obtained with the ridge extraction for the first and last signal samples. Since the frequency of the prolongation is no longer zero, the transition is less sharp and the new transform is less perturbed. The process can be repeated until the estimated frequency of the prolongation does not change significantly. This works well for signals of relatively constant frequency at the transition points, assuming that the ridge is correctly identified in the first place. For example, Figure 7-3 shows the error between the actual phase of a linear chirp and the skeleton phase obtained after 0, 1, 2, 5 and 10 iterations.

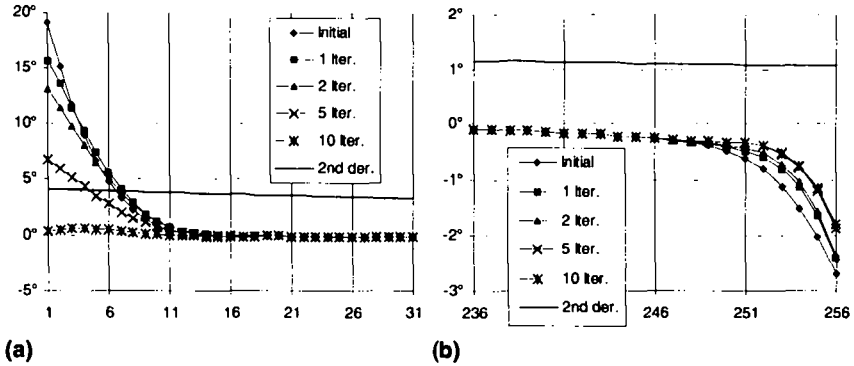


Figure 7-3. (a) Error (In degree) of the skeleton phase after correction of the second derivative phase deviation at the beginning of a $\pi/3$ - $2\pi/3$ chirp; (b) Same near the end of the signal.

The chirp frequency goes from $\pi/3$ at the beginning (Figure 7-3(a)) up to $2\pi/3$ (Figure 7-3(b)). The signal covers 256 time samples. The error plotted in these graphs is actually the error that remains once the systematic error due to the second derivative of the phase has been subtracted from the skeleton’s phase. This quantity is also plotted as “2nd der”. Hence, the actual phase error is the sum of this contribution plus the curves labeled “ n Iter” where n is the number of iterations. The improvement is obvious at the signal’s start while it is marginal at the end where the error is already small before starting the iterations.

A second example shows however that convergence can be very slow when the instantaneous frequency has a faster time evolution. This is illustrated in Figure 7-4 where the chirp frequency now goes from $\pi/6$ up to $5\pi/6$. We see that the error disappears slowly near the end of the signal (Figure 7-4(b)). We must note that the frequency gets sufficiently close to π in this region so that interference effects make the ridge extraction difficult. The situation is more complicated at the beginning (Figure 7-4(a)) where the error increases with the number of iterations. It appears that the frequency used to create the signal support converges towards a frequency close to $\pi/5.1$ instead of $\pi/6$ (35° instead of 30°). The problem is that the average frequency $\langle \omega_s \rangle$ of the signal is higher than $\pi/6$ over the analysis window ($sup = 45$ for the first sample). Hence, the frequency obtained from the ridge extraction overestimates the instantaneous frequency for the first time sample. Using this estimation to create the signal prolongation actually strengthens this effect.

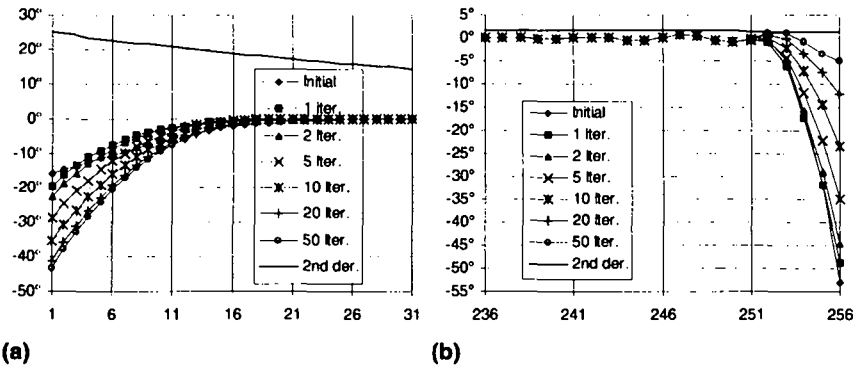


Figure 7-4. (a) Error (in degree) of the skeleton phase after correction of the second derivative phase deviation at the beginning of a $\pi/6$ - $5\pi/6$ chirp; (b) Same near the end of the signal.

The major drawbacks of the second prolongation scheme are thus the increased processing time and an error correction that is not guaranteed. Hence, this method is available in the program Wavelet for demonstration purposes but it is not used in the current version of the program DPSTools.

7.2.3 Mother wavelet sampling

Since the analysis frequency is changed repeatedly during ridge extraction, new wavelet samples have to be computed at each iteration. The real and imaginary parts of these samples are even, respectively odd, functions of time. Hence, the wavelet needs only be constructed over one half of the analysis window support by calculating the coefficients shown in (7-2) for integer values of the time t .

$$\begin{aligned}
 \text{Re}(g(t)) &= \text{Re}(g(-t)) = \frac{1}{a} \exp\left(-\frac{t^2}{2a^2}\right) \cos\left(\frac{\omega_0}{a} t\right) \\
 \text{Im}(g(t)) &= -\text{Im}(g(-t)) = -\frac{1}{a} \exp\left(-\frac{t^2}{2a^2}\right) \sin\left(\frac{\omega_0}{a} t\right)
 \end{aligned}
 \tag{7-2}$$

To get an idea of the number of sine, cosine and exponential calculations that are required we make a rough estimation with the following parameters: a sequence of 512 images containing 512×512 pixels is analyzed with $\omega_0 = 2\pi$. We suppose that the instantaneous frequency ω_x of each pixel is constant over the 512 time samples. We also consider that ω_x is distributed within $[\pi/6, 5\pi/6]$ with a triangular distribution law, maximum for $\omega_x = \pi/2$, zero at $\pi/6$ and $5\pi/6$. This results in the estimation of about 4.3 millions sines, cosines and

exponentials per time sample per iteration for a complete image. Assuming that the ridge extraction converges in 3 steps for each of the 512 time samples, a total of about 20 billions such functions have to be estimated.

To speed things up we remark that the different wavelets are actually of same shape. Hence, we simply sample the mother wavelet once, with a number of samples sufficiently high for the estimation to be reasonable at all possible analysis frequencies. The wavelet coefficients for a given frequency are then simply obtained by downsampling the mother wavelet samples. For example, sampling the mother wavelet in phase steps of 5 mrad results in a maximum error of 0.0025 on the wavelet coefficients, when the larger coefficient is equal to 1. This maximum error is obtained for the real part when $\omega_0 a t$ is close to $\pm\pi/2$. We verified on different signals that such errors induce negligible phase errors in the final transform (on the order of 1°). The option to calculate exactly the coefficients remains in DPSTools in order to compare at will the two solutions. In the case $\omega_0 = 2\pi$, about 2×4700 wavelet samples have to be evaluated at the beginning of the processing.

7.2.4 Ridge extraction

As mentioned in Chapter 6, the ridge extraction algorithm needs a starting point. Different strategies are possible. One solution consists in choosing an initial frequency of $\pi/2$ for the first time sample. This works usually well for experiments where the $\pi/2$ reference phase step is introduced. Because of the necessary signal extension discussed in paragraph 7.2.2 it is actually better to start the ridge extraction from a time sample not too close to the origin.

A more general solution, used in DPSTools, consists in looking for the maximum of the instantaneous spectrum computed for a given time. The search is actually limited to a band of frequency centered on $\pi/2$. This prevents starting at a time sample where the instantaneous signal frequency is too high or too low. If the maximum of the transform's modulus is under a given threshold, the search is repeated at a later sample. The time domain explored in this way corresponds to the part of the signal that the user wants to analyze. The estimation of the instantaneous spectrum is performed by calculating the wavelet transform for a discrete number of values of the scaling factor a . Since the frequency analysis window is narrower at low frequencies, it is necessary to use smaller frequency steps in the low-frequency region of the spectrum. We use the progression law $a_{i+1} = f a_i$ where the factor f depends on ω_0 and a fixed percentage value (95% in our implementation), which defines the height where the two frequency analysis windows centered at ω_0/a_i and ω_0/a_{i+1} cross.

Once a first time sample b_0 and analysis frequency ω_0/a_0 have been chosen, the ridge extraction algorithm starts:

- 1) The samples of the wavelet corresponding to ω_0/a_0 are calculated.
- 2) The transform is computed for a series of time points $S(a_0, b_0+k)$, $k \in [-n, n]$. The phase φ_s of these estimations is unwrapped and the phase increments are summed. This gives a measure of the phase variation during a $2n$ -long time interval. A new instantaneous frequency ω_1 and scale factor a_1 are thus calculated.
- 3) ω_1 is compared to the limits of the frequency domain chosen by the user (the default is $[\pi/36, 35\pi/36]$). The iteration number is also compared to a fixed threshold. If these tests pass, a_1 and a_0 are compared. If the difference is larger than 1% the algorithm goes back to 1) using a_1 in place of a_0 .
- 4) Once a final value a_i is obtained the corresponding wavelet coefficient $S(a_i, b_0)$ is computed. This yields the estimations of the signal's modulation and phase at time b_0 . The interferogram modulation I_M is actually obtained as $2/\sqrt{2\pi} |S(a_i, b_0)|$.
- 5) The algorithm proceeds to time $b_1 = b_0+1$, using a_i as the new starting point, until the complete signal has been processed.

When one of the tests performed in 3) fails for the sample b_i , the phase is linearly extrapolated from the previous successfully analyzed time samples b_{i-1} and b_{i-2} and the scale factor a_{i-1} is used for the iteration of the following time sample b_{i+1} . If the ridge extraction fails for the time sample b_0 or b_1 , no such extrapolation can be performed. The phase and modulation are then chosen equal to zero and a default scale factor (corresponding to $\omega = \pi/2$) is used for the next time samples.

There are different possibilities to choose the time interval n used in 2). The fastest solution is obtained when n equals 1. We also use a second solution where n is chosen equal to the half-period of the analysis frequency. In this way, the phase increment is estimated over one signal period. This provides some additional robustness to the ridge extraction but increases the computation time.

Using the same parameters that are used in paragraph 7.2.3, we can now estimate the number of operations that are required to process a 512-image sequence. We consider that the ridge extraction is performed using a support equal to the signal's period. We do not take into account here the initial sampling of the mother wavelet described in 7.2.3. We also assume that the starting point of the ridge extraction is found at the first spectrum evaluation. The total number of required operations is summarized in the following table.

Operation	Number in millions	Number in billions
Square root	134.	0.13
Arctangent	1440.	1.44
Multiplication, addition	122440.	122.

The processing of the 512 time samples of a single pixel takes about 0.10 to 0.15 seconds when the signal modulation is sufficiently high. This figure includes the disk read and write operations. The end result of one ridge extraction is two double-precision floating-point buffers containing the wrapped phase and modulation of the signal.

7.2.5 Temporal unwrapping

The phase is unwrapped along the time dimension for each separate pixel signal. The process is very simple since the phase increment between two successive time samples is within $]0, \pi[$. Hence the phase is a strictly monotonic function of time.

The actual unwrapping starts with the first time sample where the fringe order $n(1)$ is defined as 0. The second time sample is unwrapped with respect to the first with the following algorithm:

- 1) Correction of the fringe order: $\varphi(b+1) = \varphi(b) + n(b)2\pi$.
- 2) If $\varphi(b+1) > \varphi(b)$, do nothing more. $\varphi(b+1)$ is the unwrapped phase value and $n(b+1) = n(b)$.
- 3) If $\varphi(b+1) < \varphi(b)$, increase the fringe order by one: $n(b) = n(b) + 1$. The unwrapped phase value is $\varphi(b+1) + 2\pi$.

Additionally, the user can specify that a certain time instant acts as the reference point for the phase estimation of each pixel. The phase calculated for this time value is then subtracted from the unwrapped phase buffer. This is useful with speckle interferometry experiments where the initial phase of each pixel is randomly distributed in $[0, 2\pi]$.

7.2.6 Phase best-estimate

This last step of the processing is optional. Its goal is to filter the estimated phase of each pixel by combining it with the phase of its neighbors. This means that we make the hypothesis of a similar phase evolution for groups of 3×3 pixels, which is usually verified except at the boundaries of the object and for physical discontinuities such as cracks. Hence, if the hypothesis is not respected locally, only a limited number of pixels are affected.

As seen in Appendix A, this procedure can provide us with the local maximum-likelihood phase value. This is particularly interesting in the case of speckle interferometry where both phase errors due to speckle decorrelations and electronic noise can thus be reduced.

The exact implementation of the maximum-likelihood criterion consists in computing a weighted-average of the phase of the 9 pixels in each 3x3 cell of the image. The weights are given by the squared modulation of each pixel: I_M^2 . However, we use a slightly different solution. First, we do not take into account pixels where the modulation is below a user-defined threshold T . A typical value for T is between 2 and 5 grey levels. In particular, this eliminates points where the ridge extraction failed. Next, except for the first time sample, we do not calculate the weighted-average of the unwrapped phase values themselves but rather of the local phase increment per time sample $\Delta\phi$.

This procedure is applied only on the time interval $[t_1, t_n]$ selected by the user. The filtered phase of the central pixel in a 3x3 window at time t_1 is either fixed equal to 0 in the case of speckle interferometry (since the phase of each pixel is random) or calculated as the weighted-average of the points that have a sufficient modulation:

$$\tilde{\varphi}(t_1) = \frac{\sum_i I_{M_i}^2(t_1)\varphi_i(t_1)}{\sum_i I_{M_i}^2(t_1)} \quad i \in \{1 \leq i \leq 9, I_{M_i}(t_1) > T\} \quad (7-3)$$

The equivalent modulation is given by:

$$\tilde{I}_M(t_1) = \sqrt{\sum_i I_{M_i}^2(t_1)} \quad i \in \{1 \leq i \leq 9, I_{M_i}(t_1) > T\} \quad (7-4)$$

The phase values for the following time samples are obtained using:

$$\tilde{\varphi}(t_{k+1}) = \tilde{\varphi}(t_k) + \frac{\sum_i I_{M_i}^2(t_{k+1})(\varphi_i(t_{k+1}) - \varphi_i(t_k))}{\sum_i I_{M_i}^2(t_{k+1})} \quad (7-5)$$

$$i \in \{1 \leq i \leq 9, I_{M_i}(t_{k+1}) > T\}$$

The modulation is again obtained using (7-4).

We use the phase increments rather than the phase values themselves for the simple reason that the ridge extraction can fail locally before coming back on track, as illustrated in Figure 7-5. In this case, the wrapped phase values are

correct in the last part of the skeleton but the corresponding unwrapped phase is not because the fringe order is incorrectly estimated in the region where the algorithm fails, resulting in a random phase offset.

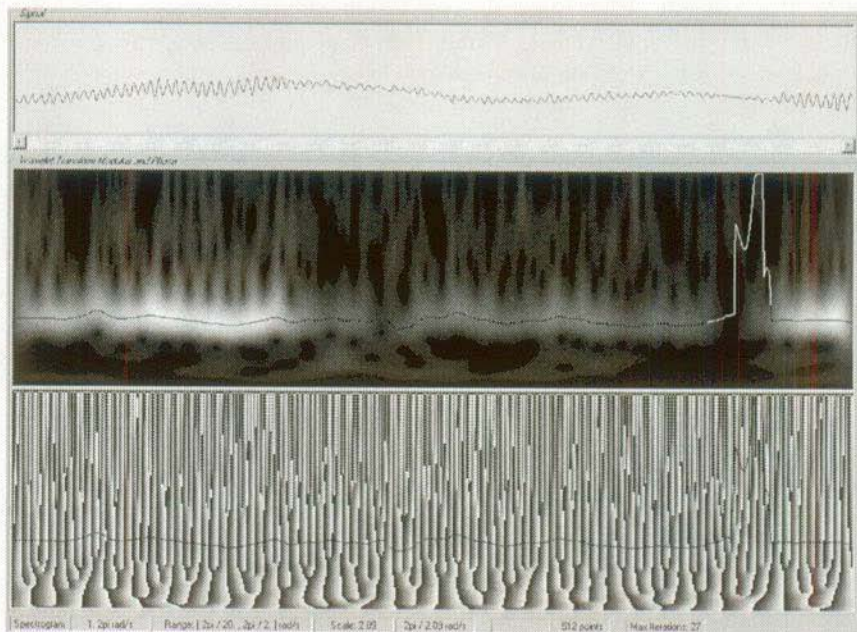


Figure 7-5. Ridge extraction failure in the case of a low-modulation signal obtained in speckle interferometry.

Figure 7-5 shows a signal measured using in-plane speckle interferometry. There is a large image-plane decorrelation during this experiment, which results in large variations of the modulation of the different pixels. We can extract the unwrapped phase of this signal and of its 8 neighbors and then subtract a linear phase term that removes the overall phase evolution. The remaining phase fluctuations are plotted in Figure 7-6. The thick black line represents the best-estimate phase computed with the algorithm just described (using the phase increments). The thick grey line represents a weighted-average calculated using the unwrapped phases directly. The phase of the central pixel exhibits a brutal increase near the end of the plot, which corresponds to the ridge excursion in Figure 7-5. Once the ridge extraction locks back on the correct ridge, the phase evolution is again correct (same slope as the other signals) but there is an offset of about one fringe and a half. If we use directly this value in the calculation of

the weighted-average (grey line) this offset results in a shift of the estimate, whereas it does not influence the estimation at all if only the phase increments (black line) is taken into account like in (7-5). There are indeed large phase slopes in the region where the ridge extraction fails but the corresponding modulation is very low. Hence, their effect is negligible once the squared modulation is used as a weight.

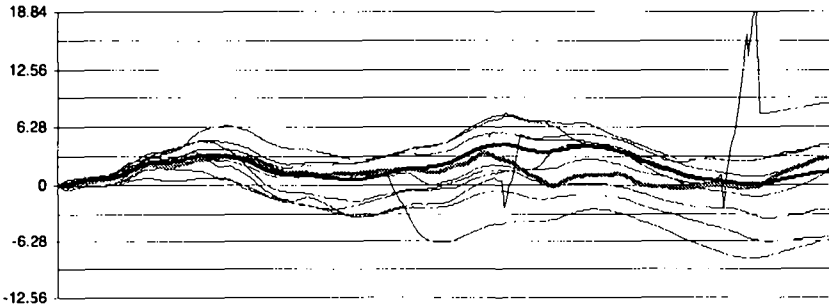


Figure 7-6. Phase evolution (in radians) of 9 adjacent pixels, after subtraction of a linear phase term. The thick black line corresponds to the best-estimate of the phase of the central pixel, calculated with the phase increments. The thick grey line corresponds to the weighted-average calculated with the phase values themselves.

We must emphasize here that the calculation of the weighted-average actually brings much more than just a noise filtering. As seen in Figure 7-6, the phase evolution of the central pixel is actually reconstructed in the region where the information is lost because of the modulation loss. This is very important since the interferogram modulation is susceptible to rise and drop randomly at each pixel during a speckle interferometry experiment where large decorrelations occur. In other words, we cannot expect a single pixel to have a high modulation for the complete duration of the measurement. However, there is a high probability to find at each instant at least one good pixel within a group of 9. Hence, combining 9 pixels largely increases the probability of performing a correct, continuous phase evaluation, which could not be obtained with single pixels.

Bibliography

- 1 D. Venet, "Techniques automatiques de raccordement de phase", Rapport de travail de diplôme, Université de Bruxelles, 1996.

8. Dynamic Phase-Shifting application examples

The purpose of this chapter is to present some results obtained by direct application of the dynamic phase-shifting principle. We first discuss the acquisition hardware (camera and phase-shifting devices) which was used for these experiments. Next, image sequences corresponding to holographic and speckle interferometry are processed in various ways, using the 5-image phase-shifting algorithm and the wavelet-based analysis. These two methods are compared when possible. This emphasizes their complementary nature. The optical arrangements used for these examples are described in Chapter 2.

8.1 Acquisition set-up

Since the various experimental optical arrangements are described in Chapter 2, we only discuss here the elements that are specific to dynamic phase-shifting measurements: the camera and the phase-shifting devices. The same digital CCD camera was used for all the examples of this chapter. However, alternative solutions exist to perform the digital recording of the image series. For example, our laboratory just bought an image acquisition board coupled to a dedicated hard disk array that permits to record 768×572 -pixel images at a rate of 25 images per second during up to eight minutes. We note also that commercial cameras are now available, for example the SpeedCam from Weinberger in Switzerland, which provides 1 kHz acquisition rate in a digital format. Such new systems can be used to observe much faster phenomena.

8.1.1 Hisis 2001 digital camera

This non-standard camera features a 512×512 -pixel frame-transfer CCD. Using this image resolution, sequences of 512 images can be recorded in a 128 MB memory buffer at a maximum rate of 160 images per second. The maximum

acquisition rate becomes 285 images per second when using a lower resolution of 256 x 256 pixels. 2048 images can be recorded in this case. The camera can also be externally triggered. This allows to adjust the acquisition rate with respect to the deformation speed of the object while providing at the same time a means to synchronize with the phase-shifting device used to create reference phase steps. However, the maximum rate is limited to 80 frames per second in this mode of operation. We can note incidentally that one problem with digital series of images is the huge storage space needed. The solution we adopted is to store these sequences on writable CDROM.

The Hisis camera presents distinct advantages compared to standard video cameras. First, the acquisition rate at full resolution is up to six times higher than the conventional 25 Hz rate. This rate can moreover be adjusted with respect to the particular requirements of a given experiment. The second important point is the digital nature of the recorded signal. The electrical charges accumulated in each pixel on the CCD are processed individually by fast analog-to-digital converters. The corresponding 8 bits digital values are then stored in the memory buffer. This must be compared to a usual image acquisition system where the charges of individual pixels are combined to create continuous lines of analog video signal. This video signal is then sampled and digitized by the acquisition board. Quite frequently, this board creates a number of pixels per line of video signal that is different from the number of pixels on a line of the CCD. This means that the charges of the original pixels are smoothed out and mixed, even in the absence of pixel-jitter (synchronization mismatch between the camera and the board). Moreover, the transmission of analog signals is always a source of noise because of antenna effects in the electrical cables. By contrast, the Hisis camera delivers an accurate sampling of the light intensity over a square grid.

This camera suffers from two limitations. First, the exposure time is fixed at 6.25 ms and 3.5 ms for the 512^2 and 256^2 resolutions respectively. Hence, we need to use a mechanical shutter to decrease the exposure time when needed. This is also a problem when we use the camera with a lower frame rate, in which case we would like sometimes to increase the exposure duration. This wish is actually a consequence of the second limitation, the low sensitivity of the device. The manufacturer data-sheet reports a sensitivity of "400 ISO", which is not a factor that we can easily compare with the energy values that we measure with optical powermeters. Anyway, if we compare the response of this camera to other state-of-the-art Sony CCD cameras, we observe that it requires about 4 times as much light. In other words, the lens aperture has to be increased by a

factor of 2. This will prove to be a problem as soon as we try to perform measurements on large surfaces with a limited amount of light.

However, despite these limitations, the Hisis camera has been an essential element in the investigation of the feasibility of dynamic phase-shifting. It moreover permitted to perform non-trivial demonstration experiments, as illustrated in the next paragraphs.

8.1.2 Production of a reference phase step

The interest of introducing a known phase step between the acquisition of successive images has been demonstrated in Chapter 4. It is a means to determine the absolute sign of the deformation while at the same time providing a carrier frequency for the wavelet analysis. Moreover, it allows to estimate the modulation of the interferogram in regions where the deformation is very slow. This helps to make a mask of the valid pixels in an image.

Different solutions to produce the required phase steps can be conceived: piezoelectric transducers (PZT), LCD cells, electro-optic phase modulators... However, we decided to use available PZT for our applications since the maximum frame rate of our camera is not very high (80 frames/s). The length of these PZT can be adjusted by varying the voltage applied to the piezoelectric stack. This is used to move precisely one of the mirrors located on one arm of the interferometric set-up, thus producing the required phase steps.

We actually use open-loop and close-loop PZT. In the open-loop case, the actual elongation of the PZT is not controlled when the applied voltage is changed. In this case, hysteresis effects lower the precision of the device. Additionally, if a rapid voltage transition is applied to the device, the mechanical inertia of the mirror increases the stabilization time of the PZT, resulting in a vibration of the mirror. The corresponding rise-time has been measured for PZT operating under various voltage ranges. To this end, we used a fiber Fizeau interferometer using a laser diode emitting at 1.5 micron. We adjusted the air gap between the reference end of the fiber and the mirror in order to observe the intensity variations of the interferometer where they are linear as a function of the phase. In other words, the air gap created a $\pi/4$ phase difference (at 1.5 micron) between the two interfering waves. We then applied repeated tension steps to the PZT to measure the time it takes the mirror to stabilize. The advantage of this set-up is the very short response time of the photodetector (<1 ns), which permits to observe the phase fluctuations with a high resolution.

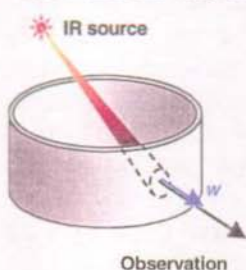
The best PZT available in the laboratory gave a stabilization time close to 20-30 ms. We next tested PZT driven in a feedback loop thanks to strain gages

glued directly on the element. These gages allow to measure the actual elongation and adjust the applied voltage to reach the target elongation value. The PZT we use in this case are manufactured by Physik Instrumente. Their rise-time of 6 ms is independent of the height or frequency of the voltage steps. Hence, we rather use these PZT when the acquisition rate of a given experiment is higher than 30 Hz. Standard PZT can be used without the feedback loop below this value. This permits to use cheaper and simpler electronics.

Alma di Tullio, a visiting scholar from the University of Cagliari in Sardinia, conducted the above study of PZT elements. She also developed a program to prepare and control an acquisition with the Hisis camera, synchronously with the phase stepper device. A custom electronic driver was built to this end. It receives the same trigger signal as the camera and creates the stepped analog voltage applied after amplification to the PZT.

8.2 Thermal loading of a carbon-carbon composite

This experiment was performed in the course of the evaluation of a low-thermal-expansion carbon-carbon composite structure manufactured by Aérospatiale for the European Space Agency. Such a structure would ultimately be used as the body of a lightweight telescope for optical communication between satellites. Our goal was to verify that thermally induced deformations were within the very small tolerances required for this application.



Real-time holography was used for this experiment. We present here the result of one measurement where the internal wall of the cylindrical structure is heated locally by an infrared lamp. The Hisis camera observes the external wall in the heated region. 512 images are recorded at a rate of 4 Hz. A PZT is used to introduce a $\pi/2$ reference phase step. Figure 8-1(a) and (b) show the interferograms recorded in the 3rd and 203rd images of the sequence. (b) actually corresponds to the instant

of maximum deformation along the observation direction (end of thermal loading). The phase of these interferograms is computed with the 5-image algorithm. The two wrapped phase maps are then subtracted modulo- 2π , as seen in (c). The greyed region in (d) is the part of the image that is unwrapped and presented in (e). Wavelet-based phase extraction is applied to the same pixel selection. This gives us an image of the absolute object deformation between images #3 and #203, see (f). The scale is the same in (e) and (f).

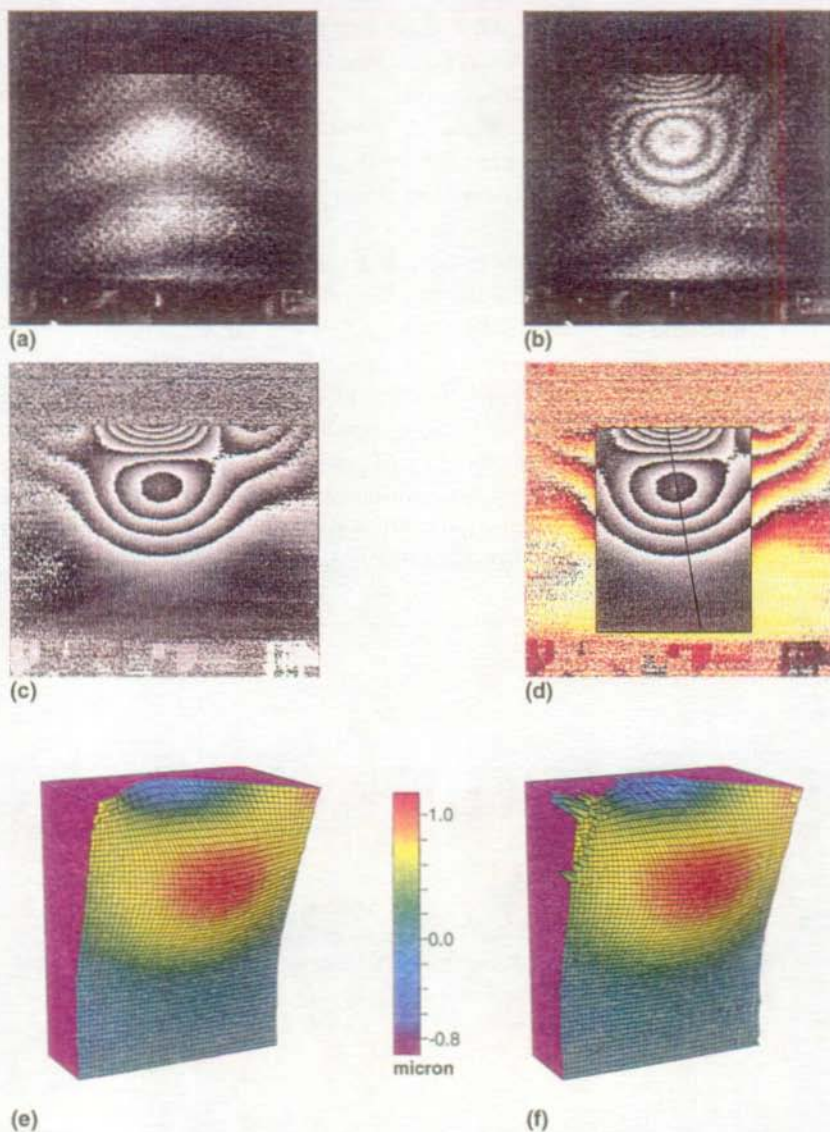


Figure 8-1. (a) and (b) interferograms #3 and #203; (c) wrapped phase map computed with the 5-image algorithm; (d) same as (c) with masking areas (see text); (e) and (f) deformation maps computed with the 5-image algorithm and the wavelet analysis, respectively.

It is important to recognize that the unwrapped phase map obtained from (c) is only a relative phase map. There is no information on the absolute deformation w of the object. In other words, we do not know where the points of zero deformation are in (e). In contrast, an absolute value is obtained with the wavelet processing. In particular, the maximum out-of-plane deformation is $1.16 \mu\text{m}$. This value can now be used to remove the ambiguity in (e) since the two maps are very similar.

The green dots that appear in the top-left selection region in (d) represent the pixels where the modulus of the wavelet transform along the ridge is lower than a threshold of 5 grey levels. These points are excluded from the final image, which creates the holes seen at the top-left of the surface shown in (f).

The two phase maps (e) and (f) differ at the top-center of the deformed surface. This is a consequence of errors committed during ridge extraction in this region. The transform of one of these pixels is shown in Figure 8-2. We observe two perturbed regions that correspond to the beginning and end of thermal loading (first third of the signal). The ridge extraction mistake creates a phase error of -2π , that is, an error of $-0.25 \mu\text{m}$ on the final deformation value.

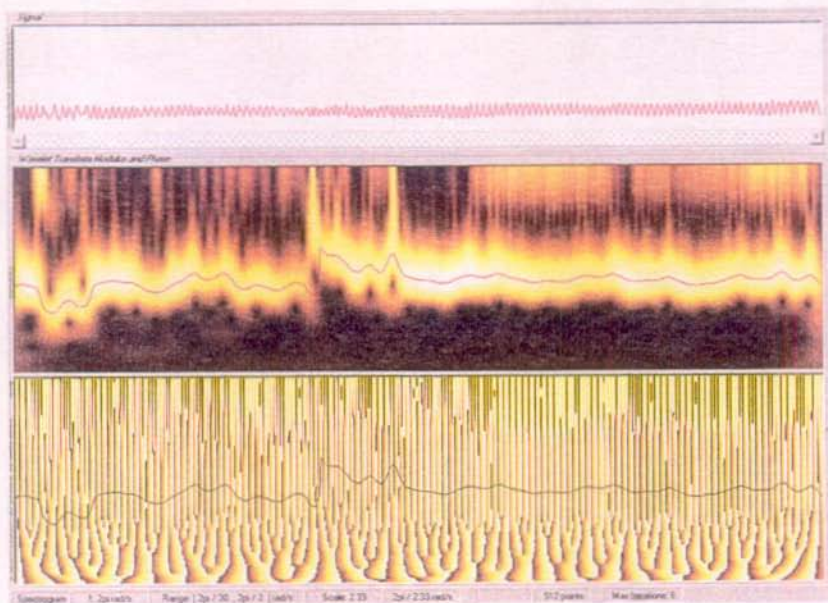


Figure 8-2. Ridge perturbations when the thermal load starts and ends. Pixel located at the top of the vertical line in Figure 8-1(d).

To conclude with this example we show another possible representation of the phase calculated with the wavelet transform. In this case, the deformation measured along a line of pixels is represented as a function of time. The selected pixels correspond to the vertical black line of Figure 8-1(d). We can observe the negative exponential relaxation of the object once loading has ended. Also, this representation shows that the structure's response to the load is very fast.

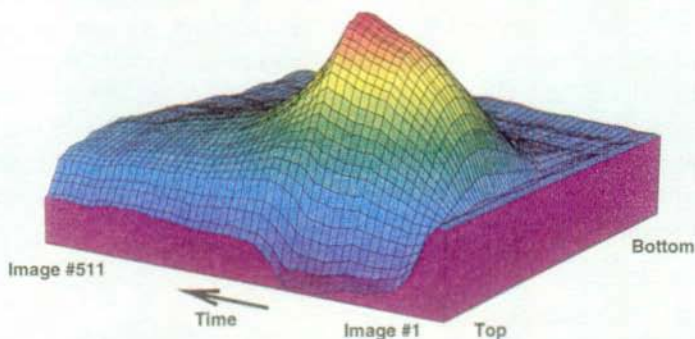
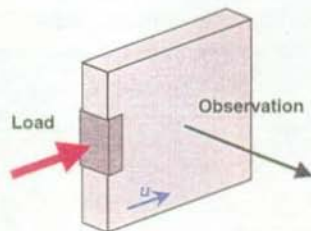


Figure 8-3. Deformation along the vertical line of Figure 8-1(d), plotted as a function of time. The deformation peak-valley is $2\ \mu\text{m}$.

8.3 In-plane horizontal deformation of a rubber element

This particular experiment was made up to test a demonstration model of the Hisis camera. It was actually our first application of the dynamic phase-shifting technique in the context of speckle interferometry. The object is a square piece of rubber, 60 mm on a side and 8 mm thick. It is loaded horizontally on one side by a long-range PZT. An in-plane speckle interferometer is used to measure the object displacements in the horizontal direction u . The sensitivity of the set-up is $0.5\ \mu\text{m}$ per fringe. A sequence of 128 images is recorded at 20 Hz while a voltage ramp is applied to the loading PZT. A reference phase step of $\pi/2$ is also introduced by a second PZT located on one illumination beam of the interferometer.



The random wrapped phase map of image #10 is computed with the 5-image algorithm and subtracted from the random phase map of image #120,

obtained in the same way. This image is then low-pass filtered once in the sine and cosine domain. The final result is shown in Figure 8-4. We see that the fringes do not have the same quality to the left and right of the object. There are two reasons for this. First, one camera pixel covers about 0.17 mm on the object. The total displacement at left is close to 12 μm , which represents 7% of image plane decorrelation during the experiment. The displacement is only 2 μm at right and results in a negligible decorrelation. The second cause for the lower quality at left is the instantaneous phase increment value $\Delta\phi$, which is higher than $3\pi/4$ (145°) in this region. As seen in Chapter 5, such values are not optimum for the algorithm and more phase errors are committed. In contrast, $\Delta\phi$ is on the order of $2\pi/3.44$ (105°) at the extreme right of the selection, which is much closer to the optimum of $\pi/2$. It must be emphasized again that these *absolute* displacement values are obtained by application of the wavelet processing. The 5-image algorithm only yields the *relative* displacement between points on the object.

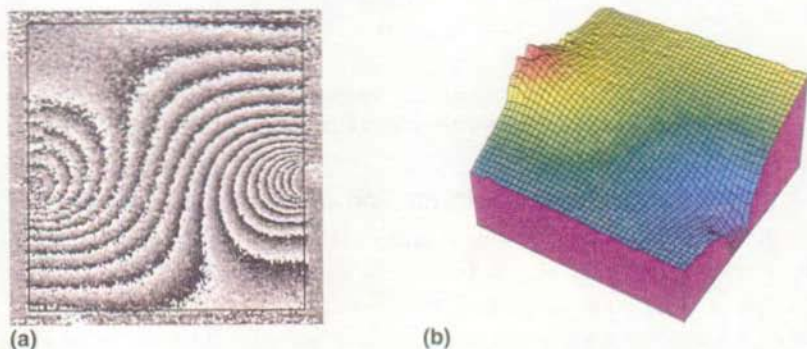


Figure 8-4. (a) Wrapped phase map of the horizontal in-plane deformation, computed with the 5-image algorithm; (b) Unwrapped phase map of the region delimited in (a). The deformation peak-valley is on the order of 10 μm .

Once we apply the wavelet processing to the image sequence we obtain a second evaluation of the deformation that occurred between images #10 and #120. As mentioned above, this time the results are absolute displacement values. This new information is then used to give an absolute scale to Figure 8-4(b) (this point is discussed later in the text), which permits to compare the two displacement maps. They are presented in Figure 8-5 with a new color scale to emphasize their differences.

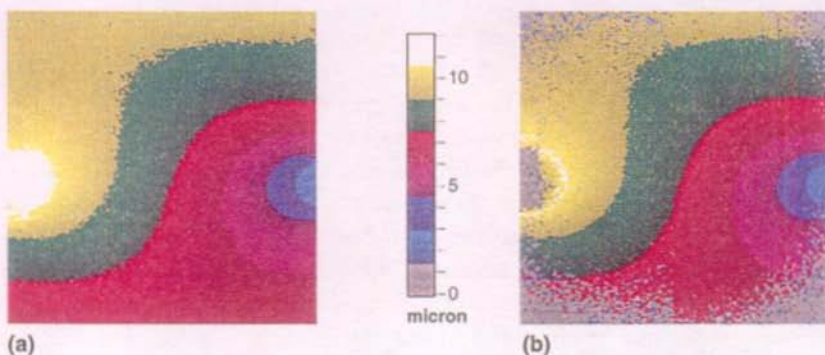


Figure 8-5. (a) Absolute deformation map obtained with the 5-image algorithm (after offset correction); (b) Corresponding map obtained with the wavelet processing. Insufficient pixel modulation is represented as grey dots.

The first observation is that analysis is not possible in some regions of the interferogram in the wavelet case (see Figure 8-5(b)) for lack of sufficient pixel modulation. The threshold used in this case is 5 grey levels. The shape of the region where pixels are eliminated is roughly circular. This corresponds to the intensity variations of the Gaussian laser beams that illuminated the object. Some pixels are also discarded at the left edge of the image. The reason is that the instantaneous frequency of the signal in this region gets close to the Nyquist cut-off frequency, which prevents a successful ridge extraction. Such signals were used in Chapter 6 to illustrate this problem. One possible solution, complex signals, is also proposed in Chapter 9 where the same example is used.

The difference between the two phase maps of Figure 8-5 is presented in Figure 8-6(a). The scale in this figure covers $0.25 \mu\text{m}$ or half a fringe. The pixels that sit outside of the range $[-0.125, 0.125 \mu\text{m}]$ are discarded. The image appears to be made of two halves with a distinct boundary. This is actually due to a miscalibration of the amplifiers used in the camera. This effect could also be observed with incoherent light. It is probably a third cause of the noise observed in Figure 8-4(a).

We can compute the same difference with the initial unwrapped phase map of Figure 8-4(b), where the fringe order has been arbitrarily chosen by the unwrapping algorithm. This simply shows that an offset of about $8.45 \mu\text{m}$ needs to be added to this map to obtain absolute deformation values. We note that 98.2% of the values of the difference between the 5-image and wavelet phase maps fall within the range $[8, 8.8 \mu\text{m}]$. The points discarded during the wavelet

processing are not taken into account in this estimation. The histogram of the points located in the range $[8.2, 8.7 \mu\text{m}]$ is given in Figure 8-6(b). The distribution of the difference has an average value of $8.44 \mu\text{m}$ and a standard deviation of $0.05 \mu\text{m}$. This last value corresponds to one tenth of a fringe or 36° . A Gaussian fit gives a slightly smaller deviation and an average of $8.45 \mu\text{m}$.

One observation can be made regarding this last result. In principle, the phase obtained with the two methods should be exactly equal up to the addition of an integer number of 2π radians. In other words, the offset that we can estimate with Figure 8-6(b) should be an integer number of $0.5 \mu\text{m}$ (one fringe). In our case we find an offset of $8.45 \mu\text{m}$. Hence, there is a deviation of about $0.05 \mu\text{m}$ with respect to the closest value of $8.5 \mu\text{m}$. This corresponds again to an error of one tenth of a fringe. Its origin lies probably in the frequency variation created at the beginning of the recording when the loading began. We know from Chapter 6 that an absolute phase error is obtained in this case with the wavelet phase extraction (this is due to the second derivative of the phase of the signal).

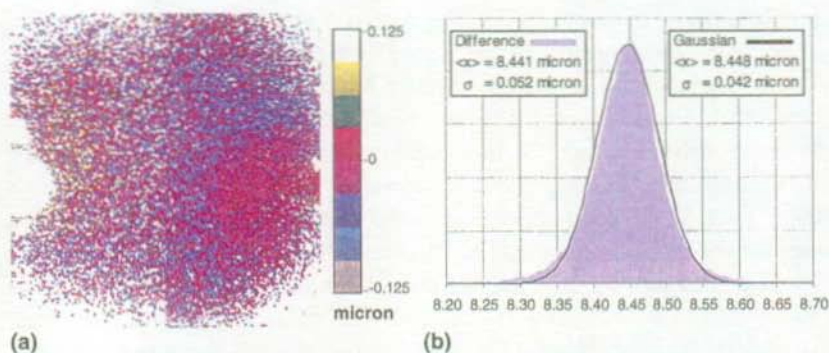


Figure 8-6. (a) Difference between Figure 8-5(a) and Figure 8-5(b); (b) Histogram of the same difference without addition of the absolute offset for the phase map obtained with the 5-image algorithm.

This preliminary experiment gave us much more information than we initially planned. We see that a careful processing shows a good agreement between the two methods with a discrepancy on the order of one tenth of a fringe. This remaining error cannot be pinned down directly on one method or the other. Further interpretation would require to estimate the noise distribution in both Figure 8-5(a) and Figure 8-5(b). However, a visual comparison of the wrapped phase map of Figure 8-4(a) with a wrapped phase map created from

Figure 8-5(b) shows that much less noise is obtained with the wavelet processing, as illustrated in Figure 8-7.

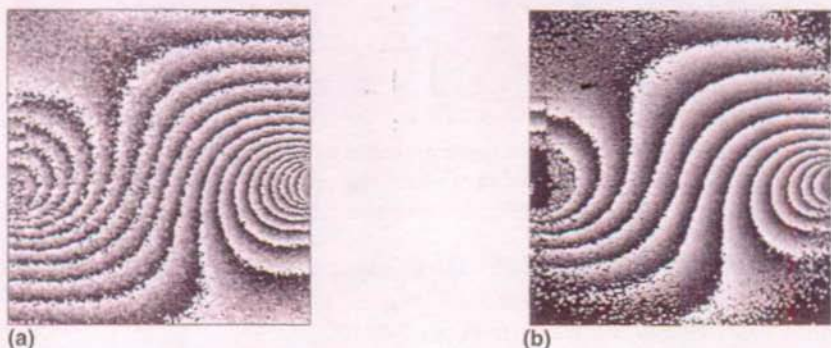
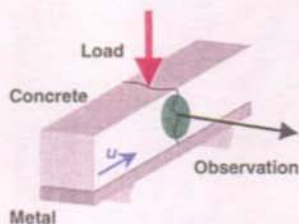


Figure 8-7. (a) Wrapped phase map obtained with the 5-image algorithm; (b) Less noisy wrapped phase map obtained with the wavelet transform.

8.4 In-plane horizontal deformation of a concrete beam

This second in-plane experiment was conducted on a small concrete beam that had been previously fractured. The concrete was actually poured in a box with one metallic wall that remained glued to the final beam, about $1 \times 0.15 \times 0.15$ m large. The experiment described here presents a limited interest for the civil engineer since the beam had already been ruptured but it was useful to test the dynamic phase-shifting method in "adverse" conditions.



We performed a measurement of the in-plane displacement of a region located near one large fracture. The set-up sensitivity was $0.93 \mu\text{m}$ per fringe. Because the loading jacks produced a lot of vibrations when a force was applied, we ended up measuring the displacement when the force was diminishing, simply by letting the pressure drop in the hydraulic circuit. The

acquisition was performed at 40 Hz with a feedback-loop PZT producing the reference $\pi/2$ step. We later discovered that the small solid-state laser induced vibrations in the interferometer. This created beam-pointing instability and periodic intensity fluctuations in the images as illustrated in Figure 8-8. A second problem with this experiment was the large vertical displacement of the object during unloading. This ultimately created a large speckle decorrelation.

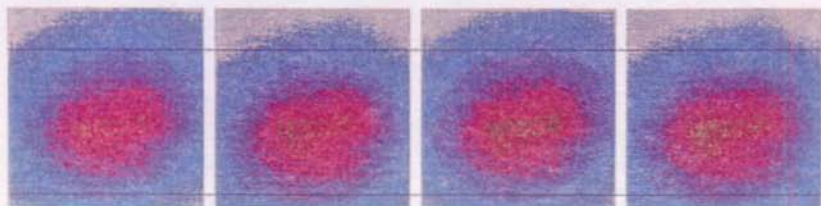


Figure 8-8. 4 successive images recorded with the Hisis camera. The intensity fluctuations are due to vibrations created by the laser. Black lines are added to emphasize the beam vertical movement.

We can first try to process the image sequence with the 5-image algorithm. Hence, we compute the wrapped phase maps of image #3 and image #503. Their difference modulo- 2π is shown in Figure 8-9(a).

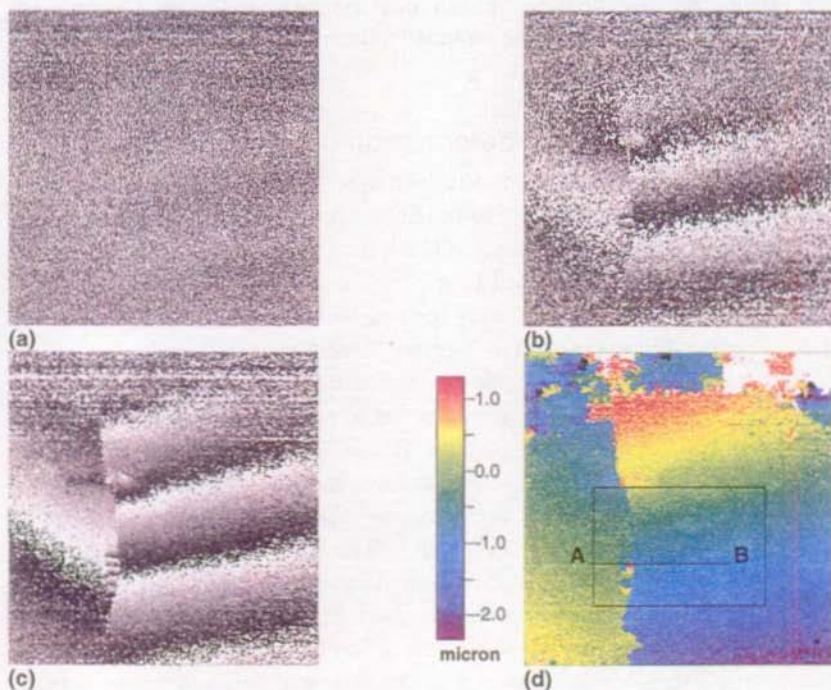


Figure 8-9. (a) Direct subtraction of the wrapped phase map of images #3 and #503; (b) Same calculated as a sum of filtered incremental steps; (c) Same after vertical translation by one pixel of the random phase map of image #3; (d) Unwrapped version of (c).

The effect of the image-plane decorrelation is obvious here: the fringes are barely visible. Since a direct subtraction gives such a poor result, we can try to compute wrapped phase increments, filter them and finally sum them modulo- 2π . The image shown in Figure 8-9(b) was obtained this way with a step of 100 images. In other words, the wrapped phase maps of images #3, #103, #203, #303, #403 and #503 are computed. Next, we filter in the sine and cosine domain the differences #103-#3, #203-#103... #503-#403. These differences are then added. The idea here is to filter most of the phase error induced by the decorrelation before it becomes too large, that is, larger than π . The improvement due to this procedure is striking when (a) and (b) are compared.

An even better result can be obtained in the particular case of this measurement since the vertical image-plane translation of the speckle field is on the order of 1 pixel. This value is actually obtained by trying different possibilities. This is a simple process where the wrapped phase map #3 is translated by 1 pixel in every direction before being subtracted from the phase map #503. Fortunately in this case the overall displacement is close to one integer pixel (the worst case would be a displacement of 0.5 pixel) and the resulting fringe pattern is quite nice after filtering (see Figure 8-9(c)). The fringes actually disappear at the top of the images because of insufficient object illumination.

If we look more closely at Figure 8-9(c) we can observe a crack that runs through the whole height of the object. Hence, there is no information on the relative fringe order of the two regions it separates, since there is no physical path between them on the specimen surface. Moreover, their absolute displacement is also unknown. Therefore, the unwrapped phase map in Figure 8-9(d) relies on an arbitrary choice of fringe orders. Actually, the unwrapping algorithm uses a phase "valley" to cross the crack and the resulting relative position of the two areas is meaningless. We can also note a small independent region in (c), near the middle of the crack. The horizontal equispaced fringes that cover it indicate a pure in-plane rotation during the experiment. This region is also incorrectly unwrapped in (d).

We can now try to apply the wavelet processing to the image sequence. We first extract the phase of the pixels located along the black horizontal line AB drawn in Figure 8-9(d). The mother wavelet frequency is 4π for this calculation and pixels of modulation lower than 3 grey levels are discarded. The phase best-estimate is used to show the evolution of the phase along this line as a function of time. A few pixels had to be interpolated from their neighbors to obtain the final curve shown in Figure 8-10.

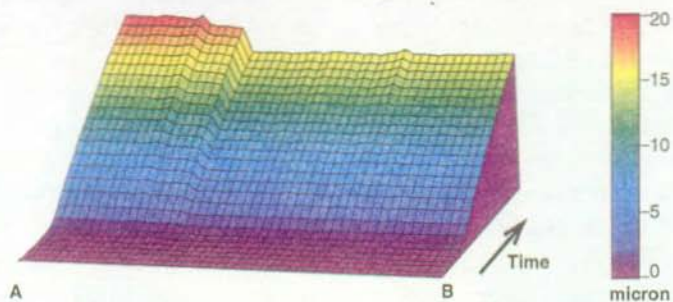


Figure 8-10. Absolute displacement measured along line AB of Figure 8-9(d), plotted as a function of time.

This figure illustrates again one main feature of the wavelet processing, namely, the calculation of absolute phase values. A horizontal displacement is positive when going from left to right in our images. The figure above shows that the specimen region located to the left of the crack moves by $20\ \mu\text{m}$ to the right. At the same time, the part located to the right moves by about $16\ \mu\text{m}$ in the same direction. Hence, we deduce that the crack width decreases by about $4\ \mu\text{m}$. This fits very well with the fact that the concrete beam moves up when the load is decreased, which results in a decrease of the tensile stress in the lower part of the sample and consequently a closing of the cracks. We can also remark in this figure the intermediate step that separates the two main regions. This corresponds to the small independent area mentioned earlier.

It must be emphasized here that we get a wealth of information from the wavelet processing, even though an almost total image-plane decorrelation is introduced during the experiment. Moreover, if we actually look at the pixel temporal signals, we observe that they have on average a very low modulation and that the intensity fluctuations shown in Figure 8-8 affect significantly the wavelet transform. This is illustrated in Figure 8-11 where one typical signal measured on the line AB is shown with the modulus of its transform. Needless to say, many ridge extractions fail and the use of the phase best-estimate is necessary to create the often missing information.

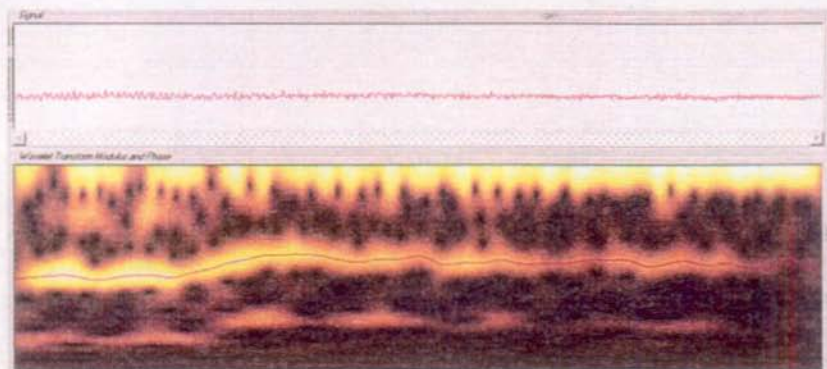


Figure 8-11. Signal and its transform for a pixel located to the right of the crack, on the line AB.

To conclude with this example we process the area delimited with a black rectangle in Figure 8-9(d) since the interferogram modulation is higher in this region. The final displacement map is shown in Figure 8-12(a) where the scale has been adjusted to show the displacement gradient in the two regions of the image. It is also possible to subtract the unwrapped phase map of Figure 8-9(d) to compare the gradients obtained with the 5-image algorithm and the wavelet processing. The difference is presented in Figure 8-12(b) with the same scale.

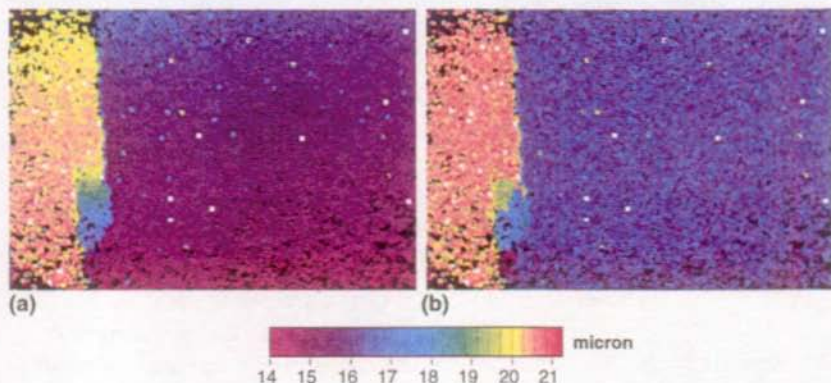


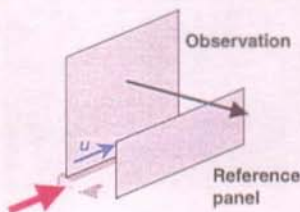
Figure 8-12. (a) Absolute in-plane displacement obtained with wavelet processing; (b) Same after subtraction of the unwrapped phase map obtained with the 5-image algorithm (Figure 8-9(d)).

We get additional information in Figure 8-12(a). In particular, it permits to understand the pure in-plane rotation of the small independent region located next to the crack. We observe that its top, respectively bottom extremities move by the same amount that the left, respectively right part of the specimen. This creates a clockwise rotation of the region, additionally to an average horizontal displacement of about $18 \mu\text{m}$.

The observation of Figure 8-12(b) shows that the two independent phase measurements using the 5-image algorithm and wavelet processing give the same displacement gradients in the two parts of the specimen. The remaining displacement offsets of these areas are due to the arbitrary fringe orders chosen during spatial unwrapping of the phase map shown in Figure 8-9(c). However, much more information was gained by application of wavelet processing. It is important to emphasize that an accurate absolute measurement is obtained in this last case, despite a large decorrelation added to intensity perturbations. This speaks well for the robustness of the technique in adverse conditions.

8.5 Measurement in the case of total decorrelation

The preceding example showed that an absolute phase measurement is still possible with the wavelet processing in the case of decorrelations. To further test the method we devised an experiment where image-plane decorrelations are much larger. This time, a rough metallic surface is translated at a constant speed in front of the speckle interferometer sensitive to the horizontal in-plane displacement. A 100 mm macro-objective is used to image the diffusing object on the CCD of the Hisis camera. The corresponding magnification is close to -1.125 . A motionless reference diffuser occupies a part of the field of view. It is used to detect possible drifts of the set-up. A sequence of 512 images is recorded at 160 Hz without introduction of a reference phase step. The translation speed of the object is adjusted to produce a carrier frequency close to $\pi/2$. The in-plane sensitivity of the interferometer is $0.65 \mu\text{m}$ per fringe. The total displacement measured by the translation stage controller is on the order of $70 \mu\text{m}$ but this is not a very precise estimation since the motor is manually triggered during the image acquisition. Actually, the number of fringes that pass in the interferometer rather indicate a movement of about $65 \mu\text{m}$ (100 fringes).



Since all points on the moving diffuser undergo the same in-plane translation, their phase changes at the same rate. Hence, the total phase variation measured at each pixel should be exactly the same at the end of the experiment. However, as explained in Appendix A, the large in-plane decorrelation of the speckle field introduces phase errors that are accumulated during the experiment. In this example, a camera pixel is about $17.5 \mu\text{m}$ wide. The image-plane displacement is thus larger than 4 pixel widths.

We can try to use the 5-image algorithm to estimate the relative phase fluctuations of the different pixels. Of course, a direct subtraction of the wrapped phase maps calculated at the beginning and end of the image sequence is useless. We must first translate one phase map with respect to the other to recorelate the images. This is done manually until the best visual fringe pattern is obtained. In this case, a horizontal translation of 5 pixels gives the best result. The corresponding phase map is shown in Figure 8-13(a), after low-pass filtering in the sine and cosine domain. It must be emphasized that this manual recorelation is possible only because we are in presence of a large but simple image-plane decorrelation. A pupil-plane decorrelation would actually change the microstructure of the speckle field in the image plane and the operation described here would be totally useless. However, from the point of view of the phase fluctuations of a pixel's signal, the result would be strictly the same. Consequently, a wavelet-based processing is equally "affected" by image-plane or pupil-plane decorrelations. The purpose of this example is to show that this type of processing actually permits to get rid of most phase errors.

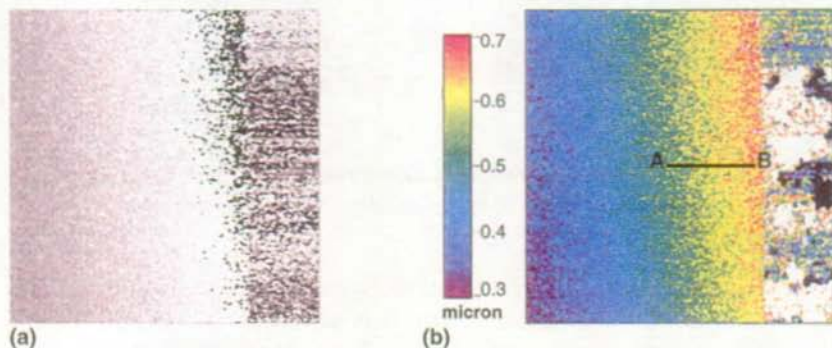


Figure 8-13. (a) Wrapped phase map obtained after recorelation; (b) Unwrapped phase map showing a small displacement gradient.

The observation of Figure 8-13(a) shows that there is a small phase gradient of about π radians between the recorrelated phase maps. The random band on the right is due to the motionless reference plate. The camera is rotated to the right in these images, hence the horizontal reference plate appears vertical. Since the moving plate is not deformed during this experiment we can readily interpret the observed phase gradient as the result of a small in-plane rotation, due to imperfections of the translation stage. The field of view covers about 6 mm on the moving plate and the difference of displacement in Figure 8-13(b) is close to $0.4 \mu\text{m}$. Hence, we can estimate the rotation to be on the order of $67 \mu\text{rad}$, which seems to be quite reasonable for a mechanical translation device.

We can now apply the wavelet-based processing to this image sequence. Since there are phase fluctuations due to the decorrelation, it is interesting to compare the result of the processing with and without the calculation of the phase best-estimate. This is done in Figure 8-14 where the temporal phase evolution along the line AB of Figure 8-13(b) is plotted as a function of time. We use a banded look-up-table to emphasize the difference between the two results.

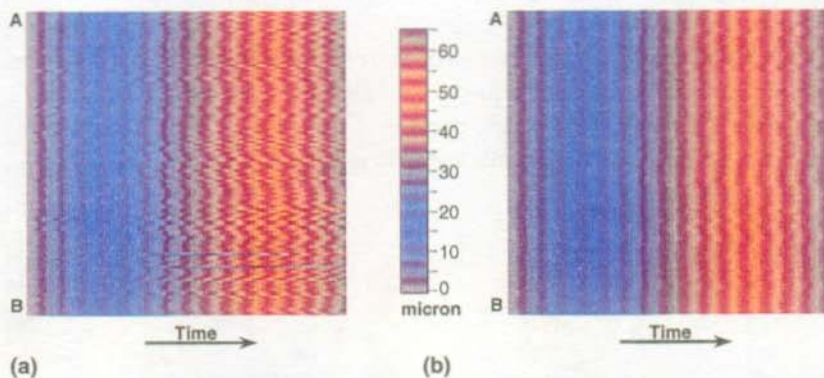


Figure 8-14. (a) Phase evolution along the line AB as a function of time. Direct wavelet processing. (b) Same after best-estimate phase evaluation.

These figures show first that the overall horizontal displacement of the plate is close to $65 \mu\text{m}$. Second, the effect of the best-estimate calculation is evident in (b) where the phase evolution of each pixel is much closer to that of its neighbors.

We next process the whole part of the image that corresponds to the moving surface. We obtain the displacement map shown in Figure 8-15(a). The scale is adjusted to show the effect of the remaining phase fluctuations once the best-estimate has been computed. We observe a small displacement gradient as was the case for the image obtained with the recorrelated 5-image algorithm.

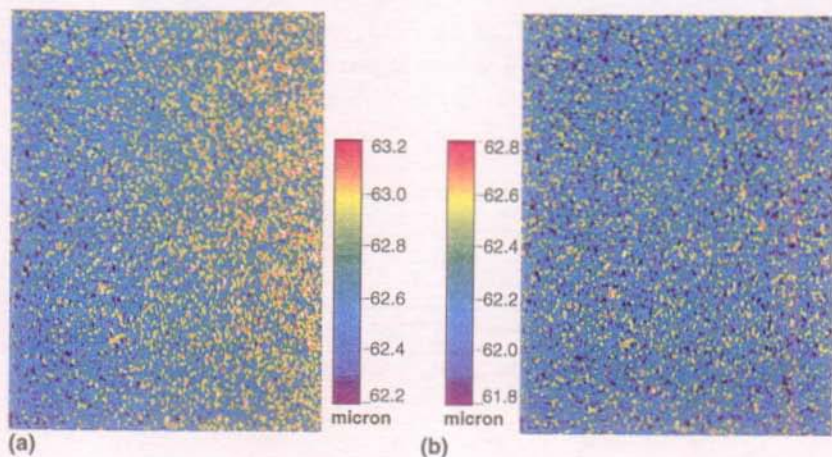


Figure 8-15. (a) Absolute displacement map of the moving plate, calculated with the wavelet processing; (b) Same after subtraction of the left part of Figure 8-13(b).

The image presented in Figure 8-15(b) is obtained after subtraction from (a) of the unwrapped phase map shown in Figure 8-13(b). Again, the uniformity of the resulting image illustrates the very good agreement between the two methods, within the remaining noise level. The average value in Figure 8-15(b) is $62.2 \mu\text{m}$ and the standard deviation is $0.2 \mu\text{m}$. The distribution is moreover perfectly Gaussian. The relative error committed on the estimation of the plate displacement is only 0.3%, which is quite impressive. Such a precision might not always be obtained if the overall displacement is small with respect to decorrelations. For example if the plate moves by a small amount in the horizontal direction and by a large amount in the vertical direction, larger errors will be induced. Nevertheless, the important fact is that a decorrelation does not prevent from performing a measurement with the wavelet-based processing, it is only another source of inaccuracy. The wavelets indeed perform very well in this experiment where the equivalent decorrelation amount is "500%". In contrast, a method that relies on the creation of fringe patterns, like usual

phase-shifting techniques, will fail completely as soon as say 100% decorrelation is attained.

We can further investigate the effect of speckle decorrelation. First, it is interesting to look at the signal of two close pixels located in the center of the image. As seen in Figure 8-16, one can estimate that about 95 and 93 fringes pass in these signals. Since we know that this is not due to a different geometrical displacement, we have here a good example of the phase error induced by a decorrelation. We observe in particular one or two regions where the modulation drops sufficiently that an educated guess is required to estimate the actual phase evolution.

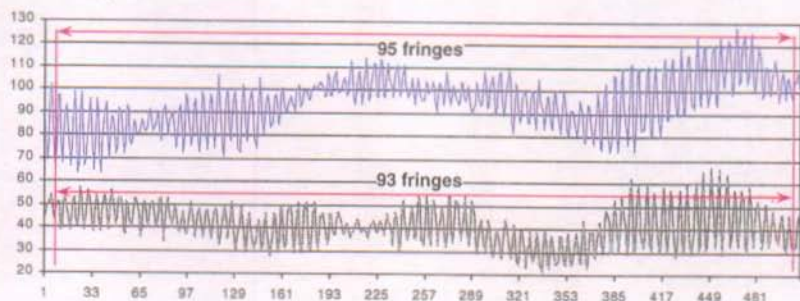


Figure 8-16. Signal of two pixels located 5 pixels apart. Different numbers of fringes pass during the experiment.

We know that large phase errors are possible when the signal modulation becomes small (see Appendix A). The above figure confirms it. We can go one step further by computing the phase evolution of 9 pixels, computing the phase best-estimate for this group and looking at the phase deviation of individual signals with respect to this reference. We can plot this deviation in a polar diagram showing at the same time the instantaneous phase deviation (angle) and modulation (vector length) of the signal. We actually obtain the trajectory of the tip of the modulation vector I_M described in Appendix A. The three trajectories shown in Figure 8-17 represent an estimation of the random phase contribution of the decorrelation. In (a) a complete revolution is made around the origin (center of the graph). Hence, an error close to 2π is created at this pixel over the whole experiment. The excursion is smaller in (b) where the total deviation is less than a fourth of a fringe. (c) is more complicated and the size of this figure does not permit to see clearly the end result. Actually, an enlarged figure would show that the accumulated error amounts to $-2\pi/3$ at the end of the experiment, while the largest deviation is $-3\pi/2$.

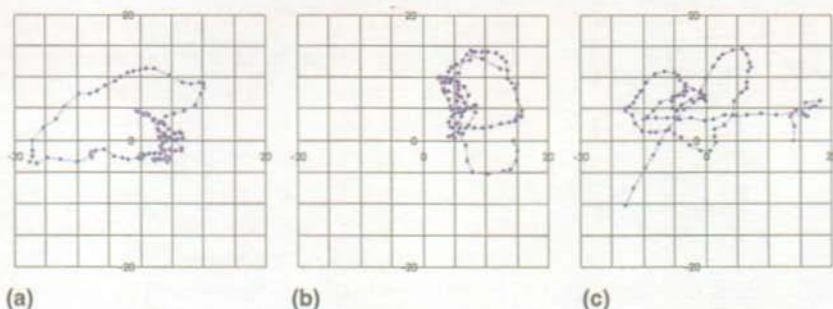


Figure 8-17. (a), (b) and (c): polar diagrams showing the evolution of the phase deviation and modulation of 3 pixels. Both horizontal and vertical axes cover the interval $[-20, 20]$, measured in grey levels.

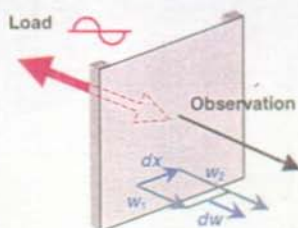
One must however be careful in the interpretation of these diagrams since the largest phase deviations are obtained when the modulation is close to 0 and this is precisely the situation where the ridge extraction becomes difficult. Hence, we cannot rely on the wavelet processing to measure exactly the phase errors due to decorrelations. Only a qualitative behavior can be deduced from these graphs.

As a conclusion to this example, we emphasize the fact that very large decorrelations do not prevent a correct phase extraction with the wavelet processing. In particular there is no need to try to recorrelate images obtained at different time instants. Moreover, image-plane or pupil-plane decorrelations are equivalent error sources from the point of view of the temporal phase extraction. This is another argument in favor of the wavelet technique for performing continuous deformation measurements in presence of large displacements, which usually result in large speckle field movements and decorrelations.

8.6 Cyclic loading measured with pulsed shearing speckle interferometry

This last example was recorded in the laboratory of Holo3 (Saint-Louis, France). The initial goal was to test the combination of the Hisis camera with a pulsed laser in dynamic phase-shifting conditions. The repetition rate of the doubled Nd:YAG laser is 25 Hz, which defines the acquisition rate for these measurements.

We present here the result of an experiment where a clamped metallic plate is loaded cyclically in its center. The load is actually created by a 0.1 mm-range PZT to which a 0.5 Hz alternative voltage is applied. The actual amplitude of



deformation is close to $19 \mu\text{m}$. A Michelson interferometer placed in front of the observation objective creates the image shear required in shearography. One of the mirrors is mounted on a small PZT to introduce the $\pi/2$ reference step. We recall from Chapter 2 that a shearing speckle interferometer is sensitive to differences of displacement. In the case of this experiment, the image shear is horizontal. The phase change in the interferometer is proportional to the difference of out-of-plane displacement $dw = w_2 - w_1$ of object points distant by a quantity dx . The field of the camera covers the 30×30 cm plate and the 5-pixel shear corresponds to $dx \approx 2.9$ mm on the object.

In order to choose the images where the deformation is maximum we first process the signal of a pixel located halfway between the center and right edge of the plate. The corresponding wavelet transform is shown in Figure 8-18.

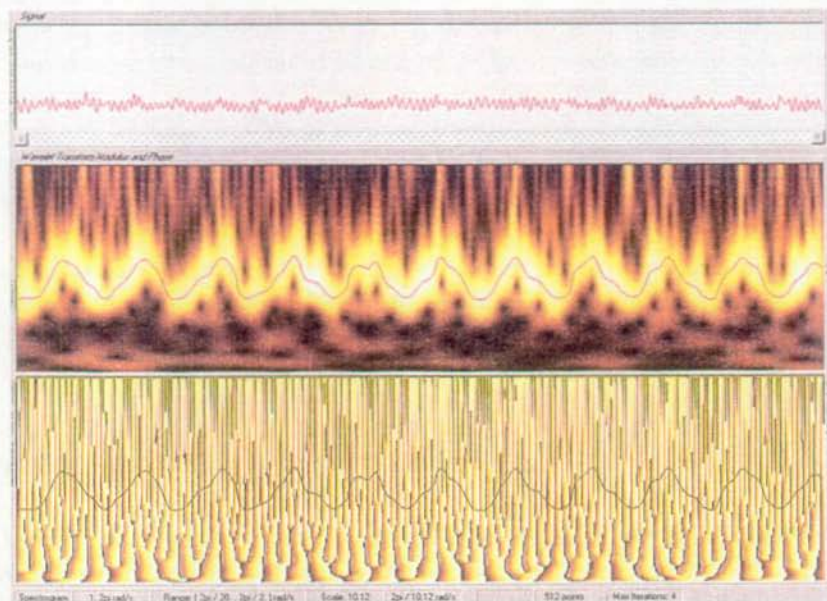


Figure 8-18. Wavelet transform of the signal recorded at one pixel.

We observe that the instantaneous frequency varies cyclically. About ten and a half periods are present in the image sequence, which corresponds to the 0.5 Hz cyclic loading observed at 25 Hz during 512 images. We can also plot the phase

of the interferogram measured along the transform's skeleton after removing the $\pi/2$ rad/s carrier frequency. This is presented in Figure 8-19.

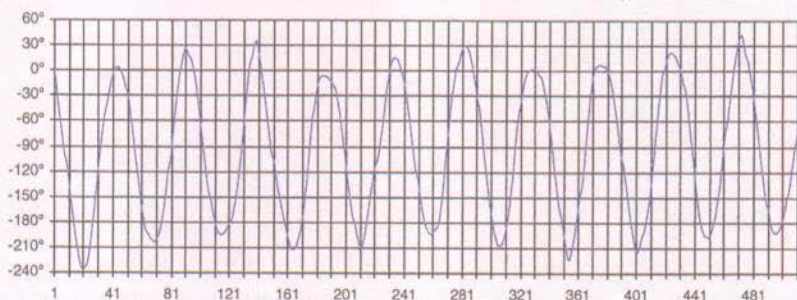


Figure 8-19. Phase variation measured along the ridge of Figure 8-18.

The initial phase of this signal has been arbitrarily fixed as 0. The next step is to compute the phase of a horizontal line of pixel, passing in the middle of the object. This yields Figure 8-20 below.

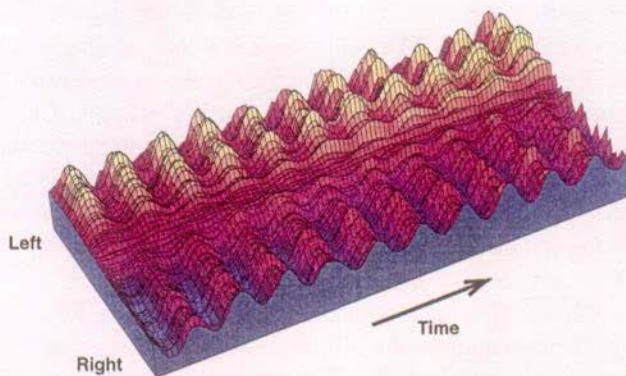


Figure 8-20. Phase evolution measured along a horizontal line of pixels, plotted as a function of time. Peak-valley is about 6π rad.

We present phase values in these graphs. Actual displacement values would be obtained by integrating the measured phase along horizontal lines of the image. The interpretation of Figure 8-20 is interesting. The cyclic loading of the plate creates a bump of varying height on its surface. Since the interferometer is sensitive to differences of displacement along horizontal lines, this difference is

positive, respectively negative, to the left, respectively right, of the image when a positive bump is created (positive is along the observation direction). This is sketched in Figure 8-21.

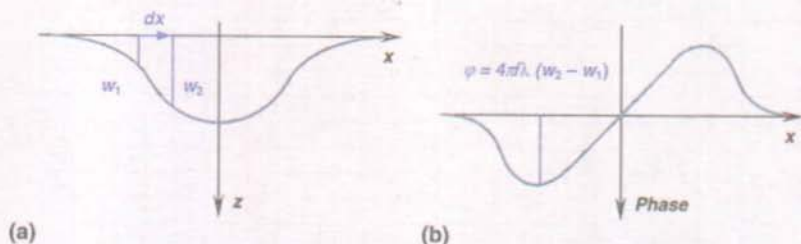


Figure 8-21. (a) and (b): Object out-of-plane displacement and corresponding phase variation.

The starting point of the image recording is not synchronized with the plate excitation but, fortunately, the sequence presented here started when the plate was in its flat initial state. Hence, the phase measured to the left of the bump varies sinusoidally between a maximum positive value and zero while the phase measured to the right varies between zero and a maximum negative value.

We can see in Figure 8-20 that the phase evolution of some pixels starts to diverge near the end of the sequence. This corresponds to ridge extraction errors around phase dislocations. This particular point is detailed in Chapter 9. The result is usually the addition or subtraction of exactly 2π to the measured phase. Actually, the processing of this image sequence is quite demanding since the phase of the interferogram comes back to zero periodically, which underlines particularly the accumulated phase errors.

Since there is no decorrelation in this experiment, we can compute phase differences with the 5-image algorithm. This is done in the following figures. We compute the random phase map of image #3, which acts as the reference of deformation. Next, we calculate the phase maps of images #21 and #451, which correspond to two instants of maximum deformation of the plate, as seen in Figure 8-19. The difference with the phase reference is presented in Figure 8-22. These images are obtained after subtraction of the number of $\pi/2$ phase steps corresponding to their index in the image sequence.

A limited number of fringes actually appear as the shear of the interferometer is small, resulting in a low sensitivity of the interferometric set-up. We note also that the phase is zero at the position to the center of the bump. The unwrapped versions of these images are presented in Figure 8-23.

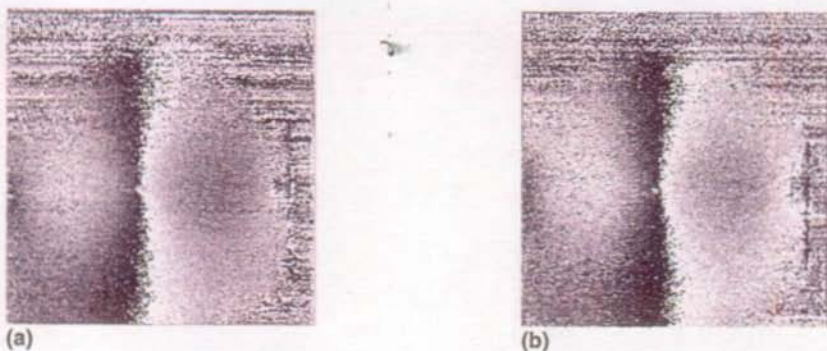


Figure 8-22. (a) Wrapped phase map measured between images #3 and #20 with the 5-image algorithm; (b) Same between images #3 and #450. Both images are shown after correction of the reference step.

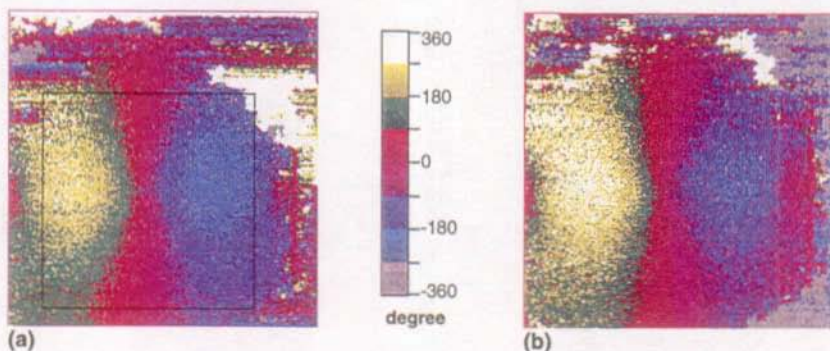


Figure 8-23. (a) and (b): unwrapped versions of Figure 8-22(a) and (b).

Applying the wavelet processing to the area delimited in Figure 8-23(a) we obtain the absolute phase maps shown in Figure 8-24. Images (a), (c) and (e) correspond to images #21, #261 and #451, where the phase should be close to its maximum value. Images (b), (d) and (f) correspond to images #41, #281 and #471, where the phase should be close to zero everywhere. This example is actually the most disadvantageous application of wavelet processing since it cannot profit from one of its most important strengths, which is the ability to accept many passing fringes (hence the small relative errors). Consequently, the effect of accumulated ridge extraction errors is visible in these images. However, the general evolution of the interferogram is still clearly visible. One must also note that the images chosen here do not strictly correspond to the two extreme positions of the plate since the oscillation period is not exactly 0.5 Hz.

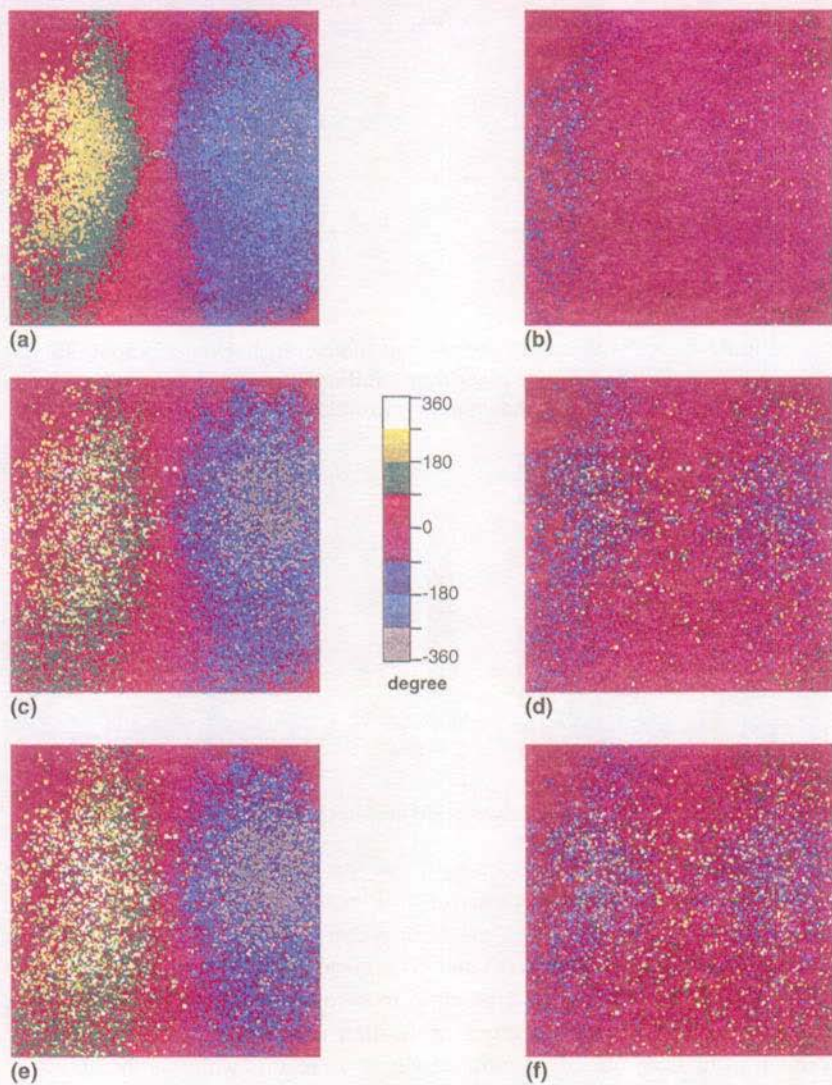


Figure 8-24. (a), (c) and (e): phase values obtained near the maximum deformation in image #21, #261 and #451; (b), (d) and (f): phase values obtained close to the minimum deformation in image #41, #281 and #471.

8.7 Final observations

The first conclusion obtained from these examples is that a wealth of information is contained in image sequences recorded in dynamic phase-shifting conditions. We have seen that we can exploit part of it through a “spatial” method, the 5-image algorithm, or through a temporal method, the wavelet processing. We showed repeatedly that both methods agree very well with one another, in terms of wrapped or unwrapped phase maps. This is very important since in one case only two groups of 5 images are used while the whole sequence is used in the other. Hence, the reliability of both techniques has been amply demonstrated. In particular, no phase errors are accumulated in the wavelet case, apart from integer numbers of 2π .

We did not attempt to process the image series temporally with the 5-image algorithm because experience showed us that phase errors are repeatedly introduced along the time dimension. Any modulation loss or phase perturbation of the phase of a pixel is susceptible to cause errors that are difficult to detect when performing the temporal unwrapping. In contrast, wavelet processing appears to be quite robust with respect to intensity noise, phase perturbations and modulation losses. In particular, the combination of the phase of different pixels permits to interpolate the actual phase evolution of a poorly modulating pixel. Taking the best from both the 5-image and wavelet approaches is indeed possible. We will see in Chapter 9 that the 5-image algorithm can be used to work on temporal signals when combined with a preliminary wavelet processing. This is actually one solution to eliminate the phase error caused by the second derivative of the signal’s phase.

As a concluding point we want to emphasize the particular properties of the wavelet-based phase extraction in the case of speckle decorrelations. As mentioned in the introduction of this dissertation, whole-field speckle techniques have the potential to make very interesting tools outside of the laboratory. However, external perturbations make it necessary to desensitize the optical set-ups. Consequently, decorrelation effects arise when only few fringes have appeared in the field of view. Hence, visual evaluation of the phenomenon is difficult and requires a frequent refreshing of the reference state of the interferometer. In this context, the ability to perform a continuous measurement with the wavelet processing, regardless of decorrelations, is essential for the applicability of these methods. Indeed, decorrelations produce random phase fluctuations that can be partially eliminated with the combination of ridge extraction and phase best-estimate calculation. In other words, a measurement is possible in conditions where no correlation fringes can be obtained.

Decorrelations are seen as another source of uncertainty in the calculations, not as a fundamental effect preventing these calculations. This comes mainly from the fact that the wavelet processing provides directly unwrapped phase values. Of course, there will be situations where the phase noise created by decorrelations is larger than the phase variations we wish to measure. Fortunately, the combination of the phase of different pixels is a very efficient means of increasing the corresponding signal-to-noise ratio. This result must be retained as one of the most important features of wavelet-based processing in the context of continuous deformation measurements.

9. Wavelet analysis extension

We presented the very promising properties of wavelet analysis in Chapter 6. The examples of Chapter 8 confirm that phase measurements in the context of dynamic phase-shifting are possible with such processing tools. We also identified in these chapters the types of phase evolution laws that constitute the typical domain of application. In particular, the technique is not designed to handle brutal frequency variations or interference effects near the Nyquist cut-off frequency. We also studied in details the phase error that appears when the frequency variations of the signal are no longer negligible in the temporal analysis window. The goal of this chapter is to present possible enhancements of the wavelet-based phase extraction, which address these specific limitations and extend the domain of application. One solution consists in using chirped wavelets instead of constant frequency wavelets. This helps correct systematic phase errors and improves the response of the ridge extraction for brutal frequency variations. The second solution consists in using complex signals. Such signals actually provide the possibility to go beyond the Nyquist frequency.

9.1 Chirped wavelets and combined phase-shifting/wavelet algorithm

As seen in Chapter 6, the second derivative of the signal's phase produces a systematic error in the phase measured along the ridge of the transform. Fortunately, it was shown that this error is limited to $\pm\pi/4$ and is not accumulated by the phase extraction process. However, it would be interesting to be able to remove it directly.

Our first idea was to work with the phase measured along the ridge. However, it quickly became obvious that the solutions are complicated. For

example, if we calculate the second derivative of the measured phase, we obtain a third degree polynomial in the second derivative of the signal's phase, which might pose the problem of the choice of one solution among three. Other possibilities were then studied and we finally propose two interesting solutions: the combination of wavelet analysis with a classical phase-shifting algorithm or the use of chirped wavelets.

9.1.1 Combination of the 5-image algorithm with wavelet analysis

As was mentioned during the study of the 5-image algorithm, one difficulty is the determination of the instantaneous phase increment $\Delta\phi$. Since this is readily achieved using the ridge of the wavelet transform, combining the two will greatly enhance the domain of application of the phase-shifting method. As long as the signal's frequency ω_s does not change too brutally (the second derivative of the phase is constant), the instantaneous frequency measured along the ridge is very close to ω_s since the phase error is constant. This gives us a good estimation of the average phase increment $\Delta\phi$. Moreover, it is possible to choose the signal samples that are used with the 5-image algorithm when $\Delta\phi$ is lower than $\pi/2$. For example, if ω_s is within $[\pi/3, \pi/2]$, successive signal samples are used. If ω_s is within $[\pi/5, \pi/3]$, one sample every two is used. If ω_s is within $[\pi/7, \pi/5]$, one sample every three is used, and so on. The result is that the 5-image algorithm works with an equivalent $\Delta\phi$ value as close as possible of $\pi/2$, which is the optimum value. Of course, no such downsampling can be performed when $\Delta\phi$ is higher than $\pi/2$.

The advantage of this combination results from the fact that the 5-image algorithm is much less sensitive to the second derivative of phase since it works on much smaller temporal windows than the wavelet analysis. Moreover, using such closely spaced samples helps restore the time localization of the analysis, enhancing phase details (but also noise details...). Thus, it very effectively corrects the systematic phase error obtained along the ridge. Another interesting point is that the temporal phase unwrapping can be conducted on the basis of the unwrapped skeleton's phase, which is precise to $\pm\pi/4$. Moreover, the phase of a sample must be close to the phase of the preceding one plus $\Delta\phi$. This wealth of information permits to correct for false phase values calculated with the 5-image algorithm when noise affects the signal.

The results obtained with this combination of the two methods are illustrated in the next paragraphs, conjointly with the results obtained for the chirped wavelets.

9.1.2 Chirped wavelet analysis

This solution was actually proposed in Ref.1, in the frame of acoustic signal processing. However, the authors of this paper do not pay attention to the phase error correction but rather emphasize the fact that more correct ridge trajectories are obtained with the Gabor transform when the signal amplitude varies rapidly.

One can view the process of ridge extraction as trying to find the constant-frequency signal that best matches the portion of the original signal selected in the analysis window. It is clear that only a compromise can be obtained when the signal's frequency changes within this temporal interval. Using a chirped wavelet gives us one more parameter to adjust, the frequency variation rate, which permits to get a better fit. The chirped wavelet takes the form:

$$M(t) = \exp\left(-\frac{t^2}{2}\right) \exp(-i\omega_0 t) \exp\left(-i\frac{ct^2}{2}\right) \quad (9-1)$$

All the developments found in Appendix B can be rewritten in this case by replacing everywhere the term φ_s'' by the term $(\varphi_s'' - c)$. If the signal's modulation changes linearly within the analysis window, we obtain a modified expression for the wavelet coefficients along the ridge:

$$S(a(b), b) = \sqrt{2\pi} \left(1 + a^4(b)(\varphi_s''(b) - c)^2\right)^{-\frac{1}{4}} \exp\left(i\frac{1}{2} \arctan a^2(b)(\varphi_s''(b) - c)\right) B(b) \exp(i\varphi_s(b)) \quad (9-2)$$

A new ridge extraction algorithm must now be constructed to get at the same time an estimation of a and c . In the Morlet wavelet case, the ridge extraction consists in evaluating the instantaneous frequency of the signal by measuring the transform's phase variation on a small time interval Δb , for a fixed analysis frequency ω_0/a . In the chirped wavelet case, the algorithm tries to measure the transform's phase variation along a line $\Delta b - \Delta a$ in the time-frequency domain (the analysis frequency is no longer constant).

Beginning with an initial value a_0 and c_0 for the two parameters, the estimations a_1 and c_1 are obtained with:

$$\frac{\omega_0}{a_1} = \frac{\partial \varphi_{S(a_0, b)}}{\partial b} + c_0 \frac{\partial \varphi_{S(a_0, b)}}{\partial \omega} \quad (9-3)$$

$$c_1 = \frac{\partial}{\partial b} \left(\frac{\partial \varphi_{S(a_0, b)}}{\partial b} + c_0 \frac{\partial \varphi_{S(a_0, b)}}{\partial \omega} \right) + c_0 \frac{\partial}{\partial \omega} \left(\frac{\partial \varphi_{S(a_0, b)}}{\partial b} + c_0 \frac{\partial \varphi_{S(a_0, b)}}{\partial \omega} \right) \quad (9-4)$$

where $\varphi_{S(a,b)}$ is the phase of the transform calculated at the frequency $\omega = \omega_0/a$. We compute derivatives of this phase with respect to ω instead of a . This is more convenient since the frequency variation $d\omega$ used to compute the phase differences is simply equal to c . Calculating the transform for the analysis frequency $\omega + d\omega$ then corresponds to using a scale factor $a' = a\omega_0/(\omega_0 + ad\omega)$.

Once convergence is obtained for a_i and c_i , the algorithm proceeds to the next time sample $b+1$, using $a_0 = a_i\omega_0/(\omega_0 + a_i c_i)$ and $c_0 = c_i$. In practice, since there is an additional parameter to optimize, the algorithm has more freedom and can follow sharper frequency transitions, which can reflect the actual signal evolution or a local noise perturbation. Hence, this method is also more sensitive to phase noise, which creates inconsistent signal samples.

This new analysis method has been added to the program Wavelet. Practically, each ridge iteration requires the calculation of 13 values of $S(a,b)$, as shown in this table:

		$S\left(\frac{a\omega_0}{\omega_0 + ac}, b\right)$			
	$S\left(\frac{2a\omega_0}{2\omega_0 + ac}, b-1\right)$	$S\left(\frac{2a\omega_0}{2\omega_0 + ac}, b\right)$	$S\left(\frac{2a\omega_0}{2\omega_0 + ad\omega}, b+1\right)$		
$S(a, b-2)$	$S(a, b-1)$	$S(a, b)$	$S(a, b+1)$	$S(a, b+2)$	
	$S\left(\frac{2a\omega_0}{2\omega_0 - ac}, b-1\right)$	$S\left(\frac{2a\omega_0}{2\omega_0 - ac}, b\right)$	$S\left(\frac{2a\omega_0}{2\omega_0 - ac}, b+1\right)$		
		$S\left(\frac{a\omega_0}{\omega_0 - ac}, b\right)$			

The different derivatives of (9-3) and (9-4) are estimated as the finite differences of the phase of the 13 elements calculated above. The computation time is of course longer with this more complicated algorithm. The value of c is tested after each iteration to make sure that the chirped wavelet frequency does not become negative or larger than π near the edges of the temporal analysis window.

The two advantages of the chirped wavelet processing, correction of the error induced by the second derivative of the signal's phase and better behavior in the presence of rapid frequency transitions, are illustrated in the next two paragraphs.

9.1.3 Examples of correction of the phase systematic error

In a first example we use a rapid chirp to demonstrate the effectiveness of the second derivative correction. The frequency of this signal changes from $\pi/6$ to $5\pi/6$ in 256 time samples. We plot the difference between the actual phase of the signal and the phase measured along the ridge of the transform for a normal and chirped Morlet wavelet. The mother wavelet frequency ω_0 is 4π in this example. The phase error obtained by combining the 5-image algorithm with the phase of the normal wavelet is also presented. The two greyed regions correspond to the parts of the transform perturbed by the signal's support extension with a constant value.

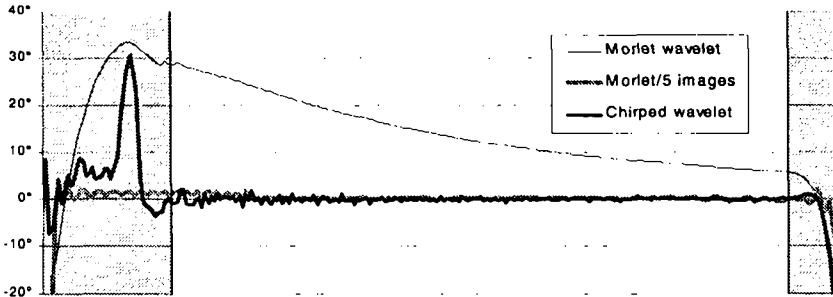


Figure 9-1. Error due to the second derivative of a linear chirp's phase. The signal support is extended in the grey regions.

We observe that the error disappears completely with the two proposed solutions in the non-perturbed part of the transform. Moreover, the 5-image algorithm provides an appreciable correction in the perturbed region since it requires only 13 signal samples when ω_0 is close to $\pi/6$. This explains why an error is committed only for the first 6 time samples when the 5-image algorithm is used. By comparison, the Morlet or chirped wavelets require 180 samples for the same frequency. Hence, they “suffer” more from the signal extension.

A more interesting example is obtained with the sinusoidal frequency modulation signal already used in Chapter 6. We recall that we measured a sinusoidal phase evolution in the case of the cyclic loading of a metallic plate. We then used a model of this phase evolution law to evaluate the error due to the second derivative of the phase. We now show in Figure 9-2 the theoretical phase error due to this derivative, the phase error obtained with a normal wavelet analysis, the phase error obtained with the chirped wavelet and the phase error obtained with the 5-image algorithm.

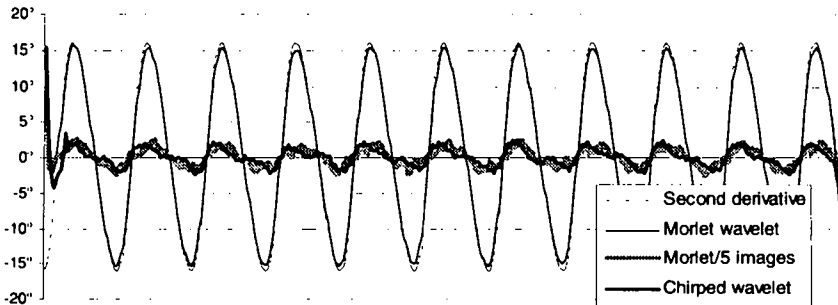


Figure 9-2. Simulated sinusoidal phase evolution: plot of the theoretical error due to the second derivative of phase and the error obtained for the Morlet and chirped wavelets and 5-image algorithm.

As seen in Chapter 6, the major part of the error is due to the second derivative of the phase when the standard Morlet wavelet is used. This error is greatly reduced if the skeleton's phase is calculated with a chirped wavelet or calculated by combining the Morlet wavelet with the 5-image algorithm. The remaining error is due to the higher derivatives of the phase.

9.1.4 Improved robustness for rapid frequency transitions

To illustrate the better behavior of the ridge extraction algorithm when a chirped wavelet is used, we go back to the example of the measurement performed on a piece of rubber with in-plane speckle interferometry. It was used in Chapter 6 (paragraph 6.5) to illustrate the difficulty of following rapid frequency transitions. The result of the ridge extraction with a normal Morlet wavelet with $\omega_0 = 4\pi$ is shown in Figure 9-3(a). The starting point of the ridge is chosen at a time where the instantaneous frequency is already high. We observe that the backward propagation of the ridge does not permit to identify correctly the downward frequency transition near the signal's beginning. The corresponding ridge obtained with a chirped wavelet is shown in (b). The ridge is correct in this case, for the same value of ω_0 .

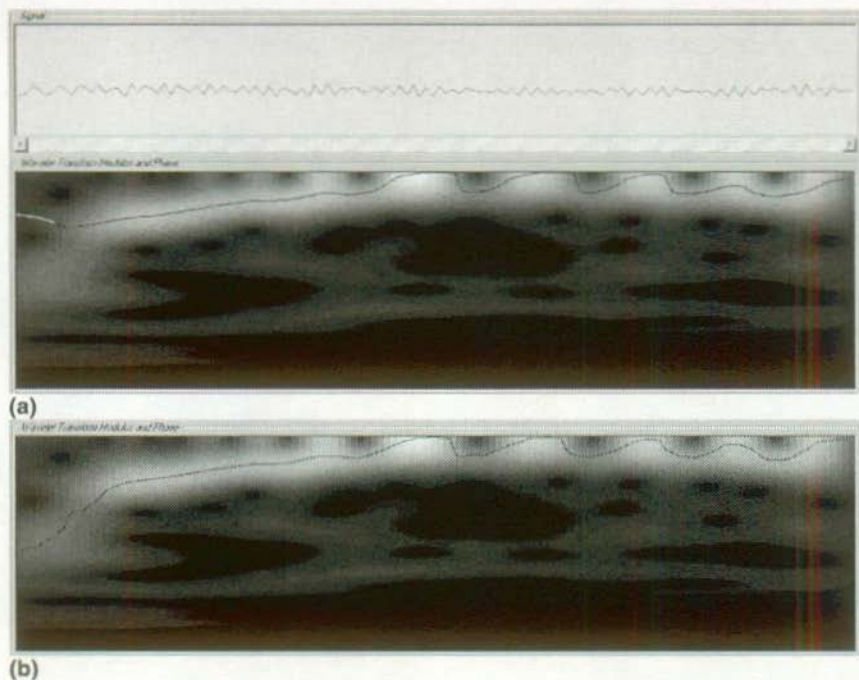


Figure 9-3. Wavelet transform modulus showing the ridge obtained with a Morlet wavelet in (a) and a chirped wavelet in (b). Signal obtained using in-plane speckle interferometry.

The benefit of the chirped wavelet is apparent in the preceding example. However, once rapid frequency variations and phase noise are combined, the normal and chirped approaches are less stable, as illustrated in Figure 9-4. No particular method appears to be superior in these types of situations.

These images are actually a good occasion to observe the number of 2π -multiples that are wrongly added or subtracted from the phase that is measured along the ridge of the transform. We recall that going around a modulus hole amounts to add or remove one fringe to the estimated phase. Just counting the holes gives us directly the error in number of fringes. For example, in (a), the estimated ridge goes twice above a hole (first and third oscillations of the frequency), adding 4π to the unwrapped phase of the skeleton. However, the ridge goes under two holes at the fifth oscillation, which results in subtracting 4π . The end result, in this particular example, is that the unwrapped skeleton's phase in the last part of the signal is "exact", from the point of view of the number of fringes that went by during the measurement. Unfortunately for the

chirped wavelet in this example, the ridge goes underneath 5 holes in (b), resulting in a total error of 10π in the unwrapped phase at the end of the skeleton.

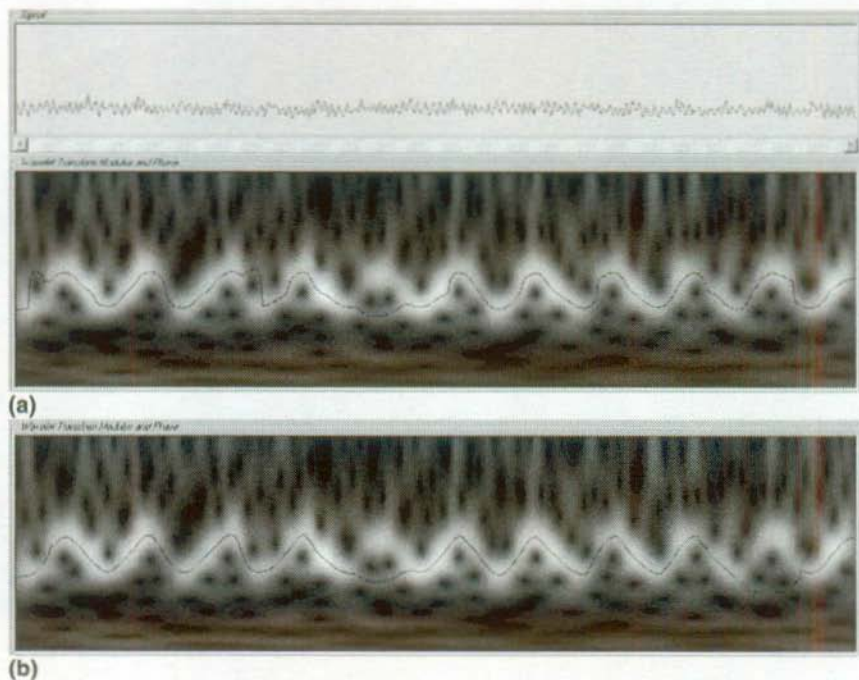


Figure 9-4. Wavelet transform modulus showing the ridge obtained with a Morlet wavelet in (a) and a chirped wavelet in (b). Signal obtained using shearing speckle interferometry.

9.2 Overcoming interference effects near the Nyquist limit

9.2.1 The need for a complex signal

As seen in Chapter 6, the analysis window used in the frequency domain during wavelet processing is larger near the Nyquist limit. Hence, when the signal frequency becomes close to π rad/s, its two frequency components can be present simultaneously in the analysis window, resulting in an interference effect that makes ridge extraction impossible. This effect can be limited to a small band of signal frequencies by increasing ω_0 but the resulting loss of time localization can actually be a bigger nuisance since rapid frequency transitions are more difficult to follow.

The interference effect is actually due to the simultaneous presence of the two signal peaks in the analysis window. These two peaks have the same weight since the measured signal is real. It is clear that the perturbation would be much less of a trouble if we could eliminate one of the peaks, or at least reduce one of them significantly. This actually requires the creation of an imaginary part for the real signal $s(t)$:

$$\begin{aligned} s(t) &= A(t) + B(t)e^{i\varphi_s(t)} + B(t)e^{-i\varphi_s(t)} \\ &= A(t) + 2B(t)\cos\varphi_s(t) \end{aligned} \quad (9-5)$$

Since we are interested in the behavior of the transform near the Nyquist frequency, the background intensity $A(t)$ is dropped in the next equations. The complex signal we wish to create can then be written as:

$$\begin{aligned} z(t) &= C(t)e^{i\varphi_s(t)} + D(t)e^{-i\varphi_s(t)} \\ &= (C(t) + D(t))\cos\varphi_s(t) + i(C(t) - D(t))\sin\varphi_s(t) \end{aligned} \quad (9-6)$$

Our goal is to have $C \gg D$, the ideal case being $D = 0$. $z(t)$ actually corresponds to $s(t)$ when $C = D = B$. The transition between these different situations is illustrated in Figure 9-5 where the transform of a simulated chirp is shown when $D = C$ (in (a)), $D = C/4$ (in (b)) and $D = 0$ (in (c)). The chirp frequency goes from $\pi/4$ to $\pi + \pi/5$ and the transform is plotted for frequencies ranging from $\pi/10$ up to $2\pi/1.25$, which is *higher* than the Nyquist limit of π rad/s. This limit is represented as a horizontal white line. The ridge extraction using the Morlet wavelet is also shown in these images.

The two frequency components of the signal appear clearly in (a) where the signal is real. The signal aliasing appears when the “negative” frequency component ($-\varphi_s \equiv 2\pi - \varphi_s$) drops under the Nyquist limit while the positive component passes over it. Interference effects in the transform are visible around this transition region. This causes the ridge to oscillate and the corresponding skeleton’s phase does not represent the signal’s phase. Moreover, the increasing and decreasing phase evolutions create two symmetrical ridges of equal energy. The choice of one trajectory instead of the other during the ridge extraction is then arbitrary since both represent a possible frequency evolution law.

The situation becomes interesting in (b) where the negative frequency component is reduced by the adjunction of a small imaginary part to the real signal. The interference effect is greatly attenuated which results in an almost correct ridge extraction. Moreover, and contrary to what is found in (a), the strengthening of the positive frequency component of the signal removes the ambiguity on the actual frequency evolution law.

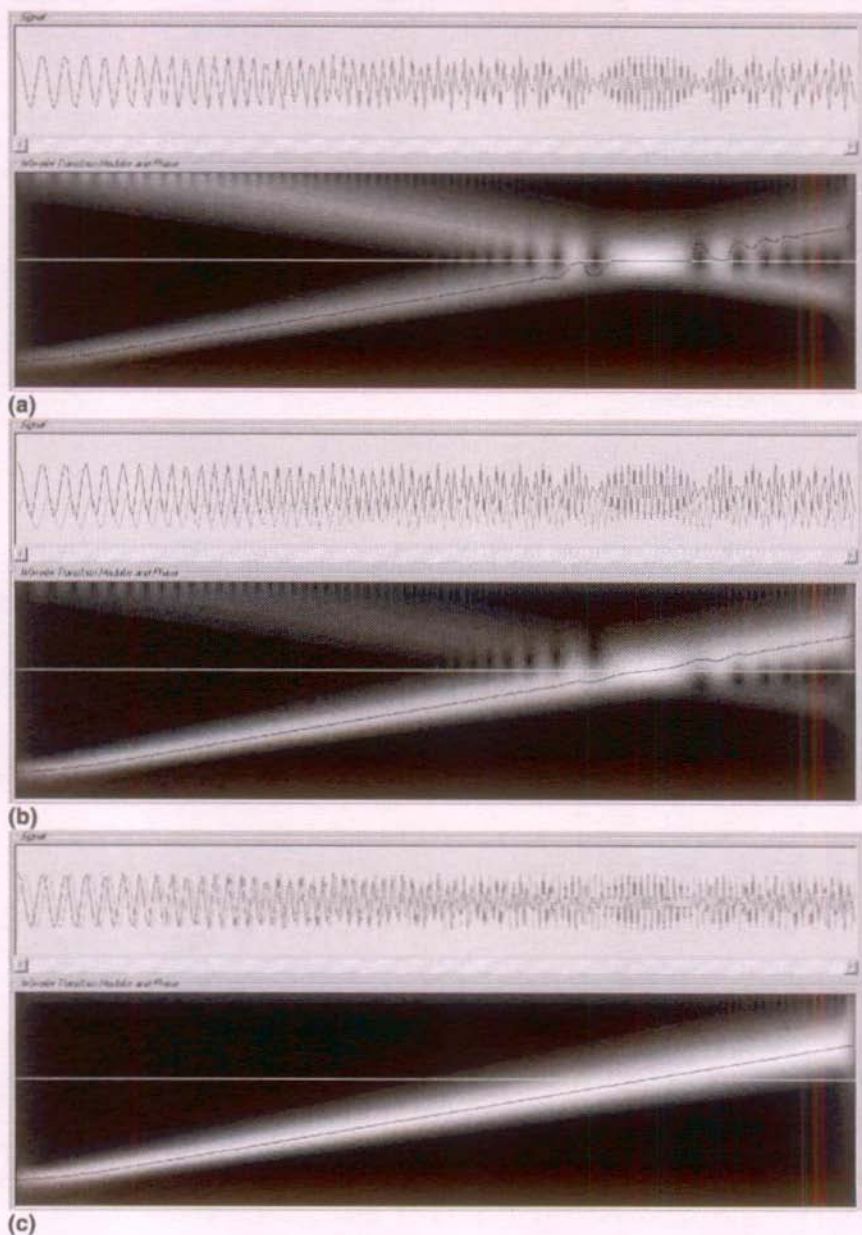


Figure 9-5. Transform of: (a) real chirp; (b) complex chirp with small imaginary part; (c) complex chirp with equal real and imaginary parts. The white horizontal line represents the Nyquist limit.

The use of equal amplitude real and imaginary parts in (c) creates a “perfect” transform since the second frequency component has completely vanished. The immediate benefit is that the ridge extraction is not perturbed at all and a phase measurement can be obtained above the Nyquist limit. In this case the maximum tolerable signal frequency becomes 2π instead of π .

9.2.2 Creation of a complex signal

Clearly, we cannot create an imaginary part to the real signal s without additional information. This information can be found in the surrounding pixels, assuming that they all modulate with the same instantaneous frequency ω . The ideal situation would be to find a second pixel that is in phase quadrature and has a similar modulation. Since the probability of this occurrence is relatively low, we rather construct a complex signal using the 9 pixels of a 3×3 -pixel cell.

The 9 signals are written as:

$$s_k(t) = B_k(t) \cos(\omega_s t + \varphi_k) \quad (9-7)$$

where φ_k is the signal initial phase at the time $t = 0$. We will discuss below how φ_k is actually obtained. The complex signal is then constructed as:

$$z(t) = \sum s_k(t) e^{-i\varphi_k} = \sum s_k(t) \cos \varphi_k - i \sum s_k(t) \sin \varphi_k \quad (9-8)$$

We can see this operation as trying to synchronize and then add the 9 signals. $z(t)$ is also equal to:

$$z(t) = \sum B_k(t) \cdot e^{i\omega_s t} + \sum B_k(t) e^{-i2\varphi_k} \cdot e^{-i\omega_s t} \quad (9-9)$$

If the φ_k values are randomly distributed, as is the case with speckle interferometry, the second sum has a smaller modulus than the first:

$$\left| \sum B_k(t) e^{-i2\varphi_k} \right| < \left| \sum B_k(t) \right| = \sum B_k(t) \quad (9-10)$$

Writing the second sum in the form of a modulus and a phase θ we obtain finally:

$$z(t) = C(t) e^{i\omega_s t} + D(t) e^{i\theta} e^{-i\omega_s t} \quad \text{with } C(t) > D(t) \quad (9-11)$$

The success of this construction depends on the initial phase values of the different signals. Not much will be gained in regions of small phase gradient in interferograms obtained with classical or holographic interferometry since φ_k is more or less constant in a 3×3 -pixel cell. In contrast, the interferograms

obtained in speckle interferometry present a naturally random phase distribution, ideally suited for this technique.

The practical implementation in the program Wavelet is built as follows:

1) The usual ridge extraction is performed for each of the 9 signals of a pixel cell.

2) If the instantaneous frequency of a signal reaches a threshold frequency ω_L , the corresponding time b_k is recorded.

3) The smallest b_k value among the 9 signals acts as the time origin and a complex signal is constructed as in (9-8) using the phase φ_k calculated for each signal at the time b_k .

4) A new ridge extraction is performed on the complex signal, providing the frequency evolution law in the domain close to the Nyquist frequency. The phase evolution of each pixel can thus be reconstructed in this region. Once the instantaneous frequency gets lower than ω_L , the normal ridge extraction can again be used for each signal taken individually, until ω_L is reached again.

The frequency $\omega_L = \omega_0/a_L$ is defined as the frequency for which the analysis window has a weight ε (typically 10^{-3}) for the negative frequency component of the signal:

$$a_L = \frac{2\omega_0 - \ln \varepsilon}{2\pi} \quad (9-12)$$

Since the creation of the complex signal amounts to synchronizing the different real signals, we could imagine computing a reference phase for each one at an initial time and use this value once and for all. It is important to recognize that the φ_k values used in the construction (9-8) do not need to be known very precisely. Hence, in the case of speckle interferometry, the random phase errors due to decorrelations that are accumulated along time are not critical. This is also illustrated in the example shown in 9.2.4 where some ridge extractions fail altogether for some pixels. It is also possible to use a different algorithm where new φ_k values are calculated each time ω_L is reached by one of the signals.

9.2.3 Example of measurement in the Nyquist region

To illustrate the interest of creating a complex signal we use one of the image sequences recorded while measuring the deformation of a piece of rubber with in-plane speckle interferometry (also used in Chapter 5, 6 and 8). We did not intend to get high deformation speeds while making this experiment but it appeared afterwards that the instantaneous frequency goes just above the Nyquist limit in the region where the load was applied to the object. We show in Figure 9-6 the transform and ridge of the signal measured for one pixel located

in this region. The frequency scale goes from $\pi/5$ up to $2\pi/1.4$ in this spectrogram. The strong interference effects near the Nyquist limit at π rad/s prevent a successful ridge extraction.

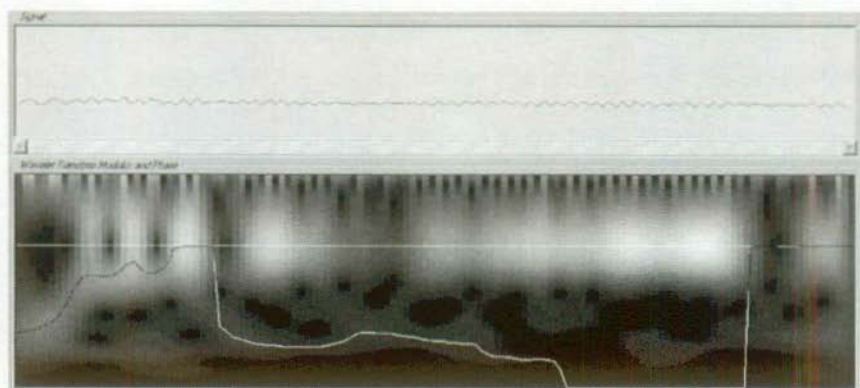


Figure 9-6. Transform of a signal of instantaneous frequency close to π rad/s (white line). The ridge extraction fails because of the strong interference effects in this region. Analysis for $\omega_0 = 2\pi$ rad/s.

We then combine this signal with that of the 8 neighboring pixels to create a complex signal. The frequency limit ω_c , close to $2\pi/3$ for $\epsilon = 10^{-3}$, is attained near the 8th time sample (there are a total of 128 samples). The resulting transform is shown in Figure 9-7.

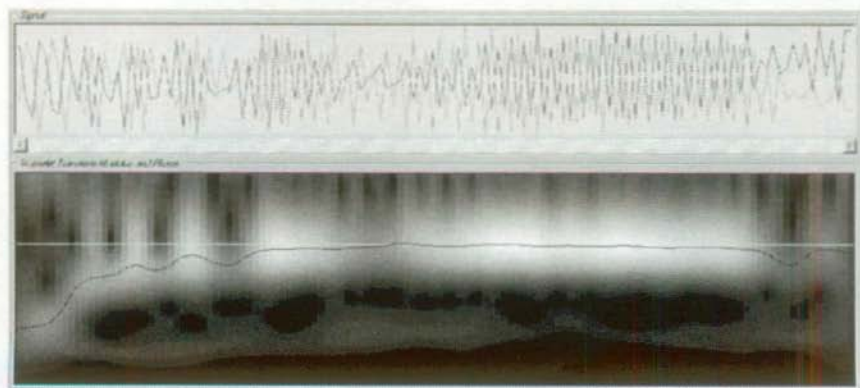


Figure 9-7. Transform of the complex signal created with the 3×3 -pixel cell corresponding to the single pixel of Figure 9-6.

The attenuation of the negative frequency component is small but nevertheless sufficient to permit a reasonable ridge extraction. In particular, the three regions where the transform's modulus drops to zero in Figure 9-6 are largely smoothed out in Figure 9-7.

This experiment is quite interesting since the signal's instantaneous frequency stays in the region of maximum interference effects for most of the signal duration. A second example is shown in Figure 9-8 for a nearby pixel cell. The central pixel does not modulate much in (a) but the corresponding complex signal provides a very smooth transform in (b), thanks to the 8 neighbors.

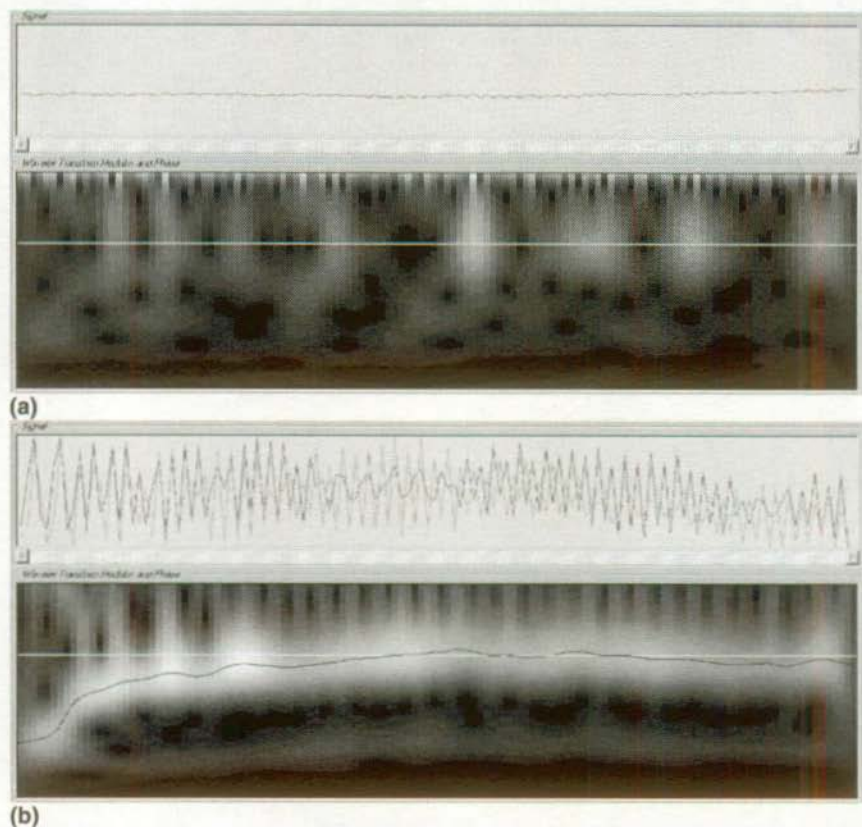


Figure 9-8. (a) Transform of the signal of the central pixel of a 3 x 3 cell; (b) Transform of the complex signal created with all 9 pixels.

9.2.4 Benefit of the complex signal in the absence of interference effects

We saw in Chapter 7 that the combination of the phase of small groups of pixels allows to reconstruct the phase evolution of one of them when its modulation gets too low. The two examples of the preceding paragraph show that creating a complex signal is a second method to interpolate or recreate the missing information. Only this time the work is performed on the actual signals instead of their phase. We can then wonder if the creation of complex signals would not also bring additional robustness to the wavelet analysis method in regions where no perturbing interference effects are present.

To test this idea we use again the signal obtained in speckle shearing interferometry applied to a cyclically loaded metallic plate. We extract the signal of the 9 pixels of a 3×3 cell and compute their individual transforms. The result is shown in Figure 9-10. The vertical frequency scale goes from $\pi/5$ to $4\pi/5$. We observe that only two pixels (top of columns (a) and (c)) provide a sufficiently clear signal to distinguish the sinusoidal frequency evolution law. Accordingly, most ridge extractions fail with these 9 signals. However, creating a complex signal from this 3×3 -pixel cell yields a surprisingly good result, see Figure 9-9.

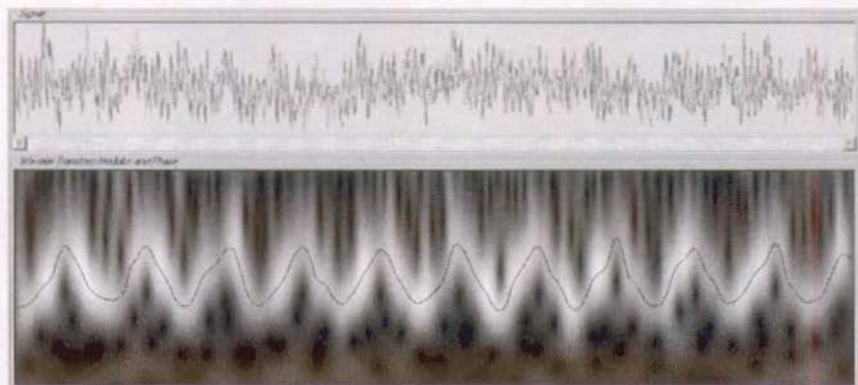
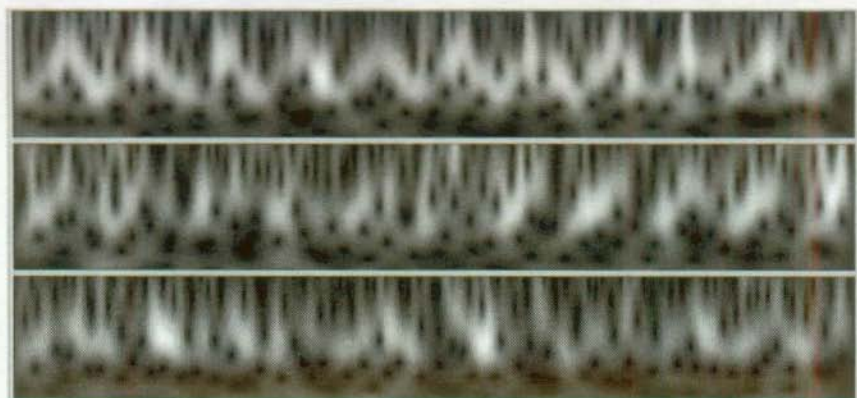
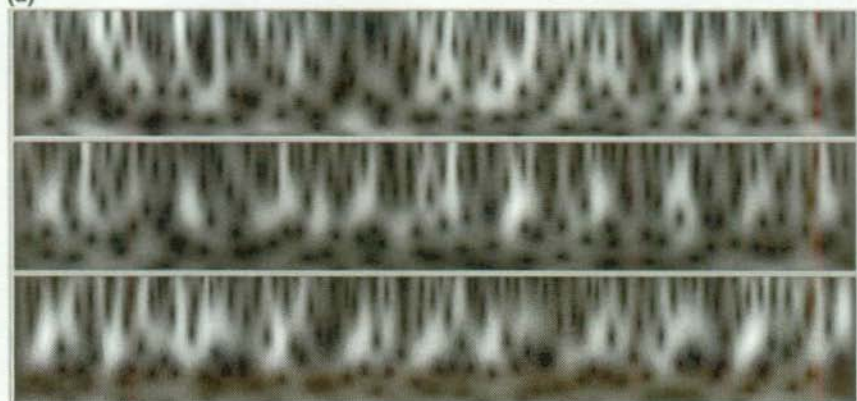


Figure 9-9. Transform of the complex signal built with the 9 signals shown in Figure 9-10.

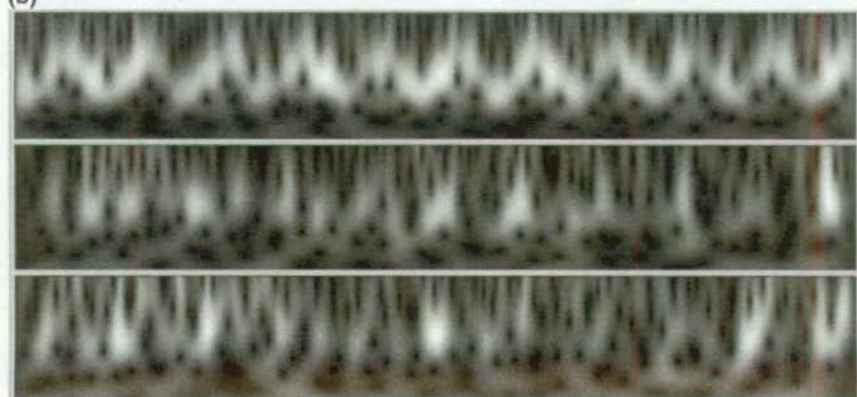
We can thus observe that the combination of mostly poor signals permits to create a complex signal sound enough to perform the ridge extraction without errors. This result is very important for the robustness of the method in the case of speckle interferometry.



(a)



(b)



(c)

Figure 9-10. (a), (b) and (c): Transform of 3 columns of 3 pixels.

9.2.5 Beyond Nyquist?

The results shown in Figure 9-5 are quite interesting since it appears feasible to estimate a frequency evolution law going above the Nyquist cutoff frequency. This would actually appear to contradict the Shannon theorem. However, looking back at the formulation of this theorem², we see that a real signal s such that $\hat{s}(\omega) = 0$ when $|\omega| > \Omega$, that is, its frequency spectrum is contained within $[-\Omega, \Omega]$, can be reconstructed from samples taken at a rate 2Ω . In the case of a complex signal that has no negative frequency components, the spectrum is in fact reduced to $[0, \Omega]$. In other words, the spectrum width is half as large. We can then tolerate a doubling of the maximum frequency contained in the signal and still remain in correct sampling conditions.

Another way of looking at this paradox is to consider that twice as much information is available in the complex case since the real and imaginary parts of the signal constitute two real signals instead of one. This actually amounts to using twice as many samples because the real and imaginary parts are entirely correlated in the case of the sinusoidal signals we wish to process.

However, the negative frequency component is never completely eliminated in practice. Hence, there are small interference effects as shown in Figure 9-5(b). Still, assuming that the possible ridge trajectories found in the transform correspond to the positive and negative frequency components, the creation of a complex signal helps distinguish and select the positive component, since its amplitude is significantly larger. We don't actually need more information to perform a correct ridge extraction in most situations.

These properties of complex signals need to be further explored. At stake is the potential doubling of the measurement range of the dynamic phase-shifting method, at least when speckle interferometry is used. Of course, many new problems have to be tackled. For example, the sampled wavelet function becomes a very simple Gaussian low-pass filter when the analysis frequency ω_x/a tends towards 2π . The phase component of the wavelet is then close to $2\pi t$, which does not oscillate at all when the sampling points t are integer. Additionally, changing the frequency measurement range from $]0, \pi[$ to $]0, 2\pi[$ would imply that the reference phase steps could be as large as π , which would place the carrier frequency in the most difficult region for ridge extraction. Indeed, since an initial phase value has to be found for each real signal, the problem of ridge extraction near π rad/s still exists. It then seems more reasonable to increase the reference phase steps to a lower value, say $3\pi/4$, in which case the maximum phase increment due to object deformation could be

raised to $\pm 3\pi/4$ instead of $\pm\pi/2$. One major problem remains in any case, namely, the determination of an initial phase value to create the complex signals.

Bibliography

- 1 P. Guillemain, R. Kronland-Martinet, "Characterization of acoustic signals through continuous linear time-frequency representations", Proceedings of the IEEE, Vol. 84 (1996), No. 4., pp. 561-585.
- 2 G. Kaiser, "A friendly guide to wavelets", Birkhäuser, 1994, ISBN 0-8176-3711-7.

10. Conclusion and future prospects

10.1 Summary of completed work

The main goal of this thesis was the development of a new approach permitting quantitative measurements in non-static conditions, using interferometric or related whole-field optical methods. As seen in Chapter 3, none of the currently available fringe analysis techniques provide a fully satisfactory solution to this need. The new method we propose, called dynamic phase-shifting, opens the way to a new type of interferogram analysis. Indeed, the phase variations caused by the deformation or displacement of the object under study are no longer seen as unwanted perturbations but are rather considered to be the vector of information. Concretely, the process relies on the “natural” phase-shifting created in real-time by the deformation, to subsequently apply phase evaluating techniques to the interferogram. We also show that additional information can be gained by introducing a known phase step between each recorded image. In particular, the absolute sign of the deformation can be obtained.

The study of dynamic phase-shifting in Chapter 4 showed that a correct measurement is possible as long as the deformation rate of the object remains lower than a certain threshold, directly proportional to the image acquisition rate of the recording device. This condition is a direct consequence of the Shannon sampling theorem. The practical consequence is that at least 4 images have to be recorded while 1 complete fringe passes at any point of the interferogram. Depending on the particular optical set-up used, this fringe might represent a change of shape of up to tens of centimeters (moiré) or a displacement of a fraction of a micron (interferometric techniques). We must also emphasize that it is possible in some cases to overcome the Nyquist limit by creating a complex temporal signal (see Chapter 9). Only 2 images are then required for a complete signal sampling.

We propose two solutions to process an image sequence recorded in dynamic phase-shifting conditions. The first one is adapted to short measurements, localized in time. It is constructed as a particular 5-image algorithm. Its primary use is the evaluation of the interferogram phase for a given state of the object. However, contrary to more classical fringe analysis techniques, the object does not have to be still during recording of 5 images. The necessary phase unwrapping step has to be conducted spatially in the obtained phase map. By extension, this processing tool can be applied repeatedly in time. In this case one can follow the evolution of the phase of the interferogram at discrete instants. However, as long as the sequence is not strictly continuous, the information about the absolute deformation of the object remains unknown. It is also possible to lose all information if large decorrelations appear between successive sampling periods, when speckle interferometry is used.

The 5-image algorithm can still be applied when continuous image series are recorded. However, we also presented a more robust method based on a time-frequency analysis. The idea is to consider the temporal signal recorded at each pixel. This signal can be processed with a wavelet transform, which yields its instantaneous frequency spectrum. One advantage of this type of processing comes from the fact that a variable stretch of the signal is isolated for the evaluation, depending on its instantaneous frequency. This provides a finer analysis of the frequency content and good noise immunity. The next step is to recognize that the phase of the wavelet transform, measured along the trajectory of the instantaneous signal frequency in the time-frequency domain, is exactly equal to the phase we wish to measure. A particular extraction algorithm is presented to perform this task automatically. The temporal unwrapping of the obtained phase is much simpler and eliminates most of the problems encountered with classical spatial unwrapping.

The robustness of the wavelet-based processing can be enhanced in different manners. First, the phase evolution of neighboring pixels can be combined in a weighted average using the measured interferogram modulation as weights. The result is that the phase of any pixel can be interpolated from its neighbors when its modulation is too low to permit a successful phase extraction. This is essential in speckle interferometry. A second technique consists in creating one complex signal from several real signals. The main result is the possibility to approach or even go beyond the Nyquist cut-off frequency. Additionally, the technique permits to improve the signal quality and facilitate the phase extraction. A third enhancement of the wavelet-analysis addresses the problem of the systematic phase error created when the signal

frequency changes rapidly. We showed that this error could be altogether eliminated by use of a chirped wavelet or a combination of the 5-image algorithm with standard wavelet processing.

10.2 Future prospects

The examples of Chapter 8 demonstrated that the standard algorithms described in Chapter 6 and 7 are powerful tools suitable for continuous deformation measurements in various conditions. The enhancements proposed in Chapter 9, namely, chirped wavelets and complex signals, have been successfully applied to several individual pixels or pixel groups. One task now is to integrate these new methods in the software package we developed to process complete sequence of images.

We essentially investigated the application of our method to deformation measurements. However, some shape measurement techniques where the pitch of the projected fringes decreases progressively to remove shape ambiguities could also be conducted in a faster, continuous manner in dynamic phase-shifting conditions. The same principle can also be applied to speckle interferometry contouring, with the added benefit of decorrelation reduction.

Another subject that has not yet been addressed is the automatic detection of ridge extraction errors. We showed that the various phase noises that appear during an experiment outside of the laboratory create dislocations in the time-frequency phase plot of the wavelet transform. The ridge extraction algorithm can make two types of mistakes in the presence of these discontinuities. One is to take a wrong track and lose the correct ridge in the remainder of the signal support. In this case, the modulation measured along the erroneous ridge is usually sufficiently low to detect the error and discard this particular pixel. The other possibility is that the algorithm follows a wrong path for a while before coming back on the correct ridge. In this case, the error in the following unwrapped phase values is an exact integer number of 2π . Hence, we could imagine checking periodically that some pixels within a group do not suddenly exhibit a deviation on the order of a few fringes. In this case, the algorithm could try to back-propagate a ridge extraction based on the instantaneous frequency of the pixel group. The goal would be to isolate the region where the error was committed and eventually correct it.

The wavelet processing as proposed in this thesis work has demonstrated a high potential for robust processing of continuous image sequences. Our choice of the Morlet wavelet was guided by its interesting phase properties. It is now

appropriate to look at other possible choice of mother wavelets. Some might provide more efficient algorithms or more robustness to the complete process. One can also think of the endless possibilities of combining different types of wavelet analysis, including combined forward and backward ridge propagation. Moreover, we studied here two distinct approaches. One is of a resolutely spatial nature (5-image algorithm plus spatial unwrapping) while the other is purposely limited to a temporal processing (ridge extraction and temporal unwrapping). It is clear however that both techniques could be combined, for example in using spatial phase maps to get a larger “picture” of the distribution of instantaneous frequencies present in the interferogram or to synchronize phase evolutions in areas larger than 3×3 -pixel cells. Reciprocally, the wavelet processing of a limited number of pixels could be sufficient to calculate absolute deformation values from spatially unwrapped images. Again, numerous possibilities come to mind.

A lot of work can also be done with respect to the acquisition set-up. In particular, it might be possible to process in real-time a limited number of pixels or photodiodes with the wavelet analysis, in order to adjust the introduced reference phase steps to the local deformation speed of various interferogram regions. This would increase the system measurement dynamic. A potentially essential element for such adaptable acquisition set-ups is the spatial light modulator (SLM), based on LCD panels. It seems that the current products could offer acquisition rates of a few tens of hertz. A refinement of the method would consist in a set-up where a feedback loop tries to compensate in real-time the instantaneous phase increment at each point of the interferogram in order to produce a quasi-constant apparent frequency at each pixel. In this case, the feedback signal gives the information on the actual phase variations created by the deformation.

We remark that the wavelet phase extraction can actually be applied to any type of sinusoidal signal. For example, the technique could also be used with the signals obtained in particle velocimetry set-ups where small measurement volumes are probed.

As seen above, our initial development of a wavelet-based phase processing in dynamic phase-shifting conditions brings forward a wealth of possible research directions. Hopefully, the results of such investigations, through improved robustness and measurement dynamic, should increase the applicability of whole-field interferometric methods outside of the controlled laboratory environment. Civil engineering would be among the first disciplines to take advantage of this extended range of applications.

Appendix A: Speckle pattern properties

The goal of this appendix is to present an overview of the speckle pattern properties, with an emphasis on their consequences in the case of speckle interferometry. Of practical importance is the relationship between the number of speckles that are integrated by one pixel of the detector and the resulting distribution of modulation in the interferogram. One major limitation of speckle interferometry, decorrelation, is also discussed. Statistical arguments lead to an optimum filter of the phase errors due to these decorrelations as well as errors due to electronic noise in the acquisition system.

Numerous papers have been published on the topic of speckles, as they are relevant to coherent wave phenomena such as acoustical or radar imaging (including synthetic aperture radars), or optical experiments. A standard reference for the properties of the speckle pattern itself is the work of Goodman¹. More recent papers oriented towards speckle applications and in particular speckle interferometry will be proposed along the text.

A.1 Properties of a single speckle pattern

A.1.1 Intensity and phase statistics

Let us consider a material surface of roughness deeper than the wavelength of light, illuminated with a coherent source S (see Figure A-1). Each elementary area of this surface absorbs and diffuses the light it receives. Hence, these areas can be considered as individual coherent light sources S_i . A point M in space is illuminated by these individual sources. Each corresponding wave has a complex amplitude $a_i \exp(i\varphi_i)$ at the point M. These complex vectors are sometimes called random "phasors". Their phase and modulus are random,

because of the roughness and absorption of the material. The sum of these phasors is the complex amplitude $A(M)$. This amplitude is equivalent to the result of a random walk in a plane.

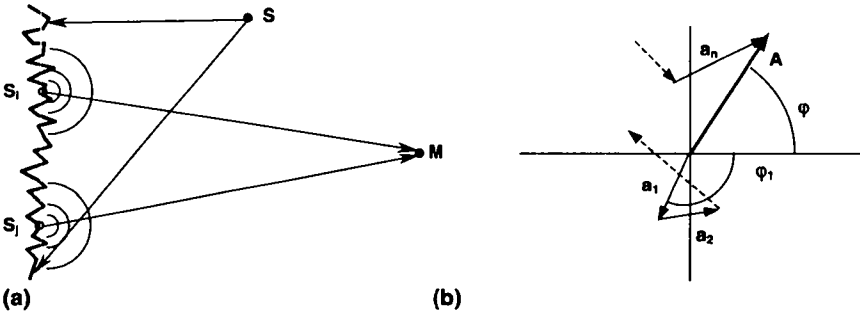


Figure A-1. (a) Objective speckle formation; (b) Random phasors in M

Accordingly, the real and imaginary parts A_r and A_i of the phasor A are Gaussian random variables. A is called a “circular complex Gaussian random variable¹”. If we apply a variable transformation between the couple (A_r, A_i) and the couple (I, φ) , we obtain the probability density functions of the intensity I and phase φ . The phase is uniformly distributed over $[0, 2\pi]$ while the intensity, defined as $I = AA^*$, obeys a negative exponential distribution:

$$p(I) = \frac{1}{\langle I \rangle} \exp\left(-\frac{I}{\langle I \rangle}\right) \quad (\text{A-1})$$

where $\langle I \rangle$ is the mean intensity value. Its variance is:

$$\sigma_I^2 = \langle I \rangle^2 \quad (\text{A-2})$$

The probability that the intensity is larger than a given value I is quite simply:

$$P(I) = \exp\left(-\frac{I}{\langle I \rangle}\right) \quad (\text{A-3})$$

The probability density function of I is drawn in Figure A-2(a). One can note that, even though low intensities are more probable, very high intensity values can be obtained. Figure A-2(b) shows a speckle field measured on a lensless CCD camera. High intensity regions tend to saturate the detector locally but dark regions represent a larger portion of the image.

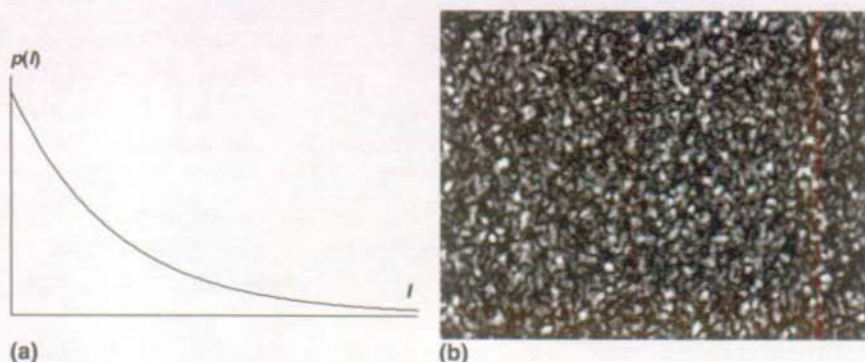


Figure A-2. (a) Probability density function of the intensity of a speckle pattern; (b) Actual pattern recorded by a CCD camera.

The statistics given above correspond to a measurement of the intensity using an infinitely small detector. If the intensity is measured with a finite dimension detector, such as a camera pixel, the probability density function of the resulting intensity I' can be approximated by¹:

$$p(I') = \frac{1}{\Gamma(m)} \left(\frac{m}{\langle I' \rangle} \right)^m I'^{m-1} \exp \left(-m \frac{I'}{\langle I' \rangle} \right) \quad (\text{A-4})$$

where m is the number of "correlation cells" that fit within the detector surface. There are actually a few such correlation cells in what appears visually as speckle grains. For large m values, the probability density function of I' tends towards a Gaussian distribution, as illustrated in Figure A-3. We can observe that as soon as m is larger than 1, the most probable intensity value I' is no longer zero.

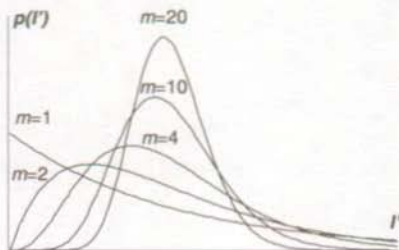


Figure A-3. Influence of speckle integration on the probability density function of the intensity. m is the number of correlation cells.

One must note that the intensity and phase are uncorrelated random variables. Hence, there is no reason why the intensity and phase distributions would present extrema located at the same spatial positions. Consequently, there are phase variations within intensity-defined speckle grains. The statistics of these phase gradients have been investigated in Ref.2 and experimentally measured in Ref.3. The average phase gradient in the whole pattern is on the order of 160° per speckle width in the case of a surface illuminated by a circular Gaussian beam. The average phase variation *inside* a grain is on the order of 45° to 90° per half speckle width.

A.1.2 Average speckle dimensions

Figure A-2(b) shows speckle “grains”, which can be defined as regions of roughly constant intensity, or intensity extrema. The average lateral size of these grains is estimated by taking the first zero of the autocorrelation of the intensity. This size depends on the shape of the illuminated diffusing region. For a circular area, the lateral and longitudinal average widths s_l and s_L are⁴:

$$s_l \approx \frac{\lambda d}{\phi} \quad \text{and} \quad s_L \approx \frac{8\lambda d^2}{\phi^2} \quad (\text{A-5})$$

where λ is the wavelength of light, d is the distance between the illuminated diffusing area of width ϕ and the plane where the speckle is observed; see Figure A-4(a) below.

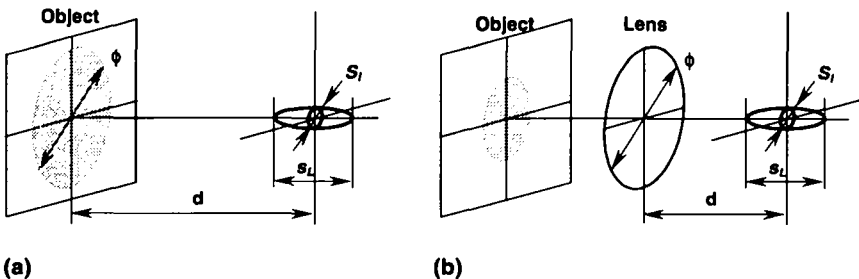


Figure A-4. (a) Objective speckle size; (b) Subjective speckle size.

The free-space pattern obtained in Figure A-4(a) is called an objective speckle. If the speckle pattern is formed after a lens, as in Figure A-4(b), the exit pupil acts as the free-space diffuser. Hence, the same formula apply for the speckle size, with d now corresponding to the distance between the pupil of diameter ϕ and the plane of observation (not necessarily the image plane). As noted in Ref.1, the autocorrelation of the intensity is independent of the phase of

the speckle field. Thus, lens aberrations, which correspond to additional phase contributions, do not influence the speckle size. In the case of focused speckle observation, the only quantity of interest is the lens numerical aperture, which is related to its stop- or F- number and magnification. This is illustrated in the focused and defocused images (a) and (b) of Figure A-5 showing a small metallic tip in front of a diffuser. Defocus is an optical aberration of the first order. It is clear that, though it dramatically blurs sharp features of the image, it does not influence significantly the speckle size. There is actually a small size variation as defocusing results in a small variation of the numerical aperture of the 50-mm macro-objective used.

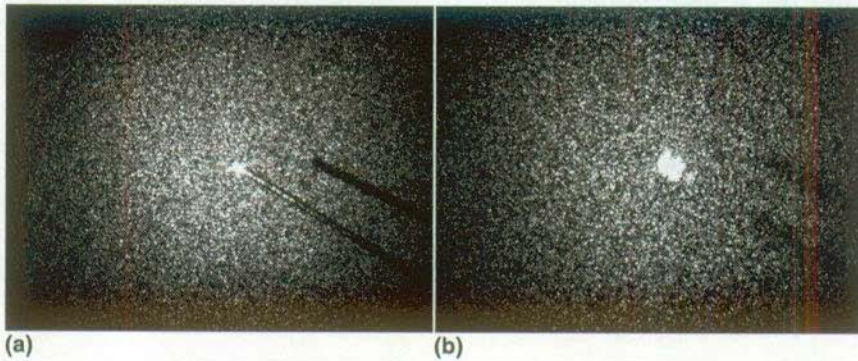


Figure A-5. (a) Focused observation of a bright metallic tip in front of a diffuser; (b) Defocused image showing speckles of same size.

A.1.3 Speckle pattern evolution during object deformation

An important property of speckle patterns is their “stability” for small variations of the illumination direction or object position in space. This means they conserve their shape and appear as being rigidly linked to the diffuser that generates them, for small displacements of this diffuser. Large displacements or deformations will ultimately change the fine grain structure of the speckles, creating a new speckle pattern, no longer correlated with the initial one. However, before reaching this situation, speckle grains appear to retain their shape while their geometrical location in space, as well as their phase, change. This makes it possible to use them in metrological applications such as speckle photography or speckle interferometry. In the first case, the grains are used as markers and their position in space is compared before and after deformation to estimate the object displacements. The movement of the speckle grains is

usually larger than their size. In the second case, speckles do not move by more than a fraction of their size. It is the interference phenomenon with a second speckle pattern or a reference wavefront that reflects their phase change, related to the object displacement. The resulting sensitivity to these displacements is higher than in the case of speckle photography.

A.2 Speckle interferometry

Speckle interferometry is a very convenient metrological tool, as presented in Chapters 2 and 3. The speckle interferogram can be created by the interference of two speckle patterns (in-plane and shearing interferometry) or one speckle pattern and a smooth reference wavefront (out-of-plane interferometry). We recall from Chapter 2 that this interferogram can be described as a function I

$$I = I_0(1 + V \cos \varphi) \quad \text{or} \quad I = I_0 + I_M \cos \varphi \quad (\text{A-6})$$

where I_0 is the background intensity, I_M the modulation, V the visibility and φ the phase of the interferogram.

For fringe visualization and analysis purposes, the quantity of interest is the modulation I_M , which should be as high as possible. In a series of recent papers⁵⁻⁸, Lehmann has studied the corresponding statistics in the case of resolved and unresolved speckles as well as the phase errors introduced by “decorrelation”. We will just detail here the practical results of this work.

A.2.1 Statistics of the modulation

If we first consider an infinitely small detector in the case of a 2-speckles interferogram, it is surprising to observe that the visibility V is higher than 87% in 50% of the cases⁵. In the same time, the background intensity obeys a probability density function very close to the one obtained for a single speckle field. In the case of a speckle of mean intensity $\langle I \rangle$ interfering with a smooth reference wave of constant intensity I_R , the probability density function of I_M is governed by the product $I_R \langle I \rangle$. Hence, it is possible to compensate for “weak” speckle fields by increasing the intensity of the reference.

It is next interesting to see how these theoretical distributions change when a given number of correlation cells, or speckles, are integrated by a finite dimension detector⁶. It is easy to demonstrate that the resulting intensity will still be described as in (A-6). Intuitively, one would guess however that the resulting modulation I_M is going to be lower than that obtained with a resolved speckle interferogram. The development of the probability density functions of this new modulation is involved and does not always lead to an analytic

solution. However, simple approximations of the mean modulation $\langle I_M \rangle$ can be obtained as soon as the number n of speckles integrated by the detector element is large enough. For the interferogram created by two speckle fields of mean intensity $\langle I \rangle$, $\langle I_M \rangle$ is given by:

$$\langle I_M \rangle \approx \sqrt{\frac{\pi}{n}} \langle I \rangle \quad \text{with} \quad n \geq 10 \quad (\text{A-7})$$

The consequence is interesting. Let us consider that, in the case of a camera, n speckles contribute to the intensity measured by a pixel. As seen in paragraph A.1.2, n is a function of the imaging lens aperture. If, for a given object illumination, we double the aperture surface, roughly twice as many speckles will be integrated by each pixel. At the same time, the mean intensity $\langle I \rangle$ in the image plane is doubled. The net result is an increase of the mean modulation of the interferogram by a factor $\sqrt{2}$, which is rather good news. The practical consequence is that one should crank open the aperture of the imaging lens. The limit is however attained when pixels start to saturate. Saturated pixels are useless for a quantitative analysis and it is no use increasing the average modulation while at the same time losing potentially useful points in the image.

The case of a speckle field interfering with a constant, smooth reference wave is slightly different. In this case $\langle I_M \rangle$ is given by:

$$\langle I_M \rangle = \sqrt{\frac{\pi}{n}} \sqrt{I_R \langle I \rangle} \quad (\text{A-8})$$

If both the object illumination and the reference intensity are kept constant, opening the lens stop does not change the mean modulation. Hence, working at F/4 or F/16 does not change the “amount of modulation” present in the image. However, working at higher apertures is beneficial as first, it improves the tolerance of the set-up to decorrelations (see paragraph A.2.2) and second, it decreases the width of the probability density function of the background intensity I_0 . As a consequence, less pixels are susceptible to saturate. The optimum modulation distribution is obtained for the highest I_R value, short of pixel saturation. Since the reference beam represents a very small fraction of the total laser power, I_R can be easily adjusted to reach the optimum, without changing $\langle I_M \rangle$ significantly.

These theoretical observations are confirmed experimentally in Ref.7. The conclusion is that resolving the speckle grains in the image is far from necessary, contrary to what has been widely believed in the early days of speckle interferometry. Optimum modulation distributions can actually be obtained if a “large” number of speckles are integrated by the camera pixels.

A.2.2 Effect of speckle decorrelations

Decorrelations correspond to an alteration of the amplitude and phase of speckle fields between the two exposures that allow to measure a deformation. Many causes are possible but we only consider here so-called image-plane and pupil-plane decorrelations. Of prime interest for us is the corresponding phase error statistics.

Each pixel of the detector initially records an intensity resulting from the interference of sums of random phasors plus eventually a constant reference field (the situation is the same whether the speckles are resolved or not). As mentioned in paragraph A.1.3, speckle patterns reflect the movements of the object that produces them. The same holds in the image plane of the detector. If a region of an object is displaced in a direction orthogonal to the viewing direction, its image on the detector is also translated by an amount given by the magnification of the lens. Hence, the speckle field that covers a given pixel is shifted and some of the phasors that initially contributed to the measured intensity disappear from the collecting area of the pixel while new random phasors are brought in. This replacement of some phasors results in a variation of the quantities I_0 , I_M and φ , concurrently with the geometrical phase change $\Delta\varphi$ (due to the deformation itself) that we wish to calculate. This situation is called an image-plane decorrelation. It is usually caused by rigid-body motions of the object that affect the whole image. As $\Delta\varphi$ is obtained from the difference between the phase of the interferogram after and before deformation, the decorrelation-induced variation of φ results in an error on the estimation of $\Delta\varphi$. The amount of error is of course function of the portion of phasors that are replaced, i.e. the amount of decorrelation.

Pupil-plane decorrelations arise when the speckle pattern present at the entrance pupil of the objective is shifted, for example because of a tilt or a large in-plane displacement of the object. Again, some of the initial random phasors no longer enter the pupil while new contributions appear. The result is an alteration of the speckle pattern produced in the image plane by diffraction of the pupil amplitude. In the same way as that described for image-plane decorrelations, random phase variations are introduced over the whole image.

Lehmann studied both types of decorrelations in Ref.8, for the cases of resolved and unresolved speckles, and for interference patterns resulting from two speckle fields or one speckle field plus a smooth reference wave. To summarize, the derived statistics show that these different situations are actually equivalent, except for the case of very well resolved speckles, which is seldom the case in practice. In particular, the standard deviation of the phase error is

shown to be to a very good approximation inversely proportional to the modulation of the pixel:

$$\sigma_{\delta\varphi} \propto \frac{1}{I_M} \quad (\text{A-9})$$

Interestingly, these results are independent of the actual number of speckles integrated by this pixel. These theoretical investigations confirm the results derived earlier by Huntley⁹ with the help of simulations. This author shows also that electronic noise present in the image acquisition chain generates similar distributions of phase errors. Hence, most sources of errors affecting the phase measurement process can be described in a consistent way.

The actual dependence of the phase error standard deviation on the modulation of the pixel can be understood easily with the help of Figure A-6. One can view the effect of decorrelations as a modification of the complex vector $I_M = I_M \exp(i\varphi)$ by a random quantity dI_M . The variance of dI_M is function of the amount of decorrelation. Figure A-6 compares two situations where it appears clearly that a given dI_M value will usually create higher phase errors $\delta\varphi$ for pixels of low-modulation. The circles in the figures represent the standard deviation of the modulus of dI_M .

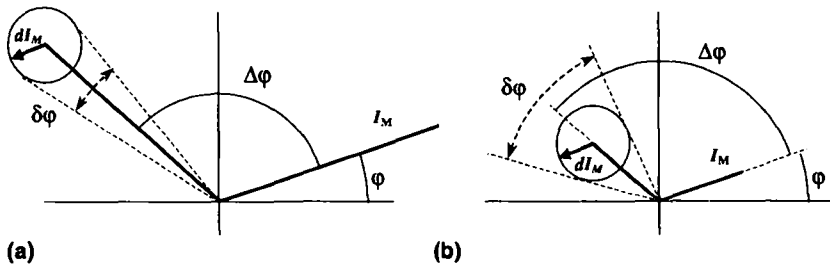


Figure A-6. (a) Phase error $\delta\varphi$ caused by a decorrelation-induced modification of modulation and phase; (b) Same situation for a pixel with low modulation.

One last point concerning the statistics of phase errors must also be emphasized. All the theoretical derivations presented in the aforementioned papers consider the situation where the phase φ of the speckle interferogram is measured before and after object deformation. The phase change $\Delta\varphi$ related to this deformation is next obtained by subtraction and the result is a wrapped phase map, i.e. its values lie within $[0, 2\pi]$. If the decorrelation tends towards high values, the phase error becomes a uniformly distributed random variable over the same interval. Hence, the noise has the same dynamic as the signal and

all information is lost. However, in the case of continuous deformation measurements made possible with the dynamic phase-shifting technique, the computed phase is unwrapped along the time axis. In this case, phase errors due to decorrelations can accumulate and become larger than 2π . Unfortunately, it seems that no mathematical argument permits to compute easily the statistics of the unwrapped phase errors, since different phase evolutions (rotations of I_M) can lead to the same final result. In particular, without additional information, we do not know how many fringes are actually due to the decorrelation in a phase variation of n fringes, whereas in the wrapped phase case the phase error is always smaller than 2π . Simulations are used in Ref.8 to estimate these new distributions. It must be noted that they are no longer independent of the number of speckles integrated in a pixel. Some measurements of these unwrapped phase errors are presented in the application Chapter of this dissertation.

There is no simple means to limit image-plane decorrelations, apart from actually moving the camera during deformation. High lens magnifications make a given set-up particularly sensitive to this problem. In the case of pupil-plane decorrelations, a given displacement of the speckle pattern results in a proportionally larger decorrelation for a small pupil than for a large one. Opening the lens aperture is thus highly beneficial. It diminishes the effect of pupil-plane decorrelations. It increases the interferogram mean modulation in the case of 2-speckle fields interferometers. In turn, this lowers the variance of the phase errors for both pupil-plane and image-plane decorrelations. Furthermore, it lowers the amount of light required to illuminate a given object or allows to look at larger objects with the same laser power.

A.2.3 Optimum phase estimation

As mentioned in the preceding paragraph, phase errors produced by decorrelations and electronic noise present the same statistics. For small decorrelations, the phase error distribution can be quite well approximated by a Gaussian distribution of variance inversely proportional to the square of the pixel modulation⁸. Similarly, electronic noise can be usually well described by Gaussian distributions. These observations lead to the “design” of an optimum phase filter, as remarked by Huntley and Lehmann.

The starting point of this development is to consider that we dispose of a number N of estimations $\Delta\phi_i$ of a phase value $\Delta\phi$. We suppose moreover that these estimations are unwrapped with respect to one another. To each of these measurements corresponds an error that follows a Gaussian distribution of variance σ_i^2 . A maximum likelihood argument can then be used to calculate the

best possible estimation $\Delta\tilde{\varphi}$ of the phase $\Delta\varphi$. This argument simply states that $\Delta\tilde{\varphi}$ is obtained as the result of a weighted average of the values $\Delta\varphi_i$, using weights that are inversely proportional to the variance of the error distributions:

$$\Delta\tilde{\varphi} = \left(\sum_1^N \frac{1}{\sigma_i^2} \right)^{-1} \sum_1^N \frac{\Delta\varphi_i}{\sigma_i^2} \quad (\text{A-10})$$

In the case of speckle interferometry, one usually considers that the computed phase value $\Delta\varphi$ corresponding to the deformation varies slowly across adjacent pixels. Hence, a group of nine pixels organized in a 3×3 window gives nine estimations of the phase of the central pixel. The error variance in this case is inversely proportional to the product of the modulations of each pixel, before and after deformation. For small decorrelations we can consider that the modulation does not change significantly. In this case, the phase estimation becomes:

$$\Delta\tilde{\varphi} = \left(\sum_1^N I_{Mi}^2 \right)^{-1} \sum_1^N I_{Mi}^2 \Delta\varphi_i \quad (\text{A-11})$$

In the context of the central point of this dissertation, continuous deformation measurements, we will use (A-11) (with $N=9$) as a very efficient tool to attenuate the effect of decorrelations, while at the same time providing a means to estimate phase values of low-modulation pixels. This is an important point as the modulation of any pixel is susceptible to vary quite considerably in the course of a continuous measurement.

Apart from the particular case of continuous deformation measurements where obtaining unwrapped phase values is straightforward, this optimum phase filter can be applied to the wrapped phase maps obtained in the case of classical phase-shifting. In this case, and using similar arguments⁹, it is the two quantities $\sin\Delta\tilde{\varphi}$ and $\cos\Delta\tilde{\varphi}$ that are obtained by calculating a weighted average of the N estimations $\sin\Delta\varphi_i$ and $\cos\Delta\varphi_i$. The weights are the same as in (A-11). A simple arctangent calculation then yields the filtered wrapped phase $\Delta\tilde{\varphi}$. This solution can actually be directly included in the process of the phase determination, in the case of some particular phase-shifting algorithms⁹.

Bibliography

- 1 J. Goodman, Chapter 2 in "Laser Speckle and Related Phenomena", Ed. J.C. Dainty, 1975, Springer Verlag, ISBN 3-540-07498-8.
- 2 E. Ochoa, J.W. Goodman, "Statistical properties of ray directions in a monochromatic speckle pattern", *J. Opt. Soc. Am.* Vol. 73 (1983), pp. 943-949.
- 3 N. Shvartsman, I. Freund, "Speckle spots ride phase saddles sidesaddle", *Opt. Com.* Vol. 117 (1995), pp. 228-234.
- 4 L. Leushacke, M. Kirchner, "Three-dimensional correlation coefficient of speckle intensity for rectangular and circular apertures", *J. Op. Soc. Am. A*, Vol. 7 (1990) No. 5, pp. 827-832.
- 5 M. Lehmann, "Optimization of wavefield intensities in phase-shifting speckle interferometry", *Opt. Com.* Vol. 118 (1995), pp. 199-206.
- 6 M. Lehmann, "Phase-shifting speckle interferometry with unresolved speckles: A theoretical investigation", *Opt. Com.* Vol. 128 (1996), pp. 325-340.
- 7 M. Lehmann, "Measurement optimization in speckle interferometry: the influence of the imaging aperture", *proc. SPIE* Vol. 2782 (1996), pp. 408-419.
- 8 M. Lehmann, "Decorrelation-induced phase errors in phase-shifting speckle interferometry", *Appl. Opt.*, scheduled for publication April 1997.
- 9 J.M. Huntley, "Random phase measurement errors in digital speckle pattern interferometry", *Proc. SPIE* 2544 (1995), pp. 246-257.

Appendix B: Mathematical derivations

B.1 Morlet wavelet transform approximation

The goal is to calculate the wavelet transform $S(a,b)$ of a signal $s(t)$ of the form:

$$s(t) = B(t) \exp(i\varphi_s(t)) \quad (\text{B-1})$$

where:

$$\begin{aligned} \varphi_s(t) &= \varphi_s(b) + \varphi'_s(b)(t-b) + \frac{1}{2} \varphi''_s(b)(t-b)^2 \\ B(t) &= \sum_{k=0}^{\infty} \frac{1}{k!} B^{(k)}(b)(t-b)^k \end{aligned} \quad (\text{B-2})$$

The Morlet wavelet transform is defined as:

$$S(a,b) = \frac{1}{a} \int_{-\infty}^{+\infty} s(t) \exp\left(-\frac{(t-b)^2}{2a^2}\right) \exp\left(-i \frac{\omega_0}{a}(t-b)\right) dt \quad (\text{B-3})$$

Replacing $s(t)$ by its development gives:

$$\begin{aligned} S(a,b) &= \frac{1}{a} \int_{-\infty}^{+\infty} \left(\sum_{k=0}^{\infty} \frac{1}{k!} B^{(k)}(b)(t-b)^k \right) \exp\left(-\frac{(t-b)^2}{2a^2}\right) \\ &\quad \times \exp\left(i\varphi_s(b) + i\left(\varphi'_s(b) - \frac{\omega_0}{a}\right)(t-b) + \frac{i}{2} \varphi''_s(b)(t-b)^2\right) dt \end{aligned} \quad (\text{B-4})$$

$$S(a,b) = \frac{e^{i\varphi_s(b)}}{a} \int_{-\infty}^{+\infty} \left(\sum_{k=0}^{\infty} \frac{1}{k!} B^{(k)}(b)(t-b)^k \right) \dots \tag{B-5}$$

$$\dots \times \exp\left(i \left(\varphi'_s(b) - \frac{\omega_0}{a} \right) (t-b) \right) \exp\left(- \left(\frac{1}{a^2} - i\varphi''_s(b) \right) \frac{(t-b)^2}{2} \right) dt$$

Let $q = \frac{\omega_0}{a} - \varphi'_s(b) \quad q \in \mathbf{R}$ (B-6)

$$\beta^2 = \frac{1}{2a^2} (1 - ia^2\varphi''_s(b))$$

Since $\text{Re}(\beta^2) > 0$ we can write β^2 as:

$$\beta^2 = \frac{1}{2a^2} \sqrt{1 + a^4\varphi''_s{}^2(b)} e^{i\theta} \quad \text{with } \theta = -\arctan a^2\varphi''_s(b), \quad \theta \in \left] -\frac{\pi}{2}, \frac{\pi}{2} \right[\tag{B-7}$$

We choose the positive solution for β :

$$\beta = \frac{1}{a\sqrt{2}} (1 + a^4\varphi''_s{}^2(b))^{\frac{1}{4}} \exp\left(-i\frac{1}{2} \arctan a^2\varphi''_s(b) \right) \tag{B-8}$$

Using β^2 and q (B-5) becomes:

$$S(a,b) = \frac{e^{i\varphi_s(b)}}{a} \int_{-\infty}^{+\infty} \left(\sum_{k=0}^{\infty} \frac{1}{k!} B^{(k)}(b)(t-b)^k \right) \tag{B-9}$$

$$\times \exp(-iq(t-b)) \exp(-\beta^2(t-b)^2) dt$$

Replacing t by $x + b$ yields:

$$S(a,b) = \frac{e^{i\varphi_s(b)}}{a} \sum_{k=0}^{\infty} \frac{1}{i^k k!} B^{(k)}(b) \int_{-\infty}^{+\infty} (ix)^k e^{-\beta^2 x^2} e^{-iqx} dx \tag{B-10}$$

We find in Ref.1 that:

$$\int_{-\infty}^{+\infty} (ix)^k e^{-\beta^2 x^2} e^{-iqx} dx = 2^{-\frac{k}{2}} \sqrt{\pi} \beta^{-k-1} \exp\left(-\frac{q^2}{8\beta^2} \right) D_k \left(\frac{q}{\beta\sqrt{2}} \right) \tag{B-11}$$

when $\text{Re}(\beta) > 0$ and $\text{Re}(k) > -1$, which is true here. D_k is defined as:

$$D_k(z) = (-1)^k \exp\left(\frac{z^2}{4} \right) \frac{\partial^k}{\partial z^k} \exp\left(-\frac{z^2}{2} \right) \quad \text{for } k \geq 0 \tag{B-12}$$

We can now rewrite (B-10) using (B-11) and (B-12):

$$S(a,b) = \frac{e^{i\varphi_s(b)}}{a} \sum_{k=0}^{\infty} \frac{(-i)^k}{k!} B^{(k)}(b) 2^{-\frac{k}{2}} \sqrt{\pi} \beta^{-k-1} \exp\left(-\frac{q^2}{8\beta^2}\right) \times (-1)^k \exp\left(\frac{q^2}{8\beta^2}\right) \left(\frac{\partial^k}{\partial z^k} \exp\left(-\frac{z^2}{2}\right)\right) \Bigg|_{z=\frac{q}{\beta\sqrt{2}}} \quad (\text{B-13})$$

$$S(a,b) = \frac{e^{i\varphi_s(b)}}{a} \sum_{k=0}^{\infty} \frac{i^k}{k!} B^{(k)}(b) 2^{-\frac{k}{2}} \sqrt{\pi} \beta^{-k-1} \left(\frac{\partial^k}{\partial z^k} \exp\left(-\frac{z^2}{2}\right)\right) \Bigg|_{z=\frac{q}{\beta\sqrt{2}}} \quad (\text{B-14})$$

$$S(a,b) = \sqrt{\pi} \frac{e^{i\varphi_s(b)}}{a} \beta^{-1} \sum_{k=0}^{\infty} \frac{i^k}{k!} B^{(k)}(b) (2\beta^2)^{\frac{k}{2}} \left(\frac{\partial^k}{\partial z^k} \exp\left(-\frac{z^2}{2}\right)\right) \Bigg|_{z=\frac{q}{\beta\sqrt{2}}} \quad (\text{B-15})$$

Using relations (B-6) and (B-8) we obtain:

$$S(a,b) = \sqrt{2\pi} e^{i\varphi_s(b)} \left(1 + a^4 \varphi_s^{\prime\prime 2}(b)\right)^{\frac{1}{4}} \exp\left(i\frac{1}{2} \arctan a^2 \varphi_s^{\prime\prime}(b)\right) \times \sum_{k=0}^{\infty} \frac{i^k}{k!} B^{(k)}(b) \left(\frac{a^2}{1 - ia^2 \varphi_s^{\prime\prime}(b)}\right)^{\frac{k}{2}} \left(\frac{\partial^k}{\partial z^k} \exp\left(-\frac{z^2}{2}\right)\right) \Bigg|_{z=\frac{\omega_0 - a\varphi_s'(b)}{\sqrt{1 - ia^2 \varphi_s^{\prime\prime}(b)}}} \quad (\text{B-16})$$

Noting that:

$$\text{for } z = \frac{\omega_0 - a\varphi_s'(b)}{\sqrt{1 - ia^2 \varphi_s^{\prime\prime}(b)}} \quad \frac{\partial \varphi_s'}{\partial z} = -\frac{\sqrt{1 - ia^2 \varphi_s^{\prime\prime}(b)}}{a} \quad \frac{\partial^2 \varphi_s'}{\partial z^2} = 0 \quad (\text{B-17})$$

and since one can show by recurrence that:

$$\frac{\partial^k f(z)}{\partial z^k} = \left(\frac{\partial X}{\partial z}\right)^k \frac{\partial^k f(z(X))}{\partial X^k} \quad \text{when } \frac{\partial^2 X}{\partial z^2} = 0 \quad (\text{B-18})$$

we obtain:

$$\left(\frac{\partial^k}{\partial z^k} \exp\left(-\frac{z^2}{2}\right)\right) \Bigg|_{z=\frac{\omega_0 - a\varphi_s'(b)}{\sqrt{1 - ia^2 \varphi_s^{\prime\prime}(b)}}} = (-1)^k \left(\frac{1 - ia^2 \varphi_s^{\prime\prime}(b)}{a^2}\right)^{\frac{k}{2}} \dots \times \left(\frac{\partial^k}{\partial X^k} \exp\left(-\frac{(\omega_0 - aX)^2}{2(1 - ia^2 \varphi_s^{\prime\prime}(b))}\right)\right) \Bigg|_{X=\varphi_s'(b)} \quad (\text{B-19})$$

The substitution of (B-19) in (B-16) finally gives:

$$S(a,b) = \sqrt{2\pi} \exp i \left(\varphi_s(b) + \frac{1}{2} \arctan a^2 \varphi_s''(b) \right) \left(1 + a^4 \varphi_s''^2(b) \right)^{-\frac{1}{4}} \\ \times \sum_{k=0}^{\infty} \frac{(-i)^k}{k!} B^{(k)}(b) \left(\frac{\partial^k}{\partial X^k} \exp \left(-\frac{(\omega_0 - aX)^2}{2(1 - ia^2 \varphi_s''(b))} \right) \right) \Big|_{X=\varphi_s'(b)} \quad (\text{B-20})$$

B.2 Morlet wavelet transform along the ridge

The ridge of the transform is defined as the set of points $(a(b), b)$ for which

$$\frac{\omega_0}{a(b)} = \varphi_s'(b) \quad (\text{B-21})$$

The restriction of the transform to the ridge, called the skeleton, is thus:

$$S(a(b),b) = \sqrt{2\pi} \exp i \left(\varphi_s(b) + \frac{1}{2} \arctan a^2(b) \varphi_s''(b) \right) \left(1 + a^4(b) \varphi_s''^2(b) \right)^{-\frac{1}{4}} \\ \times \sum_{k=0}^{\infty} \frac{(-i)^k}{k!} B^{(k)}(b) \left(\frac{\partial^k}{\partial X^k} \exp \left(-\frac{(\omega_0 - a(b)X)^2}{2(1 - ia^2(b) \varphi_s''(b))} \right) \right) \Big|_{X=\frac{\omega_0}{a(b)}} \quad (\text{B-22})$$

One can show by recurrence that:

$$\left(\frac{\partial^{2p+1}}{\partial z^{2p+1}} \exp \left(-\frac{z^2}{2} \right) \right) \Big|_{z=0} = 0 \quad (\text{B-23})$$

Hence, all odd k values in the sum in (B-22) disappear:

$$S(a(b),b) = \sqrt{2\pi} \exp i \left(\varphi_s(b) + \frac{1}{2} \arctan a^2(b) \varphi_s''(b) \right) \left(1 + a^4(b) \varphi_s''^2(b) \right)^{-\frac{1}{4}} \\ \times \sum_{k=0}^{\infty} \frac{(-1)^k}{(2k)!} B^{(2k)}(b) \left(\frac{\partial^{2k}}{\partial X^{2k}} \exp \left(-\frac{(\omega_0 - a(b)X)^2}{2(1 - ia^2(b) \varphi_s''(b))} \right) \right) \Big|_{X=\frac{\omega_0}{a(b)}} \quad (\text{B-24})$$

Calculating the sum in (B-24) up to the second order yields:

$$S(a(b),b) = \sqrt{2\pi} \exp i \left(\varphi_s(b) + \frac{1}{2} \arctan a^2(b) \varphi_s''(b) \right) \left(1 + a^4(b) \varphi_s''^2(b) \right)^{-\frac{1}{4}} \\ \times \left(B(b) + \frac{a^2(b) \exp(i \arctan a^2(b) \varphi_s''(b))}{2\sqrt{1 + a^4(b) \varphi_s''^2(b)}} B''(b) \right) \quad (\text{B-25})$$

Curriculum vitae

Name: Xavier COLONNA DE LEGA

Current title: Optics Engineer, Dipl. Ecole Supérieure d'Optique

Status: French, married, born on the 12th of December 1966, Nancy, France

Office address:

Institut de Mesure et Analyse des Contraintes
Département de Génie Civil
Ecole Polytechnique Fédérale de Lausanne
CH-1015 Lausanne Suisse
Tel. (41) 21 693 2455 Email: colonna@imac.dgc.epfl.ch

Home address:

Ch. de Renens, 10
CH-1004 Lausanne Suisse
Tel. (41) 21 625 1194

Education:

- 1984 Bachelor degree C (scientific section), Bar-le-Duc, F.
- 1984-86 Preparation classes (math and physics), Metz, F.
- 1986-89 Ecole Supérieure d'Optique, Orsay, F.
- 1994-97 PhD student, Swiss Federal Institute of Technology.

Experience:

- 1985-86 Summer internships at Essilor: vacuum deposition of antireflection coatings; optical leveling instruments maintenance.
- 1988 Essilor, student-engineer internship (3 months): lens design.
- 1989 Saint-Gobain, school-industry internship (1 month): study of windshields defects using interferometry.
- 1989 Junior Enterprise: mechanical and optical design of a projection lens for Société des Ciments Français.
- 1989 Angénieux, Diploma work (3 months): software tools for the computation of the optical polychromatic modulation transfer function of lenses.
- 1989 Essilor (Sept.-Dec.), lens designer position: creation of a telescopic visual-aid combination including an aspherical spectacle lens and an intraocular lens.
- 1990-91 Thin Films Laboratory, Optical Sciences Center, University of Arizona, USA: development of a cat's eye lens interferometer for in situ measurement of stress buildup in thin dielectric films on silicon and glass substrates. Study of stress variations induced by ion aided deposition in TiO₂ and SiO₂ films.
- 1991-97 Stress Analysis Laboratory (IMAC), Swiss Federal Institute of Technology, research assistant: development of image acquisition systems and analysis algorithms for the processing of interferometric fringe patterns; industrial research contracts; supervision of hands-on laboratories for final semester students.

Oral presentations:

“Low-vision aid using high-minus intraocular lens”, B. Garnier, X. Colonna de Lega, *Ophthalmic and Visual Optics Conference*, Optical Society of America, Santa Fe (USA), February 1991.

“Exemples d’application des techniques de lumières structurée en génie civil et médical”, séminaire *L’optique dans les contrôles non destructifs*, organisé par le club holographie de la SFO, Orsay (F), November 1992.

“Interferometric deformation measurement using object induced dynamic phase-shifting”, X. Colonna de Lega, P. Jacquot, *Lasers, optics and vision for productivity in manufacturing*, Europto SPIE, Besançon (F), June 1996.

“Continuous deformation measurement using dynamic phase-shifting and wavelet transforms”, X. Colonna de Lega, *Applied Optics and Optoelectronics*, IOP, Reading (UK), September 1996.

Publications:

“Low-vision aid using high-minus intraocular lens”, B. Garnier, X. Colonna de Lega, *Applied Optics* Vol. 31 (1992), No. 19, pp. 3632-3636.

“Common-path holographic interferometer for flatness testing”, P. Jacquot, X. Colonna de Lega, P.M. Boone, *SPIE* Vol. 2248, pp. 125-134.

“Deformation measurement with object-induced dynamic phase-shifting”, X. Colonna de Lega, P. Jacquot, *Applied Optics* 35 (1996), No. 25, pp. 5115-5121.

“Interferometric deformation measurement using object induced dynamic phase-shifting”, X. Colonna de Lega, P. Jacquot, *Proceedings SPIE, Europto Series*, Vol. 2782 (1996), pp. 169-179.

“Continuous deformation measurement using dynamic phase-shifting and wavelet transforms”, X. Colonna de Lega, *Proceedings Applied Optics Division Conference*, Reading 1996, Institute of Physics Publishing, pp. 261-267.